Nano-Bonding of Silicon Oxides-based surfaces at Low Temperature: Bonding Interphase Modeling via Molecular Dynamics and Characterization of Bonding Surfaces Topography, Hydro-affinity and Free Energy.

by

Shawn D. Whaley

A Dissertation Presented in Partial Fulfillment
of the Requirements for the Degree
Doctor of Philosophy

Approved November 2011 by the
Graduate Supervisory Committee:

Robert Culbertson, Chair
Nicole Herbots
Ralph Chamberlin
Stuart Lindsay
Robert Marzke
Peter Rez

ARIZONA STATE UNIVERSITY

December 2011

ABSTRACT

In this work, a new method, "Nanobonding™" [1,2] is conceived and researched to bond Si-based surfaces, via nucleation and growth of a 2 D silicon oxide SiO_xH_x *interphase* connecting the surfaces at the nanoscale across macroscopic domains. Nanobonding cross-bridges two smooth surfaces put into mechanical contact in an O_2/H_2O mixed ambient below T ≤200 °C via arrays of SiO_xH_x molecules connecting into a continuous macroscopic bonding interphase. Nano-scale surface planarization via wet chemical processing and new spin technology are compared via Tapping Mode Atomic Force Microscopy (TMAFM) , before and after nano-bonding.

Nanobonding uses precursor phases, 2D nano-films of β-cristobalite (β-c) SiO_2, nucleated on Si(100) via the Herbots-Atluri (H-A) method [1]. β-c SiO_2 on Si(100) is ordered and flat with atomic terraces over 20 nm wide, well above 2 nm found in native oxides. When contacted with SiO_2 this ultra-smooth nanophase can nucleate and grow domains with cross-bridging molecular strands of hydroxylated SiO_x, instead of point contacts. The high density of molecular bonds across extended terraces forms a strong bond between Si-based substrates, nano-bonding [2] the Si and silica.

A new model of β-cristobalite SiO_2 with its <110> axis aligned along Si[100] direction is simulated via ab-initio methods in a nano-bonded stack with β-c SiO_2 in contact with amorphous SiO_2 (a-SiO_2), modelling cross-bridging molecular bonds between β-c SiO_2 on Si(100) and a-SiO_2 as during nanobonding. Computed total energies are compared with those found for Si(100) and a-SiO_2

and show that the presence of two lattice cells of β-c SiO_2 on Si(100) and a-SiO_2 lowers energy when compared to Si(100)/ a-SiO_2

Shadow cone calculations on three models of β-c SiO_2 on Si(100) are compared with Ion Beam Analysis of H-A processed Si(100). Total surface energy measurements via 3 liquid contact angle analysis of Si(100) after H-A method processing are also compared.

By combining nanobonding experiments, TMAFM results, surface energy data, and ab-initio calculations, an atomistic model is derived and nanobonding is optimized.

[1] US Patent 6,613,677 (9/2/03), 7,851,365 (12/14/10),

[2] Patent Filed: 4/30/09, 10/1/2011

ACKNOWLEDGMENTS

The writer would like to acknowledge all of the people that assisted in the research of this thesis and/or helped me personally during the tasks involved in this thesis.

Dr. Nicole Herbots is personally responsible for pervading the idea of coming back to graduate school to pursue my Ph. D. She also provided the research ideas that lead to the research and findings in this thesis. I believe that this dissertation would not exist at all without her input. I would also want to thank Dr. Robert Culbertson for being the chair of my committee. He has provided guidance throughout that was helpful in many ways.

My committee consists of several other individuals whom I admire and deserve my appreciation. Peter Rez has guided me through the simulations that form a crucial portion of this thesis. It not only provide another avenue to explore, but has formed a cornerstone of this dissertation. I am deeply indebted to him. Dr. Stuart Lindsay has provided me with opportunities over the last several years and continues to help me as I take on teaching at a university level. Dr. Robert Marzke is one of the first professors that I worked for at ASU nearly 20 years ago. He showed me what it was to care about students, which is why I asked him to be on my committee. He has shown that the caring can make a difference. Finally, Dr. Ralph Chamberlin has shown his kindness in talking to me during the thermodynamics class that I sat in on to prepare for my oral exams, remembering when I took his class and how difficult it was. I thank him for his work that is involved to be on this committee.

I have had many co-workers during the last three years. Each helped in big and small ways to form me, through interaction and work. These include Murdock Hart, J.D. Bradley, Qian Bradley, David Sell, Ashlee Murphy, Ross Bennett-Kennett, San Farmer, and Matthew Bade. Without these individuals, I would not have accomplished as much, nor learned as much.

I need to thank a lot of individuals that assisted me in both ways that directly relate to the thesis and in support as friends and collogues. This includes all the support that I have had from Jon Mull, telling me that I could accomplish this task. David Wright had small input into numerous issues along the way. Ken Mossman help in a number of matters that involved the AFM imaging of samples. Dr. Michael Thorpe, who encouraged me to be the best teacher that I could be and always made me feel that my input, in the course that I worked with him, was valuable. Barry Wilkens has helped with various inputs that no one could measure the importance of. His help has been immense.

The biggest thanks must go to my wife, Chandra. The support that I have received from her outweighs that from anyone. She believes in me. I am glad that I have had her help and she is glad the she has learned numerous facts about “silicone geraniums”, whatever that is.

TABLE OF CONTENTS

Page

CHAPTER Page

LIST OF TABLES

LIST OF FIGURES

Figure Page

Figure Page

Chapter 1: Introduction and Thesis Motivation

1.1 What is Nano-Bonding™, why study it, why model it?

The present dissertation research was undertaken under the to investigate a new mechanism of bonding directly large surface domains between silicon-based substrates using only silicon-based materials at the nano-scale using only the nucleation of oxide molecules as molecular cross-bridges between the two.

The goal of this work is to nucleate and grow a silicon oxide –based molecular phase and bond via a large number of cross-bridging molecular strands two silicon-based surfaces *hermetically* and *without* the use of any external bonding material. The new method that the present research optimized experimentally and attempted to model atomistically is now called Nano-Bonding™

The motivation behind Nano-bonding™ is to nucleate and grow oxides nano-phases that enable the formation of an interfacial bond both compatible with silicon electronics processing and with the demands of hermeticity in medical electronics used for human device implants and other adverse saline environments where integrated sensing electronic devices are needed.

The following premise is used to enable Nano-bonding™: a new class of nano-phases, consisting of new, ordered, 2 nm thick oxides ("nano-oxides") was recently discovered and patented in the Combined Ion and Molecular Deposition (CIMD) SiO_2 Research Group in the Department of Physics at Arizona State University. These nano-phases consist of ordered, dis-commensurate and/or

commensurate heteroepitaxial phases of tetragonally distorted molecular sheets of cubic β-cristobalite SiO_2 on Si(100). Both ordered and heteroepitaxial phases are stabilized via a three-step far-from equilibrium kinetic mechanism, the Herbots-Atluri method [1], and part of two US patents , 6,617,637, granted to ASU in 2003 and 7,581, 365 granted to ASU in 2010.

This 3-step far-from-equilibrium kinetic mechanism is called either the "Herbots-Atluri Clean, Process or method", a.k.a as the "H-A clean or method" depending on whether the application focuses solely on surface preparation (clean) or on interphase formation (method).

The H-A clean or process involves an ordered sequence of three key geometric, chemical and physical steps [1]:

(1) The geometric planarization of Si(100) surfaces via the Herbots-Alturi method where atomic terraces are extended on average to 200 nm in width, from the average 2 nm width found in high grade Si1(100) wafer with a <100> axis miscut less than 0.25°.

(2) The chemical termination of Si(100) at 80°C as a (1x1)OH-Si(100) surface

(3) The nucleation and growth of the initial two molecular layers of silicon oxide in the form of a solid solution with a 1:1 ratio of hydrogen to oxygen to reduce electrostatic repulsion between oxygen atoms, and reduce the buckling of oxide molecular sheets under the well-known 40% volume expansion occurring during silicon oxidation.

This geometric, chemical and electrostatic kinetic stabilization leads to the formation of about two molecular layers of flat, ordered cubic ß-cristobalite SiO_2 monolayers, in the form of a stack whose height is about two unit cells above the surface. This nano-phase extends in a two-dimensional molecular sheet whose aspect ratio between its areal dimensions A and height H, $r = A/H >> 1$.

This two-dimensional nano-oxide phase is shown in the present thesis to act as precursor phase to Nano-Bonding™. It enables the nucleation and growth of a bonding nanophase between two planarized surface via its unique geometry and chemistry.

The present doctoral thesis describes the first systematic experimental and atomistic modeling study of Nano-bonding™ between Si(100) and thermally oxidized Si(100) wafers and substrates

Experimental work conducted in this work involves both

(a) systematic synthesis of the bonding nanophases and

(b) detailed characterization of the nano-bonded surfaces before and after Nano-Bonding at the optical and nano-scale.

Nano-Bonding™ itself is conducted in a class 10 environment compatible with semiconductor 1"-16" wafer processing. The experiments used a variety of class 10 Wet Chemical Laminar flow hood benches, glove-boxes, and spin processing apparatus, the latter in a state-of-the-art manufacturing facility at Entrepix, Inc, in Tempe. Besides the spin processing conducted at Entrepix, Inc, facilities, all of the synthesis Nano-Bonding™ experiments were conducted in the class 100 CIMD/SiO_2 laboratory, which is located inside the Ion Beam Analysis

of Materials (I-BeAM) facility in the Goldwater Building at Arizona State University. The I-BeAM facility is part of the Leroy Eyring Center for Solid State Science and the CIMD clean room laboratory is part of the Department of Physics.

The design, upgrade and construction of the Nano-Bonding™ tools, including the Class 10 wet chemical processing bench for the H-A clean & process of the substrates to be bonded and of the Class 100 environment where the subsequent Nano-Bonding™ process takes place are all part of the experimental component of the present dissertation.

Characterization and modeling of Nano-Bonding™ of Si-based surfaces involve mainly two experimental methods and several *ab-initio* calculations approaches.

The first experimental characterization method is topographical analysis via optical microscopy followed by detailed, systematic large and small area Tapping Mode Atomic Force Microscopy (TMAFM). Both optical analysis and TMAFM is conducted on the susbtrates surfaces (1) before the Herbots-Atluri clean, (2) after the Herbots-Atluri clean, (3) after Nano-bonding™ and (4) debonding. Quantitative analysis of the several scales used for acquiring TMAFM topographs involve power spectral density analysis.

A second, independent experimental surface characterization method is a new quantitative measurement method of *hydro-affinity* . Hydro-affinity is typically observed optically first as the qualitative property of a surface being *hydrophilic* or *hydrophobic*. To measure hydro-affinity, a new technique

developed by Carré in 2008 measures the total surface energy and its three components based on the Van Oss model for semiconducting and insulating surfaces [2]. The Van Oss theory uses sessile drop contact angle analysis (SDCAA) with *three different liquids* and the modified Young-Dupré equation [2].

A special class 100 measurement bench for SDCAA using 18 MΩ DI water, glycerin and alpha-bromo-napthalene was designed, constructed and optimized to collect this data in optimum conditions for this work.

Ab-initio calculations are conducted to model Nano-bonding™. The nanophase stack simulated includes a Si(100) substrate with a heteroepitaxial phase of ß-cristobalite SiO_2 rotated 45° around the [001] direction . Simulations are conducted using several approximations to compute and compare the total energy for different atomistic model of the precursor phase.

1.2 Genesis of Nano-Bonding

The 3-step far-from-equilibrium kinetic mechanism is called either the "Herbots-Atluri Clean or Process" (H-A clean or process) depending on whether the application focuses solely on surface preparation or on interphase formation.

The three-step far-from equilibrium kinetic mechanism, enabling nucleation and growth of the new Nano-Bonding™ oxide phases is predicated on the Herbots-Atluri (H-A) method, a wet chemical cleaning processes that creates a smooth Si(100) surface [1]. The H-A method extends on Si(100) surfaces the size of atomic terraces into large surface domains which average 20 nm in width without disruption from atomic steps or debris. These dimensions are an order of

magnitude larger than can be obtained by the classic "RCA clean", the standard for Si surface processing in the semiconductor industry. The so-called RCA clean was developed by W. Kern of the RCA Corporation in 1965 and published in 1970 [3]. The RCA clean uses wet chemistry in two steps, a first to remove particles, organic contamination, the so-called "SC1" , which scrubs the surface clean, and a second step, the so-called "SC2", which oxidizes the surface to remove alkali and heavy metal contamination while creating a new, porous chemical oxide on top of the original oxide. The RCA clean creates a Si(100)/SiO_2 interface where the atomic terraces exhibit surface domains that are ten times smaller, at 2 nm in width, than the H-A method.

Five High Resolution Transmission Electron Microscopy (HRTEM) micrographs of Si(100) /SiO_2 interfaces after processing by the RCA method (A) and the H-A method (B) are shown in Figure 1-1 [1].

After the RCA clean in (A), the interface of the Si(100) surface with the Silicon oxide exhibits a large number of atomic steps every few inter-atomic distances (a_{Si} = 0.543 nm, thus 4 interatomic distances are about 2.2 nm), which disrupts order at the interface and show buckling of the oxidized layers.

After Si(100) has undergone the H-A method in (B), only one atomic step is observable after 26 interatomic distances (thus about 14 nm) as counted from the left towards the central step, marked "1" in the (B) part of the image, and 39 interatomic (210 nm) distances from the central step towards the right edge of the image.

The extended HRTEM micrographs show in Figure 1-2 are four different 45 nm segments of SiO_2 /Si(100) interfaces taken on different samples [1]. Each exhibits the same characteristic interface smoothness with extended atomic terraces. One single atomic step is seen along the 45 nm interface segment.

The H-A clean also produces an ordered surface. Independent experiments detect both ordering and planarity. Reflection High Energy Electron Diffraction (RHEED) diffraction is shown at 10 keV in a 10^{-10} Torr vacuum at 0.75° incidence to Si(100) is in Figure 1-3 [1]. In (A), as-received Si(100) surface is disordered : only bulk Si(100) diffracts. In (B-C) Si(100) is first subjected to H-A processing in (B) and subsequently annealed at 600 K for 10 minutes in (C). Two-dimensional streaks in RHEED patterns, aligned with Si(100) diffraction spots, prove that H- surfaces are truly two-dimensional But H-A processed Si(100) shows a (1x1) pattern in (B) thus an ordered commensurate surface while annealed H-A Si(100) in (B) exhibits a classic (2x1) reconstruction.

Sequential Ion Beam Analysis (IBA) is another experimental technique that detects ordering and heteroepitaxial alignment of SiO_2 on Si(100) , by combining ion channeling with 3.045 ± 0.05 MeV $^{16}O(\alpha,\alpha)O^{16}$ nuclear resonance. Nuclear resonance is a nuclear reaction which increases the cross section of an atom type in the substrate undergoing IBA. The areal density of ^{16}Oyxgen and Silicon is obtained from their respective surface peak for increasing $^4He^{2+}$ ion dose. This approach developed in the CIMD SiO_2 research is called the “damage curve” and plots the areal density of Si and O against the cumulative total ion $^4He^{2+}$ dose.

Using linear regression and error analysis, the original areal densities of Si and O prior to IBA are found via the y-intercept.

Figures 1-4 and 1-5 show the data obtained from a set of damage curves taken along 3 directions, <100>, <110> <111> on H-A processed Si(100) with a SiO_2 on top of which increasingly thicker gate oxides were grown at Intel Corp [1,4]. The areal density of the (1x1) surface of bulk Si is calculated using a Monte Carlo method via the 3DSTRING computer code.

The two figures also show a regression fit, with a slope of 0.5 (perfect 1:2 ratio for Si:O in SiO_2). For the <100> and <110> directs, the data suggests that the silica includes two oxygen atoms for one silicon atom at all thicknesses even as the interface is approached. When compared to data from previous IBA analysis of Si/SiO_2 interfaces, H-A processed beta-SiO_2 on an OH(1x1)Si(100) interface show no displaced atoms at the interface, unlike any other Si/SiO_2 interface, and that a significant amount of disorder is always detected in conventional oxides on Si(100), This implies that the SiO_2 on OH(1x1)Si(100) interface transitions from crystalline Si(100) to another crystal structure without defects and that there is no disorder at the interface, within the error of the measurement.

In addition to the absence of disorder at the ß-cSiO_2/ OH(1x1)Si(100) surface, several atomic layers of Si atoms when the oxide layer is present are found to be shadowed during channeling conducted along the <111> directions, The 54.75° angle for channeling along the <111> axis with respect to the Si(100) surface increased the depth resolution by almost a factor 2 from normal. This can

be seen from the "missing" Si atoms in the areal density measurement of Si in (C) in Figure 1-5. As the oxide grows thicker, the areal density of Si atoms increases, showing that beyond a critical thickness of about two molecular layers of SiO_2, the oxide becomes amorphous.

Shadowing of Si atoms in the presence of a silicon oxide layer implies alignment of Si atoms in the oxide with Si atoms in the bulk Si(100), resulting in shadow cones that reduces the channeling yield from Si atoms within the bulk Si(100) when the silicon oxide is present on the surface.

In order to account for such alignment, a structural model is needed to account for approximately a 2 nm-thick crystalline oxide causing shadowing along <111> at the SiO_2/OH(1x1)Si(100) interface. Several polymorphs of silica were analzyed in the PhD thesis of J. D. Bradley, who demonstrated via 3-D string simulations that cubic β-cristobalite exhibits the best fit to account for the channeling yields along the <100> and the <110> directions and shadowing observed along <111> [5]. In his thesis. J.D Bradley fits the structure of tertagonally distorted β-cristobalite to Si(100), as shown in Figure 1-4, and simulates the IBA channeling data extracted from damage curves shown in Figure 1-6 for all three crystal directions, <100, <110> and <111>.

In the present thesis, a further refinement of the β-cristobalite structure is proposed. By rotating the beta-cristobalite unit cell by 45º around the <001> to match its [110] facet diagonal to two cubic diamond unit cells along their [100] cubic edges, ß-cristoalite can be fitted to Si(100) with a fairly low tetragonal

strain, as is shown in Figure 1-7 when compared to the simplest tetragonal distortion along the z-axis of the cubic unit cell.

The geometric and chemical properties of this new family of two-dimensional nano-phases are such that they could be used as new molecular chemisorbate layers, which we defined as precursor phases. Tetragonally distorted β-cristobalite molecular films ordered on Si(100) can initiate nucleation and growth of new bonding phases between Si-based materials which we called interphases because they are confined between two initially materials surfaces.

Nano-bonding™ is the result of control of chemical bonding and phase geometry occurs at the nano-scale, unlike any attempt at wafer bonding before.

It is the unparalleled control of lateral growth over macroscopic interfaces between wafers and devices, into large nano-bonded domains, that leads to the unique aspect ratio and two-dimensional character of the nano-bonding phase, nucleated from precursor phase to result in a nano-bonding phase that be grown in dry or wet conditions, under pressure or at atmospheric pressure.

The motivation for this undertaking to solve issues in wafer bonding and medical implant device integration into a monolithic implant that integrates sensors, medical electronics and/or power sources.

The key innovations brought about this thesis research is to investigate heteroepitaxial phases of tetragonally distorted molecular sheets cubic β-cristobalite on Si(100), to establish both its lattice structure as precursor phase to nano-bonding, and its role as chemical & geometric template.

The first experimental step is the present work was to investigate whether and how β-cristobalite on Si(100) can be act as a precursor phase, in order words as chemical geometric templates created by the H-A process.

That goal was to investigate whether this first experimental approach produces β-cristobalite termination on Si(100) reliably and consistently over large area of the wafer with wide, flat, atomic terraces of this precursor phase, where the β-cristobalite occupies "nano-smooth" surface domains that are approximately 20 nm-wide without disruption from atomic steps or debris.

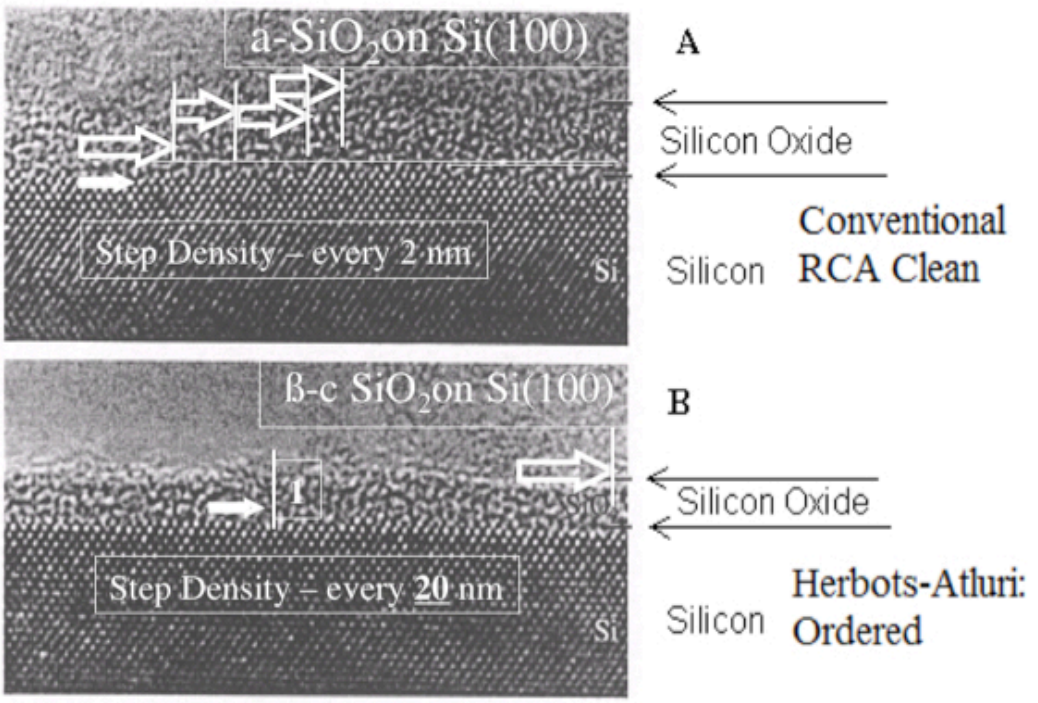

Figure 1-1: HRTEM micrographs of (A) Si(100) cleaned via the RCA clean with a SiO_2 thickness of 20 $\pm$ 2 Å , (B) Si(100) processed via the H-A method with a ß-cSiO_2 thickness of 17 $\pm$ 2 Å [1] (C) four ß-cSiO_2 /Si(100) interfaces, with 1 step along 45 nm.

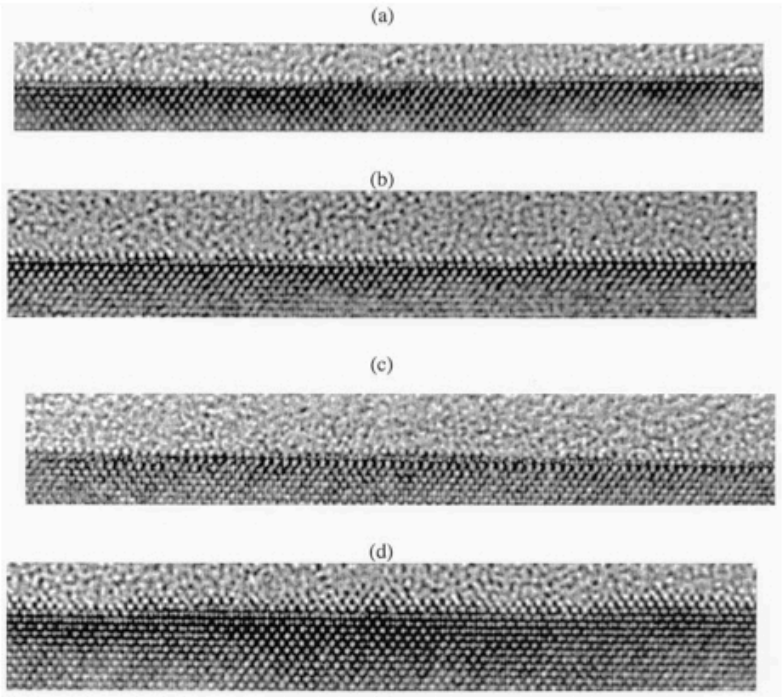

Figure 1-2: HRTEM micrographs of four different 45 nm segments of β-cristobalite/Si(100) interfaces taken on different samples [1].

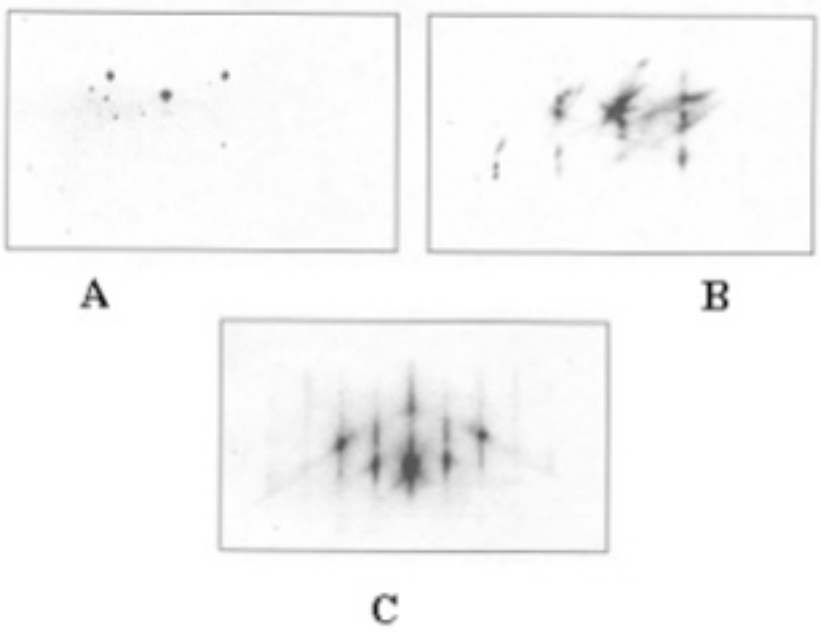

Figure 1-3: RHEED diffraction patterns at 10 keV showing (A) 3-D Unprocessed Si(100) Wafer, (B) (1x1) streak pattern showing order & planarity after H-A processing, at 300 K, (C) Reconstructed (2x1) Si(100) surface after 600 K annealed for 10 minutes. [1]

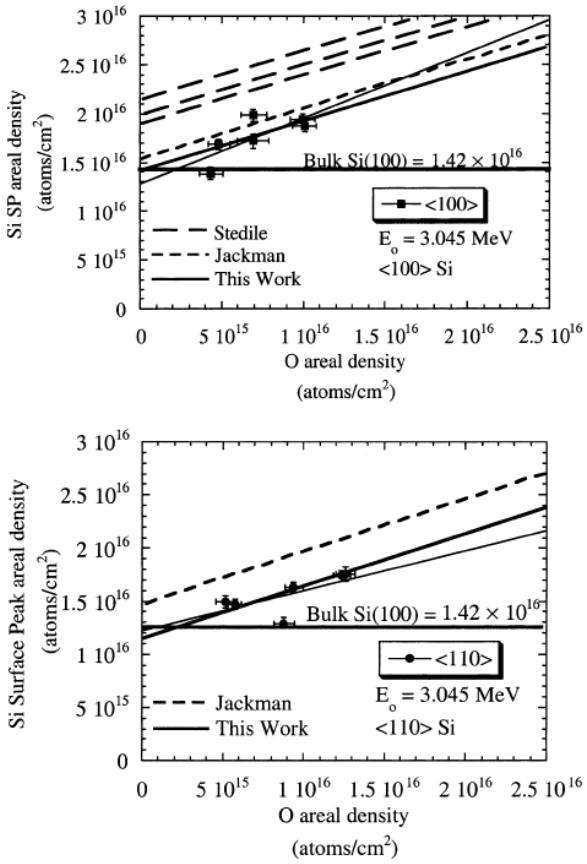

Figure: 1-4: The H-A clean <100> and <110> damage curve data, labeled as Herbots, as well as with data from other groups [1]. The Herbots data has a small deviation at the *y*-intercept for this regression fit, which indicates that there is no disorder, within the error of the measurement, at the surface. The other data shows a non-zero *y*-intercept, indicating disorder.

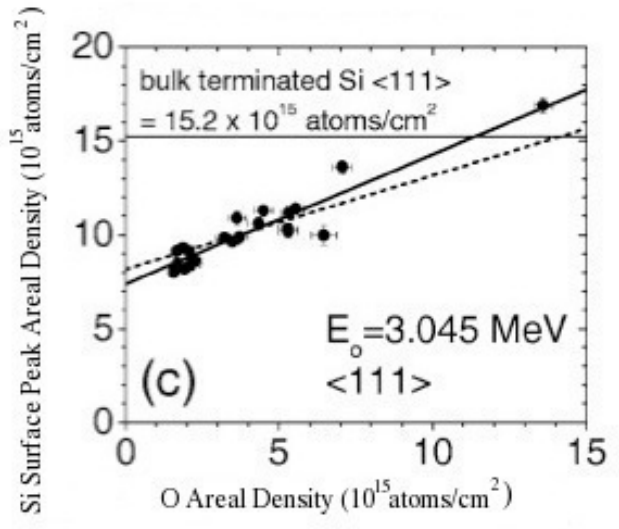

Figure 1-5: A plot of Si surface peak areal density versus that of O for Si substrates that went through the H-A clean and then underwent gate oxidization for the <111> direction [4]. Each plot has a solid regression fit based on the data, as well a dotted line which represents a regression fit with an ideal 0.5 slope. The bulk surface Si amount for each direction is shown in each graph as a horizontal line.

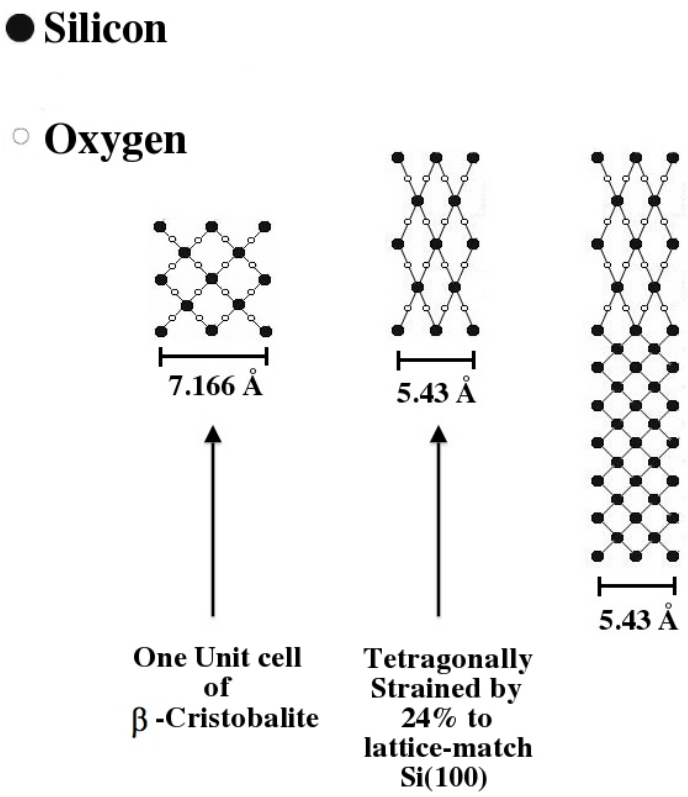

Figure 1-6: Beta-cristobalite is shown in its original cell size, then tetragonally strained to match Si(100) and the layer on a Si(100) crystal

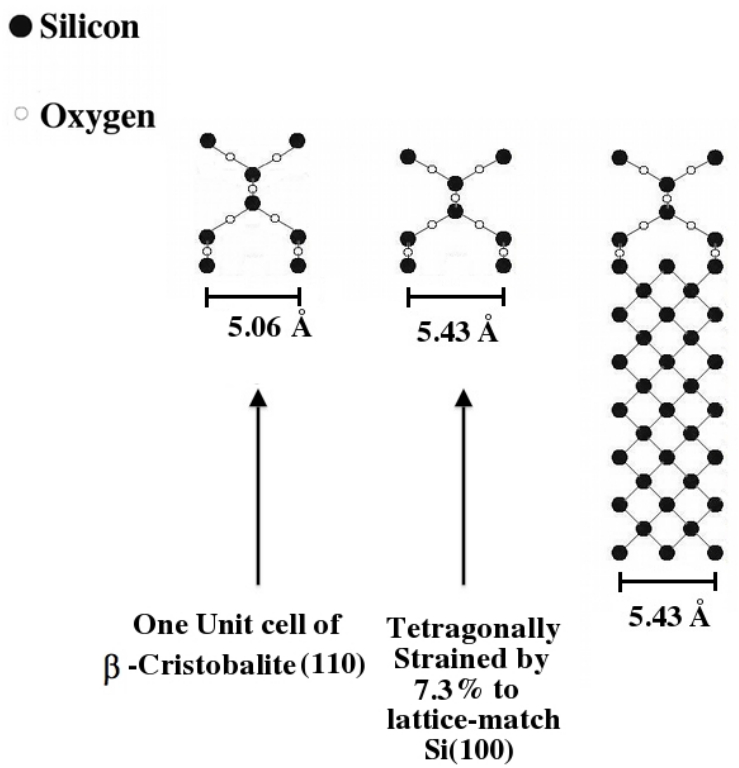

Figure 1-7: Beta-cristobalite rotate 45º to the (110) direction, in its original cell size, then tetragonally strained to match Si(100) and the layer on a Si(100) cystal.

1.3 Thesis Motivation

The motivation for this thesis is to bring a better understanding of the surfaces of Si and SiO_x substrates that undergo chemical processing. One such process may allow bonding of Si(100) to SiO_x at low temperatures ($T < 200ºC$). This type of bonding can be used in the creation of hermetic interfaces where percolation of liquids and in particular corrosive fluids or gasses is prevented. An example of a direct application are single device sensors with their own source and/or radio-emitter, such as atmospheric sensors to be submerged in sea-water [6] or pollutant-laden clouds, and single-device human implants for continuous monitoring of glucose [7], blood pressure or alpha-protein markers for various cancers [7]. In previous published work, Dr. Herbots and her group have chemically processed Si(100) with the Herbots-Atluri (H-A) method [9,1], which will be fully discussed in Chapter 3. Several substrates that underwent the H-A method have been characterized by Fourier Transform Infrared (FTIR) Spectroscopy, Ion Beam Analysis (IBA), Reflection High-Energy Electron Diffraction (RHEED), and others techniques [1].

A model of the surface [5] has been created which posits that at the surface is a several nanometer thick, crystalline oxide, which has been termed a "nano-phase" oxide. This model will be furthered refined in this thesis using calculations based on ion beam interaction with the material and analytical simulations. The results of the calculations and simulations will be compared to the previous models for the oxide nano-phase [5]. A new model of a SiO_x surface that would bond with this Si(100) must be developed. Since the Si(100) is a clean,

smooth and hydrophobic interface with low-disorder, any thin crystalline oxide, SiO_x designed to bond with the Si(100) will need to have specific features. A SiO_x surface chemically created that is hydrophilic due to dangling bonds would produce partial polarization in the smooth, ordered Si(100) surface when the two surfaces are brought in proximity to one another. This should allow initial contact of the two substrates and preliminary bonding. Wet chemistry is used on the Si(100), so the H-A method could possibility be altered to allow such properties in the SiO_x surface, especially since the first stage of the H-A method will minimize the number of particulates and other surface contamination.

Once the two substrates are in contact, minimal pressure to the outside of the bonding pair may be needed to aid in retaining physical contact between them to provide a minimization of the bow and warp differences between substrates. Using the nano-phase theory, the ambient air trapped between the bonding pair will contain O_2 and H_2O. These could react with the nano-phase oxide and form a bridge in the gap between the surfaces, thereby nano-bonding the two surfaces together. Heat treatment, or annealing, may be done at $T < 200ºC$ to increase the reaction rate of the formation of the nano-phase bridge.

The correctness of the models of Si(100) with a nano-oxide and the SiO_x with dangling bonds can be measured. Measurements of the substrate bonding that will be done during the early experimental portion of the bonding. This will start with anecdotal, gross measurements, such as the physical prying apart of the samples to ascertain if the bond is “weak”, “stronger” results were obtained, if minimal force is needed to pry bonded pair apart, etc. If reliable, repeatable

bonding is achieved, then accurate, precise wafer bonding measurements, discussed in detail in Chapter 7, can be used. The Si(100) and SiO_x substrates before processing, after cleaning, and after debonding can be imaged via AFM. At this point, the data attained can be compared to the proposed nano-bonding model to determine if the two are aligned. Any discrepancies will be used to revise the model and future experiments can be planned to broaden the understanding of the low temperature bonding.

Chapter 1 References

[1] N. Herbots, J. M., Shaw, Q. B. Hurst, M.P. Grams, R. J. Culbertson, D. J. Smith, V. Atluri, P. Zimmerman, K. T. Queeney, *Mater. Sc. & Eng* **B87** (2001), 303-316.

[2] A. Carre, *J. Adhesion Sci. Technol*. **21**, 10, 961–981 (2007)

[3] W. Kern, DA Puotinen, *RCA Rev*. **31**, 234-264, (1970)

[4] J. M. Shaw, N. Herbots, Q. B. Hurst, D. Bradley, R. J. Culbertson, V. Atluri, K. T. Queeney, *J. Appl. Phys*. **100**, 10, 104-109 (2006)

[5] J.D. Bradley, *A new heteroepitaxial silicon dioxide nanophase on OH-(1X1) silicon (100) identified via 3.05 MEV ion channeling and the new 3-D multistring code*, Arizona State University, Ph. D. Thesis 2006

[6] N. Herbots, AZ TE Technology Disclosure filed 6/6/2011. "Smart Sea-sensors for underwater applications and Smart Rocks/Smart Sands for dry land monitoring"

[7] US Patent Filed 4/30/2009, "Low Temperature Wafer Bonding including a cross-bonding nano-interphase (SILOXSI). N. Herbots, R. J. Culbertson, J.D. Bradley, M. A. Hart, D. A. Sell and S. D. Whaley

[8] N. Herbots, V. Atluri, J. D. Bradley, S. Banergee, Q. B. Hurst, X. Jiong, US patent 6,613,677 (2003)

Chapter 2: Introduction to Wafer bonding

2.1 Wafer Bonding

Silicon wafers are the main building block for the global semiconductor manufacturing industry. During the last 20 years, semiconductor technology has continued to increase the number of transistors on an Integrated Circuits (IC), relied on increasingly smaller sizes of the transistor gates, and required new and better materials and processes to accomplish these goals. One requirement of the bare silicon is to be free of contamination. Chemical wet processing, or cleaning, of the wafers is the typical way of removing these impurities. The cleaning process will be discussed in the next chapter, in detail. The wafer must also be flat on both a macroscopic level, no bow or warp to the wafer, and on a microscopic level. This microscopic level of flatness is the roughness of the silicon surface. It well known that the roughness of silicon substrate affects the carrier mobility [1].

Another important point in semiconductor processing is the need for wafer bonding. This is the process of adhering two wafers to each other without the use of glue, since glue or cement decays rapidly when exposed to heat and solar UV. Wafer bonding has been used to replace epitaxy, by either bonding a thin slice of a wafer to a second substrate or bonding two wafers and removing, via etching and/or polishing, any unwanted thickness from the top-most wafer. There is also the need to seal components of an IC chip via bonding with quartz or SiO_2 wafers. This chapter outlines the basics of wafer bonding, including the types, history, forces involved, surface energy, and bonding strength measurements. The

information presented in this section forms a basis for later discussions in this thesis.

2.1a Types of bonding

There are four main types of bonding: direct, fusion, anodic, and vacuum. Direct Bonding is the spontaneous or forced lateral annihilation of Van der Waals force when uniting, at ambient conditions, two flat reconstructed surface layers of two separate elements in a one-dimensional process, at an atomic level [3]. These two elements are solid and non-plastically deformable, but can be amorphous, polycrystalline, or single crystal. They can also be the same material or different materials, as well as organic or inorganic.

Fusion bond is clamped or direct bonding which then uses annealing at elevated temperatures to reconstruct the surfaces of the bonded materials and create chemical bonds between them. Anodic bonding is similar to fusion bonding in that annealing is performed, but an electric field is added to drive the bonding. Vacuum bonding uses a direct uniting of the two materials under a vacuum. This can be performed with the addition of annealing.

2.1b Wafer Bonding History

In the 1900s, it was found that highly polished glass pieces would stick to one another, as well as optically flat glass and fused quartz [4]. Parker and Dalladay, [5] in 1917, were the first to anneal optical glass after direct bonding. The 4th Lord Rayleigh, son of the Nobel laureate 3rd Lord Reyleigh, reported in 1936 on the room-temperature adherence of silica [6]. Direct bonding was

continued for optical uses into the 1930's for such uses as interferometers, which included patents by W. E. Williams [7], in 1928, and F. Twyman and J.H. Dowell [8], in 1930. In 1969, Wallis and Pommerantz used anodic bonding to adhere silicon to sodium-containing glasses which had similar thermal coefficients [9]. The first wafer-like bonding occurred in 1975, when Antypas and Edgecumbe [10] transferred a thin GaAs layer onto a glass substrate at elevated temperatures. Modern wafer bonding began in 1985-1986, when silicon wafers were bonded together and then annealed. There were two groups working on this technique, the first consisted of Shimbo *et al.* at Toshiba [11] and the second was Lasky *et al.* at IBM [12]. The Toshiba group investigated bonding silicon wafers without a thermal oxide so that they would be able to have a thick, crystalline, lightly doped silicon on heavily doped silicon without having to epitaxially grow the film. The IBM group used thermal oxide on one or both of the bonded silicon wafers. The top silicon wafer was etched after bonding until it was several microns thick, thus creating a silicon-on-insulator (SOI) structure. This SOI through bonding replaced Separation by Implanted Oxygen (SIMOX) application, where oxygen ions were implanted in high doses into a silicon wafer [13]. This implanted wafer was then annealed at temperatures close to the silicon melting point to form silicon dioxide that would be buried below the upper silicon surface. The SIMOX technique led to dislocations and was very expensive. Petersen and Barth [14], in 1988, worked on Si wafer bonding bonding that would allow pressure sensors. This technique had a cavity structure at the surface of one of the silicon wafers.

The Toshiba and IBM work, did not immediately lead to products for microelectronics [13]. The bonding was difficult to reliably achieve and depended upon a large number of factors. These include the cleanliness of the surface, surface properties, and atmosphere (humidity, vacuum, etc.). Particles of micron size on one of the surfaces could create voids, where bonding was prevented, and could extend for many millimeters. There were also issues with wafer thinning that would take almost a decade to perfect.

2.1c Advantages to wafer bonding

While wafer bonding require a mirror-polished surface, there are now few obstacles with this. Often thin wafers are used, so that the substrates can conform to one another during bonding. Many wafers, such as silicon or gallium arsenide, are polished before bonding using chemical-mechanical polishing (CMP), to remove any unfavorable topography. CMP is widely used in the semiconductor industry and is well understood for typical applications. The bonding process eliminates any soldering, or glues, which could lead to contamination. Wafer bonding has also been integrated in some microelectronic on micromechanical device manufacturing.

2.1d Epitaxy and Wafer Bonding

Epitaxy is a deposition method where a crystalline film is grown on a crystalline substrate. This film is known as an epitaxial film or epitaxial layer. If the film and substrate are of the same material, this is known as homoepitaxial growth and is the simplest type of epitaxy. Heteroepitaxy is the growth of an

epitaxial layer that is of different composition from that of the substrate. The heteroepitaxial film must closely match the lattice constant of the substrate, otherwise there will typically be strain in the film which will lead to misfit dislocations once a critical thickness is achieved. An example is a $Si_{0.92}Ge_{0.08}$ thin film [15]. The layer has high compressive strain until a thickness about 100 nm. At that point, the dislocation density rises and the strain decreases. Thus epitaxy limits the substrates that a film can grow upon, such as a crystalline film on a substrate that is amorphous, highly lattice mismatched, or of the same crystal structure with a different orientation of the lattice. Wafer bonding overcomes these limitations, since the film is not grown on the substrate.

2.2 Forces of Interaction between Bonding Surfaces

Wafer bonding starts with bringing two surfaces into contact at room temperature. Due to variable conditions, such as humidity, vacuum, etc., there may be different forces which dominate the interaction between the surfaces. The three main forces are van der Waals, electrostatic, and capillary.

2.2a Van der Waals Forces

Van der Waals forces are due to materials that have atoms or molecules that are polarizable. This attractive force, F_v, is short-range on a macroscopic level and diminishes as the distance d increase between two dipoles increase:

$$F_v \propto \frac{1}{d^7} \qquad \text{(Eq. 2-1)}$$

In an application such as a flat surface where there are many dipoles, the force can not be obtained by summing forces from each dipole pair. For two flat plates, the van der Waals force per unit area takes the form [16]:

$$F_v = \frac{A}{6\pi d^3} \qquad \text{(Eq. 2-2)}$$

where A is the Hamaker constant and d is the distance between the two surfaces. This equation can also be used for two surfaces with a medium between them. The Hamaker constant for various surfaces with a intermediate material is shown in Table 2-1.

Surfaces and medium	Hamaker Constant (J)	Reference
Silica-Air-Silica	6.5×10^{-20}	[17]
Silica-Water-Silica	8.3×10^{-21}	[17]
Sapphire-Water-Sapphire	6.5×10^{-20}	[18]

Table 2-1: Hamaker constants for various materials with an intermediate material.

2.2b Coulombic/Electrostatic Forces

When two wafers are bonded in a vacuum, Van der Waals forces are the only forces present. If one is not operating in a vacuum and vapor is present, then chemical and/or physical adsorption take place. Coulombic forces occur if either wafer surface is charged by the presence of electrons or ions that can be adsorbed or desorbed. Coulombic forces are strong and dominate unless water or water vapor is present, since these will compensate for charge.

When bonding two wafers, a vapor may condense in the gap between the wafer surfaces, which screens the electrostatic interaction. When two dissimilar wafer surfaces contact, chemical equilibrium will occur. This can result in a

charge transfer which results in electrostatic attraction that has a range of several microns and has forces in the range of 10 MPa [16]. At humidity levels of less than 5%, electrostatic attraction is the dominant force. If the wafers are in contact with a polar liquid, such as water, they will come into chemical equilibrium with the liquid. If ions are present in the liquid, then they may be attracted to or repelled from the wafer surfaces if a charge resides on either surface. These forces are more than an order of magnitude lower than those due to direct Coulombic forces.

Any charged surface will attract the opposite ions. Since this is a shielded charge, the force is lower than that due to just the charged surface. Therefore, in a polar liquid, there is an attractive Van der Waals force and a repulsive electrostatic force.

2.2c Capillary Force

There are multiple requirements for the formation of a capillary liquid that will cause an attractive capillary force. First, two surfaces must have a vapor which can condense on the surfaces or already have a condensed liquid on them. Additionally, the liquid has to have a contact angle of less than 90° with the surfaces. Finally, the gap between the two surfaces must be smaller than a critical distance, which depends on the condensed liquid's radius of curvature [13]. Figure 2-1 illustrates capillary condensation around an asperity contact. The meniscus curvature of a liquid establishes a Laplace pressure, p_{Lap}, on the liquid:

$$p_{Lap} = \frac{\alpha}{r} \qquad \text{(Eq 2-3)}$$

where r is the radius of curvature and α is the surface tension [13]. The Kelvin equation gives the radius of curvature

$$r = \frac{\alpha V}{kT \ln\left(\frac{p_s}{p}\right)} \qquad \text{(Eq. 2-4)}$$

where V is the molar volume of the liquid, k is Boltzmann's constant, T is the temperature in degrees Kelvin, and p/p_s is the relative vapor pressure of the liquid.

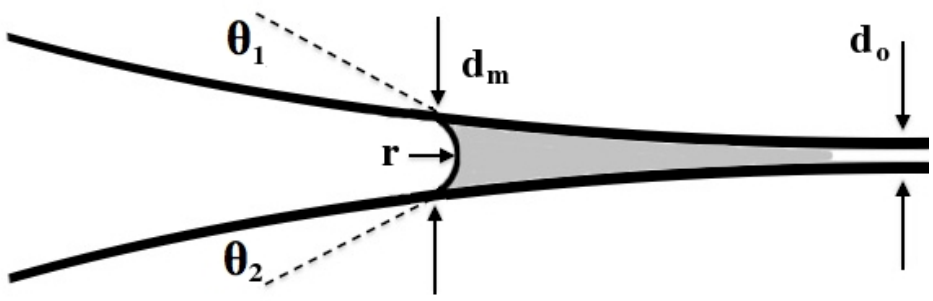

Figure 2-1: Illustration of capillary condensation around an asperity contact based on a figure by Tong and Gosele [13].

The Laplace pressure must be negative to have a force that pulls the two surfaces together. This implies that the meniscus must be concave. The critical distance at which, or below, that a liquid bridge will form is given by:

$$d_m = r(\cos\theta_1 + \cos\theta_2) + d_0 \qquad \text{(Eq. 2-5)}$$

where d_0 is the surface separation at contact and θ_1 and θ_2 are the contact angles for the surfaces [13].

The capillary force is $A\alpha/r$ for two flat surfaces with a contact area of A. The activation energy, W_c, that emanates from the capillary force for two

separated surfaces can be acquired by finding the work done to separate the surfaces against the Laplace pressure:

$$W_c = \int_{d_0}^{d_m} p_{Lap} dx \qquad \text{(Eq. 2-6)}$$

2.3 Surface Energy and Bond Strength Tests

A bonded pair of wafers have an interaction energy which is commonly referred to as the "bonding energy" [13]. The interaction energy per unit area of two bonded wafers can be defined as the work, *W*, needed to separate the wafers to an infinite distance from their contact distance, do, in adiabatic conditions:

$$W = \gamma_1 + \gamma_2 = \int_{d_0}^{\infty} f(d) \cdot dx \qquad \text{(Eq. 2-7)}$$

Where $f(d)$ is the attraction force per unit area as a function of distance and γ_i being the surface energy of each surface at the instant the wafers are separated [15]. Obviously, due to the process of separation, each wafer surface may absorb species from the ambient and therefore be no longer reversible. The wafer surfaces may also reconstruct and lower the surface energy. So, the final surfaces may not represent the original interaction energy. There are four main measurement techniques to acquire the surface energy for a pair of bonded wafers: the knife-edge or crack-opening test, the pressure burst test, the tensile-shear test, and the 4-point bend delamination test.

2.3a Knife-edge or Crack-opening Test

The knife-edge or crack-opening method is one of the ways to measure the surface energy of a bonded pair of wafers. Using the bonding forces at the apex of

the crack and the equilibrium of elastic forces of the separated portion of the bond pair, the surface energies can be obtained.

In their book on wafer bonding, Q.Y. Tong and U. Gösele develop a model for acquiring the surface energy [13]. Their derivation is presented in detail here. First, they use two beams of the same width, w, to represent the bonded wafers. The beams are modeled as two different materials and the final equations can be simplified for bonded identical wafers. A diagram of the model is shown in Figure 2-2. The inserted blade has a thickness t_b and the wafers have thicknesses of t_{w1} and t_{w2}. The bending of the wafers produces two distinct elastic energies, E_{elas1} and E_{elas2}. The insertion of the blade creates surfaces of area Lw, where L is the crack length. Therefore, the total energy is:

$$E_{total} = E_{eslas1} + E_{elas2} + (\gamma_1 + \gamma_2) Lw \qquad \text{(Eq. 2-8)}$$

with γ_i being the surface energy of each new surface. An assumption is made in this model that there is no plastic deformation occurs in this process. The derivative of the total energy with respect to the crack length, L, is set equal to zero, so that the elastic and bonding forces of the wafer pair are at equilibrium.

$$\frac{\partial E_{total}}{\partial L} = 0 \qquad \text{(Eq. 2-9)}$$

Using *Engineering Mechanics of Solids* by E. Popov [19], the elastic energy for each surface is:

$$E_{elast,i} = \frac{F_i^2 L^3}{6 E_i I_i} \qquad \text{(Eq. 2-10)}$$

where F_i is the bending force, which is given by:

$$F_i = \frac{E_i w t_{wi}^3 t_{bi}}{4L^3} \qquad \text{(Eq. 2-11)}$$

and I, is given by

$$I_i = \frac{w t_{wi}^3}{12} \qquad \text{(Eq 2-12)}$$

Substituting equations (2-10) – (2-12) into Eq. 2-8, the total energy is:

$$E_{total} = \frac{E_1 w t_{w1}^3 t_{b1}^2 + E_2 w t_{w2}^3 t_{b2}^2}{8L^3} + (\gamma_1 + \gamma_2) L w \qquad \text{(Eq. 2-13)}$$

Using Eq. 2-9 to evaluate Eq. 2-13, leads to

$$\frac{-3\left(E_1 w t_{w1}^3 t_{b1}^2 + E_2 w t_{w2}^3 t_{b2}^2\right)}{8L^4} + (\gamma_1 + \gamma_2) w = 0 \qquad \text{(Eq. 2-14)}$$

which can be solved for the summation of the surface energies:

$$\gamma_1 + \gamma_2 = \frac{3\left(E_1 t_{w1}^3 t_{b1}^2 + E_2 t_{w2}^3 t_{b2}^2\right)}{8L^4} \qquad \text{(Eq. 2-15)}$$

Since:

$$t_b = t_{b1} + t_{b2} \qquad \text{(Eq. 2-16)}$$

where t_b is the total thickness of the blade, then:

$$t_{b1} = t_b - t_{b2} \qquad \text{(Eq. 2-17)}$$

Placing Eq. 2-17 into Eq. 2-13 and 2-15, the following two equations are obtained:

$$E_{total} = \frac{E_1 w t_{w1}^3 (t_b - t_{b2})^2 + E_2 w t_{w2}^3 t_{b2}^2}{8L^3} + (\gamma_1 + \gamma_2) Lw \quad \text{(Eq. 2-18)}$$

$$\gamma_1 + \gamma_2 = \frac{3\left[E_1 t_{w1}^3 (t_b - t_{b2})^2 + E_2 t_{w2}^3 t_{b2}^2 \right]}{8L^4} \quad \text{(Eq. 2-19)}$$

Now, Eq. 2-19 is substituted into Eq. 2-18, resulting in:

$$E_{total} = \frac{E_1 w t_{w1}^3 (t_b - t_{b2})^2 + E_2 w t_{w2}^3 t_{b2}^2}{2L^3} \quad \text{(Eq. 2-20)}$$

Setting the derivative of the total energy with respect to t_b equal to zero, the following equation is acquired:

$$t_{b2} = \frac{t_b E_1 t_{w1}^3}{E_1 t_{w1}^3 + E_2 t_{w2}^3} \quad \text{(Eq. 2-21)}$$

Using the same algorithm of substitution and derivative:

$$t_{b1} = \frac{t_b E_2 t_{w2}^3}{E_1 t_{w1}^3 + E_2 t_{w2}^3} \quad \text{(Eq. 2-22)}$$

Substituting equations 2-21 and 2-22 into 2-15:

$$\gamma_1 + \gamma_2 = \frac{3 E_1 t_{w1}^3 t_b^2 E_2 t_{w2}^3}{8L^4 \left(E_1 t_{w1}^3 + E_2 t_{w2}^3 \right)} \quad \text{(Eq. 2-23)}$$

For identical wafers, $E=E_1=E_2$, $\gamma_1=\gamma_2$, and $t_{b1}=t_{b2}$, Eq. 2-23 becomes

$$\gamma = \frac{3 E t_b^2 t_w^3}{32L^4} \quad \text{(Eq. 2-24)}$$

2.3b Pressure Burst Test

The Pressure Burst test begins with two bonded wafers. A hole cut through one of the wafers (see Figure 2-3), and the hole is filled with a hydrostatic oil. The oil pressure is increased until the two wafers separate. [13]

2.3c Tensile Test

The tensile test uses a sample of the two bonded wafers that are glued to blocks on opposite sides of the bonded pair (see Figure 2-4). Force is applied to both blocks perpendicular to the bonded surfaces until debonding occurs [13].

2.3d 4-point Bend Delamination Test

In this testing method, the sample has a notch cut through on of the two wafers. Four rollers are placed against the sample, as shown in Figure 2-5 [20]. A load cell causes a force on the rollers, bending the sample until the upper wafer fractures through. The strain energy release, $\mathcal{G}$, rate is given by

$$\mathcal{G} = \frac{1.5\left(1-\nu^2\right)}{E}\left(\frac{Pl}{b}\right)\left(\frac{1}{h_1^3} - \frac{1}{\left(h_1+h_2\right)^3}\right) \qquad \text{(Eq. 2-25)}$$

where l is the inner to outer roller distance, P is the applied load, b is the specimen width, E is the Young's modulus, ν is the Poisson's ratio, and h_1 and h_2 are the thickness of the wafer 1 and wafer 2, the notched wafer [21].

Figure 2-2: Schematic of the knife-edge or crack-opening method for two bonded wafers, shown as the thick black and gray lines, based on a figure by Tong and Gosele [13]. The knife edge, of thickness t_b, is inserted between to wafers with thicknesses of t_{w1} and t_{w2}. A crack of Length L is created.

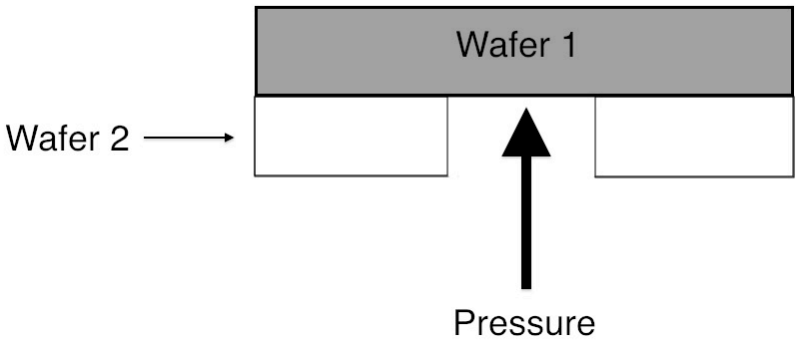

Figure 2-3: Schematic of the Pressure Burst test for two bonded wafers. The wafer number 2 of the pair has a hole cut through and pressure is applied by oil.

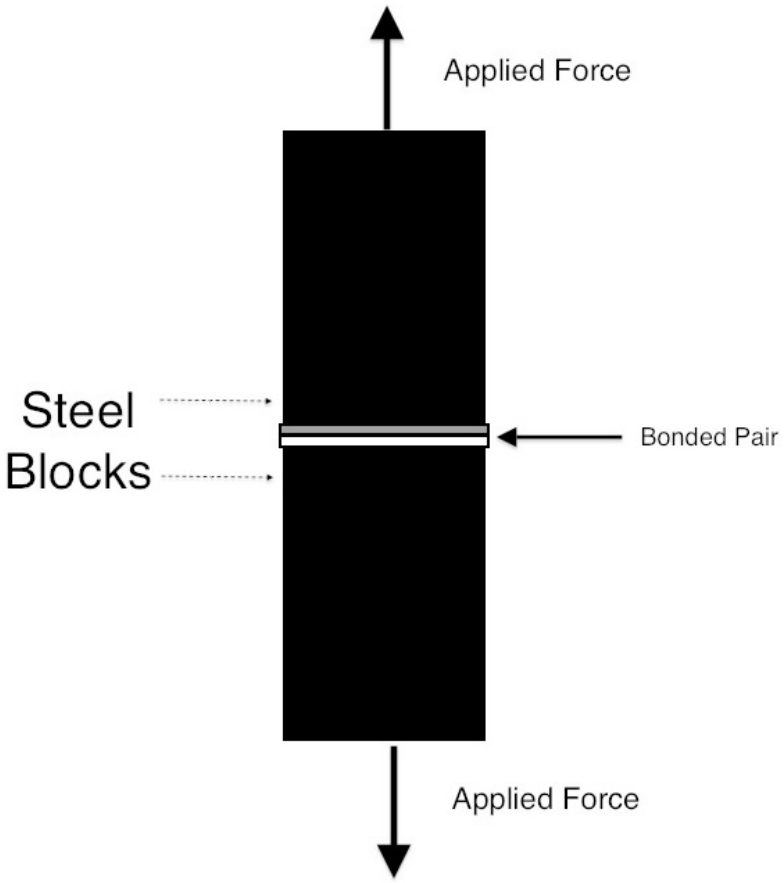

Figure 2-4: Schematic of the Tensile-Shear test for two bonded wafers. The steel blocks are adhered to the bonded pair, then force is applied to both blocks perpendicular to the bonded surfaces until debonding occurs [13].

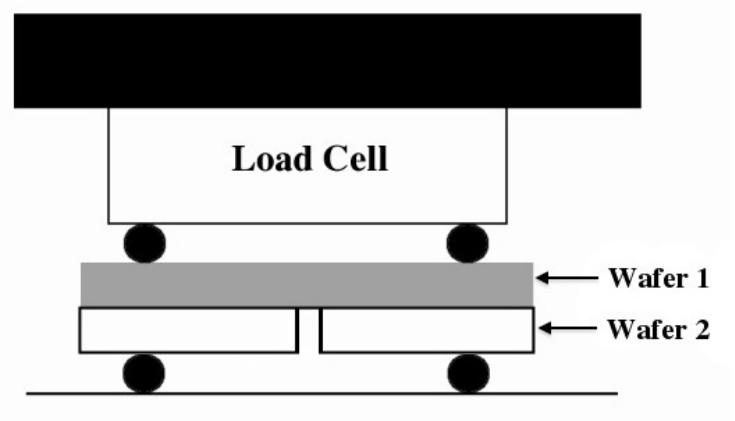

Figure 2-5: A diagram of the sample in a 4-point bending apparatus with a load cell [20]

2.4 Applications of Wafer Bonding

2.4a Glass Encapsulation of Solar Cells

For many solar cells, a glass substrate is used which protects the encapsulated cell against the atmospheric corrosion and guarantees the stability of outdoor modules [22]. Cell-to-panel bonding in solar panels in the market use hydrocarbons such as epoxy [23], but epoxy decays rapidly from heat and solar UV, which is a fundamental limit to panel longevity. Using wafer bonding for solar cells, the resin and any effects would be eliminated.

2.4b Sensor Medical

In medical applications, the interface between the sensor's substrate (which can be either silica or Si) and the supporting detection/emission electronics and power supplies has to be hermetically sealed from percolation of saline solutions [24-2-30]. Wafer bonding allows for hermetically sealing bonding interfaces against saline solutions, thereby making possible new single device implants that will help chronically ill patients. Diabetics pricking their fingertips daily still do not continuously monitor glucose as a pancreas does. With wafer bonding, continuous monitoring integrated with regulated insulin release would reduce having a person perform daily monitoring of diabetes. Additional medical applications include blood pressure monitoring, and continuous targeted chemotherapy at tumor sites modulated by monitoring of local alpha-proteins releases in blood would greatly enhance efficacy of chemotherapy while reducing damage from larger doses.

Chapter 2 References

[1] K. Nemoto, K. Watanabe,T. Hayashi, K. Tsugane, Y. Tamaki, H. Ota, T. Funakoshi,Advanced Semiconductor Manufacturing Conference, ASMC 2007. IEEE/SEMI, 157-160 (2007)

[3] M.Alexe U. Gosele, *Wafer Bonding – Applications and Technology*, Springer Series in Mater. Sci. (2004).

[4] U. Gosele, Q.-Y. Tong, *Annu. Rev. Mater. Sci*. **28**, 215–241 (1998)

[5] R G Parker , A J Dalladay, *Trans. Opt. Soc*. **17**, 107-110 (1916)

[6] Lord Rayleigh. *Proc. Phys. Soc. A*, **156**, 326 (1936)

[7] British Patent Specification, 312,534. W. E. Williams, Construction of a fabry perot interferometer (etalon), July 11, 1928, complete accepted May 30, 1929

[8] British Patent Specification 367859, F. Twyman, JH Dowell, Improvements in or relating to length measurements by interferometer; application date: Nov 26,1930, completely accepted Feb. 26, 1932

[9] G. Wallis, D. I. Pommerantz, *J. Appl. Phys*. **40**, 3946–49 (1969)

[10] G. A. Antypas, J. Edgecumbe , *Appl. Phys. Lett*. **26**, 7, 371-372 (1975)

[11] M. Shimbo, *J. Appl. Phys.* **60**, 8, 2987-2989 (1986)

[12] J. B. Lasky, *Appl. Phys. Lett*. **48**, 1, 78-80 (1986)

[13] Q. Y. Tong, U. Gosele, *Semiconductor Wafer Bonding*, Electrochem. Society, (1998)

[14] K. Petersen, *IEEE Technical Digest on Solid-State Sensor and Actuator Workshop*, **144** (1988)

[15] E. Kasper, *Surf. Sci*. **174**, 1-3, 630-639. (1986)

[16] W. P. Maszara, *J. Electrochem. Soc*. **138**, 341-347 (1991)

[17] J. Mahanty, B. W. Ninham, *Dispersion Forces*, Academic Press, London-New York- San Francisco 1976.

[18] R. G. Horn, D. R. Clarke , M. T. Clarkson, *J. Mater. Rcs*. **3**, 413-416, (1988)

[19] E. Popov, *Engineering Mechanics of Solids,* Prentice Hall (1990)

[20] S. M. Spearing, C. H. Tsau, M. A. Schmidt, *Advanced Mater. for Micro- and Nano-Systems* (AMMNS), (2004)

[21] P. G. Charalambides, J. Lund, A. G. Evans, R. M. McMeeking, *J. Appl. Mech*. **56**, 77–82 (1989)

[22] J. Poortmans , V. Arkhipov, *Thin film solar cells- fabrication, characterization and applications* , Wiley, (2006)

[23] T. Markvart , L. Castañer, *Practical handbook of photovoltaics: fundamentals and applications*, Elsevier Science (2003)

[24] M. A. Arnold, *J. Regen. Med*. **1**, 55 (2000)

[25]R. E. Carlson, S. R. Silverman, Z. Mejia, http://www.verichipcorp.com/files/GLUwhiteFINAL.pdf

[26] H. Baldus, K. Klabunde, G. Müsch, *European Workshop on Wireless Sensor Networks* **2920**, 353-363 (2004)

[27] B. Dai, A. Urbas, R. A. Lodder, *NIR News* **17**, 14 (2006).

[28] M. C. Frost, M. E. Meyerhoff, *Curr. Opin. Chem. Biol*. **6**, 633-641 (2002).

[29] J. Akers, S. M. Setter, http://www.pharmacytimes.com/issues/articles/2007-05_4633.asp

[30] M. C. Frost, M. E. Meyerhoff, *Anal. Chem*. **78**, 21, 7370-7377 (2006).

Chapter 3: Theoretical and Experimental Prior Work on Ordered SiO_2 on Si(100)

The following Chapter presents previously published work done by other researcher that relate to the development of the ordered SiO_2 on Si(100)

3.1 Prior Work

The original RCA clean was developed by W. Kern of the RCA Corporation in 1965 and published in 1970 [1]. This clean was developed to remove contamination from Si(100) surfaces. Figure 3-1 [2] illustrates the detailed steps for the (a) RCA clean, (b) Chabal Clean [3], (c) Fenner Clean [4], and (d) the Herbots-Atluri clean (H-A Clean) [2]. The RCA clean uses an Standard Clean 1 (SC1) solution, H_2O:NH_4OH: H_2O_2 (4:1:1), which removes particles, organic contamination and some metallic contamination from the surface, but does not remove the original defective oxide. The Standard Clean 2(SC2) solution, H_2O:HCl: H_2O_2 (4:1:1), helps remove alkali and heavy metal contamination. It also creates a chemical oxide on top of the original oxide, while embedding impurities into this new oxide. Many variations exist on the RCA clean. One modification is to add an aqueous HF etch step after the SC2 etch. This removes the oxide with trapped particles, but still leaves a rough surface.

There are several steps that differ the H-A clean, shown in step-by-step illustration of the Si surface during the clean in Figure 3-2, from the RCA clean. The first is an etch using DI H_2O and 49% HF in a 98:2 ratio for 60 seconds. This removes the defective oxide that covers the Silicon surface after the SC1 clean. The next modification is another etch using 49% HF and Methanol in a 1:9 ratio

which strips off the oxide layer after the SC2. This step also creates a smooth Si(100) surface and forms a stable hydroxide termination to the Si surface bonds.

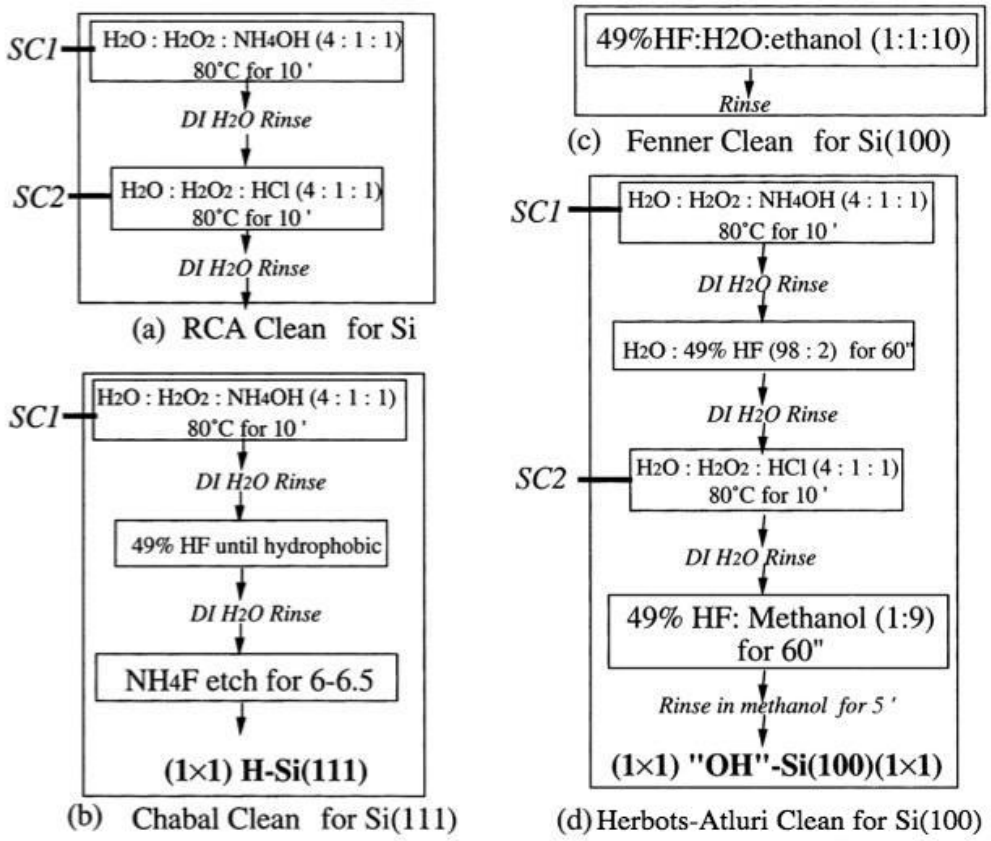

Figure 3-1: Four processes are shown. (a) The RCA clean developed by Kern [1] to remove contaminants from the Si surface. (b) The Chabal clean which orders and hydrogen terminates the Si(111) surface. (c) The Fenner Clean that passivates Si(100), but does not order the surface and does not form an SiO_2 layer. (d) The H-A Clean for Si(100), which orders and OH passivates the surface. [2]

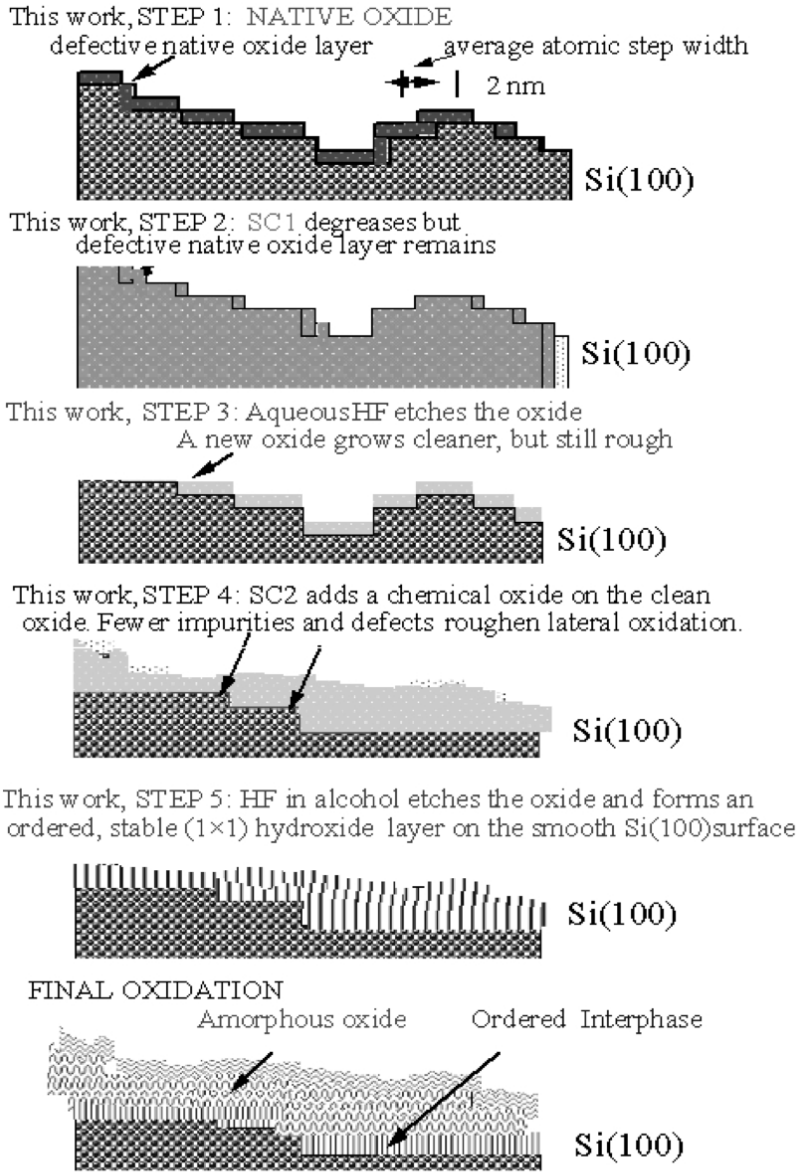

Figure 3-2: A step-by-step illustration of the Si surface during the H-A clean [2].

3.1a Reflection High Energy Electron Diffraction (RHEED)

Reflection high energy electron Diffraction (RHEED) diffraction patterns were taken at 10 keV in a 10^{-10} Torr vacuum at a 0.75° incident beam to the sample surface[2]. The samples, all Si(100) substrates, underwent RHEED before any processing, after H-A clean at 300 K, and after H-A clean with a 600 K annealed for 10 minutes. The H-A cleaned Si surface at 300 K, showed a (1x1) pattern. The H-A cleaned Si surface with a 600 K annealed for 10 minutes showed a reconstructed (2x1) Si(100) surface. These patterns are shown in Figure 3-3 below.

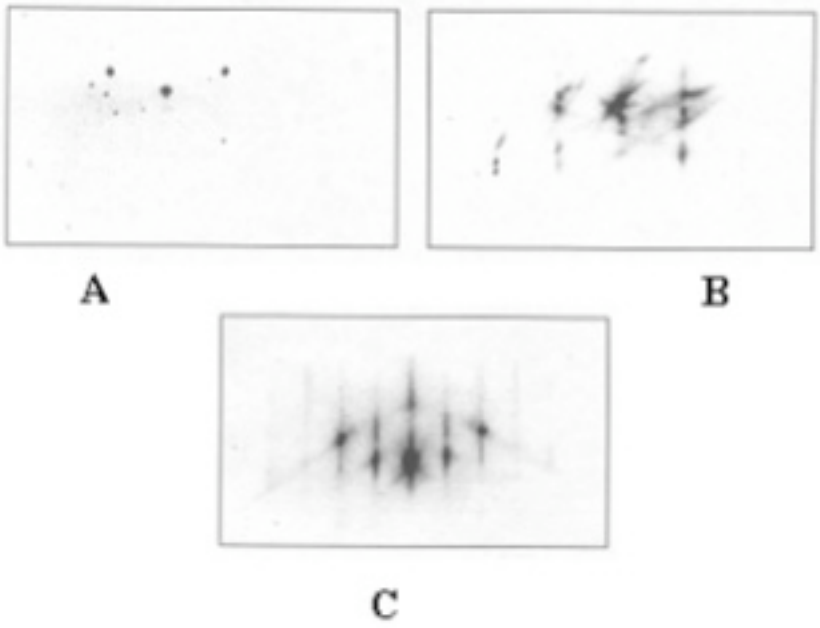

Figure 3-3: RHEED diffraction patterns at 10 keV showing (A) Unprocessed Si(100) Wafer, (B) (1x1) pattern showing order after H-A clean, at 300 K, (C) Reconstructed (2x1) Si(100) surface after 600 K annealed for 10 minutes. [2]

3.1 b High Resolution Transmission Electron Microscopy (HRTEM)

Multiple Si(100) samples cleaned with either the RCA clean or the H-A clean were allowed to form a native oxide at standard temperature and pressure. These samples then underwent High Resolution Transmission Electron Microscopy (HRTEM) at Arizona State University in the Center for Solid State Science. The HRTEM was done at 400 keV to measure the width of the atomic steps. Figure 3-4 illustrates the contrast in step size between the two sample types. Further data is shown in Figures 3-5 through 3-7, which are highly detailed HRTEM micrographs of the interface for both cleaning types. All of these micrographs exhibit a ten-fold increase in the atomic step width for the H-A clean versus the RCA clean. The RCA Clean atomic step width is 2 nm , while the H-A Clean atomic step width is 20 nm. This increases the smoothness of the surface

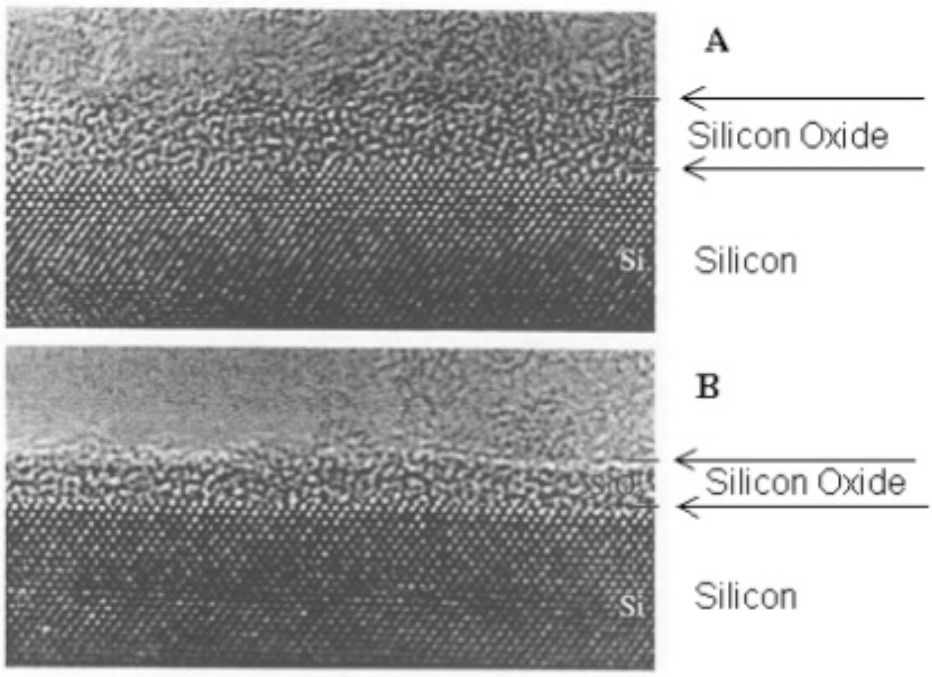

Figure 3-4: HRTEM micrographs of Si(100) samples. (A) Sample cleaned with the RCA clean with a SiO_2 thickness of 20 $\pm$ 2 Å , (B) Sample cleaned with the H-A clean with a SiO_2 thickness of 17 $\pm$ 2 Å . [2]

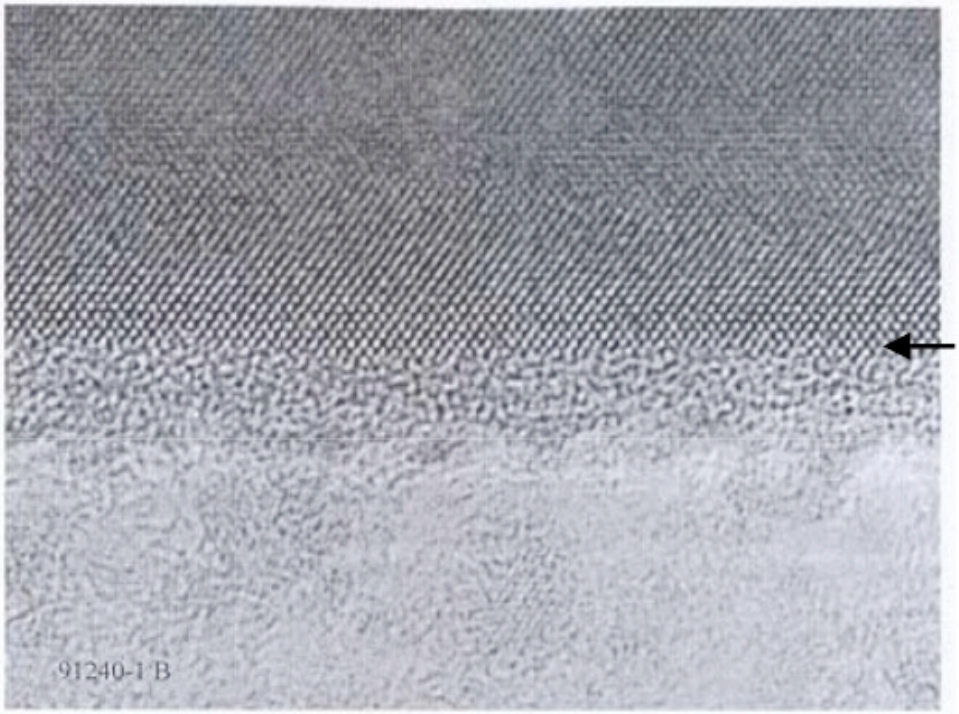

Figure 3-5: HRTEM of sample 91240-1B, Cleaned using an RCA Clean. The arrow indicates the Si/SiO2 interface. The atomic step width is 2 nm. [5]

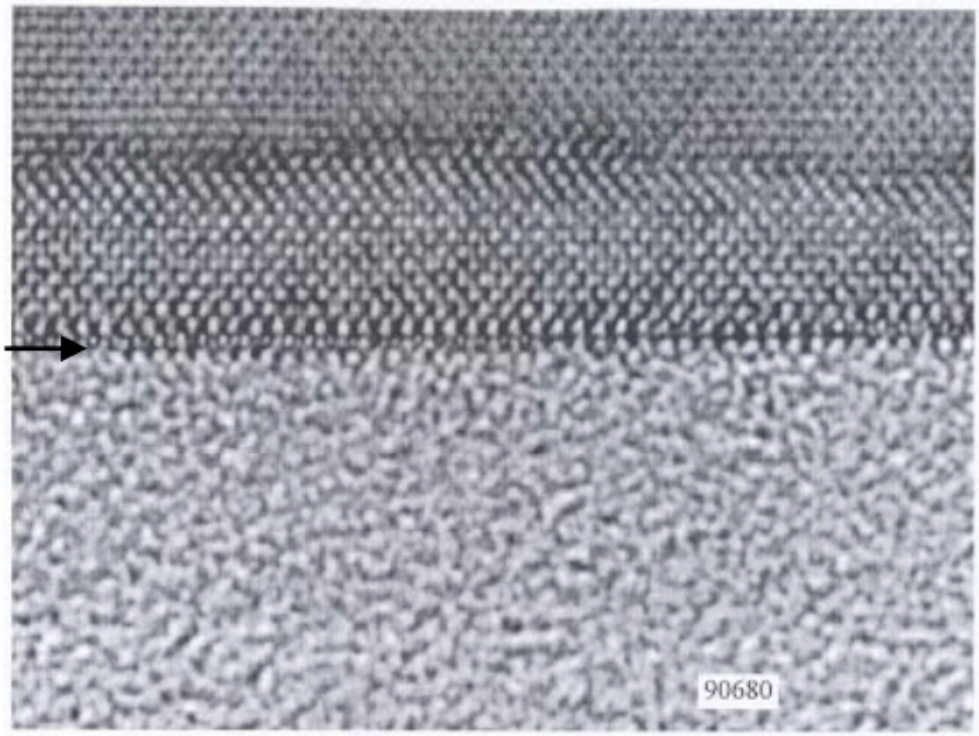

Figure 3-6: HRTEM of sample 90680 cleaned via the H-A clean. The arrow indicates the Si/SiO2 interface. The atomic step width is 20 nm, ten times that of the RCA cleaned sample. [5]

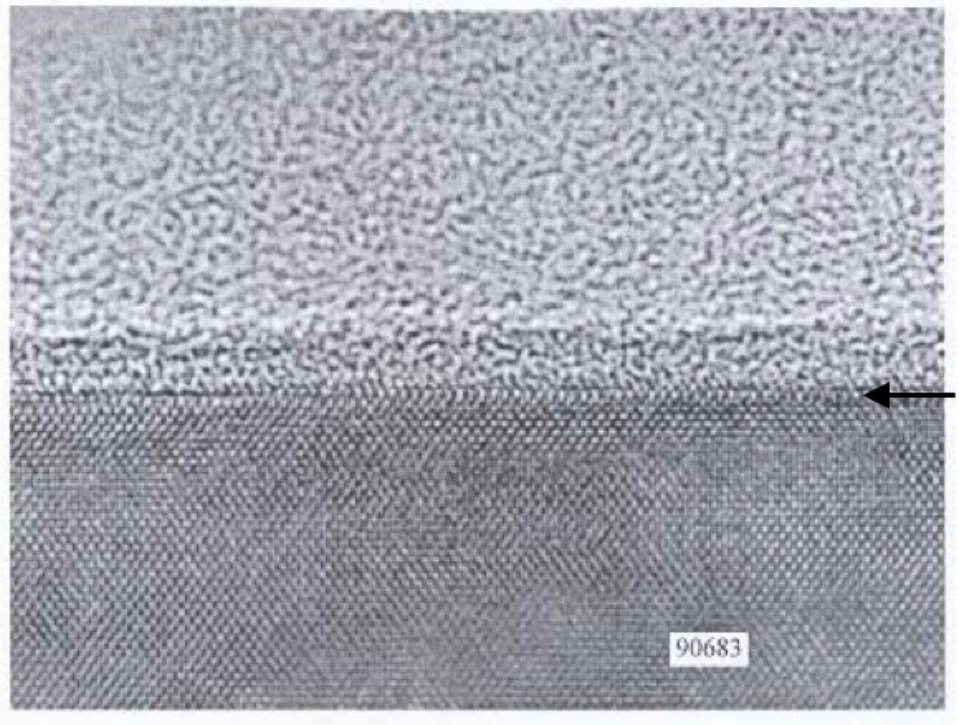

Figure 3-7: HRTEM of sample 90683 cleaned via the H-A clean. The arrow indicates the Si/SiO2 interface. The atomic step width is 20 nm, ten times that of the RCA cleaned sample. [5]

3.1c Ion Beam Analysis (IBA)

In Herbots *et al.* [2], 1x1 cm^2 Si pieces where subjected to Ion Beam Analysis (IBA) using He^{2+} with a vacuum of 10^{-8} Torr using a 1.7 MV General Ionex Tandetron Accelerator. The samples underwent normal IBA, channeling, and nuclear resonance analysis (NRA). The channeling is done by performing IBA along a crystal axis, which lowers the background Si signal by a factor of approximately 30. NRA was performed at the 3.05 MeV $^{16}O(\alpha,\alpha)^{16}O$ resonance energy, to enhance the oxygen peak by a factor of 27. The NRA and channeling was also combined for a greater enhancement.

A number of sequential IBA runs were performed on the Si substrates. This obtained the areal density of a particular element, obtained from the element's surface peak, for greater and greater He^{2+} ion dose. The areal density is plotted against the cumulative total ion dose. This plot is referred to as a damage curve, as it plots the successive damage from the ion beam. By using linear regression, the areal density of an element with no ion dose, the intercept of the fit line, can be acquired from a damage curve.

Figure 3-8(a) shows a damage curve for O areal density on a Si(100) sample cleaned in aqueous HF. Both the random and channeled spectra are shown for a 3.05 Mev $^{16}O(\alpha,\alpha)^{16}O$ resonance energy. This figure shows smaller error on the channeled spectra which allows an increasing in the O areal density as the ion dose increases.

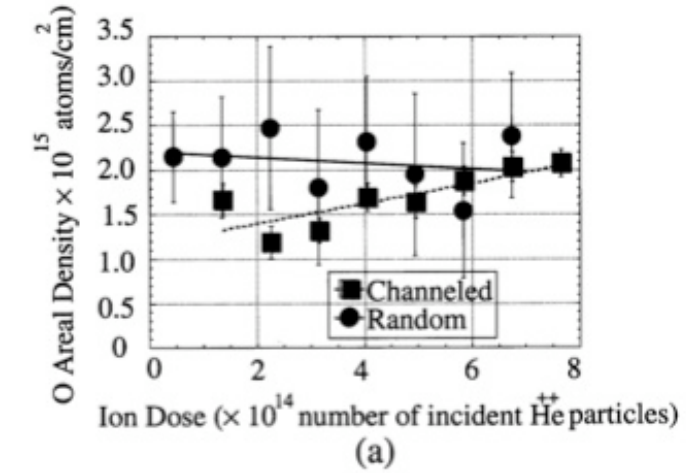

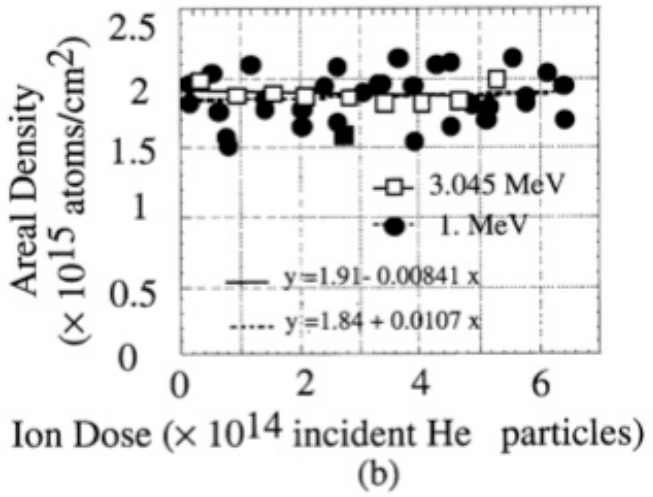

Figure 3-8: (a) A damage curve for O areal density on a Si(100) sample cleaned in aqueous HF, for both the random and channeled spectrums at 3.05 Mev $^{16}O(\alpha,\alpha)^{16}O$ resonance energy. 8 increments were used in the plot. There is a smaller error on the channeled spectra, which shows an increase in the O areal density as the ion dose increases. (b) A damage curve for the O areal density for a Si sample processed with the H-A clean, showing no significant slope for either the 1.0 MeV IBA or the 3.05 Oxygen NRA. 30 increments were used in the plot [2]

A damage curve for the O areal density for a Si sample that was processed with the H-A clean is presented in Figure 3-8(b). The linear fit showed no significant slope as ion dose increased. Therefore, this plot provided evidence that Si cleaned with this technique do not significantly desorb oxygen or grow an oxide at 10^{-7} Torr during IBA. This also confirmed that the Si surfaces are stable with respect to oxygen in ambient air conditions.

Figure 3-8 shows data, gathered by IBA which included 3.05 Mev $^{16}O(\alpha,\alpha)^{16}O$ NRA, from a paper by J. Shaw *et al.* [6]. These are plots of Si surface peak areal density versus that of O for Si substrates that went through the H-A clean and then underwent gate oxidization. Plots were done for the <100>, <110>, and <111> directions. Each point on the three graphs represent the damage curve data of both Si and O areal density from a single Si substrate. The bulk surface Si amount for each direction is shown in each graph as a horizontal line, which is the amount of Si expected without a surface or oxide contribution. The bulk Si amount was calculated using a Monte Carlo methods with 3DSTRING computer code, which will be discussed in further detail later in this chapter. A dotted line is shown that is the data with a regression fit, where the slope is 0.5 (perfect 1:2 ratio for Si:O in SiO_2). There is a small deviation at the *y*-intercept for this regression fit and the fit for the data in Figure 3-9 (a) and (b). This indicates that there is no disorder, within the error of the measurement, at the surface. This implies that the interface proceeds from the crystalline silicon to another cystal formation.

Figure 3-10 shows this <100> and <110> data [2], labeled as Herbots, in

contrast with data with other groups [7, 8], which reported net disorder. Table 3-1 presents the H-A clean damage curve data, with zero Si monolayers (ML) of disorder, and compares it with these other group's data, which range from 2.1 to 10.9 MLs of disorder.

Figure 3-9 (c) shows the <111> direction Si surface peak areal density versus that of O. The linear regression line has a *y*-intercept below that of the bulk Si from the simulation. The explanation presented in the paper stated that the Si atoms in the oxide must shadow the Si substrate atoms. Shadowing is presented in the next section of this chapter. The oxide Si must align, or register, with the crystal Si structure in the substrate. The O atoms would need to be along the <111> direction and the shadowing must be minimal or absent along the <100> and <110> direction to match the IBA data. The Herbots *et al.* paper also stated that due to the increase with O coverage above two MLs pointed to an interphase region which had registry and ordering that would be approximately 1-2 nm thick, due to the fact that the Si surfcae peak yield will increase more rapidly in a disordered structure than an ordered structure.

When channeling <channeling is not defined> takes place in a crystalline structure, shadowing can occur. IBA creates a surface peak from the surface atoms that have high scattering probabilities. Due to the geometry of a crystal, this surface atom can reduce the scattering probabilities of atoms below the surface. These bulk crystal atoms are blocked by the shadow cone created by the surface atom. The shadow cone will have a radius, R_s, which is dependent on the energy of the beam, the cross-section of the atom that is creating the cone, and the

distance between atoms in the crystal. Figure 3-11 shows a simple illustration of a shadow cone for a crystal in one-dimension with identical crystal atoms aligned with the incident beam direction [5]. Figure 3-12 shows a more complex simulation of a shadow cone, using 2 Pt Atoms with a 10KeV He beam at an angle of 14.1° [10]. This is the type of shadowing that takes place in the <110> and <111> directions on H-A processed Si(100)

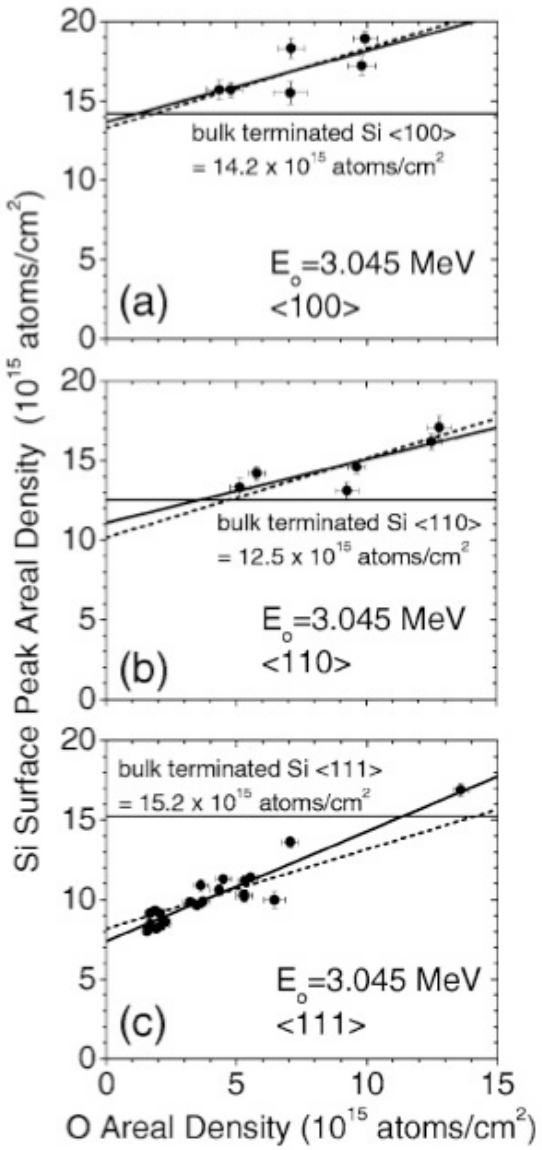

Figure 3-9: These are plots of Si surface peak areal density versus that of O for Si substrates that went through the H-A clean and then underwent gate oxidization for the (a) <100>, (b) <110>, and (c) <111> directions. Each plot has a solid regression fit based on the data, as well a dotted line which represents a regression fit with an ideal 0.5 slope. The bulk surface Si amount for each direction is shown in each graph as a horizontal line. [6].

Channel	Incident ion Energy (MeV)	Net disorder in Si ($x10^{15}$ atoms cm^{-2})	Equivalent disordered Si monolayers	Reference	Initial surface process
<100>	3.045	-0.2	0.0	[6]	H-A clean
	0.8	1.4	2.1	[7]	Not reported
	0.8	7.4	10.9	[8]	RCA
	0.8	6	8.8	[8]	HF in ethanol
	0.8	5.3	7.8	[8]	Rapid thermal cleaning
<110>	3.045	-1	0.0	[6]	H-A clean
	0.8	2.2	2.3	[9]	Aqueous HF
	0.8	2.2	2.3	[7]	Not reported

Table 3-1: The H-A clean damage curve data, with zero Si monolayers (ML) of disorder, and compares it with data from other groups, which have a range from 2.1 to 10.9 ML of disorder [6].

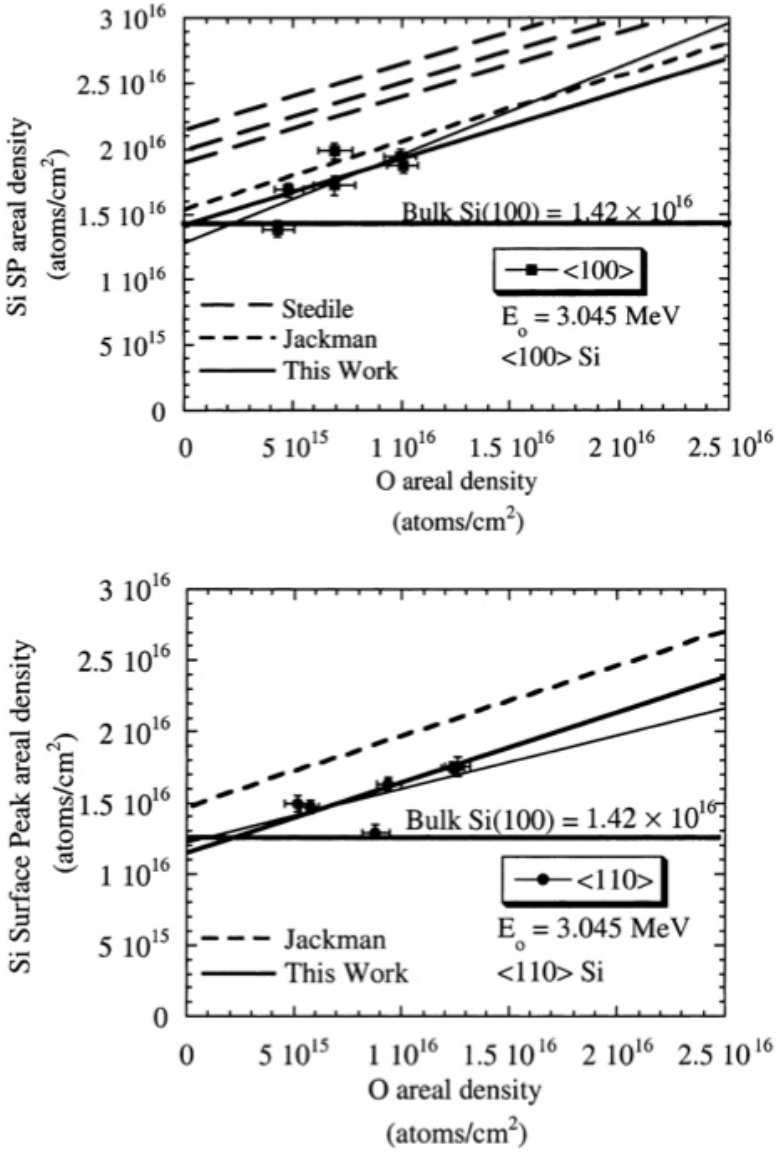

Figure 3-10: The H-A clean <100> and <110> damage curve data, labeled as Herbots, as well as with data from other groups [7, 8]. The Herbots data has a small deviation at the *y*-intercept for this regression fit, which indicates that there is no disorder, within the error of the measurement, at the surface. The other data shows a non-zero *y*-intercept, indicating disorder.

3.1d Time-of-Flight Secondary Ion Mass Spectrometry

Time-of-Flight Secondary Ion Mass Spectrometry (ToF-SIMS) carbon profiles are shown in Figure 3-13. It shows a Si(100) substrate processed by the H-A clean, Figure 3-13(a), that has been exposed to ambient air. The carbon yield is two or more orders of magnitude below Si(100) substrates cleaned by an RCA clean, even after extended storage in a clean room of several months after the cleaning process. This indicates that the initial carbon residues and carbon build-up for the H-A clean are below that of the RCA clean. Uncapped gate oxides after RCA cleans of the underlying substrate, have an equivalent thickness of 0.7 nm on top of the uncapped oxide due to carbon accumulation [11]

Figure 3-13(b) shows a Si(100) substrate processed by the H-A clean and then oxidized 24 hours later by rapid thermal annealing for 90 s at T = 1050 °C in pure nitrogen and left uncapped. This gave an oxide thickness of 2.2. nm. The carbon profile showed a two order of magnitude drop after oxide anneal and stayed at that level for 12 months. In normal manufacturing, carbon accrues in days if the oxide is not topped with a polysilicon layer.

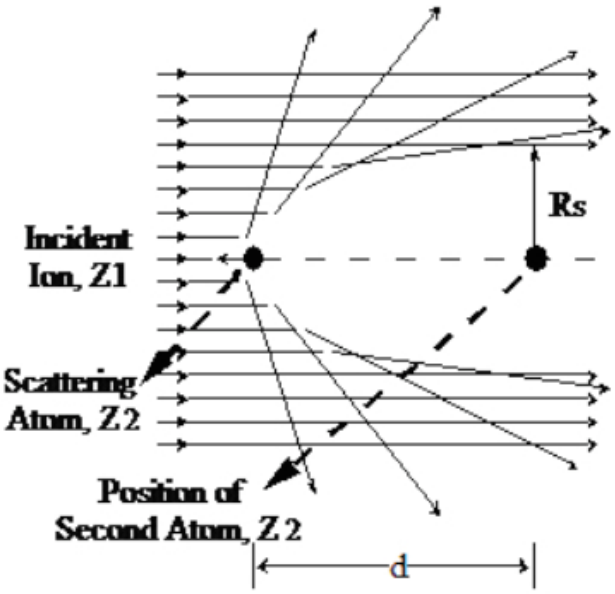

Figure 3-11: An Illustration of shadowing occuring when a incident ion, of atomic number Z1, impinges on a crystal composed of atoms with a Z2 atomic number. R_s is the radius of the shadow cone and d is the distance between the atoms in the crystal [5].

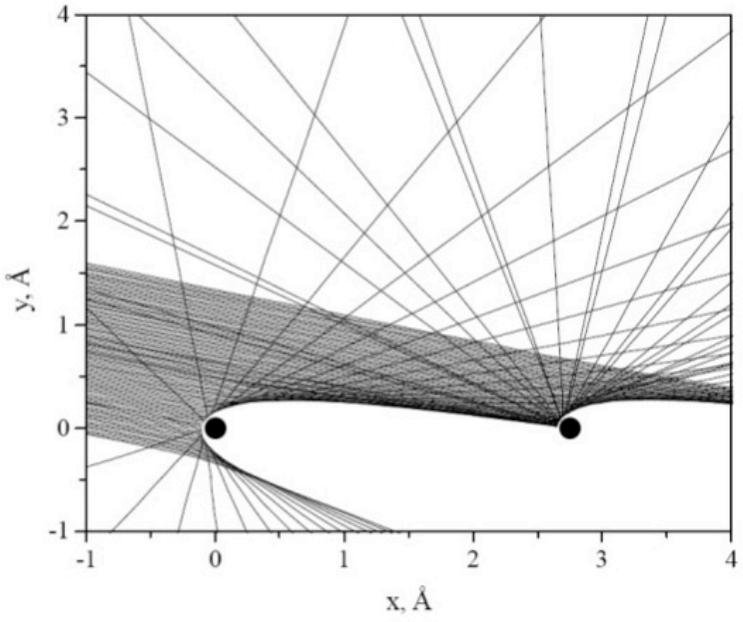

Figure 3-12: Simulation of a shadow cone, using 2 Pt Atoms with a 10KeV He beam at an angle of 14.1° [10]

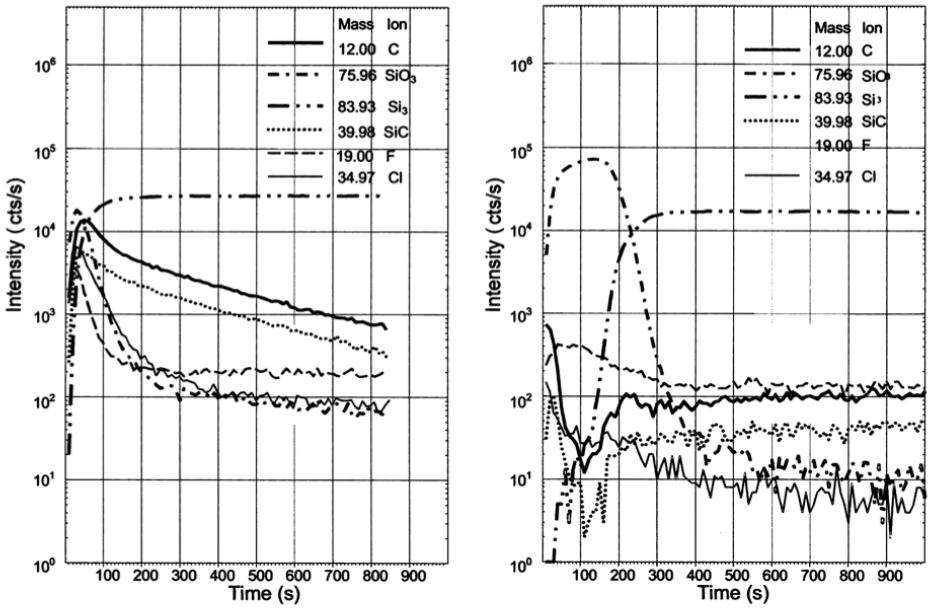

Figure 3-13: ToF-SIMS carbon profile (a) a Si(100) substrate processed by the H-A clean, (b) Si(100) substrate processed by the H-A clean and the oxidized by rapid thermal annealing for 90 s at T = 1050 °C in pure nitrogen. [2]

3.1e Infrared Analysis

Infrared Analysis was used to examine the Si/SiO_2 interface of samples that underwent with the H-A clean [12]. Using the analysis developed by K. Queeny *et al.* [13] where dilute HF is used to thin the SiO_2 layer until it is 6Å. During this etching, an examination is done of the optical phonon modes to observe if any frequency shifts occur. If these shifts occur near the interface, then it would mean that there is a stoichiometric change in the SiO_x. IR spectroscopy was used to compare two different Si substrates. The first was cleaned using standard RCA clean, while the second was cleaned using the H-A clean. Each Si substrate had a thermal oxide of 25-40Å grown on top.

Initial infrared spectra was collected on both samples with 25Å of oxide. This is shown in Figure 3-14. There are no demonstrable differences between the two samples. There is a 1062 cm^{-1} transverse-optic (TO) peak, with 50 cm^{-1} FWHM, and a 1251 cm^{-1} longitudinal-optic (LO) peak, with a 79 cm^{-1} FWHM. This is due to the bulk IR signature overwhelming any signature from the interface.

The oxide layers of both substrates where then etched and differences in the phonon modes became apparent as the interfacial oxide region began to dominate. These measurements are show in Figure 3-15. Both LO and TO modes show a redshift as the film thickness decreases, which occurs due to a stoichiometry of the SiO_x, where $x< 2$, at the interface. Figure 3-16 plots the TO and LO peak frequencies as a function of film thickness for the H-A cleaned substrate (solid triangles) and the RCA cleaned substrates (open circles). Figure 3-16(a) shows

that there is little difference between LO peak frequency for the two substrates, yet Figure 3-16(b) shows a significant difference in the TO peak frequencies. At 10Å, the difference appears between the two substrates, with the RCA clean substrate plateau occurring at 1051 cm^{-1} and the H-A cleaned substrate plateau occurring at 1056 cm^{-1}. Since peak frequencies are determined within 1 cm^{-1}, this TO peak difference of 5 cm^{-1} is significant. This peak difference is also greater than 40% of the 12 cm^{-1} shift for the RCA cleaned substrate.

The TO shift is due to a ~990cm^{-1} shoulder that appears as the oxide is thinned by etching. SiO_x ,with $x< 2$, would account for this broader peak, if there were a spread on the possibilities for the x as one reached the interface. A homogeneous SiO_x would lead to two discrete modes (one for SiO_x and one for SiO_2). Therefore the broader the peak, the more inhomogeneous the SiO_x .

Figure 3-16 shows a comparison a 22˚grazing incidence spectra for a ~4.8Å oxide film on a H-A cleaned substrate (solid line, labeled ordered) and a ~5.3Å oxide film on an RCA cleaned substrate (the dotted line, labeled control). According to Queeney *et al.* [12], the LO mode supports the H-A cleaned substrate as the higher quality substrate,

> *"… film inhomogeneity near the Si/SiO_2 interface effectively screens some of the SiO_2 oscillators from one another, decreasing the Coulombic contribution to the LO intensity. The higher intensity of the LO mode in the thinner ordered interfacial oxide film therefore supports the picture of this interface as a more abrupt, higher quality one, with less disruption of the final SiO_2 layer by intervening substoichiometric bonding configurations."*

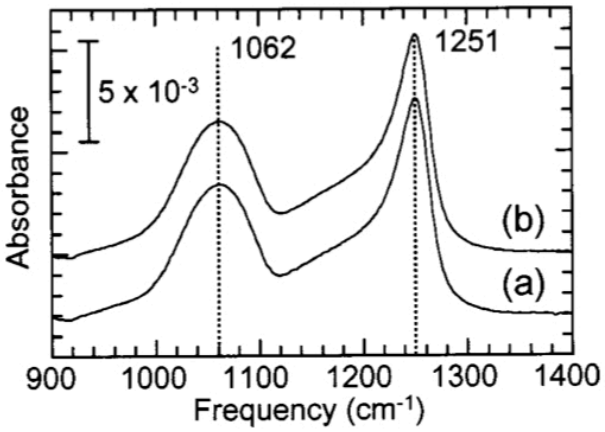

Figure 3-14: A 22˚ grazing incidence infrared spectrum from (a) Si substrate with the H-A clean and (b) Si Substrate with the RCA clean. Both substrates have 25 Å of thermal SiO_2. The dominant TO and LO phonon modes are shown. [12]

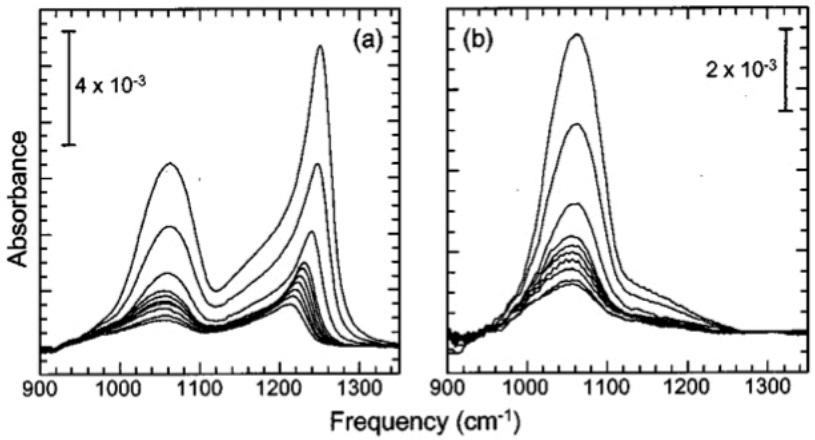

Figure 3-15: Infrared spectra from H-A cleaned substrate, initially with a film of 25 Å of thermal SiO_2, with successive etching. Spectra (a) was acquired using a 22˚ grazing incidence and shows both TO and LO. Spectra (b) was acquired using a normal incidence with only the TO mode, which was used to calculate the film thickness. [12]

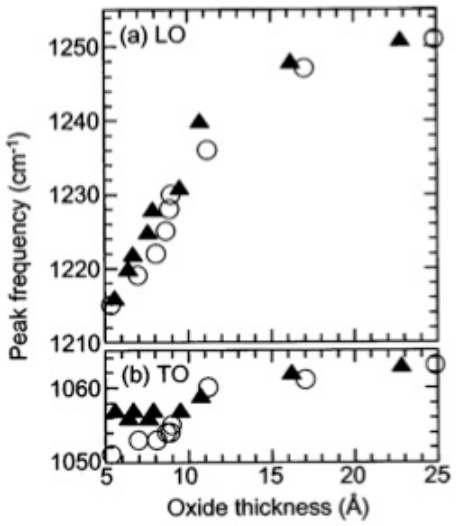

Figure 3-16: The TO and LO peak frequencies as a function of film thickness for the H-A cleaned substrate (▲) and the RCA cleaned substrates (○) [12].

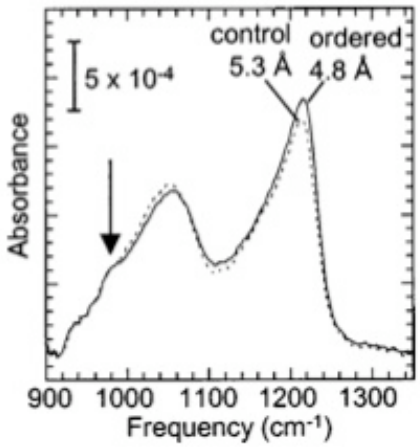

Figure 3-17: Comparison a 22˚grazing incidence spectra for a ~4.8Å oxide film on a H-A cleaned substrate (solid line, labeled ordered) and a ~5.3Å oxide film on an RCA cleaned substrate (the dotted line, labeled control) [12].

3.2 Structures for Ordered SiO_2 on Si(100)

J. Bradley, in his PhD thesis [5], examined six silica polymorphs: α-Quartz, β-Quartz, β-Tridymite, α-Cristobalite, β-Cristobalite, and Keatite to deduce which of these were the best candidate(s) to simulate as a layer on Si(100) using the ion channeling code 3DSTRING, which is described in the next section. The correct silica would need to interface with the Si(100) surface and also match the channeling data in the <100>, <110>, and <111> directions from IBA. In particular, the Si deficit seen due to shadowing must be present.

3.2a β-Tridymite

β-Tridymite is hexagonally symmetric which differs immensely from the face center cubic (fcc) structure found in the unit cell of Si. Figure 3-18 through Figure 3-21 show Si crystal superimposed on β-tridymite in the <100>, <110>, and <111> direction. There is no registration between the atoms of Si crystal and β-tridymite to account for the IBA data. Therefore it was not the appropriate silica polymorph.

3.2b α-Quartz

α-Quartz is trigonally symmetric and is shown in the <100>, <110>, and <111> direction in Figure 3-22. It will not have the shadowing to match the IBA data and has lack of registration with Si crystal atoms. Therefore it was ruled out as a candidate for being the appropriate silica polymorph.

3.2c β-Quartz

β-Quartz is tetragonally symmetric and is shown in the <100>, <110>, and <111> direction in Figure 3-23. β-Quartz (100) has some amount of registration with Si (111), but not the registration for Si(100). Therefore it was ruled out as a candidate for being the appropriate silica polymorph.

3.2d α-Cristobalite

α-Cristobalite is tetragonally symmetric and is shown in the <100>, <110>, and <111> direction in Figure 3-24. α-Cristobalite does not have the proper registration with Si (100), even though α-Cristobalite(100) and Si(100) have channels of a similar shape. Therefore it was not a candidate for being the appropriate silica polymorph.

3.2e β-Cristobalite

β-Cristobalite has cubic symmetry, the same as bulk silicon. Figure 3-54 shows the possibility of proper registration with Si in the <100>, <110>, and <111> directions. β-cristobalite <111> has aligned Si and O atoms along the z-direction, which could account for Si reduction in channeling along the <111> direction in IBA. Therefore, β-cristobalite was chosen for simulation by 3DSTRING.

3.2f Keatite

Keatite, a synthetic silica polymorph, is tetragonally symmetric and is shown in the <100>, <110>, and <111> direction in Figure 3-26, which clearly

shows that keatite does not have the proper registration with Si (100) and is not the appropriate silica polymorph needed.

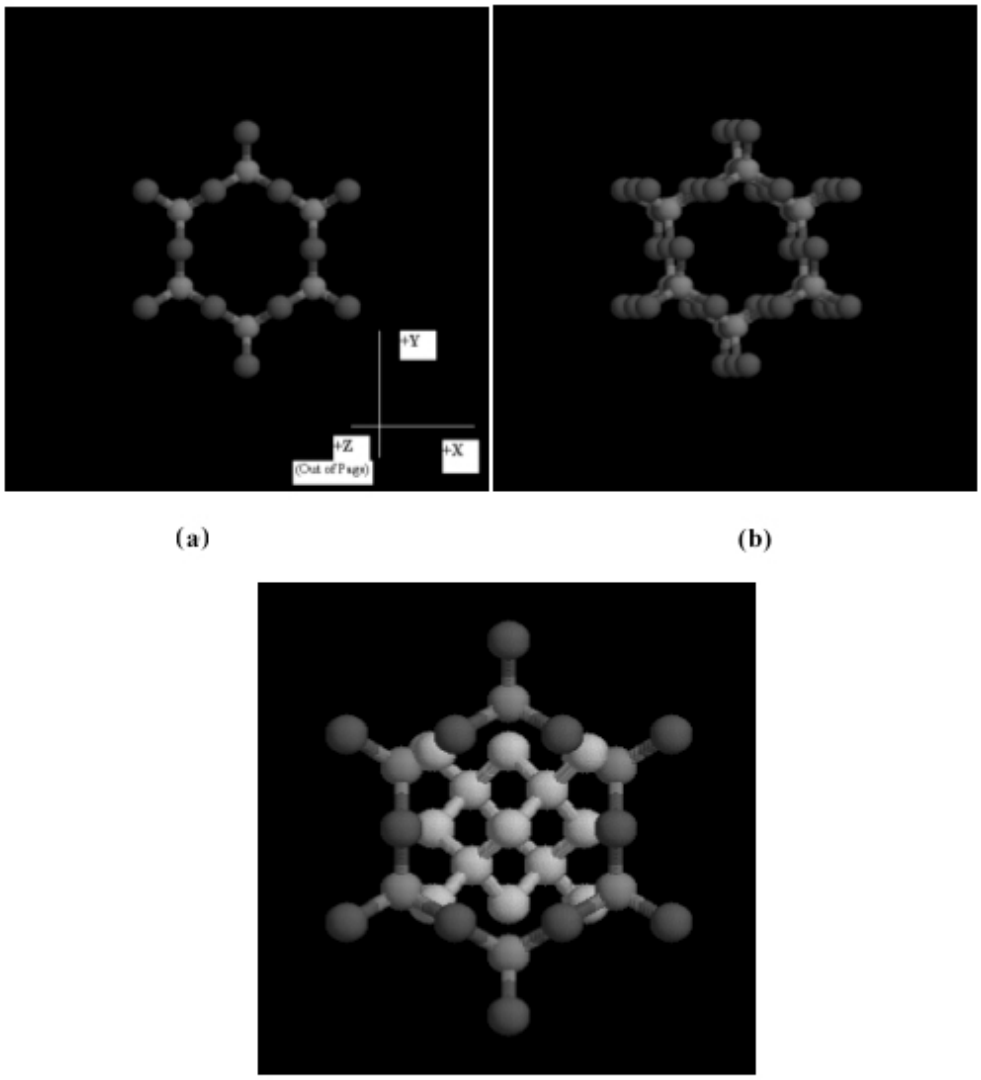

Figure 3-18: (a) β-tridymite(100), where tan atoms represent Si and red atoms represent oxygen. (b) β-tridymite(100) at a slight offset to show shadowing effects. (c) β-tridymite(100) with Si(100) (gray atoms) superimposed. These figures, and all subsequent silica polymorph atomic representations are from the thesis of J.D. Bradley [5].

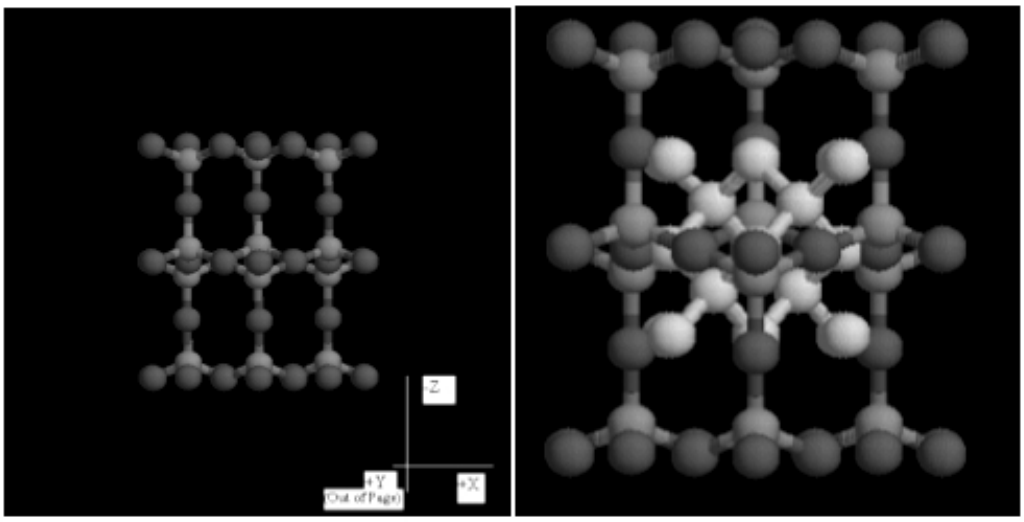

(a) (b)

Figure 3-19: (a) β-tridymite(100) shown in the <001-> orientation. (b) β-tridymite(100) with Si(100) superimposed. [5]

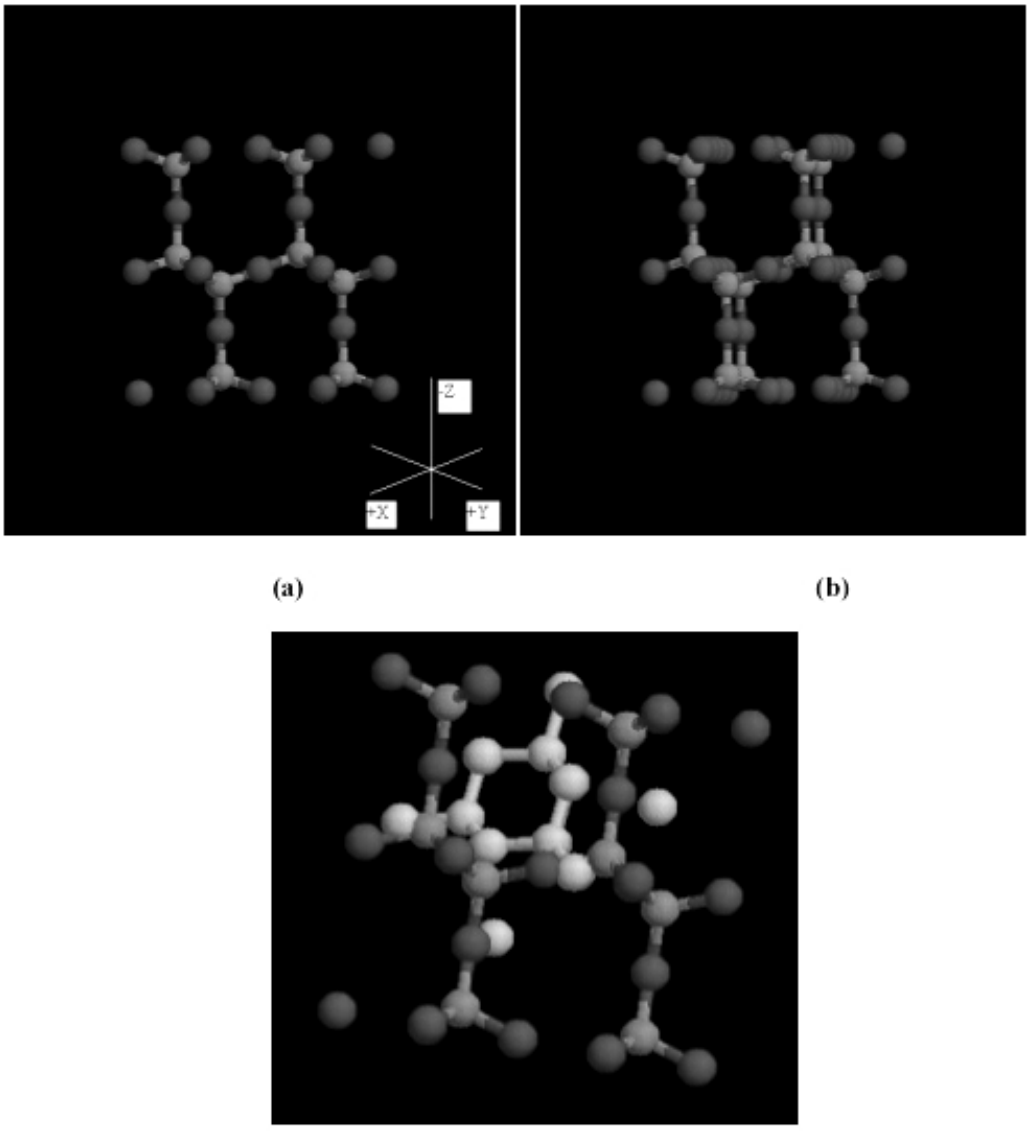

Figure 3-20: (a) β-tridymite in <110> orientation. (b) β-tridymite <110> at a slight offset to show shadowing effects. (c) β-tridymite <110> with Si<110> superimposed. [5]

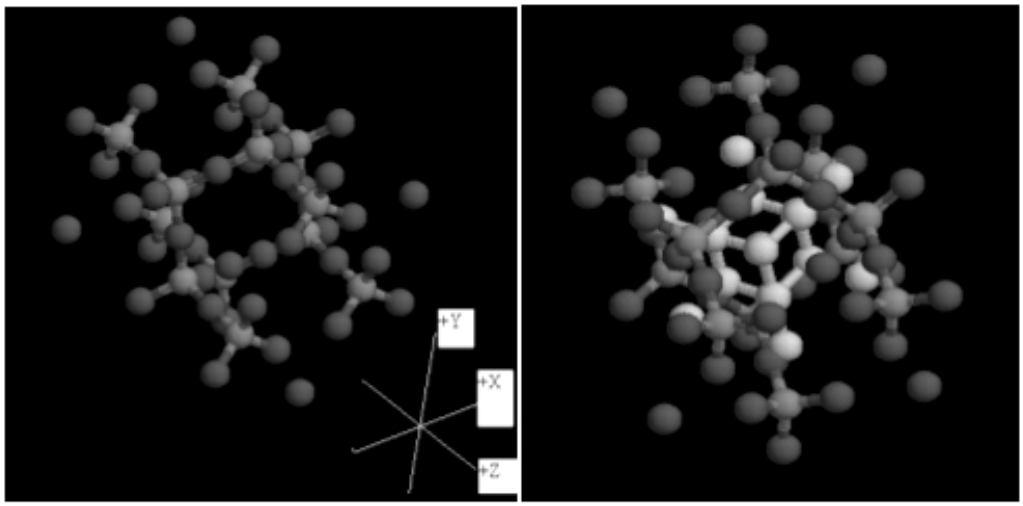

Figure 3-21: (a) β-tridymite in <111> orientation. (b) β-tridymite <111> with Si<111> superimposed. [5]

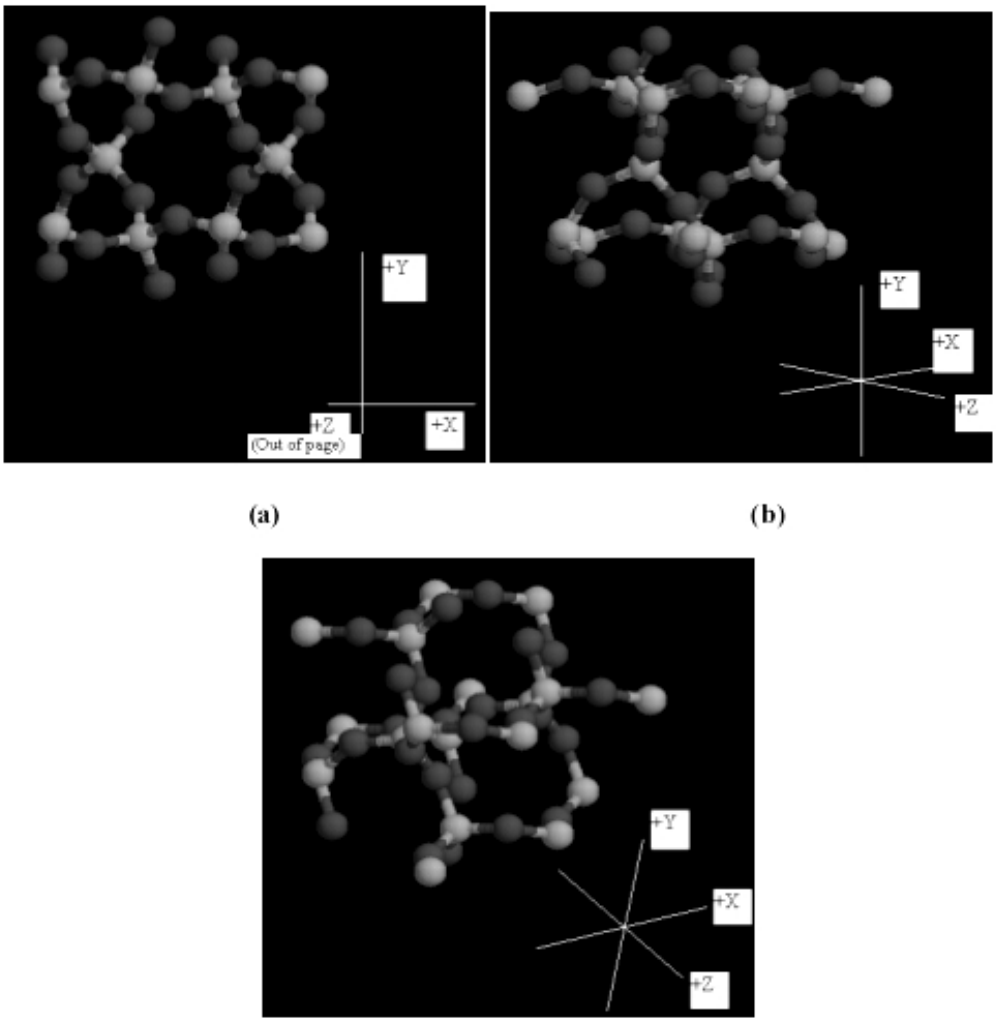

Figure 3-22: Atomic representations of α-quartz in the (a) <100> orientation, (b) <110> orientation, (c) <111> orientation [5]

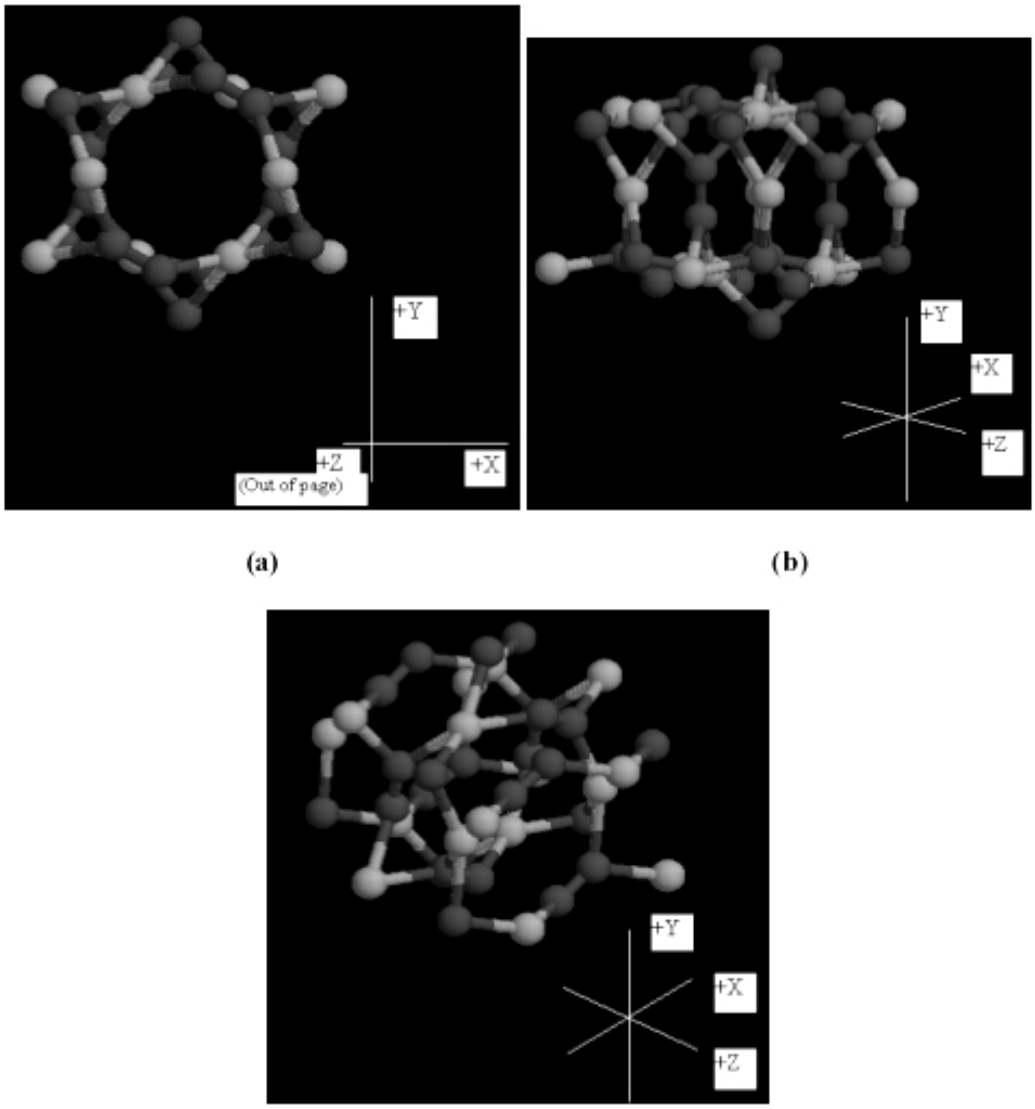

Figure 3-23: Atomic representations of β-quartz in the (a) <100> orientation, (b) <110> orientation, (c) <111> orientation [5]

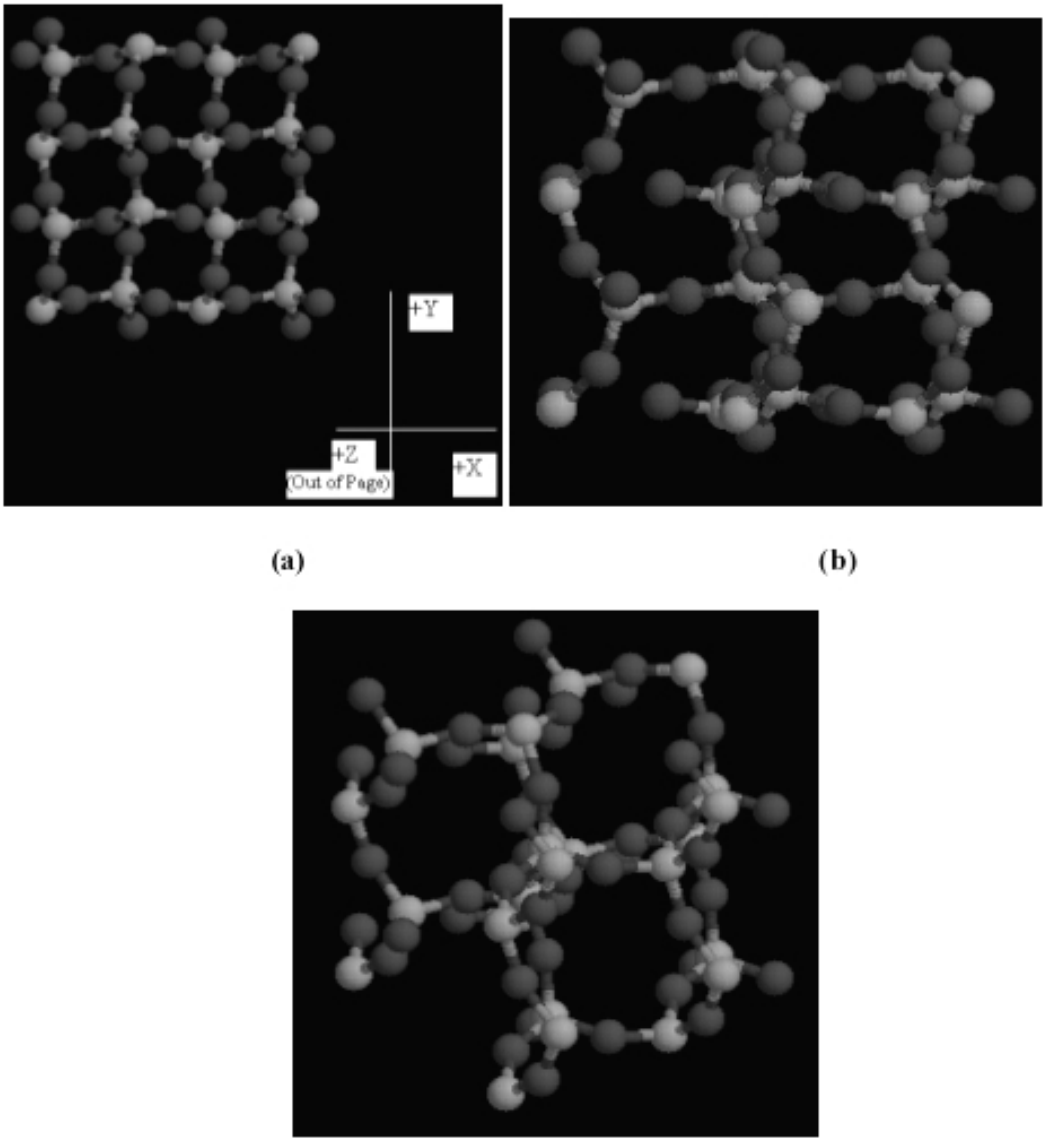

Figure 3-24: Atomic representations of α-cristobalite in the (a) <100> orientation, (b) <110> orientation, (c) <111> orientation [5].

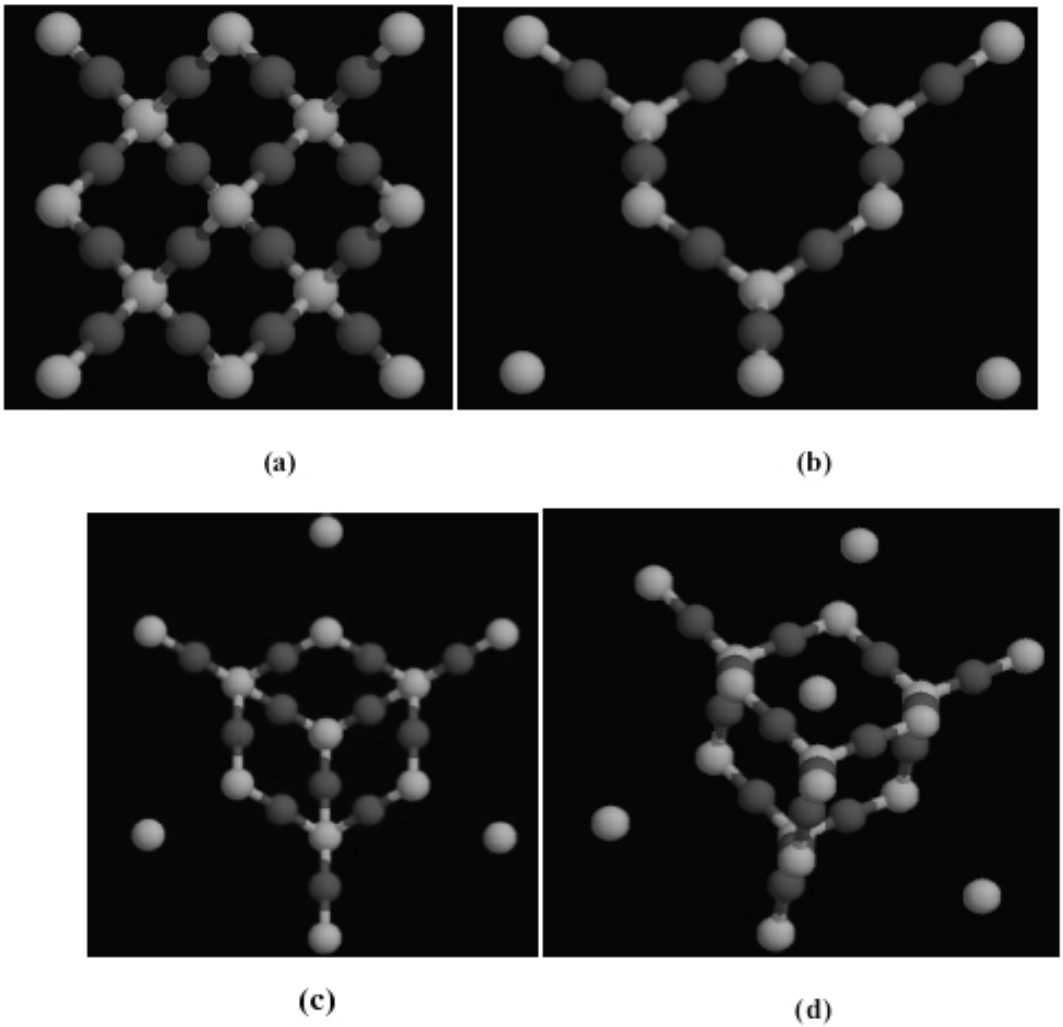

Figure 3-25: Atomic representations of β-cristobalite in the (a) <100> orientation, (b) <110> orientation, (c) <111> orientation, (d) <111> orientation at a slight offset to show shadowing effects [5].

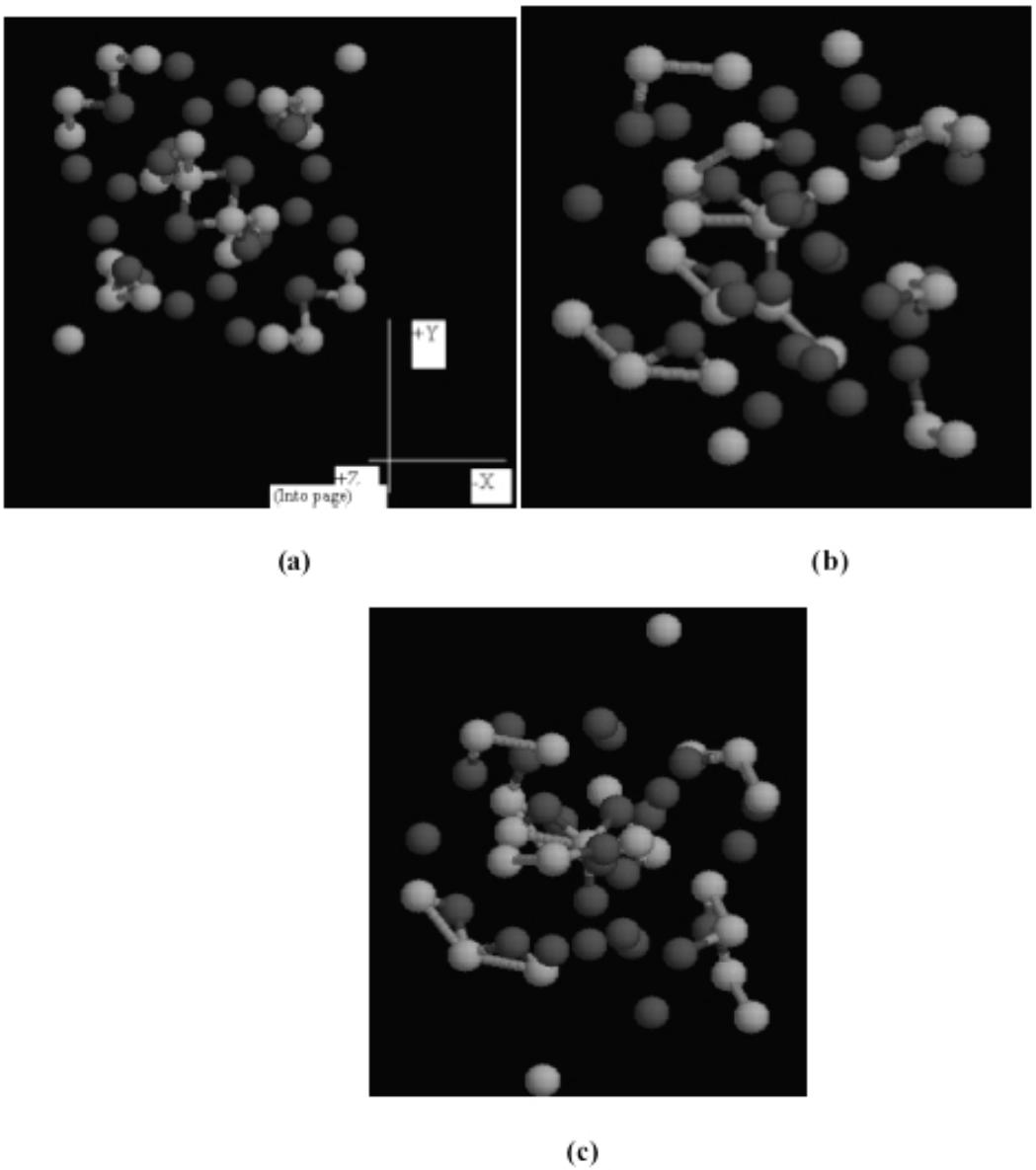

Figure 3-26: Atomic representations of Keatite in the (a) <100> orientation, (b) <110> orientation, (c) <111> orientation [5].

3.3 3DSTRING Simulation Method

3DSTRING is a Monte Carlo simulation method that was developed in the late 1970's by L. Feldman's group to simulate ion collision, channeling and blocking of Si(100) and Si(111) reconstructed surfaces[14]. The code was based on code first written by I. Stensgaard in 1979, and R.J. Culbertson, in 1980, for Si surfaces [15]. A three-dimensional version was developed by H. J. Gossman [16].The code was later rewritten by Q.B. Hurst to account for different atomic masses. For his thesis work, J. D. Bradley again modified the code, so that simulations could be performed in the <100>, <110> , and <111> directions with variable compensation.

L. Feldman *et al*, used a Moliere approximation of the Thomas-Fermi potential was chosen, Eq. 3-1. This was deemed to be the best approximation since for $0 \leq r/a \leq 6$, the values are with 0.2% of the Thomas-Fermi potential.

$$\Phi(r) = 0.35e^{(-0.3r/a)} + 0.55e^{(-1.2r/a)} + 0.1e^{(-6.0r/a)} \qquad \text{(Eq. 3-1)}$$

To prepare for the simulations, J. D. Bradley had to model, using RASMOL, the β-cristobalite in each of the <100>, <110> , and <111> directions. Then it was necessary to redevelop the strings. Each string would be atom(s) that lie upon a single line, parallel to the direction of the IBA beam. Using Cartesian coordinates, this would mean that that each atom in a string would share x and y coordinates, but have separate *z* coordinates. Figure 3-27 shows the model for the four strings required for the Si atoms in β-cristobalite in the <110> direction [5]. Each string is along the *z* axis and is assembled from 3 atoms. An input file had to be created for each crystal directions with information on each string needed to

replicate the β-cristobalite crystal in the particular direction. 3DSTRING uses the input file and simulates an incoming incident ion along the string, performing binary collision on each layer using the Moliere potential. The code then assembles a normalized nuclear encounter probabilities for atomic row in the crystal. Figure 3-28 shows an example of the 3DSTRING output for scattering probability for a doubly ionized He at 3.05 MeV in a Si <100> crystal versus the number of Si layers. The collision probability falls off as the ion penetrates the crystal due to the shadowing of the surface Si atoms.

J.D. Bradley's thesis then shows Silicon versus Oxygen Areal densities from the 3DSTRING simulation. Concentrating on the <111> direction, Figure 3-29 shows a graph of the output of the simulation for β-cristobalite <111> layered on a crystal Silicon <111> substrate. The importance of this graph is the downward slope the data. Figure 3-30, which is one of the plots from Figure 3-9, it shows the Si surface areal density versus the oxygen areal density for the <111> direction from a Si substrate cleaned by the H-A clean. The regression fit of the data, the solid black line, is well below the bulk surface Si <111> line where the oxygen areal density is equal to zero, which is the silicon surface.

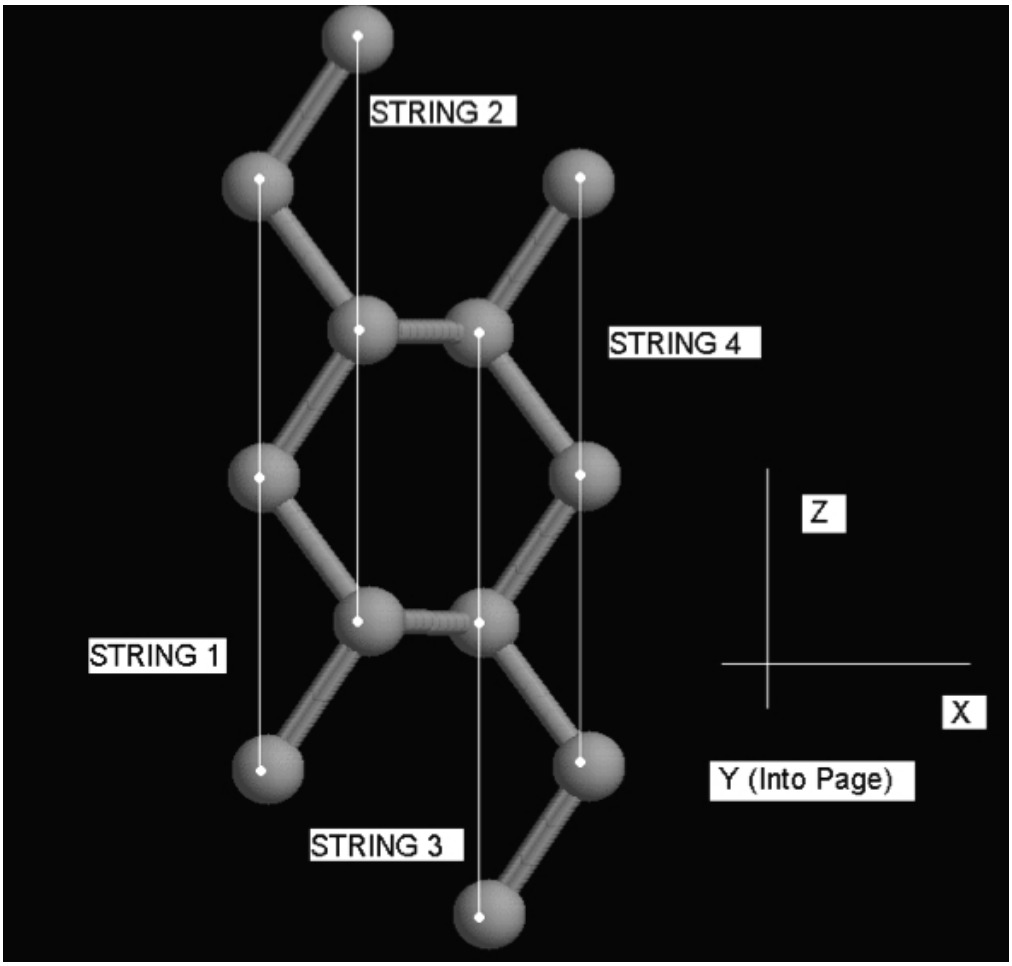

Figure 3-27: A RASMOL model showing the four strings required for the Si atoms in β-cristobalite in the <110> direction. Each string is assembled from 3 atoms. Each string is along the *z* axis [5].

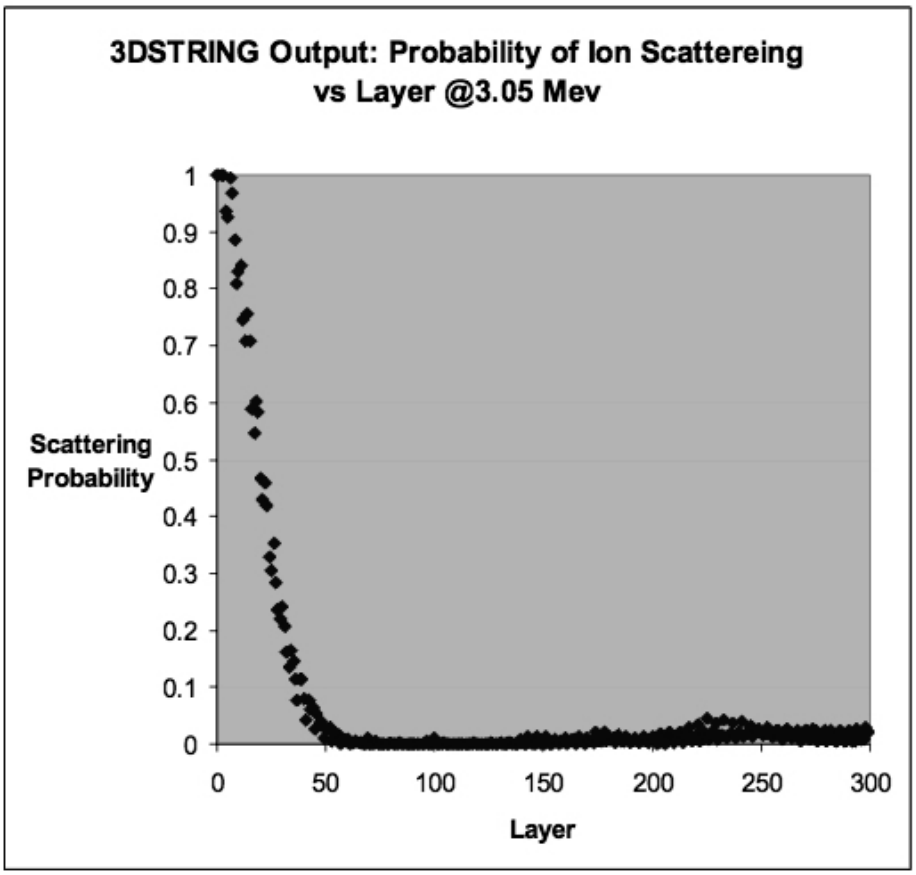

Figure 3-28: The 3DSTRING output for scattering probability of a doubly ionized He at 3.05 MeV in a Si <100> crystal versus the number of Si layers [5].

Using all of this data, Figure 3-31 is constructed. It is a graph of the silicon areal density versus the oxygen areal density [5], where the experimental <111> IBA data for a silicon substrate cleaned by the H-A clean, the calculated bulk Silicon areal density, and the 3Dstring simulation data for β-Cristobalite(100) on Si(100) along the <111> direction are plotted.

Next, Figure 3-32 adds to the previous figure the 3Dstring simulation of the data for are 100% stretched β-Cristobalite(100) on Si(100) along the <111> direction [5]. It can be seen from the graph that simulation data of stretched β-Cristobalite(100) is creating an intercept with the IBA <111> that is to the left, or counter-clockwise in rotation, from the outstretched simulation data. This suggests that this 100% stretch is not a perfect fit for the data and a longer stretched β-cristobalite(100) data is needed to intercept at the lowest oxygen areal density data provided by the IBA.

Dr. J.D. Bradley's thesis also presented several representative schematics, which demonstrated general information to explain the graphs in Figures 3-31 and 3-32 [5]. The first was a schematic of the Si surface peak areal density versus the oxygen areal density of a perfectly amorphous SiO_2 layered on a crystal silicon substrate, where there is no disorder at the interface. This schematic is shown in Figure 3-33 and is a near match for the IBA graph of a Si(100) substrate in the <100> direction cleaned by the H-A-clean. For no surface disorder, the line for the perfectly amorphous SiO_2 should intersect the bulk terminated Si surface peak at the point where the oxygen areal density is zero, which is the y-intercept of the graph, and have a slope of 0.5, due to the 1:2 stochiometry. The net displaced

atoms at the interface is the difference between the bulk silicon surface peak and the y-intercept of the perfectly amorphous SiO_2 layer, which is zero in the figure.

The next schematic, Figure 3-34, is very similar the previous one, except the y-intercept of the line for the perfectly amorphous SiO_2 is greater than that of the bulk terminated Si surface peak. This difference at the y-intercept indicates disorder at the interface and that there are displaced Si atoms. The third schematic, Figure 3-35, shows the same graph type with a negative slope that can occur when an ordered oxide layer is atop the Si substrate. This is due to shadowing by the layers of the oxide. The final schematic, Figure 3-36, represents the complete graph that occurs with an oxide that is ordered and shadows the underlying bulk Si and then becomes amorphous. There is a transition point where the ordered and amorphous phases meet. The negative slope is the data from the 3DSTRING simulations of ordered oxide atop a crystal Si substrate and the upward slope for amorphous, disordered oxide is a match to the IBA data.

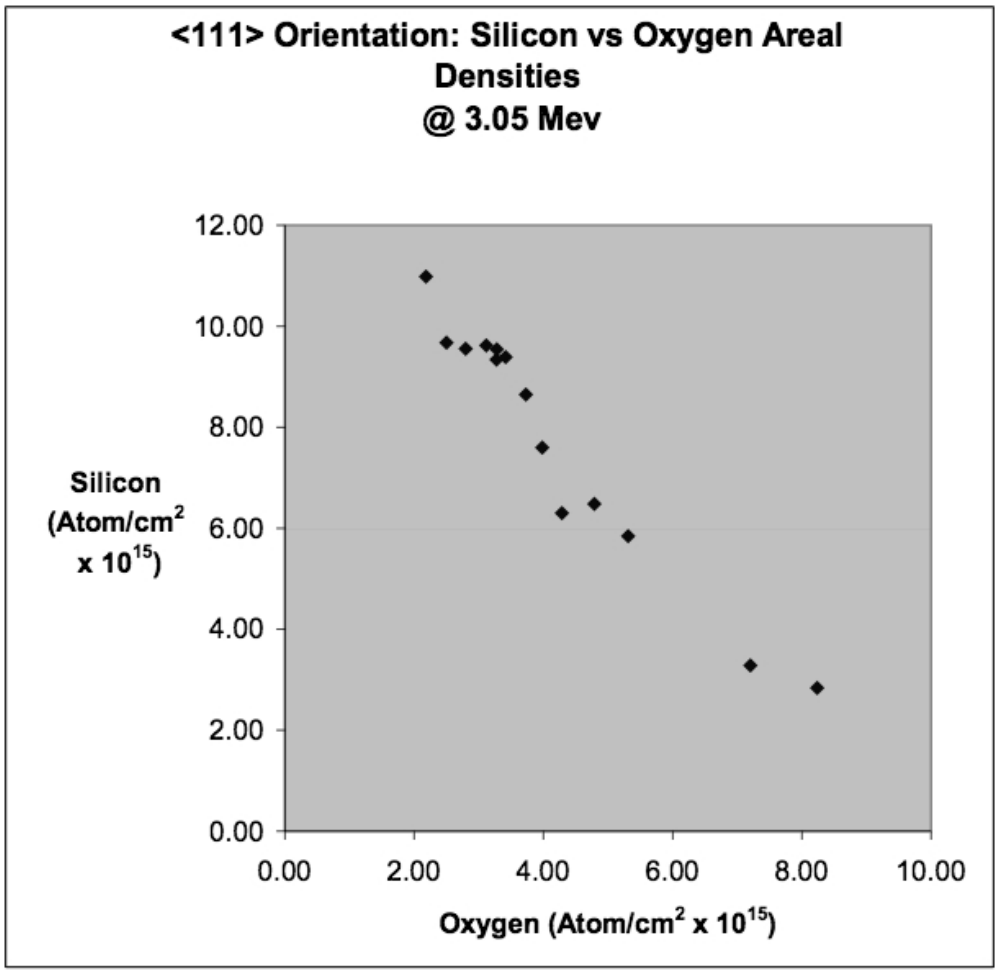

Figure 3-29: A graph of the 3DSTRING output of the simulation for β-cristobalite <111> layered on a crystal Silicon <111> substrate [5].

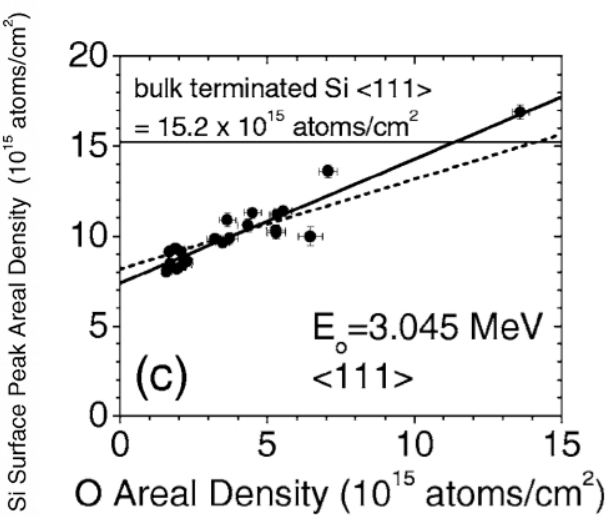

Figure 3-30: Plot of Si surface peak areal density versus that of O for Si substrates that went through the H-A clean and then underwent gate oxidization for the <111> directions. The solid regression fit based on the data, as well a dotted line which represents a regression fit with an ideal 0.5 slope. The bulk surface Si amount for each direction is shown as a horizontal line. [4].

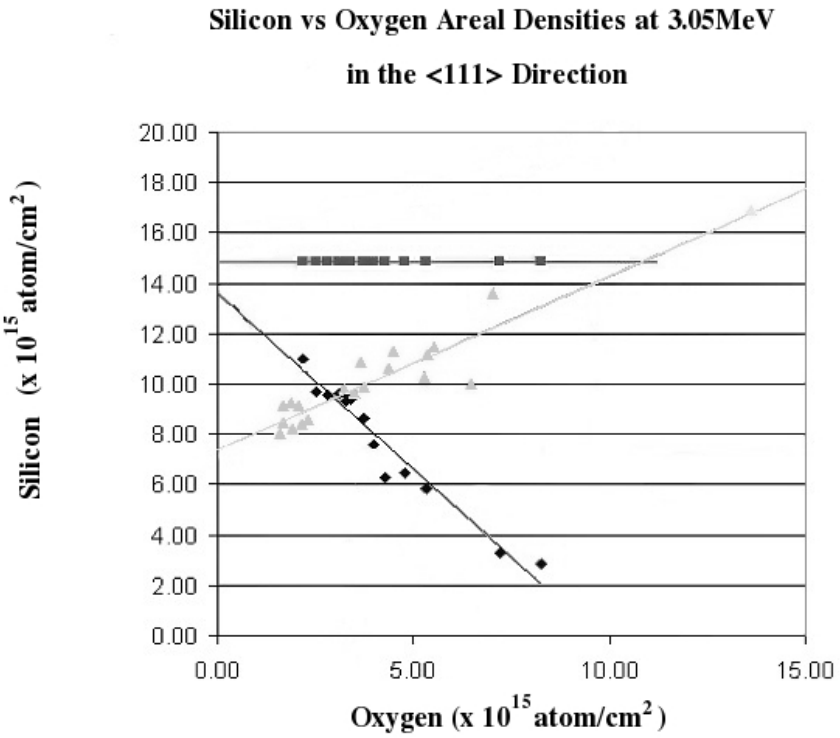

Figure 3-31: Graph of the Silicon areal density versus the oxygen areal density, where the light gray triangles are the experimental <111> IBA data for a silicon substrate cleaned by the H-A clean, the gray squares are calculated Bulk Silicon areal density, and the black diamonds are the 3Dstring simulation of the data for β-Cristobalite(100) on Si(100) along the <111> direction [5].

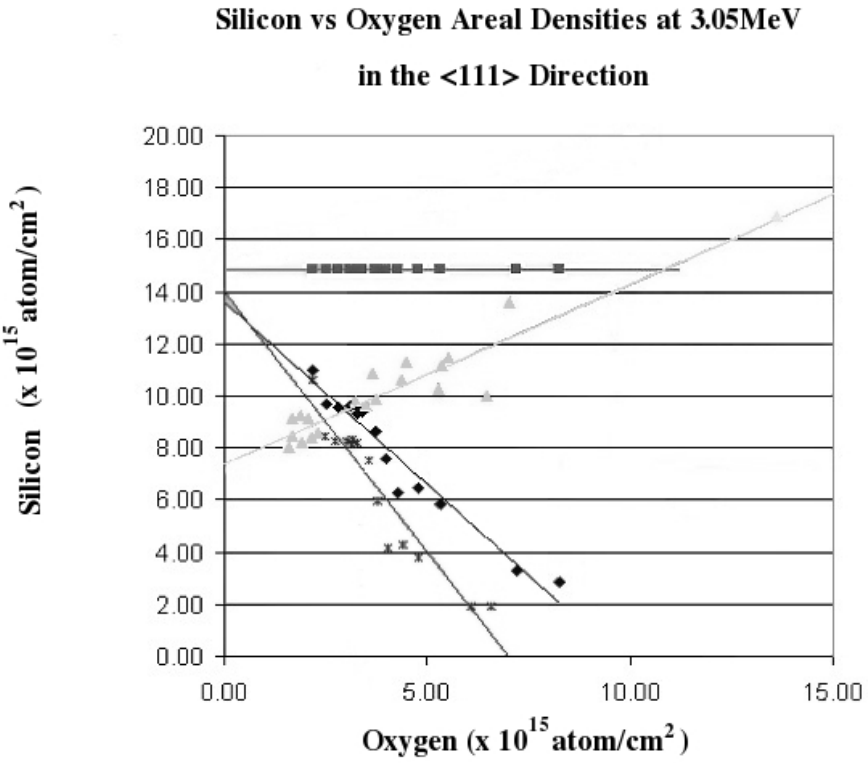

Figure 3-32: Graph of the Silicon areal density versus the oxygen areal density, where the light gray triangles are the experimental <111> IBA data for a silicon substrate cleaned by the H-A clean, the dark gray squares are calculated Bulk Silicon areal density, the black diamonds are the 3Dstring simulation of the data for β-cristobalite(100) on Si(100) along the <111> direction, and the dark gray Xs are the 3Dstring simulation of the data for 100% stretched β-cristobalite(100) on Si(100) along the <111> direction [5].

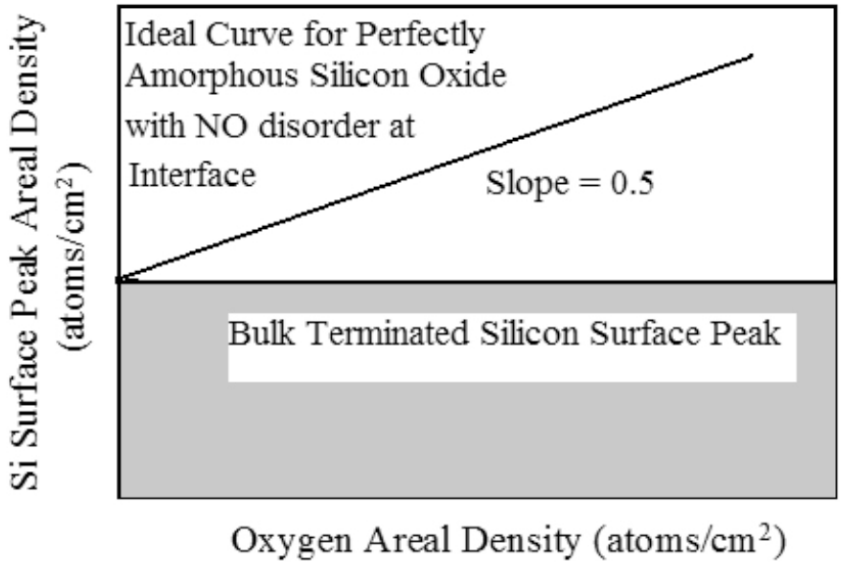

Figure 3-33: A schematic of the Si surface peak Areal density versus the oxygen areal density of a perfectly amorphous SiO_2 layered on a crystal silicon substrate, where there is no disorder at the interface. The line for the amorphous SiO_2 should intersect the bulk terminated Si surface peak at the point where the oxygen areal density is zero, which is the y-intercept of the graph, and have a slope of 0.5. The net displaced atoms at the interface is the difference between the bulk silicon surface peak and the y-intercept of the perfectly amorphous SiO_2 layer, which is zero in this graph [5]

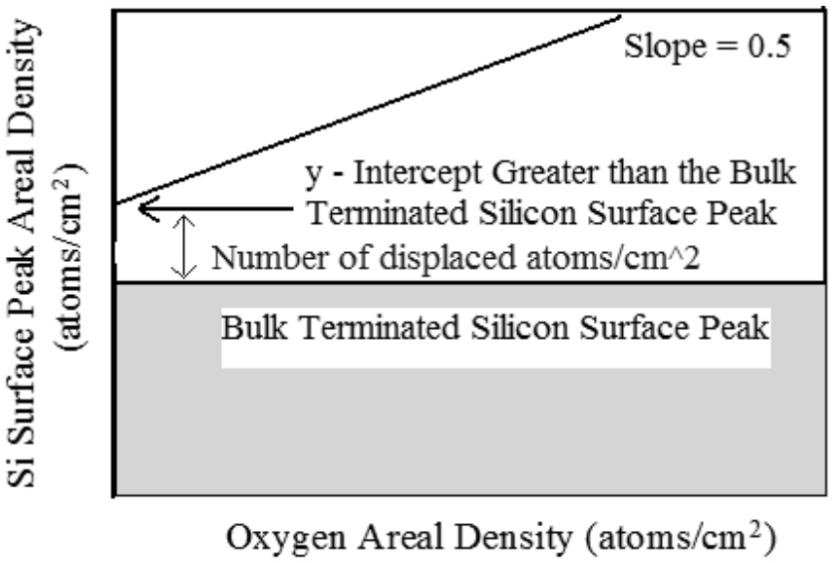

Figure 3-34: A schematic of the Si surface peak Areal density versus the oxygen areal density of a perfectly amorphous SiO_2 layered on a crystal silicon substrate, where there is disorder at the interface. The line for the amorphous SiO_2 at the y-intercept is greater than that of the bulk terminated Si surface peak. The net displaced atoms at the interface is the difference between the bulk silicon surface peak and the y-intercept of the perfectly amorphous SiO_2 layer, therefore there is disorder at the surface [5].

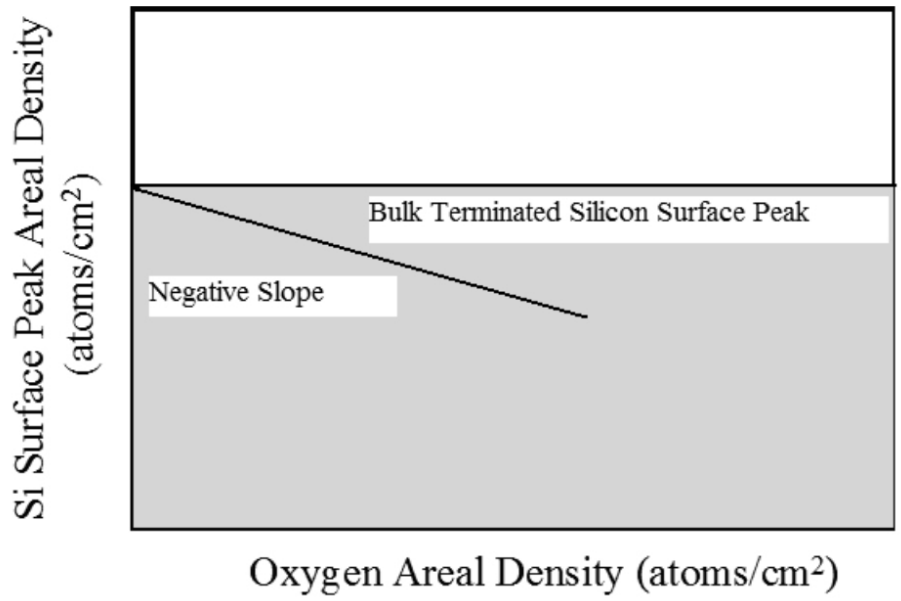

Figure 3-35: A schematic of the Si surface peak Areal density versus the oxygen areal density of a perfectly ordered oxide layered on a crystal silicon substrate. The negative slope is due to shadowing by the layers of the oxide [5].

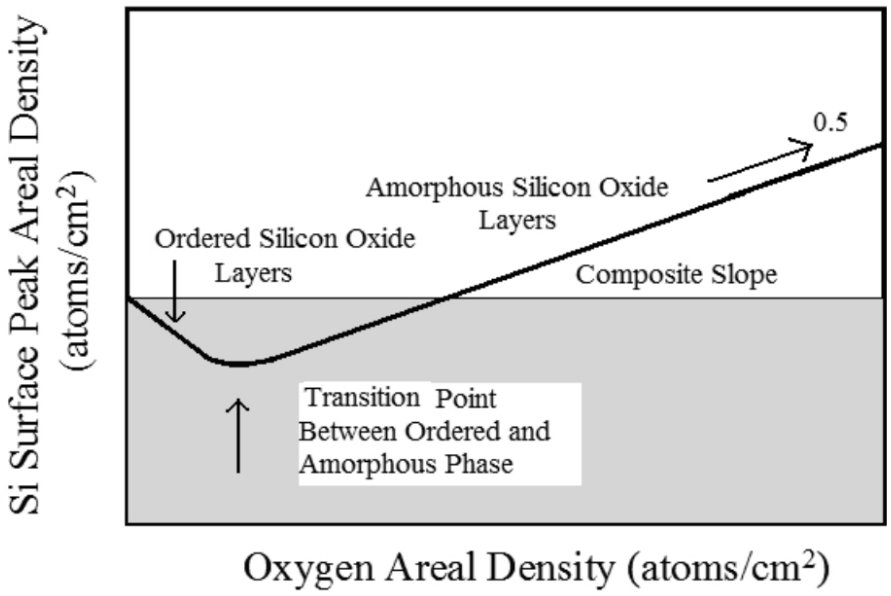

Figure 3-36: A schematic of the Si surface peak Areal density versus the oxygen areal density. This graph that occurs with an oxide that is ordered and shadows the underlying bulk Si and then becomes amorphous. There is a transition point where the ordered and amorphous phases meet [5].

Chapter 3 References

[1] W. Kern, DA Puotinen, *RCA Rev*. **31**, 234-264, (1970)

[2] N. Herbots, J. M. Shaw, Q. B. Hurst, M. P. Grams, R. J. Culbertson, D. J. Smith, V. Atluri, P. Zimmerman, K. T. Queeney, *Mater. Sc. & Eng*, **B87**, 303-316 (2001)

[3] Chabal Clean G.S. Higashi, Y.J. Chabal, G.W. Trucks, K. Raghavachari, *Appl. Phys. Lett*. **56** (7) (1990) 656

[4] Fenner Clean D.B. Fenner, D.K. Biegelsen, R.D. Bringans*, J. Appl. Phys*. **66** (1) (1989) 419.

[5] J.D. Bradley, *A new heteroepitaxial silicon dioxide nanophase on OH-(1X1) silicon (100) identified via 3.05 MEV ion channeling and the new 3-D multistring code*, Arizona State University, Ph. D. Thesis 2006

[6] J. M. Shaw, N. Herbots, Q. B. Hurst, D. Bradley, R. J. Culbertson, V. Atluri, K. T. Queeney, *J. Appl. Phys*. **100**, 10, 104-109 (2006)

[7] T. E. Jackman, J. R. MacDonald, L. C. Feldman, P. J. Silverman, I. Sternsgaard, *Surf. Sci.* , **100**, 1, 35-42 (1980)

[8] F. C. Stedile, I. J. R. Baumvol, I. F. Oppenheim, I. Trimaille, J.-J. Ganem, S. Rigo, *Nucl. Instrum. Methods Phys. Res. B*, **118**, 1-4, 493-498 (1996)

[9] N. Cheung, L. C. Feldman, P. J. Silverman, I. Sternsgaard, *Appl. Phys. Lett.* **35**, 11, 859-861 (1979)

[10] O. Kutana, *Structure And Gas Adsorption Kinetics For Monocrystalline Surfaces Studied With Low Energy Ion Scattering, University of Houston*, Ph. D. Thesis (2003)

[11] G. B. Alers, D. J. Werder, Y. Chabal, H. C. Lu, E. P. Gusev, E. Garfunkel, T. Gustafsson, R. S. Urdahl, *Appl. Phys. Lett*. **73**, 11, 1517-1519 (1998)

[12] K. T. Queeney, N. Herbots, J. M. Shaw, V. Atluri, V. Y. J. Chabal, *Appl. Phys. Lett*. **84**, 4, 493-496 (2004)

[13] K. T. Queeney, M. K. Weldon, J. P. Chang, Y. J. Chabal, A. B. Gurevich, J. Sapjeta, R. L. Opila, *J. Appl. Phys*. **87**, 3, 1322-1330 (2000)

[14] L. C. Feldman, J. W. Mayer, S. T. Picraux, *Materials Analysis by Ion Channeling*, Academic Press, N.Y. (1982)

[15] N. W. Cheung, R. J. Culbertson, L. C. Feldman, P. J. Silverman, K. W. West, J. W. Mayer, *Phys. Rev. Lett*. **45** ,2, 120-124 (1980)

[16] H. J. Gossman, Notes Preceeding 3DSTRING Source Code, Rev 7, 1987

Chapter 4: Review of Silicon Wafer Bonding Literature

A literature review was performed to locate publications relating to the wafer cleaning or silicon wafer bonding. There are papers on the RCA clean [1], papers by the Herbots group [2-5], Si(100) cleaning used as references in those papers [6-9], and thesis by a Herbots group members [10], all of which were discuss in detail in Chapter 3 on background of publications relating directly to the current work in this thesis by members of Dr. Herbots' group.

Wafer bonding was discussed in Chapter 2. The silicon wafer bonding publications review papers [11-13] overview the entire subject. There are publications covering Silicon on Insulator (SOI) technology [14-18]. To create a SOI wafer, two silicon wafers are used. One wafer will have an etch stop formed by epitaxy or implantation or polish stop layer imbedded. The second wafer has a thermal oxide grown on its surfaces. The two wafers are contacted at room temperature and then annealed, typically at temperatures above 800C. The pair are then etched or polish to the desired thickness. Papers also cover Silicon on Sapphire (SOS) [19-23], which is a special type of SOI.

Fusion bonding publications [24, 25] cover the clamped or direct bonding which uses annealing at elevated temperatures to reconstruct the surfaces of the bonded materials and then to created chemical bonds between them. Anodic bonding papers [26-34] detail experiments of a bonding procedure that is similar to fusion bonding in that annealing is performed, but an electric field is added to drive the bonding. Papers on adhesive bonding [35-40] discuss various resins to achieve bonding between wafers.

Plasma Activation [41-57] typically use N_2, O_2, Ar, H, or He plasma treatment prior to bonding for surface activation This dry plasma treatment assists with the activation of free sites for the adsorption of OH groups and the desorption of undesired chemical species that are adsorbed to the surface. This surface activation may also be achieved with UV treatment [58] or using an argon-beam [59-62].

There are various means of using an intermediate layer for bonding. Research groups have used sodium silicate layers [63], gold [64,65], spin-on-glass (SOG) [66,67], and evaporated glass [68]. Laser bonding [69], SF_6 plasma etching [70] , RF dielectric heating [71], and electromagnetic induction heating [72] have also been studied.

In a paper by Ventosa *et al.* [73], silicon wafers were cleaned in sulfoperoxide mixture of H_2SO_4 and H_2O_2, then rinsed in DI water. The wafers underwent a further RCA clean, a second DI rinse, followed by a spin-drying. The wafers were placed together at room temperature and finally annealed at a range of temperatures from room temperature to 400 °C for 2 h

Tan *et al.* published [74] a low-temperature direct bonding of CVD oxide wafers to thermal oxide wafer. Two sets of wafers were made, the first was a n-type 150 mm Si(100) wafers covered with 5000 Å of thermal oxide, which they called handle wafers. The second set were SOI dummy structures with 5000 Å thermal oxide buried oxide (BOX) underneath a 4000 Å of undoped polysilicon deposited at 620°C. Finally the SOI structure had various 1 μm CVD oxides deposited , silane low-pressure-chemical-vapor-deposition (LPCVD) oxide at

400°C, silane plasma-enhanced chemical vapor deposition (PECVD) oxide at 400°C, or tetraethyl orthosilicate (TEOS) PECVD oxide at 350°C. These SOI dummy wafers were annealed in atmospheric pressure, N_2 ambient at 350°C for 16 h to densify the oxides. They were chemical mechanically polished (CMP) for 3 min to minimize roughness. Both sets underwent a 10 min piranha (H_2O_2 : H_2SO_4 1:3) solution clean, DI water rinse, and spin-dry. The wafer pairs were bonded at room temperature at a pressure of 1000 mbar for 2 min and annealed at a temperature range of 200-300°C in atmospheric N_2 ambient. It was shown that the to achieve bonding strengths above 400 mJ/m^2 a 300°C anneal of at least 2 hr was needed for all CVD oxides.

Q. Y. Tong *et al.*, in their 2004 Applied Physics Letters paper [75], bonded native-oxide-covered silicon wafers. The wafers were treated in with a $HNO_3/H_2O/HF$ solution, a HNO_3/HF solution, or RCA clean before room-temperature bonding. RCA cleaned wafer pairs showed significantly lower bonding energy after low-temperature annealing. The bonding energy of the $HNO_3/H_2O/HF$ and HNO_3/HF treated wafers was over 2000 mJ /m^2 after annealing at 100 °C. The slight etching and fluorine in the chemically grown oxide were thought to be the main reason for the enhanced bonding energy

H. S. Min et al. [76] published their finding on the effects of wafer cleaning and annealing on glass/silicon wafer direct bonding. 100-mm borosilicate 7740 Pyrex glass wafers and *p* -type Si wafers were used in the experiments. A piranha solution (H_2O_2 : H_2SO_4 1:4 120° C), which they termed SPM for sulfuric-peroxide mixture, and/or a RCA SC-1 was used in various combinations to clean

all of the wafers. These were only SPM, only RCA, SPM after RCA, and RCA after SPM. The wafers were then aligned by their flats and bonded at room temperature using moderate pressure applied by hand to the center of the wafers. The bonding at the center of the wafer spread over the entire wafer. The wafers were then either not annealed or annealed at 200, 300, 400 and 450°C for 28 hours. The wafers left at room temperature had a bonding strength under 25 mJ/m^2, while it took a 400°C to achieve over 200 mJ/m^2. The wafer pair annealed at 450 °C became unbonded during the anneal.

S. I. Lai *et al.* [77] experimented various cleaning methods before direct bonding. 100-mm Si(100) wafers were used. The five cleaning methods were (1) a sulfuric-peroxide mixture (SPM) H_2O_2:H_2SO_4 4:1 (2) SPM plus the HF dipping (SPM-1), (3) SPM-1 plus acetone treatment (SPM-2), (4) SPM-1 plus HNO_3 dipping (SPM-3), (5) RCA clean. After wet processing,. the wafers were bonded at room temperature and then annealed 180ºC for 20 min, while a 40 N compressive force was applied on the center of wafers. Then wafers underwent a second anneal at 1100°C for 2 h with nitrogen. Only the SPM-3 treatment attained a higher bonding strength than the RCA clean. They stated that high density of OH^- and Si–H bonds, the strong hydrophilic character, and the small thickness of bonded interface layer lead to the greater strength of the bond after SPM-3 treatment. The SPM-2 had poor bonding strength, and it was believed this was due to the removing of most OH^- and Si–H bonds by the acetone.

Q. Y. Tong *et al.*, in their 2003 Applied Physics Letters paper [78], used 75-mm p-type Si(100), designated as p^-. Some were implanted with As^+, designated

As^+. The p^- and As^+ wafers underwent a clean with the RCA SC1 solution followed by a dip in 2% HF solution. The various wafer combinations were then bonded at room temperature. The As^+/As^+ and As^+/p^- bonding pairs reached the bonding energy of 2500 mJ/m^2 at 300 to 400 °C compared with 700 °C for the p^-/p^- bonding pair. It was stated that this was due to the introduction a nanometer-scale H trapping defective silicon layer produced by As^+ implantation. The same results were obtained on silicon wafers by using a brief immersion in HF, followed by B_2H_6 plasma treatment. They concluded that adding boron atoms on bonding surfaces reduce the surface hydrogen release temperature if a defective layer is formed and that to achieve high bonding energy, released hydrogen must be removed from the bonding interface.

In the Wiegan *et al.* 2000 paper in Sensors and Actuators A-Physical paper [79], a comparison was examined of the bonding of p-type 100mm Si wafers with native oxide, thermally grown oxide, plasma-enhanced chemical vapor deposition (PECVD) oxide, PECVD oxynitride, PECVD nitride and low-pressure CVD (LPCVD) nitride. The bonding energies were measured for wafers that underwent an RCA-like clean that consisted of SC-1, HF dip, then SC-2. The wafers were annealed a temperatures between 100 and 500°C for 2 hours. The bonding strength was minimal, 200 mJ/m^2, for all wafers at 100 °C. They increased to 600-700 mJ/m^2 at 200°C and continued to rise to between 900 and 1200 mJ/m^2 at 500°C. They also experimented with 6 X 6 mm^2 samples with various percentage of bonded area, created by 30 μm recessed areas, for the native oxide, thermally grown oxide, PECVD oxide, and PECVD oxynitride annealed at 400°C for 2

hours. The native oxide and thermally grown oxide samples reached a maximum tensile strength of 3 MPa for 80% bonded substrates, while the PECVD oxide, and PECVD oxynitride maximum was three times higher at 9 MPA for 80% bonded substrates.

Ljungberg *et al.* [80] examined various HF solutions as bonding pretreatment for Si(100) and Si(111) wafers. They stated that solutions with HF concentrations between 1 and 10% were acceptable pretreatment and that water rinsing should be avoided, unless this process can be done where particle contamination is prevented. Etching in HF:NH_4F solutions should not be used as a pretreatment for bonding.

Resnik *et al.* [81] in 2000 studied low-temperature (< 400°C) direct bonding in a paper published in Sensors and Actuators A-Physical paper [310]. 75-mm Si(100) and (111) wafers were used. To alleviate surface, a chemical process was performed that began with a diluted SC1 (0.25:1:5) at 70°C. The wafers underwent a 10 minute DI rinse, a 5 minute HF:H_2O 1:100 at 25°C, and a second 10 minute DI rinse. The wafers were dried, then immersed into nitric acid HNO_3 at 70 °C or 110 °C. They undergo an extended DI water rinse and were dried with nitrogen. The wafers were contacted using of Teflon fixture in ambient and at room temperature. The wafers were then annealed at temperatures ranging from 80°C to 400°C, with nitrogen, oxygen or a low-vacuum atmosphere. Bonding energy was found to be poor at temperatures < 120°C, but it increases above this temperature and levels off at bond annealing temperature of 400°C. It was also found that bond strengthening in nitrogen had a 25% higher tensile strength

versus bonding performed in vacuum or oxygen. Bonding Si(111) to Si(111) wafers had higher bonding strength than Si(100) bonded to Si(100). The nitric acid at 110°C gave stronger bonds since it offered more bonding sites, according to the article, than the 70°C processing.

In a 1989 paper, Fenner *et al.* [82] subjected wafers to a very particular chemical process. The p-type Si(100) wafers were cleaved in squares that were 2 cm by 2 cm and underwent a process using soap, organic solvents and chromic-sulfuric acid. The wafer pieces then were flushed with DI water and absolute reagent alcohol (ARA). The ARA was 90% ethanol, 5% methanol and 5% isopropyl alcohol. All of this was in the normal lab, not a cleanroom. The wafer pieces were transferred to a glovebox with a N_2 atmosphere and rotated at 3000 rpm on a Teflon table spinner. A pipette was used to place 4-6 drops, each 0.1 ml, of HF and alcohol to etch the wafer. The wafer pieces were then placed in a UHV system at $1x10^{-7}$ mbar at 150°C for 1 hour. The conclusions were that they obtained clean and passive surfaces with unexceptional efforts. They also stated that the final etch must be done with a reagent that has an elevated alcohol content of a high grade.

Hinrichs *et al.*, in a 2004 publication [83] used a Fenner-based cleaning technique. It is stated in the paper that before etching, the Si(001) wafer was treated with DI water and ethanol, then etched for 20 min in a solution of HF:H_2O:ethanol (1:1:10). Afterwards the wafer was rinsed with ethanol. Using infrared ellipsometry, they studied Si–H stretching vibrations, 2100 and 2200 cm^{-1}, and Si–O stretching vibrations, 1000 and 1290 cm^{-1}. The most intense Si–H

stretching vibrations were that of SiH_2 groups. The Si-O vibrations were that of silicon oxides. As the samples oxidized at the surface, the SiH_2 vibrations diminished, which according to the paper, was due to Si-O-Si bridge bonds.

Chapter 4 References

[1] W. Kern, D. A. Puotinen, *RCA Rev*. **31**, 234-264, (1970)

[2] N. Herbots, J. M. Shaw, Q. B. Hurst, M. P. Grams, R. J. Culbertson, D. J. Smith, V. Atluri, P. Zimmerman, K. T. Queeney, *Mater. Sc. & Eng* **B87**, 303-316 (2001)

[3] K. T. Queeney, N. Herbots, J. M. Shaw, V. Atluri, V. , Y. J. Chabal, *Appl. Phys. Lett*. **84**, 4, 493-496 (2004)

[4] K. T. Queeney, M. K. Weldon, J. P. Chang, Y. J. Chabal, A. B. Gurevich, J. Sapjeta, R. L. Opila, *J. Appl. Phys*. **87**, 3, 1322-1330 (2000)

[5] J. M. Shaw, N. Herbots, Q. B. Hurst, D. Bradley, R. J. Culbertson, V. Atluri, K. T. Queeney, *J. Appl. Phys*. **100**, 10, 104-109 (2006)

[6] T. E. Jackman, J. R. MacDonald, L. C. Feldman, P. J. Silverman, I. Sternsgaard, *Surf. Sci*. **100**, 35-42 (1980)

[7] F. C. Stedile, I. J. R. Baumvol, I. F. Oppenheim, I. Trimaille, J.-J. Ganem, S. Rigo, *Nucl. Instrum. Methods Phys. Res. B* **118**, 493-498 (1996)

[8] N. Cheung, L. C. Feldman, P. J. Silverman, I. Sternsgaard, *Appl. Phys. Lett*. **35**, 859-861 (1979)

[9] G.B. Alers, D.J. Werder, Y. Chabal, H.C. Lu, E.P. Gusev, E. Garfunkel, T. Gustafsson, R.S. Urdahl, *Appl. Phys. Lett*. **73**, 11, 1517-1519 (1998)

[10] J.D. Bradley, *A new heteroepitaxial silicon dioxide nanophase on OH-(1X1) silicon (100) identified via 3.05 MEV ion channeling and the new 3-D multistring code*, Arizona State University, Ph. D. Thesis 2006

[11] S. H. Christiansen, R. Singh, U. Gosele, *Proc. Of The IEEE* **94**, 12, 2060-2106 (2006)

[12] J. Haisma, J, G. A. C. M. Spierings, *Mater. Sci. Eng*. *R* **37**, 1-2, 1-60 (2002)

[13] Q. Y. Tong, *Mater. Sci. Eng. B* **87**, 3, 323-328 (2001)

[14] S. H. Christiansen, R. Singh, I. Radu, M. Reiche, U. Gosele, D. Webb, S. Bukalo, B. Dietrich, *Mater. Sci. Semicond. Process*. **8**, 1-3 , 197-202 (2005)

[15] C. Harendt, C. E. Hunt, W. Appel, H. G. Graf, B. Hoffling , E. Pentek , *J. Electron. Mater*. **20**, 3, 267-277 (1991)

[16] W. P. Maszara, *J. Electrochem. Soc*. **138**, 1, 341-347 (1991)

[17] T. Abe, T. Takei, A. Uchiyama, K. Yoshizawa, Y. Nakazato, Jpn. *J. Appl. Phys. Part 2* **29**, 12 , L2311-L2314 (1990)

[18] W. P. Maszara, G. Goetz, A. Caviglia, J. B. Mckitterick, *J. Appl. Phys*. **64**, 10, 4943-4950 (1988)

[19] H. M. Manasevit, W. I. Simpson, *J. Appl. Phys*. **35**, 4, 1349-1351 (1964)

[20] I. Lagnado, P. R. de la Houssaye, *Microelectron. Eng*. **59**, 1-4, 455-459 (2001)

[21] P. Kopperschmidt, G. Kastner, D. Hesse, N. D. Zakharov, U. Gosele, *Appl. Phys. Lett*. **70**, 22, 2972-2974 (1997)

[22] T. Abe, K. Ohki, A. Uchiyama, K. Nakazawa1, Y. Nakazato, *Jpn. J. Appl. Phys. Part 1* **33**, 1B, 514-518 (1994)

[23] G. P. Imthurn, G. A. Garcia, H. W. Walker, L. Forbes, *J. Appl. Phys*. **72**, 6, 2526-2527 (1992)

[24] Z. X. Xiao, G. Y. Wu, Z. H. Li, C. B. Zhang, Y. L. Hao, Y. Y. Wang, *Sens. Actuators A* **72**, 1, 46- 48 (1999)

[25] A. Berthold, B. Jakoby, M. J. Vellekoop, *Sens. Actuators A* **68**, 1-3, 410- 413 (1998)

[26] M. X. Chen, X. J. Yi, Z. Y. Gan, S. Liu, S, *Sens. Actuators A* **120**, 1, 291-295 (2005)

[27] J. Wei, S. M. L. Nai, C. K. Wong, L. C. Lee, *Thin Solid Films* **462**, 487- 491 (2004)

[28] J. Wei, S. M. L. Nai, C. K. Wong, Z. Sun, L. C. Lee, LC, *IEEE Trans. Adv. Packag*. **26**, 3, 289- 294 (2003)

[29] S. W. Choi, W. B. Choi, Y. H. Lee, B. K. Ju, M. Y. Sung, *J. Electrochem. Soc*. **149**, 1, G8- G11 (2002)

[30] Z. H. Li, Y. L. Hao, D. C. Zhang, T. Li, G. Y. Wu, *Sens. Actuators A* **96**, 1, 34-42 (2002)

[31] D. J. Lee, B. K. Ju, J. Jang, K. B. Lee, M. H. Oh, *J. Micromech. Microeng*. **9**, 4, 313- 318 (1999)

[32] A. Gerlach, D. Maas, D. Seidel, H. Bartuch, S. Schundau, K. Kaschlik, *Microsyst. Technol*. **5**, 3, 144- 149 (1999)

[33] D. J. Lee, B. K. Ju, W. B. Choi, J. W. Jeong, Y. H. Lee, J. Jang, K. B. Lee, M. H. Oh, *Jpn J. Appl. Phys. Part 1* **38**, 1A, 1- 6 (1999)

[34] M. Nese, A. Hanneborg, *Sens. Actuators A* **37**, 8, 61- 67 (1993)

[35] C. T. Pan, P. J. Cheng, M. F. Chen, C. K. Yen, *Microelectron. Reliab*. **45**, 3-4, 657-663 (2005)

[36] F. Niklaus, P. Enoksson, E. Kalvesten, G. Stemme, *J. Micromech. Microeng*. **11**, 2, 100- 107 (2001)

[37] F. Niklaus, G. Stemme, J. Q. Lu, R. J. Gutmann, *J. Appl. Phys*. **99**, 3, 297-299 (2006)

[38] I. Christiaens, G. Roelkens, K. De Mesel, D. Van Thourhout, R. Baets, *J. Lightwave Technol*. **23**, 2, 517-523 (2005)

[39] B. Ilic, P. Neuzil, T. Stanczyk, D. Czaplewski, G. J. Maclay, *Electrochem. Solid State Lett. 2* **2**, 86-87 (1999)

[40] W. P. Eaton, S. H. Risbud, R. L. Smith, *Appl. Phys. Lett*. **65**, 4, 439-441 (1994)

[41] M. G. Kibria, F. Zhang, T. H. Lee, M. J. Kim, M. M. R. Howlader, *Nanotechnol*. **21**, 13, 134011–134020 (2010)

[42] M. M. R. Howlader, T. Suga, H. Itoh, T. H. Lee, M. J. Kim*, J. Electrochem. Soc*. **156**, 11, H846- H851 (2009)

[43] X. Ma, W. Liu, C. Chen, J. Xu, Z. Song, C. Lin, *Mater. Sci. Semicond. Process*. **12**, 4-5, 161-167 (2009)

[44] M. Eichler, B. Michel, M. Thomas, M. Gabriel, C. P. Klages, *Coatings Technol*. **203**, 5-7, 826- 829 (2008)

[45] X. Ma, W. Liu, Z. Song, W. Li, C. Lin*, J. Vac. Sci. & Technol. B* **25**, 1, 229-234 (2007)

[46] X. Zhang, B. Olbrechts, J. P. Raskin, *J. Electrochem. Soc*. **153**, 12, G1099-G1105 (2006)

[47] T. Suni, K. Henttinen, A. Lipsanen, J. Dekker, H. Luoto, M. Kulawski, *J. Electrochem. Soc*. **153**, 1, G78-G82 (2006)

[48] C. M. Tan, W. B. Yu, J. Wei, *Appl. Phys. Lett*. **88**, 11, 114102 (2006)

[49] M. M. R. Howlader, S. Suehara, T. Suga, *Sens. Actuators A* **127**, 1, 31- 36 (2006)

[50] A. Sanz-Velasco, P. Amirfeiz, S. Bengtsson, C. Colinge, *J. Electrochem. Soc*. **150**, 2, G155-G162 (2003)

[51] T. Suni, K. Henttinen, I. Suni, J. Makinen, *J. Electrochem. Soc*. **149**, 6, G348-G351 (2002)

[52] M. Wiegand, M. Reiche, U. Gosele, *J. Electrochem. Soc*. **147**, 7, 2734-2740 (2000)

[53] S. Bengtsson, P. Amirfeiz, *J. Electron. Mater*. **29**, 7, 909-915 (2000)

[54] S. N. Farrens, J. R. Dekk , J. K. Smith, B. E. Roberds, *J. Electrochem. Soc*. **142**, 11, 3949–3955 (1995)

[55] V. H. C. Watt, R. W. Bow, *Electron. Lett*. **30**, 9, 693-695 (1994)

[56] O. Zuck , W. Langheinrich, M. Kulozik, H. Goebel, *Sens. Actuators A* **36**, 3, 227-231 (1993)

[57] G. L. Sun, J. Zhan, Q. Y. Tong, S. J. Xie, Y. M. Cai, S. J. Lu, Sj, *J. De Physique* **49**, C-4, 79-82 (1988)

[58] S. L. Holl, C. A. Colinge, K. D. Hobart, F. J. Kub, *J. Electrochem. Soc*. **153**, 7, G613-G616 (2006)

[59] H. Takagi, R. Maeda, T. Suga, *Sens. Actuators A* **105**, 1, 98-102 (2003)

[60] H. Takagi, R. Maeda, T. R. Chung, T. Suga, *Sens. Actuators A* **70**, 1-2, 164-170 (1998)

[61] H. Takagi, R. Maeda, T. R. Chung, N. Hosoda, T. Suga, *Jpn. J. Appl. Phys. Part 1* **7**, 4197-4203 (1998)

[62] H. Takagi, K. Kikuchi, R. Maeda, T. R. Chung, T. Suga, *Appl. Phys. Lett*. **68**, 16, 2222-2224 (1996)

[63] H. J. Quenzer , W. Benecke, *Sens. Actuators A* **32**, 1-3, 340-344 (1992)

[64] M. M. V. Taklo, P. Storas, K. Schjolberg-Henriksen, H. K. Hasting, H. Jakobsen, J. *Micromech. Microeng*. **14**, 7, 884-890 (2004)

[65] R. F. Wolffenbuttel, K. D.Wise, *Sens. Actuators A* **43**, 1-3, 223-229 (1994)

[66] H. C. Lin, K. L. Chang, G. W. Pickrell, K. C. Hsieh, K. Y. Cheng, *J. Vac. Sci. Technol. B* **20**, 2, 752- 754 (2002)

[67] D. Goustouridis, K. Minoglou, S. Kolliopoulou, S. Chatzandroulis, P. Morfouli, P. Normand, D. Tsoukalas, *Sens. Actuators A* **110**, 1-3, 401-406 (2004)

[68] S. Weichel, R. de Reus, M. Lindahl, *Sens. Actuators A* **70**, 1-2, 179- 184 (1998)

[69] U. M. Mescheder, M. Alavi, K. Hiltmann, C. Lietzau, C. Nachtigall, H. Sandmaier, *Sens. Actuators A* **97-8**, 422- 427 (2002)

[70] M. Reiche, U. Gosele, M. Wiegand, *Cryst. Res. Technol*. **35**, 6-7, 807-821 (2000)

[71] A. Bayrashev, B. Ziaie, *Sens. Actuators A* **103**, 1-2, 16-22 (2003)

[72] K. Thompson, Y. B. Gianchandani, J. Booske, R. F. Cooper, J. *Microelectromech. Syst*. **11**, 4, 285- 292 (2002)

[73] C. Ventosa, C. Morales, L. Libralesso, F. Fournel, A, M. Papon, D. Lafond, H. Moriceau, J. D. Penot, F. Rieutord, *Electrochem*. *Solid State Lett*. **12**, 10, H373-H375 (2009)

[74] C. S. Tan, K. N. Chen, A. Fan, R. Reif, *Electrochem. Solid State Lett*. **8**, 1, G1-G4 (2005)

[75] Q. Y. Tong, Q. Gan, G. Fountain, P. Enquist, R. Scholz, U. Gosele, *Appl. Phys. Lett*. **85**, 17, 3731-3733 (2004)

[76] H. S. Min, Y. C. Joo, O. S. Song, *J. Electron. Packag*. **126**, 1, 120-123 (2004)

[77] S. I. Lai, H. Y. Lin, C. T. Hu, *Mater. Chem. Phys*. **83**, 2-3, 265-272 (2004)

[78] Q. Y. Tong, Q. Gan, G. Hudson, G,. Fountain, P. Enquist, R. Scholz, U. Gosele, *Appl. Phys. Lett*. **83**, 23, 4767-4769 (2003)

[79] M. Wiegand, M. Reiche, U. Gosele, K. Gutjahr, D. Stolze, R. Longwitz, *Sens. Actuators A* **86**, 1-2, 91-95 (2000)

[80] K. Ljungberg, Y. Backlund, A. Soderbarg, M. Bergh, M. O. Andersson, S. Bengtsson, *J. Electrochem. Soc*. **142**, 4, 1297-1303 (1995)

[81] D. Resnik, D. Vrtacnik, U. Aljancic, S. Amon, *Sens. Actuators, A* **80**, 1, 68-76 (2000)

[82] D. B. Fenner, D. K. Biegelsen, R. D. Bringans, *J. Appl. Phys*. **66**, 1, 419-424 (1989)

[83] K. Hinrichs, M. Gensch, A. Roseler, N. Esser, *J. Phys. Cond. Matter* **16**, 39, S4335-S4343 (2004)

Chapter 5: Review of Theoretical Understanding of Modelling Silica, Amorphous Silica, and Silica Polymorphs

A literature review was performed on the topic of silica computations, primarily ab-initio simulations. It should be noted that a detailed discussion of the background of simulations methods is presented in Chapter 7. The review led to a large number of possible papers. These included studies at high pressure [1-15], silica gels [16-27], α-quartz [28], and zeolites [29-37]. By examining the titles and abstracts, a subset of these papers were viewed at in more detail to obtain material relevant to the amorphous silica and β-Cristobalite simulations and energy.

In a paper by Djurabekova *et al.* [38], the authors examine the radial distribution of atoms and bond angle distributions in the several silica cells by computational methods and then the results compared to experiment that have previously been performed. The coordination defects in the amorphized quartz and Si nanocrystals embedded in amorphous silica were also studied and data was presented in the paper.

In an Applied Surface Science paper [39], Watanabe, Tatsumura, and Ohdomari studied a SiO_2/Si interface and its structure. The information in this paper included Si–O–Si angles in the oxide film, X-ray diffraction intensity profiles of SiO2 models, data from a simulated oxidation process, and Si suboxide species in the oxidation simulation.

The equilibrium geometry, as well as the total energy, of four zeolites were found and presented by B. Civalleri *et al*. [40] in their paper. These results were then compared to the values for α- and β-quartz.

There were a number of the papers [41-46] that dealt with simulations of silica at high temperatures (>2000º C). Stallons and Iglesia's paper [47] on amorphous silica's structure and properties derived via simulations found the Si-O-Si bonds radial distribution functions as a function of distance from the silica surface, as well as the Lennard–Jones potential parameters for surface oxygen-adsorbate interactions. For N_2 on the silica surface, the paper found the potential energy surfaces and adsorption energy distributions. Huang *et al.* [48] used simulations to develop the thermal conductivity of silica thin films.

Gnani, Reggiani, and Rudan [49], in a paper in Physical Review B, discussed properties of electrons in SiO_2, which were calculated from the band structure. This included density of states versus energy, group velocity versus energy, electron mobility as a function of the electric field, and average energy as a function of the electric field.

Ginhoven and Hjalmarson [50] published on the Si-O-Si angle, the Si-O bond distance, and the α–quartz formation energy in Nuclear Instruments & Methods In Physics Research Section B, using simulations. Benoit *et al.* [51] used simulations and classical mechanics to find the Si-O bond length and the Si-O-Si bond angle in silica glass. They also calculated structure factors and density of state for the system.

Herzbach, Binder, and Muser paper [52] looked at silica using simulations. The authors looked primarily at α-quartz and β quartz. The data in the paper included radial pair distribution function of α-quartz, phonon density of states in α-quartz, elastic constants of β-quartz, temperature dependence of the

volume per unit cell α-β quartz transition, and equation of state for α -quartz under pressure.

Zwijnenburg, Cora, and Bell discussed bond angles and bond lengths for polymorphs of the SiO_2, BeF_2, SiS_2, and $BeCl_2$ in their publication [53]. They also included data on fragments of the crystal structures and optimized structural parameters for these materials.

Iarlori *et al.* published a study [54] on the geometry of the hydroxylated, dehydroxylated and dimethyldiethoxysilane reacted beta-cristobalite silica surfaces using simulations. The paper also included data on the total energy of these surfaces.

Schaffer and Thomson [55] investigated condensation and reverse hydrolysis reactions of silica clusters. They included data on the mechanisms and energies of these reactions.

Capron *et al.* published [56] on the formation energy of oxygen vacancies α-quartz, β-cristobalite and Stishovite and the formation energy of silicon vacancies in α-quartz and β-cristobalite.

Takada, Richet, Catlow, and Price published [57] data using simulation to calculate temperature-induced structural transformations in Cristobalite, Coesite and Amorphous Silica. They defined four different structures, each having two SiO_4 units, that have varying of Si–O bond lengths and torsional angles between them as 'structons'. They calculated the fractions of 'structons' versus temperatures in cristobalite, amorphous silica, and coesite. They also simulated volume versus temperature of cristobalite, amorphous silica, and coesite.

C. Lee [58] performed simulations of crystalline silica polymorphs. The data included lattice parameters and cohesive energies for crystalline SiO_2 polymorphs, distribution function of 0-Si-0 and Si-0-Si angles for α-cristobalite at room temperature, construction of the (100) surface of α-cristobalite before and after relaxation, and the structure of the reconstructed oxygen rich (001) surface of α- cristobalite.

In a paper on simulation involving silica polymorphs, Chagarov, Demkov, and Adams [59] calculated molecular volumes and cohesive energies for relaxed α-quartz, and computed formation energy of optimized α-quartz and β-cristobalite, which are presented in Table 1. From their model, they also obtained the surface energy of the α-quartz (0001) passivated and nonpassivated surfaces, as well as β-cristobalite (010) passivated and nonpassivated surfaces. Data was presented for the electronic density of states for β-cristobalite Si-terminated (001) surface before and after H passivation, β-cristobalite O-terminated (001) surfaces before and after H passivation, and β-cristobalite O-terminated (001) surfaces before and after the inclusion of an oxygen bridge.

In Physical Review Letters, Neaton, Mull, and Ashcroft publish an article on the properties of the interface of Si/SiO_2 that were calculated from first principles [60]. They first calculated the electronic properties of the model Si/SiO_2 interface [61] and compared this data with the electron energy-loss spectroscopy (EELS) measurements from a Nature letter by Muller *et al.* [62]. The Muller article presented data that at least 0.8 nm of silica is necessary to maintain the required bulk electrical properties based on the electronic properties

of ultrathin (1.5 nm) SiO_2 gate oxides. They computed the unoccupied density of states and the magnitude of the local energy gap found that both are directly related to the number of oxygen second neighbors of a given oxygen atom. The authors presented data that in the oxide at 8 Å from the Si/SiO_2 interface in the oxygen atoms are coordinated as in the bulk silica. Their calculations also showed that the local energy gap of the oxide 3 Å from the interface is nearly that of bulk Si, but is equal to the local energy gap of bulk SiO_2 after 5 Å. They concluded that the electronic properties of oxide layers is different from that of bulk silica at distances of less than 5 Å from the Si/SiO_2 interface.

Silica Polymorph	Formation energy per molecule (eV)
α-quartz	7.8415
β-cristobalite (I42d)	7.7382
β-cristobalite(Fd3m)	7.7352

Table 5-1: Calculated formation energy of optimized α-quartz, β-cristobalite (I42d), and β-cristobalite(Fd3m)

Chapter 5 References

[1] Y. Belmabkhout, A. Sayari, *Chem. Eng. Sci.* **64**, 17, 3729-3735 (2009)

[2] J. Horbach, *J. Phys. Cond. Matter* **20**, 24, 244118 (2008)

[3] L. P. Huang, M. Durandurdu, J. Kieffer, *Nat. Mater*. **5**, 12, 977-981 (2006)

[4] I. Saika-Voivod, P. H. Poole, R. K. Bowles, *J. Chem. Phys*. **124**, 22, 224709 (2006)

[5] L. P. Davila, M. J. Caturla, A. Kubota, *Phys. Rev. Lett*. **91**, 20, 205501 (2003)

[6] E. Gregoryanz, R. J. Hemley, H. K. Mao, *Phys. Rev. Lett*. **84**, 14, 3117-3120 (2000)

[7] J. Badro, D. M. Teter, R. T. Downs, *Phys. Rev. B* **56**, 10, 5797-5806 (1997)

[8] R. G. DellaValle, E. Venuti, *Phys. Rev. B* **54**, 6, 3809-3816 (1996)

[9] M. S. Somayazulu, S. M. Sharma, S. K. Sikka, *Phys. Rev. Lett*. **73**, 1, 98-101 (1994)

[10] A. B. Belonoshko, Geochim. *Cosmochim. Acta*, **58**, 6, 1557-1566 (1994)

[11] M. S. Somayazulu, S. M. Sharma, N. Garg, *J. Phys. Cond. Matter* **5**, 35, 6345-6356 (1993)

[12] J. S. Tse, D. D. Klug, Y. Lepage, *Phys. Rev. B* **46**,10, 5933-5938 (1992)

[13] C. Meade, R. J. Hemley, H. K. Mao, *Phys. Rev. Lett*. **69**, 9, 1387-1390 (1992)

[14] J. R. Rustad, D. A. Yuen, F. J. Spera, *Phys. Rev. B* **44**, 5, 2108-2121 (1991)

[15] J. R. Rustad, D. A. Yuen, F. J. Spera, *Phys. Of The Earth And Planet. Inter*. **65**, 3-4, 210-230 (1991)

[16] P. Falcaro, P. Innocenzi, *J. Sol-Gel Sci. Technol*. **57**, 3, 236-244 (2011)

[17] X. Li, S. E. Rankin, *Chem. Eng. Sci*. **66**, 6,1015-1026 (2011)

[18] R. Azouani, A.Michau, K. Hassouni, K. Chhor, J. F. Bocquet, J. L. Vignes, A. Kanaev, *Chem. Eng. Res. Des*. **88**, 9A, 1123-1130 (2010)

[19] H. Aguiar, J. Serra, P. Gonzalez, B. Leon, *J. Am. Ceram. Soc*. **93**, 8, 2286-2291 (2010)

[20] H. Guleryuz, I. Kaus, C. Filiatre, T. Grande, M. A. Einarsrud, *J. Sol-Gel Sci. Technol*. **54**, 2, 249-257 (2010)

[21] P. Suresh, G. Kanchana, P. Sundaramoorthi, *Eur. Phys. J. Appl. Phys*. **45**, 2, 20701 (2009)

[22] M. Mukhopadhyay, B. S. Rao, *J. Chem. Technol. And BioTechnol*. **83**, 8, 1101-1109 (2008)

[23] C. Y. Jung, J. R. Kim, S. C. Yi, *J. Ceram. Process. Res*. **9**, 2, 184-188, 2008

[24] R. Pini, S. Ottiger, A. Rajendran, G. Storti, M. Mazzotti *J. Int. Adsorp. Soc*. **14**, 1, 133-141 (2008)

[25] M. Eriksson, L. C. Klein, E. Liden, K. Lindqvist, *Mater. Sci. Technol*. **5**, 611-614 (2006)

[26] T. Lopez, M. Asomoza, M. Picquart, P. Castillo-Ocampoa, J. Manjarrezb, A. Vázqueza, J.A. Ascencio, *Opt. Mater*. **27**, 7, 1270-1275 (2005)

[27] M. Kawazu, M. Nara, T. Tsujino, *J. Sol-Gel Sci. Technol*. **31**, 1-3, 109-112 (2004)

[28] T. P. M. Goumans, A. Wander, W. A. Brown, C. R. A. Catlow, *Phys*. *Chem*. *Chem*. *Phys*. **9**, 17, 2146-2152 (2007)

[29] K. Chihara, Y. Suzuki, S. Tomita, J. Kabe, *J. Int. Adsorpt. Soc*. **17**, 1, 201-203 (2011)

[30] M. A. Saada, S. Rigolet, J. L. Paillaud, N. Bats, M. Soulard, J. Patarin, J. Phys. Chem. C **114**, 26, 11650-11658 (2010)

[31] C. M. Zicovich-Wilson, F. Gandara, A. Monge, M. A. Camblor, J. Am. Chem. Soc. **132**, 10, 3461-3471 (2010)

[32] S. Himeno, M. Takenaka, S. Shimura, *Mol. Simul*. **34**, 10-15, 1329-1336 (2008)

[33] G. De Luca, P. Pullumbi, G. Barbieri, A. D. Famàa, P. Bernardoa, E. Drioli, *Sep. Purif. Technol*. **36**, 3, 215-228 (2004)

[34] M. G. Wu, M. W. Deem, *J. Chem. Phys*. **116**, 5, 2125-2137 (2002)

[35] J. R. Hill, J. Sauer, *J. Phys. Chem*. **99**, 23, 9536-9550 (1995)

[36] G. Schrimpf, M. Schlenkrich, J. Brickmann, P. Bopp, *J. Phys. Chem*. **96**, 18, 7404-7410 (1992)

[37] J. O. Titiloye, S. C. Parker, F. S. Stone, C. R. A. Catlow, *J. Phys. Chem*. **95**, 10, 4038-4044 (1991)

[38] F. Djurabekova, M. Backholm, M. Backman, O. H. Pakarinen, J. Keinonen, K. Nordlund, T. R. Shan, B.D. Devine, S. B. Sinnott, *Nucl. Instrum. Methods Phys. Res. Sect. B* **268**, 19, 3095-3098 (2010)

[39] T. Watanabe, K. Tatsumura, I. Ohdomari, *Appl. Sci*. **237**, 1-4, 125-133 (2004)

[40] B. Civalleri, C. M. Zicovich-Wilson, P. Ugliengo, V. R. Saunders, R. Dovesi, *Chem. Phys. Lett*. **292**, 4-6, 394-402 (1998)

[41] A. Carre´, J. Horbach, S. Ispas , W. Kob, , *Eur. Phys. Lett*. **82**, 1 (2008)

[42] K. Binder, J. Horbach, H. Knoth , P. Pfleiderer, J. *Phys.: Condens. Matter* **19**, 20 (2007)

[43] K. Binder, J. Horbach, A. Winkler, W. Kob, *Ceram. Int*. **31**, 5, 713-717 (2005)

[44] K. Yamahara, K. Okazaki, K. Kawamura, *J. Non-Cryst. Solids* **291**, 1-2, 32-42 (2001)

[45] A. Roder, W. Kob, K. Binder, *J. Chem. Phys*. **114**, 17, 7602-7614 (2001)

[46] R. M. Van Ginhoven, H. Jonsson, L. R. Corrales, *Phys. Rev. B* **71**, 2, 024208, (2005)

[47] J. M. Stallons, E. Iglesia , *Chem. Eng. Sci*. **56**, 14, 4205–4216 (2001)

[48] Z. X. Huang, Z. A. Tang, J. Yu, S. Y. Bai, *Physica B* **404**, 12-13, 1790-1793 (2009)

[49] E. Gnani, E. Reggiani, S. Rudan, *Phys. Rev. B* **66**, 19, 195-205 (2002)

[50] R. M. Van Ginhoven, H. P Hjalmarson, *Nucl. Instrum. Methods Phys. Res. Sect. B* **255**, 1, 183-187 (2007)

[51] M. Benoit, S. Ispas, P. Jund, R. Jullien, *Eur. Phys. J. B* **13**, 4, 631-636 (2000)

[52] D Herzbach, K. Binder, M. H. Muser, *J. Chem. Phys.* **123**, 12 (2005)

[53] M. A. Zwijnenburg, F. Cora, R. G. Bell, *J. Am. Chem. Soc.* **130**, 33, 11082-11087 (2008)

[54] S. Iarlori, D. Ceresoli, M. Bernasconi, D. Donadio, M. Parrinello, *J. Phys. Chem. B* **105**, 33, 8007-8013 (2001)

[55] C. L. Schaffer, K. T. Thomson, *J. Phys. Chem. C* **112**, 33, 12653-12662 (2008)

[56] N Capron, S. Carniato, A. Lagraa, G. Boureau, A. Pasturel, *J. Chem. Phys.* **112**, 21, 9543-9548 (2000)

[57] A. Takada, P. Richet, C. R. A. Catlow, G. D. Price, *J. Non-Cryst. Solids* **354**, 2-9, 181-187 (2008)

[58] C. Lee, *J. Phys. C:Solid State Phys.* **19**, 28, 5555-5568 (1986)

[59] E. Chagarov, A. A. Demkov, J. B. Adams, *Phys. Rev. B* **71**, 7, 075417 (2005)

[60] J. B. Neaton, D. A. Mull, N. W. Ashcroft, *Phys. Rev. Lett.* **85**, 6, 1298-1301 (2000)

[61] A. Pasquarello, M.S. Hybertsen, and R. Car, *Appl. Phys. Lett.* **68**, 625-627

(1996)

[62] D. A. Muller, T. Sorsch,S. Moccio, F. H. Baumann, K. Evans-Lutterodt, G. Timp, *Nature* **399**, 758-761 (1999)

Chapter 6 Experimental Methodology

6.1 Methodical Approach

6.1a Class 10 Clean-room, Laminar Flow Hood, and Chemicals

The clean-room used for the experiments in this thesis is located within the Combined Ion and Molecular Deposition (CIMD) Laboratory of Prof. Nicole Herbots. The clean-room is class 100 and is 400 square feet. It houses a Class 10 wet-chemistry laminar flow hood, the CIMD deposition chamber, a controlled atmosphere glovebox and a second laminar flow hood with a work surface for wafer preparation.

The class 10 wet-chemistry laminar flow hood, shown in Figure 6-1 has several elements, which allow the wafer processing experiments. One element is a temperature controlled, dual chamber, Pyrex bath for the SC1 and SC2 solutions. Another feature of the hood is the DI water bath with overflow basin and N_2 bubbling capability. A dual chamber, Teflon bath allows for HF acid etches and includes Teflon stir bar capability. All three of these baths are capable of processing wafers ranging in size up to 300 mm. The methanol rinse step is done in a glass bath that accepts wafers up to 200 mm. The laminar flow hood incorporates a "hood in hood" design where air from the inner "ceiling" of the hood flows over the baths to eliminate vapor and fume cross-contamination from the corrosive acids, solvents, and water used in the various baths.

All chemical baths are installed below the working surface so that a gap is present to draw air through. The hood includes a DI water sink, a DI water spray

gun and an N2 gun. The pyrex SC1/SC2 bath and the Teflon HF bath each have two chemical removal stations, one inside the cleanroom and one in an exterior station. This allows for re-use of some of the chemicals, especially SC1, for cleaning materials which enter the hood. All new materials that are used in the hood then undergo a SC1/DI Water Rinse/SC2/ DI Water Rinse cleaning before use in any experiment. Due to the corrosive nature of many of these chemicals, any person working in the hood wears an acid apron, acid gloves, and a face shield. A full mask respirator is used when wiping down or cleaning any part of the hood, which was done occasionally to minimize any chance of contamination.

Due to the cleanliness needed for the research, all experimenters went through a multiple step process before entering the cleanroom. The first step was to enter the stairway leading to the cleanroom, where booties and hair nets were put on. Then a series of clean room entrance mats, also referred to as sticky mats, were walked on to remove and contaminates on the booties. Experimenters would then enter a Changing Room, where they would first go through a air shower with vinyl strip curtain to eliminate dust, loose hair, etc. from their clothing. A first pair of gloves would be put on before gowning. The gowning consisted of donning a hood, boots and Electrostatic Discharge (ESD) coverall. Then a second pair of gloves would be worn before entering the cleanroom. Sticky mats were placed on both sides of the door leading from the Change Room to the cleanroom. Another vinyl strip curtain was placed between the main cleanroom and this door to minimize air flow from the Change room. The flooring consisted of ESD tiles that were chemically resistant.

The chemicals used in the experiments are crucially important. 18 MΩ DI water was used, which had its resistivity monitored within the cleanroom. The NH_4OH, HF, HCl, H_2O_2, and Methanol were clean-room grade chemicals. The chemicals for each experiment were used only once and then disposed of, so that there would be no cross-contamination. Each bath was thoroughly rinsed with DI water after emptying to also eliminate contamination. The wafers in the experiments were handled with tools that hand been cleaned and did not come into contact with gloved hands, unless an extremely rare occurrence happened and was noted in the log sheets for the experiment.

6.1b Experimental Wet-Chemical set-up for Physical/Chemical Synthesis

6.1b i Chemical and Water Baths

Each experiment required that the SC1 and SC2 be prepared and brought to a temperature of 80° C. The SC1 solution used consisted of DI H_2O:NH_4OH: H_2O_2 (4:1:1), while the SC2 solution consisted of DI H_2O:HCl: H_2O_2 (4:1:1). A Modutek controller was used control a resistive heater to the target temperature, within $\pm$5° C. This would be turned on so it would fill DI water bath and begin to overflow into its catch basin. The N_2 would be turned on to this bath so that bubbling would begin. One Teflon bath would be prepared with DI H_2O:49% HF (98:2) and the second with 49% HF: Methanol (1:9). The glass bath would be filled with Methanol.

6.1b ii Wafers

The wafers would be prepared in the second laminar flow hood. The wafers, which could be Si, silica, or Si with thermal SiO_2, would be removed from their original, sealed boxes in the laminar flow hood. Both whole and quartered wafers were used in the experiments. The quartered wafers were obtained by using a diamond scribe to place a small notch in the wafer's edge. Then a cleanroom wipe, which is a polyester cloth wipe low particulates, was used to place pressure on the back of the wafer until it the wafer cleaved into two pieces, due to its crystal structure. Each half-wafer then underwent the same process. All wafers or quarter wafers were scribed, using the experiment number and then a wafer/wafer-piece number so that they could be tracked during and after the experiment. The wafers/wafer-pieces were then placed in Teflon carriers using Teflon tweezers. These carriers were then transported to the class 10 wet-chemistry laminar flow hood for processing.

6.1b iii Documentation

The documentation of the experiments evolved during the course of the experiments. Early experiments had lab book records with some pictures. Later experiments, 15 onward and additional experiments for Medtronic and Entreprix, had a detailed log sheets and multiple pictures were taken during the experiment.

6.1b iv Pressure Application Mechanism and Low Temperature Annealing Oven

The pressure application mechanism method improved over the course of several experiments. All compression application and oven annealing was done

inside the Herbots group clean room, therefore all materials were able to meet the standards necessary to ensure the integrity of the clean room environment. This imposed limits on the materials that could be used. Initially closed-cell polyurethane foam rubber was used to envelope the wafer pieces during the initial tests. The initial compressing force was achieved by placing a another, clean Si(100) wafer on top of the foam with a beaker placed on top of this secondary wafer. Clean stainless steel blocks were placed in the beaker to increase the force. This was to attain an even compression across the samples. It was found that the foam is incompatible with the 200^{o}C used in the annealing step and therefore a different method would be needed.

At this point, Murdock Hart, an ASU undergraduate working in the Herbots group, began to design a system that had a much higher evenness of compression. The design called for use of two planar surfaces, each having a resilient liner on the side that would contact the outside of the bonded wafer pair. The liner would be used to evenly distribute the force, since rigid plates alone would lead to point contacts because of the difficulty of alignment.

The second pressure application apparatus consisted of two 15 cm in diameter round stainless steel plates, approximately 250 g each, with a round styrene butadiene rubber used as a liner on each plate. A long-nose lock-jaw plier welded to each plate, which provided a secure clamp and applied force to the outside of a single bonded wafer pair. A picture of this clamping mechanism is shown in Figure 6-2.

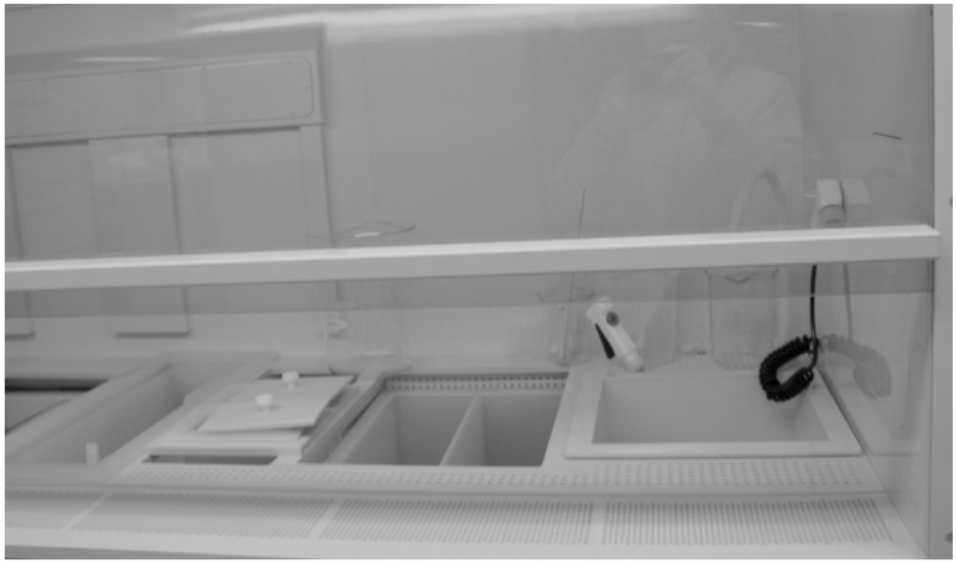

Figure 6-1: A view of the right-hand side Class 10 wet-chemistry laminar flow hood. From left to right, it shows the Di water bath, two small holding tanks with covers, the dual Teflon bath, the water spray gun, swan-neck faucet, and N_2 spray gun.

Figure 6-2: A picture of the second pressure application apparatus, consisting of two round stainless steel plates with a round styrene butadiene rubber used as a liner on each plate. A long-nose lock-jaw plier welded to each plate.

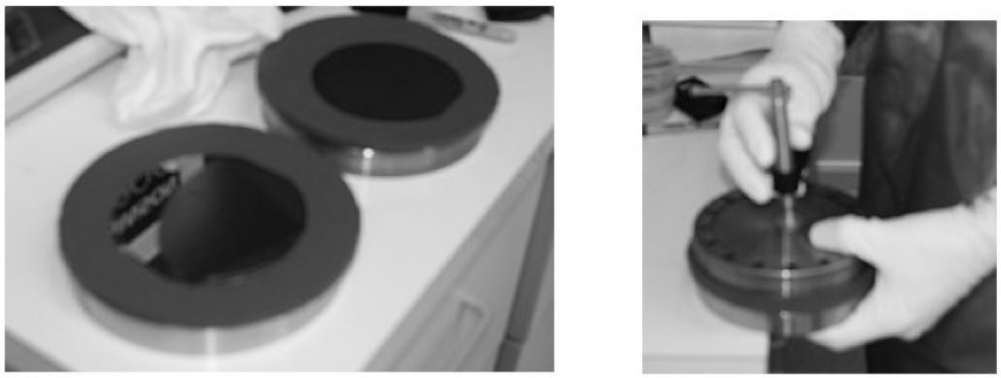

(a) (b)

Figure 6-3: Pictures of third pressure application apparatus. Image (a) shows the two 6 inch stainless steel flange caps, with a round styrene butadiene rubber used as a liner on each flange cap. Image (b) shows the stainless steel c-clamp being affixed to the flange pair, to provided a secure clinching mechanism and applied force to the outside of a single bonded wafer pair.

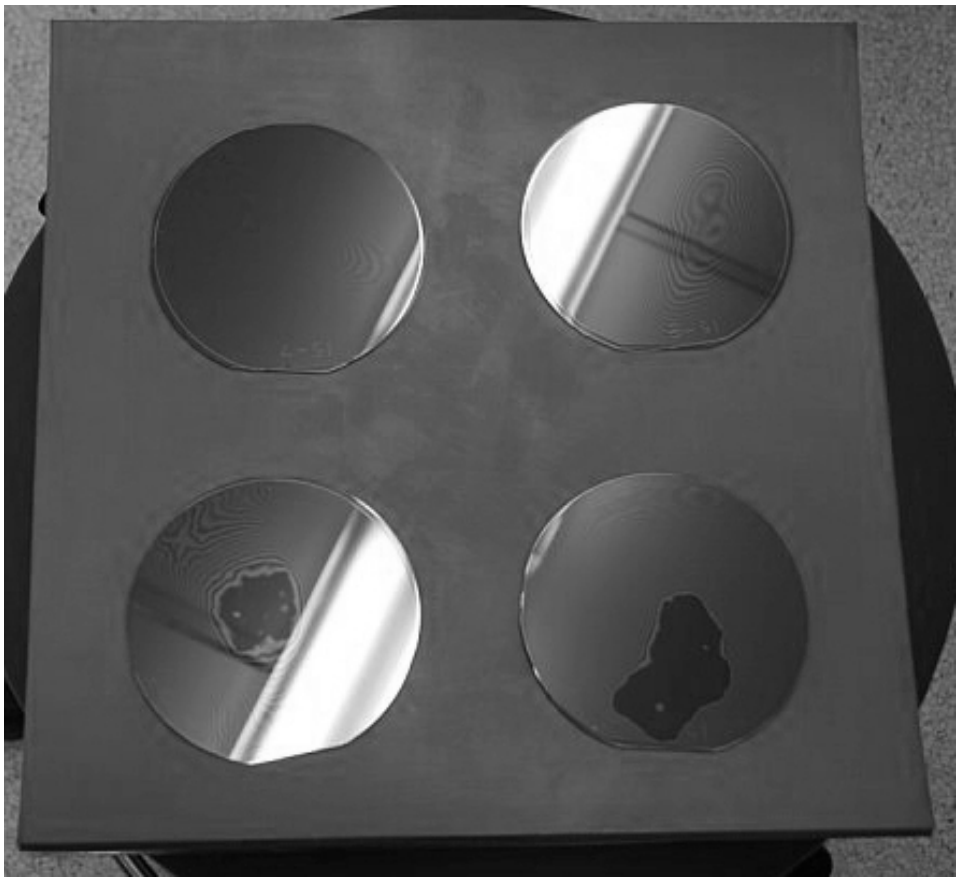

Figure 6-4: The bottom portion of the fourth pressure application apparatus, consisting of two square stainless steel plates, with a square styrene butadiene rubber sheet as a liner . This device was designed to accommodate up to four bonded wafer pairs. Some bonding between the lower two sets of bonded wafers is apparent in the image.

The third pressure application apparatus consisted of two 6 inch stainless steel flange caps, approximately 500 g each, with a round styrene butadiene rubber used as a liner on each flange cap. A stainless steel c-clamp was affixed to the flange pair, which provided a secure bracing mechanism and applied force to the outside of a single bonded wafer pair. Figure 6-3 shows the mechanisms both open and securing wafers.

The fourth pressure application apparatus consisted of two square 25 cm X 25 cm stainless steel plates, approximately 5 kg each, with a square styrene butadiene rubber sheet as a liner for each plate. This device was designed to accommodate up to four bonded wafer pairs. The weight of the upper plate, as well as an additional 25 cm X 25 cm stainless steel plate placed on top of the clamping device, exerted a force to the outside of the wafer pair. A picture of the bottom portion of this mechanism, as seen from above, is presented in Figure 6-4.

A Fisher Scientific Gravity Convection Oven was used for the low temperature anneal of the bonded wafer pairs. This oven was able to attain 200^{o}C for 24 hours, which was the requirement for the experiments. A thermometer measured the internal temperature. The oven had stainless steel on the inside which allowed the surfaces to be cleaned of any contamination. The outside of the oven was cleaned for use in the clean room.

6.3 Entrepix Processing

The wafers that were processed at the Entrepix facility in Tempe AZ were processed in a piece of semiconductor equipment that is based on a SEZ America wet-chemical apparatus. This machine is a single wafer processing tool that holds

the wafer using a patented Bernoulli wafer holder, also referred to as a Bernoulli chuck, which allows the wafer to be held and rotated 360° without any contact with the backside surface. The tool has fluid rate control of liquid chemicals (including DI water), multiple vertical process levels, separated chemical supply lines with re-circulating ability [www.entrepix.com/SEZ-Foundry.php, June 16,2010]. This experimental design allowing the wafer to spin during processing, which allows uniformity across the wafer. The liquid chemicals are applied to the wafer via a spray nozzle, which allows low consumption and precise application of the chemicals.

Tables 6-1 to 6-5 contain the complete processing data for the 24 wafers that were processed at Entrepix and then finished processing in the Herbots group clean room.

Group	Wafer #	SC1/HF/SC2 (minutes)	HF:Meth (minutes)	Methanol Dip (minutes)	Observations
Done at Entrepix			Done at ASU lab		
D	6	10/0.5/2	1	1	'"Some" spots, "some" residue: disappears within 30 seconds, wet initially, Wafer 7 was dropped onto wipe (backside)
	7	10/0.5/2	1	1	
	8	10/1/02	1	1	Wet initially, spot at tweezer site, more even dewetting (than 6,7 above), a few spots, no residue
	9	10/1/02	1	1	

Table 6-1: Data for Wafers 6-9 were processed at Entrepix and then finished processing in the Herbots group clean room.

Group	Wafer #	SC1/HF/SC2 (minutes)	HF:Meth (minutes)	Methanol Dip (minutes)	Observations
Done at Entrepix			Done at ASU lab		
C	10	2/0.5/2	1	1	Wet initially, Some residue, Less even drying [than 8,9 above], spots at tweezer site, Residue gone by 15 seconds, A few large spots
	11	2/0.5/2	1	1	
	12	2/1/2	1	1	Wet initially, Tiny amount of residue, some spotting, Residue gone by 40 seconds, Unequal spots
	13	2/1/2	1	1	

Table 6-2: Data for Wafers 10-13 were processed at Entrepix and then finished processing in the Herbots group clean room

Group	Wafer #	SC1/HF/SC2 (minutes)	HF:Meth (minutes)	Methanol Dip (minutes)	Observations
Done at Entrepix			Done at ASU lab		
B	14	3/0.5/3	1	1	Wet initially, even drying,1 spot (minimal spots), Faint residue which "quickly" disappears
	15	3/0.5/3	1	1	
	16	3/1/3	1	1	Initially wet, slightly uneven drying, slight residue, residue gone within 30 seconds, some streaks at wafer bottom (bottom 1/3), some spots
	17	3/1/3	1	1	

Table 6-3: Data for Wafers 14-17 were processed at Entrepix and then finished processing in the Herbots group clean room

Group	Wafer #	SC1/HF/SC2 (minutes)	HF:Meth (minutes)	Methanol Dip (minutes)	Observations
Done at Entrepix			Done at ASU lab		
A	18	5/0.5/5	1	1	Initially wet, even drying, some residue, residue gone in 45 seconds, minor spotting, no spots at top 1/2 of wafer
	19	5/0.5/5	1	1	
	20	5/1/5	1	1	Wet initially, even drying, residue at medium, no spots at top half, residue gone in 30 seconds, wafer 21 had more spotting
	21	5/1/5	1	1	

Table 6-4: Data for Wafers 18-21 were processed at Entrepix and then finished processing in the Herbots group clean room

Group	Wafer #	SC1/HF/SC2 (minutes)	HF:Meth (minutes)	Methanol Dip (minutes)	Observations
Done at Entrepix			Done at ASU lab		
Baseline	22	10/0.5/10	1	1	Initially wet, uneven drying, medium residue, 45 seconds for residue to disappear, medium spotting at bottom
	23	10/0.5/10	1	1	
	24	10/1/10	1	1	Initially wet, even drying, streaking, residue was strong, 45 seconds for residue to disappear, wafer 25 touched by wafer 24
	25	10/1/10	1	1	
Witness	1	No Processing			Not Processed

Table 6-5 Data for Wafers 22-25 were processed at Entrepix and then finished processing in the Herbots group clean room. Wafer 1 was not processed.

6.4 Material Characterization Technique

6.4a Atomic Force Microscopy

In 1985, Binnig, Quate and Gerber, using the Scanning Tunneling Microscopy (STM) [1] as a basis, developed Atomic Force Microscopy (AFM) as a technique which allowed scanning of non-conductive surfaces [2]. In an AFM system, a laser is focused on the topside of a cantilever where the pyramidal AFM tip resided just underneath. The laser beam would then bounce off the cantilever and onto a split photodiode. The vertical movement of the cantilever is detected by the photodiode.

There are two main types of AFM which give topographical data. The first is contact mode, in which the tip is brought into physical contact with the surface [3]. The tip is rastered in the x and y directions across the surface. This movement is achieved using Lead zirconate titanate (PZT) piezocrystals [3]. A piezocrystal will lengthen or shorten depending upon the voltage applied along the crystal and has to have gone through a calibration procedure so that is has accurate and precise movement. As the cantilever deflects due to the rise or fall of the surface features, the laser moves on the photodiode [3]. The AFM system typically operates to keep this deflection to a minimum, therefore the system will have a feedback loop that moves the cantilever in the z-direction via another piezocrystal. The movement of the z-direction piezocrystal is mapped with the x and y rastering information to produce a 3 dimensional topographical map.

The second major type, which is used in this paper, is Tapping mode AFM (TMAFM) [3]. This uses a similar cantilever with a tip, but the tip does not

contact the surface in the same way. An additional piezocrystal is placed in the mechanism which holds the cantilever in the AFM. Before imaging, when the cantilever at least tens of microns away from the sample surface, the extra piezocrystal is vibrated at various frequencies. The piezocrystal vibration causes the cantilever to vibrate and the amplitude of the cantilever motion is measured by the movement of the laser in the photodiode. By plotting the amplitude versus the frequency, the user is able to determine where the natural frequency occurs. The user selects a frequency near this point, which causes the software to put a bypass filter around the frequency. The piezocrystal near the cantilever will then only be vibrated at that frequency.

When the cantilever tip is brought near the surface, the amplitude will decrease [3]. Once an amplitude reduction, typically of 15% is met, the software sets this new amplitude as a target amplitude. The target amplitude is then constantly measured by the software. This produces two results. First, the cantilever in no longer in constant contact with the sample. This removes the horizontal force between the tip and the surface and also lowers the lateral force on the surface, since the tip in coming into contact only on the lowest portion on the sinusoidal wave. The second result is that the change in target amplitude is a direct result to the force of the tip against the surface. If the tip rasters across an area that is lower, the amplitude will increase, since the force on the tip has decreased. This causes the feedback loop to lower the cantilever until the target amplitude is met. The reverse is also true. This allows to software to produce a

topographical map based on the position of the z-piezocrystal at the average amplitude position.

6.4b Root-Mean Square (RMS) Roughness

An important measurement from an AFM image is the surface roughness. This is generally reported as the Root-Mean Square, or RMS or R_q, of the image area. This is the standard deviation of the height values (z), where N is the number of points in the image and the calculation is shown in Eq. 6-1 [4].

$$R_q = \sqrt{\frac{\sum (Z_i)^2}{N}} \qquad \text{(Eq. 6-1)}$$

There are complications when comparing the RMS values of various images. It is best to only compare the values of images that have the equivalent image sizes, image resolutions, and scanning speeds. Using the same image sizes and resolutions, the data has the same pixel size for comparison between the images. Equivalent scanning speeds ensures that the tip has traveled at the same rate across the surface in each image.

6.4c 2 Dimensional Isotropic Power Spectral Density

The 2 Dimensional Isotropic Power Spectral Density, or 2D PSD, is a plot of power as a function of spatial wavelength. This is obtained by taking the Fast Fourier Transform, FFT, of the AFM image. Then the FFT is squared and averaged over all angles [4]. Eq. 6-2 presents the PSD function.

$$PSD(f) = \frac{2d_0}{N}\left|\sum_{n=1}^{N} e^{\frac{i2\pi}{N}(n-1)(m-1)} z(n)\right|^2 \quad \text{for} \quad f = \frac{m-1}{Nd_0} \qquad \text{(Eq 6-2)}$$

d_0 is the sampling interval

Therefore, the PSD presents a plot of the power of various wavelengths, from which compose the topography of the sample. The PSDs of two samples, using the same scan size to make the comparison equal, allows an evaluation of the samples at various wavelengths, not just the variation from the average that is given by the RMS roughness. However, the PSD is related to the RMS, since the RMS is the square root of the integral of the PSD.

6.4d Contact Angle Measurement

Contact angle measurements are based on Young's equation, which is:

$$\gamma_L \cos\theta = \gamma_S - \gamma_{SL} \qquad \text{(Eq. 6-3)}$$

where γ_S is the solid interface tension, γ_{SL} is the solid-liquid interface tension, γ_L is the liquid interface tension, and θ is the contact angle [5]. Figures 6-5 and 6-6 show a liquid drop on a flat surface. Figure 6-5 shows a liquid drop with a contact angle of greater than 90°, which indicates the surface is hydrophobic, indicating the solid-liquid interface is less energetically favorable than the solid surface. Therefore if the energy necessary to construct the solid-liquid interface is larger than the energy to construct the solid surface interface, then the contact angle will be greater than 90 and the liquid will form to minimize the solid-liquid interface area [6]. Figure 6-6 shows a liquid drop with a contact angle of less than 90°, signifying a hydrophilic surface where the solid surface interface tension is higher then the solid-liquid interface tension. This hydrophilic drop is said to partially wet the surface, where total wetting would be a contact angle of 0°.

In their paper, Fabish *et al.* 20], begin with Young's equation (Eq. 6-3), and sub-divide each tension term into γ^{AB}, for the acid-base or donor-acceptor type interactions, and γ^{LW}, for Lifshiftz-van der Waals type interactions, components. This gives the following equation, which is the Free Surface Energy:

$$\gamma_i^{TOTAL} = \gamma_i^{LW} + \gamma_i^{AB} \qquad \text{(Eq. 6-4)}$$

where i denotes S, L, or SL. Because γ^{AB} is polar, it can be further subdivided into electron acceptor (γ^+) and electron donor (γ^-) components:

$$\gamma^{AB} \equiv 2\sqrt{\gamma^+\gamma^-} \qquad \text{(Eq. 6-5)}$$

Faibish [7] then use a theory from a paper by Oss and Good [8], which gave the γ^{AB} and γ^{LW} components of γ_{SL} as:

$$\gamma_{SL}^{LW} = \left(\sqrt{\gamma_S^{LW}} - \sqrt{\gamma_L^{LW}}\right)^2 \qquad \text{(Eq. 6-6)}$$

$$\gamma_{SL}^{AB} = 2\left(\sqrt{\gamma_S^+} - \sqrt{\gamma_L^+}\right)\left(\sqrt{\gamma_S^-} - \sqrt{\gamma_L^-}\right) \qquad \text{(Eq. 6-7)}$$

Combining Equations 6-3 through 6-7:

$$(1+\cos\theta)\gamma_L^{Total} = 2\left(\sqrt{\gamma_S^{LW}\gamma_L^{LW}} + \sqrt{\gamma_S^+\gamma_L^-} + \sqrt{\gamma_S^-\gamma_L^+}\right) \qquad \text{(Eq 6-8)}$$

The three components of the surface tension of a solid surface can be calculated by using three liquids and measuring the contact angles of each [9]. This leads to the following sets of equations, where the subscript L1-L3 represents each of the three liquids [10].

$$\begin{pmatrix} \sqrt{\gamma_S^{LW}} \\ \sqrt{\gamma_S^{+}} \\ \sqrt{\gamma_S^{-}} \end{pmatrix} = \frac{1}{2} \cdot \begin{pmatrix} \sqrt{\gamma_{L1}^{LW}} & \sqrt{\gamma_{L1}^{-}} & \sqrt{\gamma_{L1}^{+}} \\ \sqrt{\gamma_{L2}^{LW}} & \sqrt{\gamma_{L2}^{-}} & \sqrt{\gamma_{L2}^{+}} \\ \sqrt{\gamma_{L3}^{LW}} & \sqrt{\gamma_{L3}^{-}} & \sqrt{\gamma_{L3}^{+}} \end{pmatrix}^{-1} \cdot \begin{pmatrix} (1+\cos\theta_{L1})\gamma_{L1} \\ (1+\cos\theta_{L2})\gamma_{L2} \\ (1+\cos\theta_{L3})\gamma_{L3} \end{pmatrix} \qquad \text{(Eq. 6-9)}$$

Therefore, by using three liquids, the Total Free Surface Energy may be obtained.

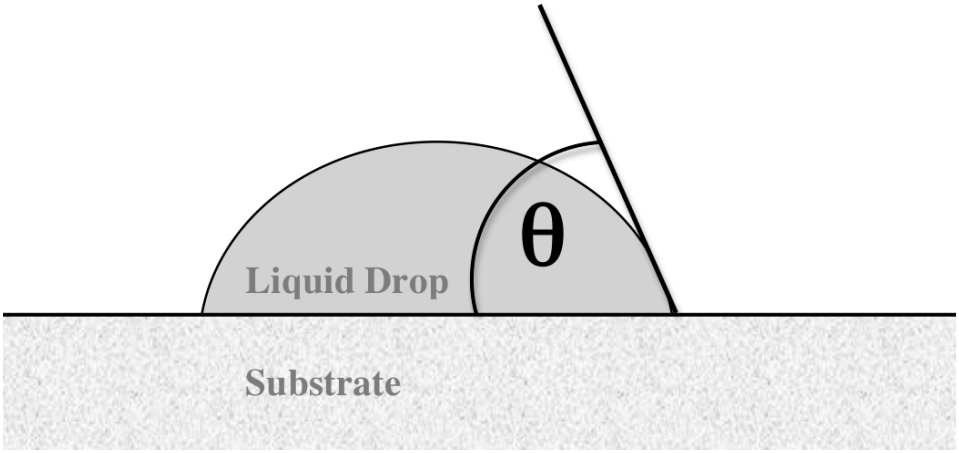

Figure 6-5: A liquid drop with a contact angle of less than 90°, signifying a hydrophilic surface where the solid surface interface tension is higher then the solid-liquid interface.

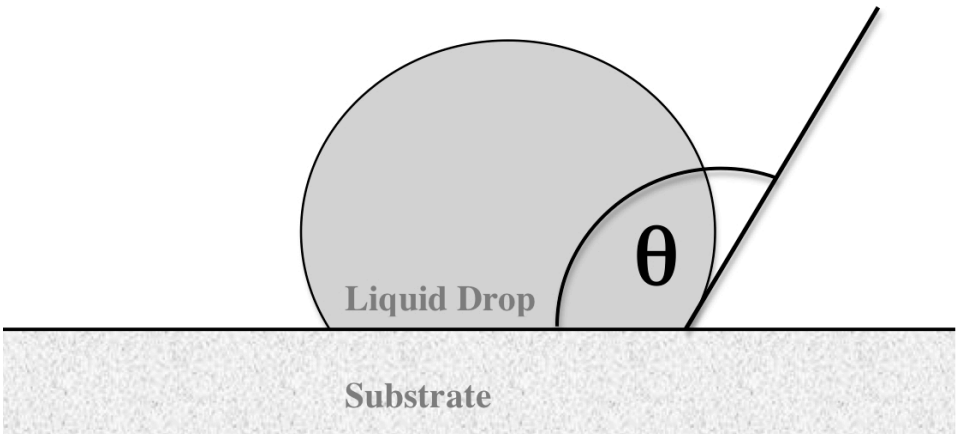

Figure 6-6: A liquid drop with a contact angle of greater than 90°, which indicates the surface is hydrophobic, indicating the solid-liquid interface is less energetically favorable than the solid surface.

Chapter 6 References

[1] G. Binning, H. Rohrer, Helv. Phys. Acta, 55, 6, 726-735 (1982)

[2] G. Binnig, C. F. Quate, C. Gerber, Phys. Rev. Lett. 56, 930–933 (1986)

[3] *Nanoscope Command Reference Manual*, Veeco Instruments Inc. (1999)

[4] *Nanoscope Software Guide 6.13*, Veeco Instruments Inc. (2004)

[5] Hans-Jürgen Butt, Michael Kappl, *Surface and Interfacial Forces*, Wiley-VCH (2010)

[6] www.dmsf.ust.hk/metrology/about_ContactAngleMeasurement.pdf, June 28, 2010

[7] R S. Faibish, W. Yoshida, Y. Cohen, *J. Colloid Interface Sci*. **256**, 2, 341-350 (2002)

[8] C. J. van Oss, R. J. Good, J. Macromol. *Sci. Chem. A* **26**, 1183 (1989)

[9] A. Carre, *J. Adhesion Sci. Technol*. **21**, 10, 961–981 (2007)

[10] N. Herbots, Q. Xing, M. A. Hart, J. D. Bradley, D. A. Sell, R. J. Culbertson, B. J. Wilkens, *Nucl. Instr. and Meth. B* (2011)

Chapter 7: Nanobonding Experimental Results and TMAFM Analysis

7.1 Nanobonding experiments

This section discusses the Wafer Bonding Experiments 15 to 26, which took place in in the summer and fall of 2008. The participants in these experiments were Murdock Hart, Doug Bradley, David Sell, and Shawn Whaley. These experiments were based on previous tests by the Herbots' group members that gave preliminary results and showed that bonding was possible.

7.1a Wafer Bonding Experiment 15

This experiment bonded Si(100) wafers and fused silica wafers. There were four Si(100) wafers and six fused silica wafers. All wafers were four inch wafers. There were four bonded pairs and two remaining cleaned fused silica wafers that were stored for later use. The Si(100) wafers underwent the standard Herbots-Atluri clean and the fused silica wafers were processed using the modified Herbots-Atluri clean with DI water replacing the Methanol in the last two cleaning steps, which will be referred to as the modified Herbots-Atluri clean for the remaining portion of this chapter. The Si(100) wafers were hydrophobic at the end of the clean and the fused silica wafers were hydrophilic, as expected. The wafers were dried using dry N_2 gas to minimize the drying time. The Si(100) wafer was placed on top of a Si wafer that was on a styrene butadiene rubber liner with an underlying stainless steel plate. This was done so that the experimental wafers would not stick to the rubber during annealing. One wafer pair, wafer 15-4 and wafer 15-10, showed immediate bonding with no pressure, just the weight of

the upper silica wafer and the response between the two surfaces. Due to the transparent nature of the fused silica, it was apparent that 50% or more of the wafers surfaces had formed an initial bond, which can be seen in Figure 7-1. Another pair, wafer 15-3 and 15-9, showed the same effect, but to a lesser degree, as shown in Figure 7-2. The last two pair did not have the same effect. The wafers then had a second Si wafer, styrene butadiene rubber liner and stainless steel plate placed on top. This four wafer clamping mechanism was placed into the Fisher Scientific Gravity Convection Oven. The heat was ramped to 200^{o} C and the wafers were annealed at that temperature for 24 hours. The oven was then turned off and allowed to cool. The wafer pair of 15-4 and 15-10 was bonded in the same way as shown in Figure 7-1. The bond pair of wafer 15-2 and 15-8 had little bonding area, as shown in Figure 7-3. When an attempt was made to remove the fused silica wafer, wafer 15-8, it cracked due to the adhesion to the underlying Si(100) wafer, which is shown in Figure 7-4.

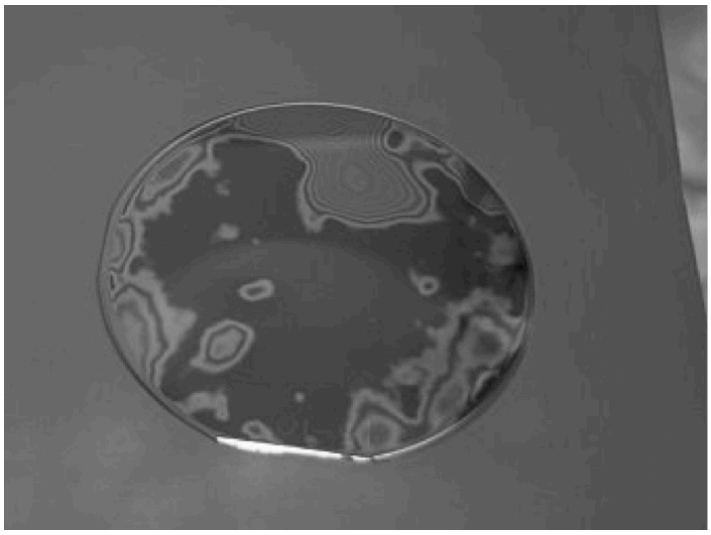

Figure 7-1: The wafer 15-4 and wafer 15-10 bond pair. It is clear, due to the transparent nature of the fused silica, that a large portion of the two wafer surfaces have formed an initial bond

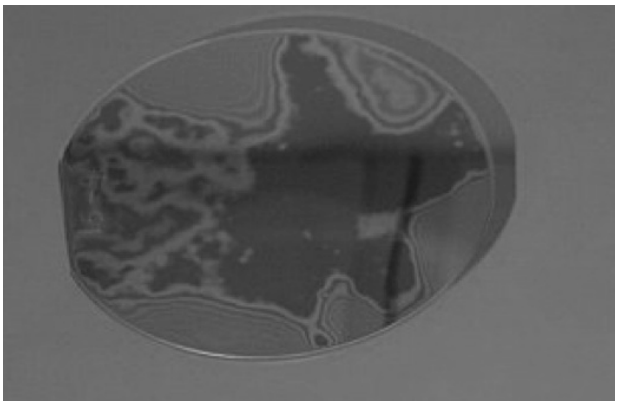

Figure 7-2: The wafers 15-3 and 15-9 bond pair. This pair shows some of the immediate initial surface bonding as seen in the wafer 15-4 and 15-10 wafer pair.

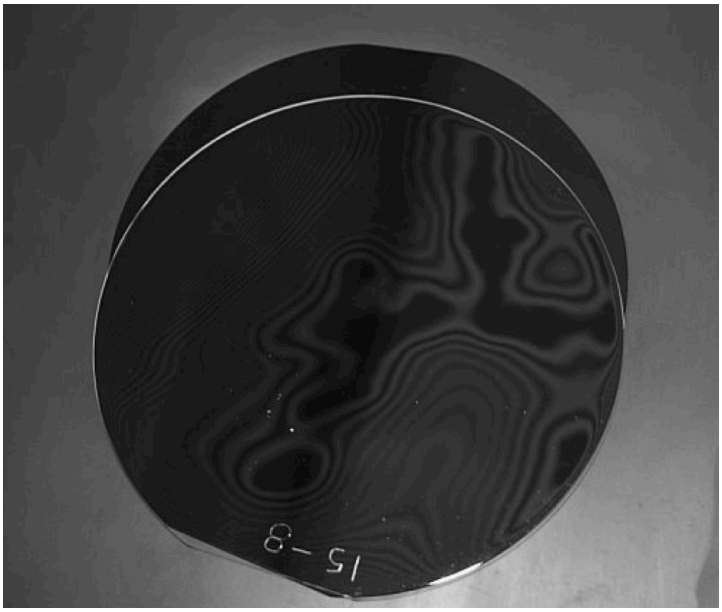

Figure 7-3: The bond pair of wafer 15-2 and 15-8. They are shown with the backing Si wafer visible.

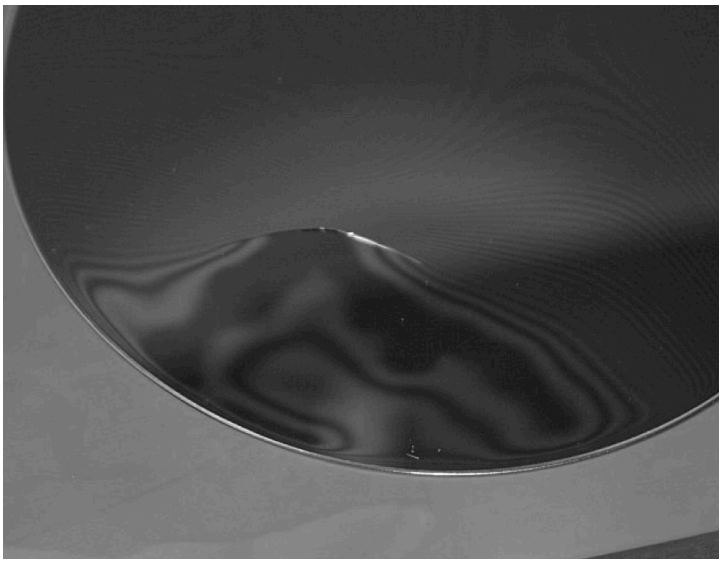

Figure 7-4: The cracking of the fused silica wafer, wafer 15-8, due to the adhesion to the underlying Si(100) wafer when an attempt was made to debond the two wafers.

7.1b Wafer Bonding Experiment 16

This also experiment bonded Si(100) wafers and fused silica wafers, as in Experiment 15. There were four Si(100) wafers and two fused silica wafers processed. All wafers were four inch wafers. There were four bonded pair using the two previously cleaned fused silica wafers from Experiment 15. The Si(100) wafers underwent the standard Herbots-Atluri clean and the fused silica wafers were processed using the modified Herbots-Atluri clean. After the clean, the time was noted between when the Si(100) wafers were removed from the Methanol rinse and when contact with the fused silica. The wafers were dried using dry N_2 gas to minimize the drying time. All times were between 90 seconds and 101 seconds. One issue occurred during drying. Multiple spots would form on the Si(100) wafers and this was referred to as "pickling". Figure 7-5 a and b shows this effect on two Si(100) wafers. Wafer 16-2, a fused silica wafer, formed point bonds with Si(100) wafer 16-6, this is shown in Figure 7-6. This surface interaction continued without an outside application of pressure. The increased size of the interaction area can be seen in Figure 7-7. There was little interaction seen between the wafer pair 16-1 and 16-5. The fused silica wafers from Experiment 15 underwent a HF and DI water dip followed by a DI water rinse, but did not bond with the newly cleaned Si(100) surfaces. All wafers were placed in the four wafer clamping mechanism and put into the oven for a 24 200^{o}C anneal. Figure 7-8 shows the wafers after anneal. The two left-most wafer pairs are the newly cleaned Si(100) wafer with the Experiment 15 fused silica and show

no bonding. The upper right wafer pair is 16-2/16-6, which shows a larger bond area after anneal. The 16-1/16-5 pair again shows little bonding after anneal.

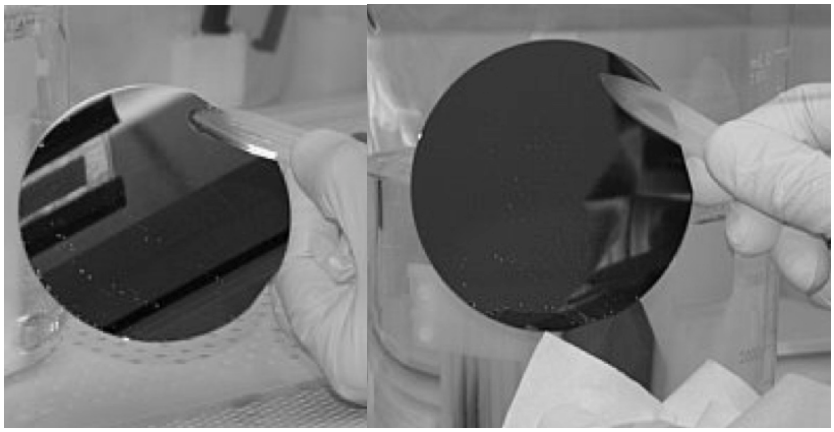

Figure 7-5: Multiple spots forming during drying on Si(100) wafers in Experiment 16, known as “pickling”.

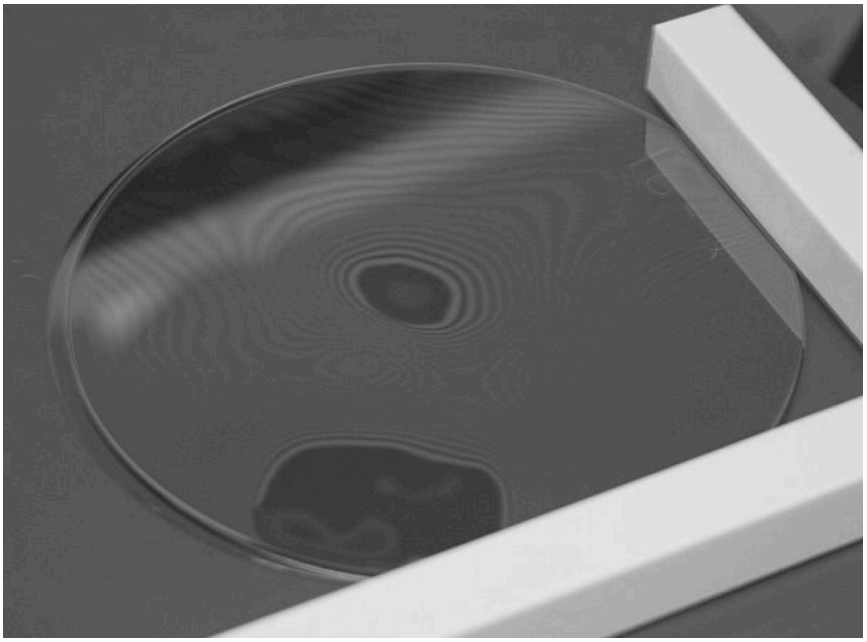

Figure 7-6: The initial bond of fused silica wafer 16-2 to Si(100) wafer 16-6.

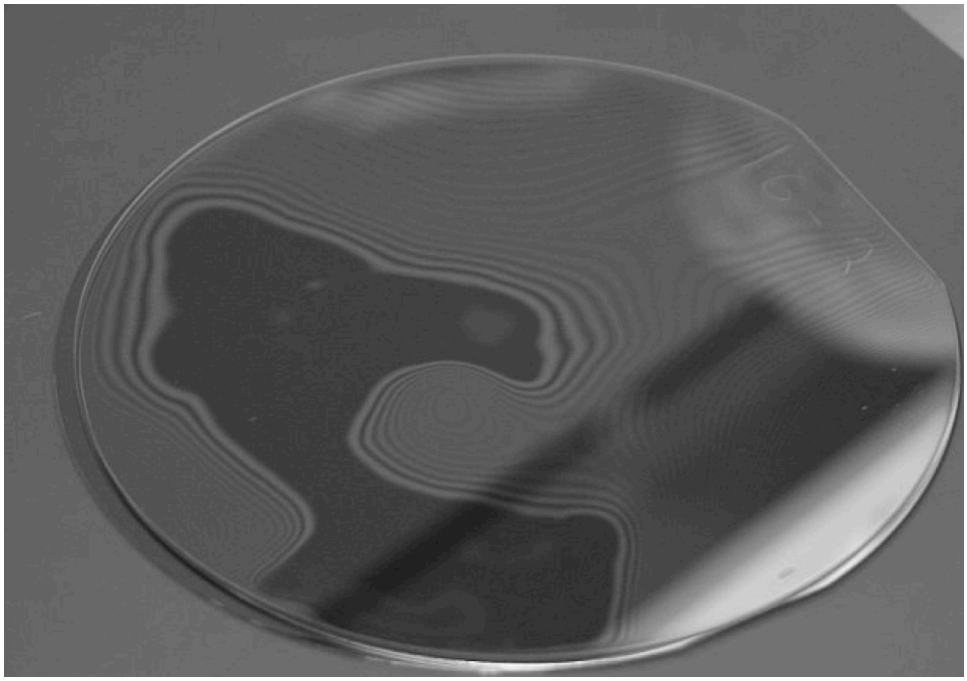

Figure 7-7: The increased area of surface interaction between wafers 16-2 and 16-6.

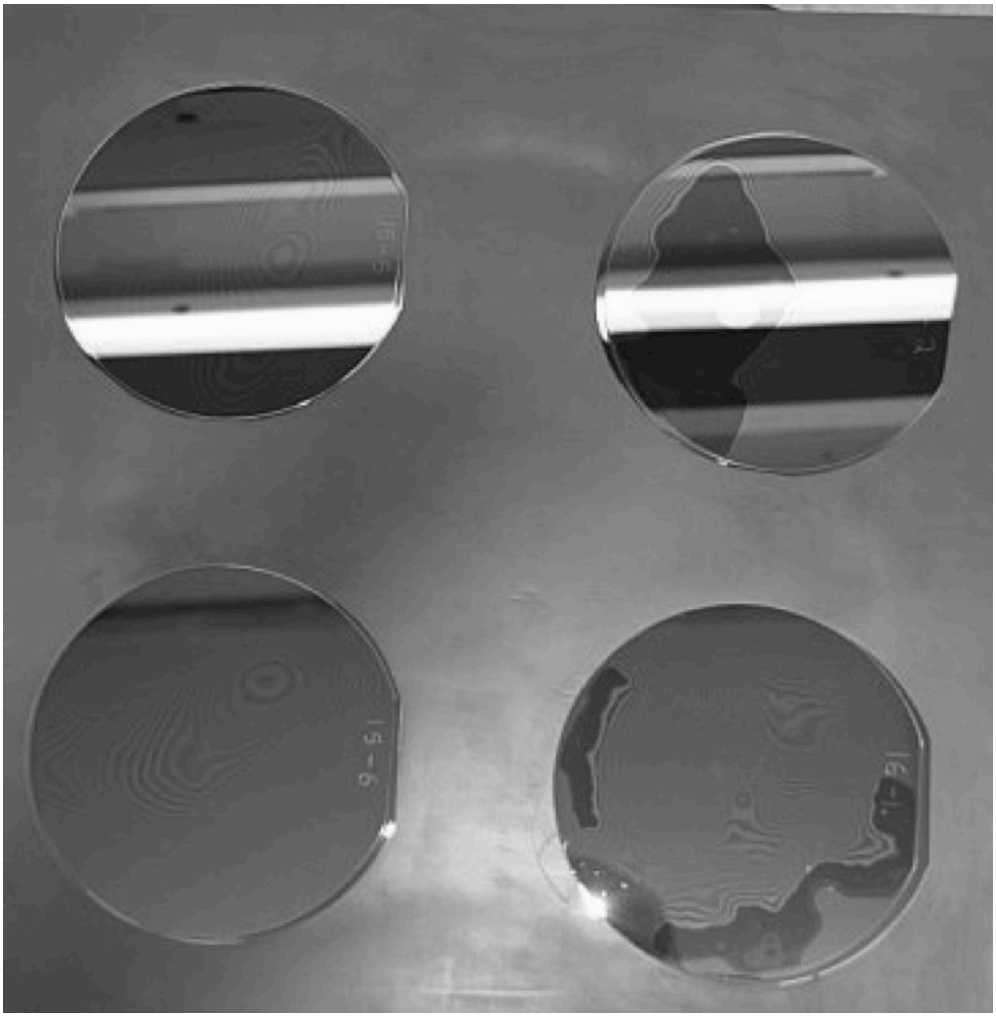

Figure 7-8: The Experiment 16 wafers after anneal. The two left-most wafer pairs are the newly cleaned Si(100) wafer with the Experiment 15 fused silica and show no bonding. The upper right wafer pair is 16-2/16-6, with larger bond area, and the 16-1/16-5 pair shows little bonding after anneal.

7.1c Wafer Bonding Experiment 17

This experiment tested bonding four inch Si(100) wafers and a ¼ piece of a six inch Si(100) wafers with a 5000Å thermal oxide. There were five Si(100) wafers and four of the ¼ piece thermal oxide wafers. The extra Si(100) wafer, 17-1, was used to check the hydroaffinity of the Si(100) after the entire clean. The Si(100) wafers underwent the standard Herbots-Atluri clean and the thermal oxide wafer pieces were processed using the modified Herbots-Atluri clean. Wafer 17-1 had severe "pickling" after cleaning, shown in Figure 7-9, and therefore had inconclusive results. The wafers were clamped and annealed as in the previous experiments. All wafer pairs did not have a measureable adhesion and did not bond.

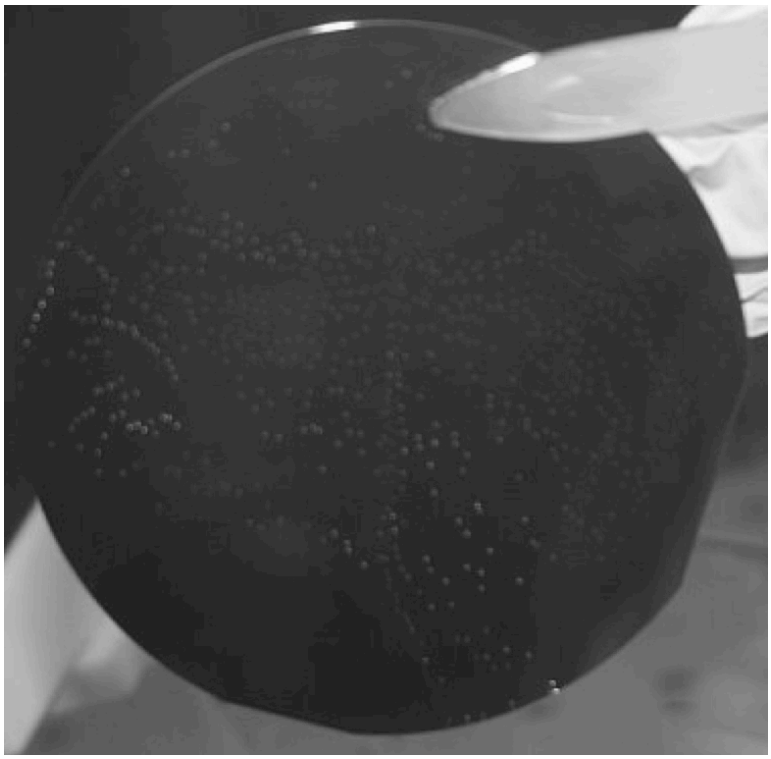

Figure 7-9: Severe “pickling” of the hydroaffinity test wafer after cleaning.

7.1d Wafer Bonding Experiment 18

Experiment 18 was very much like the previous experiment. Again, four inch Si(100) wafers and a ¼ piece of a six inch Si(100) wafers with a 1000Å thermal oxide were tested. There were five Si(100) wafers and four of the ¼ piece thermal oxide wafers. The extra Si(100) wafer, 18-7, was used to check the hydroaffinity of the Si(100) after the entire clean. The Si(100) wafers underwent the standard Herbots-Atluri clean and the thermal oxide wafer pieces were processed using the modified Herbots-Atluri clean. However, this experiment also had an extra component. The final rinse was split into two portions. Half the Si(100) and thermal oxide pieces were rinsed in the hood and half were rinsed in the glovebox. This was done to control for the humidity, since the glovebox was under dry N_2 and had a humidity below 15%. Several things were found. First, the lower humidity did not remove the "pickling", as shown in Figure 7-10. Also, using the glovebox increased the difficultly of handling the wafers and therefore increased the time to contact the wafer pairs. Clamping and annealing was done as in previous experiments. All wafer pairs did not have a measureable adhesion and did not bond. Due to the complexity of the end of the clean, the control wafer's hydroaffinity was not noted.

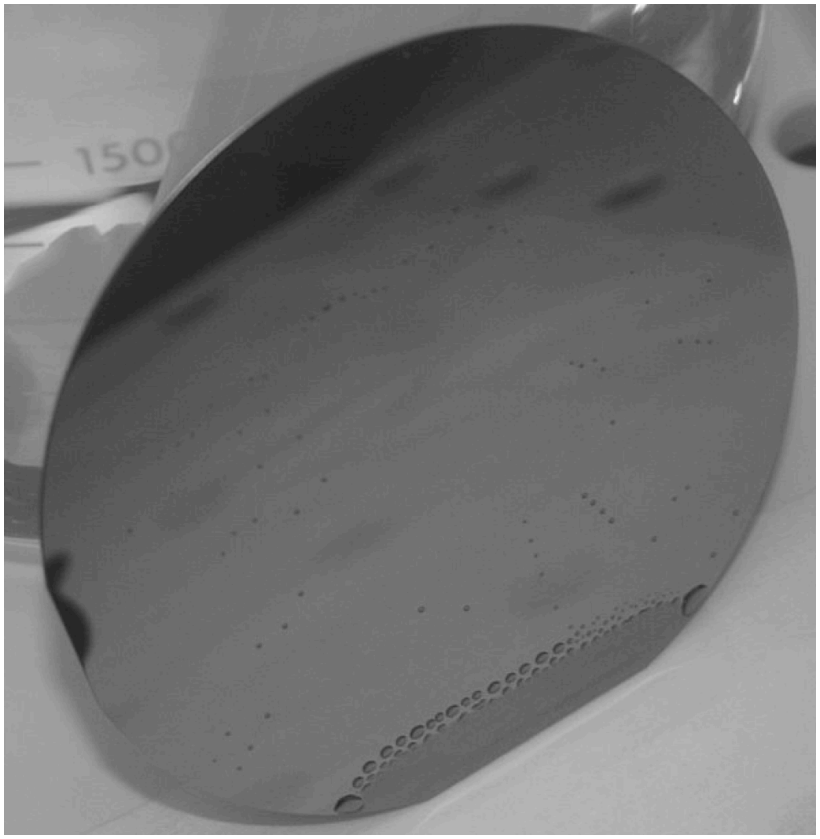

Figure 7-10: The “pickling” of a Si(100) wafer when clean was completed in the glovebox under low humidity.

7.1e Wafer Bonding Experiment 19

Experiment 19 was nearly identical to Experiment 18. Again, one half of the wafers completed the final portion of the clean in the glovebox, as before. But, the methanol was changed to clean room grade from HPLC grade. As in the last experiment, four inch Si(100) wafers and a ¼ piece of a six inch Si(100) wafers with a 1000Å thermal oxide were tested. There were four Si(100) wafers and four of the ¼ piece thermal oxide wafers. Once more, the Si(100) wafers underwent the standard Herbots-Atluri clean and the thermal oxide wafer pieces were processed using the modified Herbots-Atluri clean. As shown in Figure 7-11, the clean room methanol left residue on the wafer surface. The glovebox once again proved to be an issue by increasing the contact time. The Si(100) wafers processed in the glovebox still had visible "pickling". The wafers processed completely in the hood showed light adhesion after contact. Replicating the previous experiments, clamping of the wafers and annealing at 200C was completed. After annealing, each wafer pair was put into the sonicator. The glovebox wafers had a slightly better adhesion afterward. It was also noticed that the SC2 reactivity was somewhat less than when it is heating up. This was noted so that the SC2 could be examined in a later experiment.

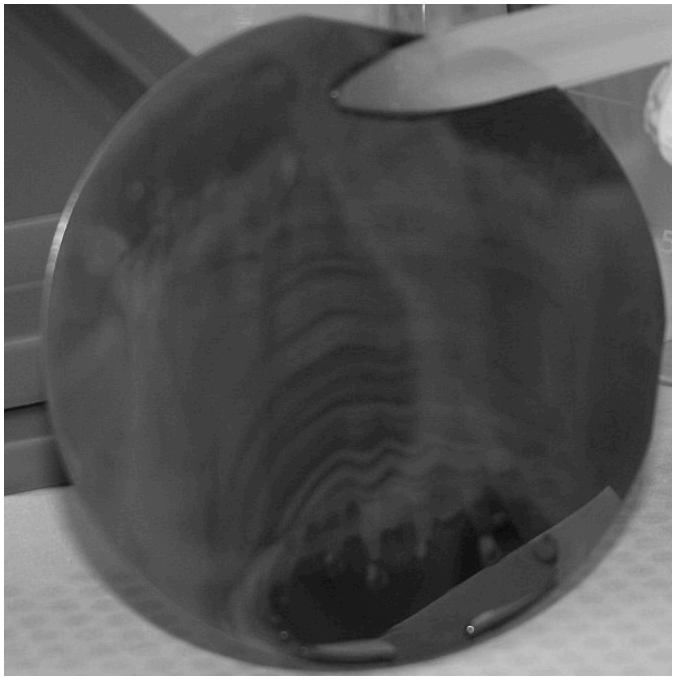

Figure 7-11: Residue left on the Si(100) wafer from clean room grade methanol

7.1f Wafer Bonding Experiment 20

Experiment 20 was developed to test both the HPLC methanol and humidity. By changing to clean room grade methanol in Experiment 19, a residue was easily noticed that appeared to never have been detected when HPLC methanol was used in previous experiments. The glovebox was again used to control for humidity and half of the wafer pairs were bonded there. Si(100) four inch wafers were again used with ¼ pieces of a six inch 1000Å thermal oxide wafer. There were four bond pairs. The wafers done in the glovebox took more time to contact the Si(100) wafers and thermal oxide pieces. There was also no adhesion of the glovebox wafers. The Si(100) wafers and thermal oxide pieces completely processed in the hood had adhesion. Pickling was still seen on all Si(1000 wafers, regardless of where the final processing took place. And, as before, the SC2 was noticed to be less reactive and led to the conclusion that the chemical bath set-up for the hood must be changed so that the SC2 chemicals were not heated to 80C at an extended time before their use. All samples were clamped and annealed. After annealing, there was no bonding of the glovebox wafers. The hood processed wafers separated in the sonicator, but there were large areas of both the Si(100) wafers and the thermal oxide pieces that showed discoloration. A thermal oxide piece is shown in Figure 7-12, where the discoloration is clearly visible. This suggests that there is some change of the surface in terms of composition, such as removal of the oxide layer, or surface roughening.

Figure 7-12: A ¼ wafer thermal oxide piece processed in the hood in Experiment 20. This piece separated from the Si(100) wafer in the sonicator, but there were large areas discoloration.

7.1g Wafer Bonding Experiment 21

The HPLC methanol showed lower amounts of residue, so the experiments from this point onward would be done in the hood with this methanol. The "pickling" had not yet been addressed. It was considered by the research group that the "pickling" to be a possible effect due to the reactivity of the SC2 chemical bath. This bath was heated up more than 30 minutes before it was used. Therefore, Experiment 21 would explore the result of heating only the DI water component and adding the HCl and H_2O_2 only a few minutes before processing the wafers in the chemical bath, enough time to bring the mixture to 80C. There would be processing in both the hood and the glovebox.

Also, the difference between the adhesion in the stainless steel plate clamping mechanism would be tested versus that of the third z, the two stainless steel flange caps with styrene butadiene rubber and stainless steel c-clamp. This had arisen as a concern that there would possibly be a greater variation in pressure across the four wafer pairs in the stainless steel plate clamp. Si(100) four inch wafers were again used with ¼ pieces of a six inch 1000Å thermal oxide wafer. There were five bond pairs. All specimens underwent their respective cleans. The final processing was done in the glovebox for two of the wafers for the plate clamp. None of the wafers showed "pickling". This suggested that this issue was due to the SC2 bath and that the new procedure for heating this bath would be followed for all future experiments. All the wafers for the plate clamp showed no adhesion during initial contact and tended to move during this process. All wafer pairs were annealed at 200C for 24 hours. The wafers in the plate clamp did not

adhere after anneal. The wafer put in the clamp with the flange cap and c-clamp did not tend to move during initial contact and adhered after anneal. This wafer pair separated after two minutes in the sonicator. Both wafers, shown in Figure 7-13 after they were separated, showed discoloration, especially the thermal oxide piece. The Si(100) wafer has clearly changed hydroaffinity after this process in the area where the wafers were bonded. There are hydrophobic areas outside this area and hydrophilic inside the area.

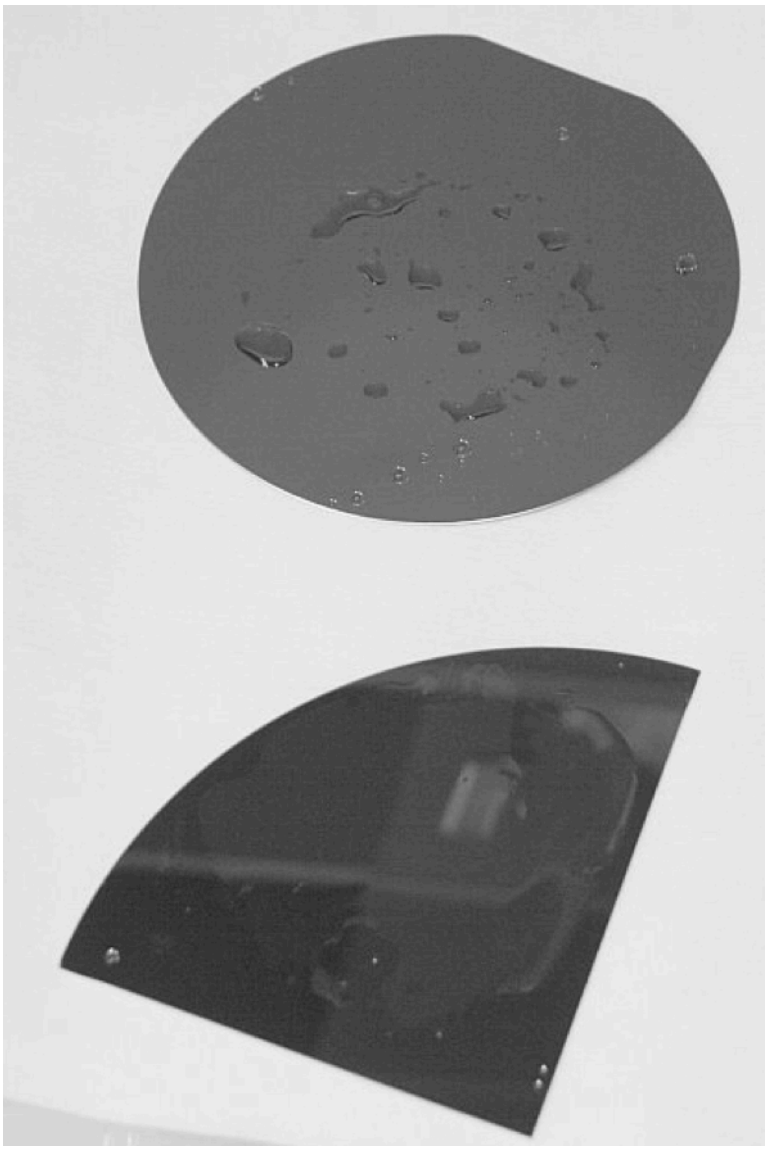

Figure 7-13: The wafer pair put in the clamp with the flange cap and c-clamp after separation in the sonicator. Both wafers showed discoloration, especially the thermal oxide piece. The Si(100) wafer has changed hydroaffinity after this process in the area where the wafers were bonded.

7.1h Wafer Bonding Experiment 22

The previous experiment produced multiple results. First, there was no "pickling" when the new SC2 solution heating method was put into place, so Experiment 22 would use the new method. Secondly, it was shown that single wafer pair clamping produced better adhesion results. Therefore, the two single wafer clamping mechanisms that were developed, the device with the c-clamp and the apparatus with the lock-jaw pliers, would be used. Finally, the glovebox did not give differing results and would no longer be used in any future experiments. In this experiment, Si(100) four inch wafers were again with ¼ pieces of a six inch 1000Å thermal oxide wafer. There were two bonded pairs, one for each clamp type. All specimens underwent their respective cleans. All wafer pairs were annealed at 200^{o}C for 24 hours. The wafer bond pair, 22-2 and 22-4, for the lock-jaw pliers clamp showed good adhesion at contact and, after the anneal, five minutes of sonication did not break the bonding between the Si(100) and the thermal oxide piece. This wafer pair is shown in Figure 7-14. These wafers were then manually separated and are shown in Figure 7-15 a and b. They showed discoloration in the bond area and the Si(100) has difference of hydroaffinity inside and outside of the bond area. The wafer in the c-clamp apparatus had medium adhesion at contact and, after annealing, the wafer pair did not separate during six minutes of sonication. This shows success in clamping and bonding.

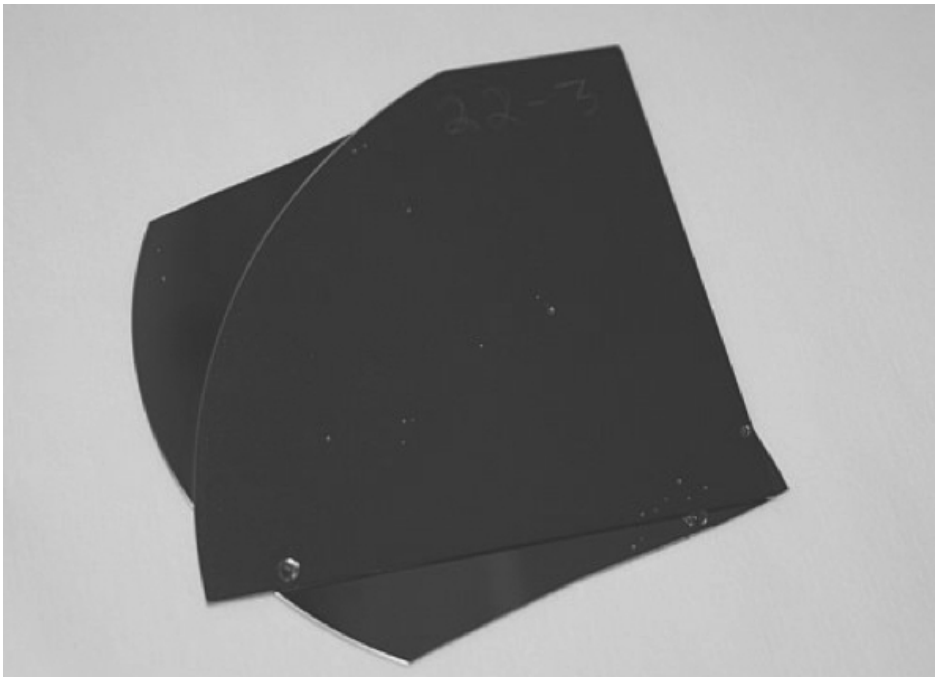

Figure 7-14: The Experiment 22 wafer pair that was in the lock-jaw pliers clamp

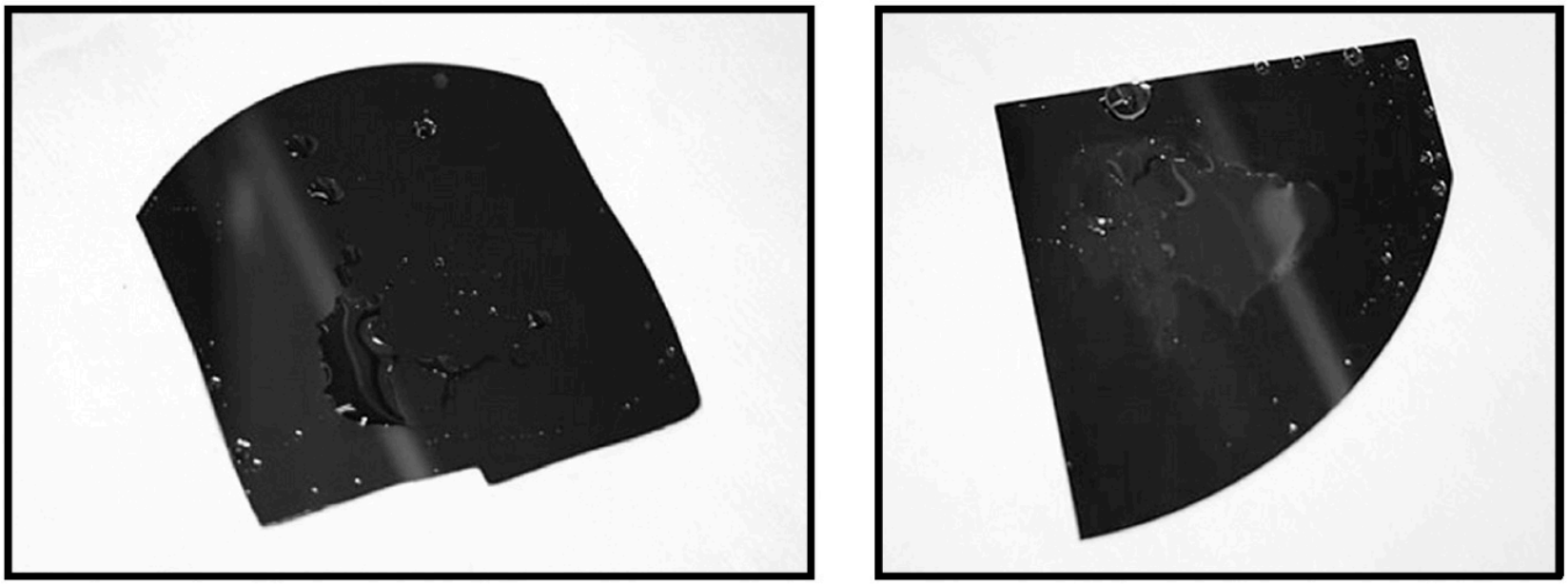

(a) **(b)**

Figure 7-15: The Experiment 22 wafer pair separated (a) Si(100) and (b) thermal oxide piece that constituted the bonded wafer pair in the lock-jaw pliers clamp. The areas where bonding occurred can be seen on both wafer pieces.

7.1i Wafer Bonding Experiment 23

This experiment was developed to confirm the results from Experiment 22. In Experiment 23 the wafers bonded but in a non-uniform manner, because the SilOx is interphase nucleated only on certain areas. This experiment is useful because it enables us to create a bonding interphase which can be broken apart (as opposed to uniform bonding interphase where the strength of the bonded interface is larger than the substrate). Upon breaking of the bonded interphase, one can observe optically that material from the wafer itself was pulled away from the substrate upon separation. A matching patch of materials on the silica side can be seen also. This demonstrates that the bonding SilOxSi interphase has a superior tensile strength to both Si and Silica (or thermal SiO2).

7.1j Wafer Bonding Experiment 24

Experiment 24 was performed to confirm the results from Experiment 22. In this experiment, Si(100) four inch wafers were again with ¼ pieces of a six inch 1000Å thermal oxide wafer. There were two bond pairs. All specimens underwent their respective cleans. One of the thermal oxide pieces were accidentally dropped on the Si(100) wafer, so the this pair of wafers were put into the oven with no pressure and they separated in the oven. The second pair were loaded into the lock-jaw pliers clamp showed some point bonding at contact. After the 24 hour, 200ºC anneal, the wafers underwent five minutes of sonication and the wafers then manually separated easily.

7.1k Wafer Bonding Experiment 25

This experiment was comparable to Experiment 24. It was executed to confirm the results from Experiment 22 while varying the clamping using glass plates and variable pressure. Si(100) four inch wafers were again used with ¼ pieces of a six inch 1000Å thermal oxide wafer. There were two bond pairs. All specimens underwent their respective cleans and had a 24 hour, 200°C anneal. Each wafer pair underwent a different amount of clamping pressure. The one with light clamping pressure, wafers 25-2 and 25-4, separated easily after sonication, but the silicon wafer, 25-4, had a hydrophilic area that was identical to the area where the thermal oxide wafer bonded to it. Wafer 25-4 is shown in Figure 7-16. The bonded pair with heavy clamping pressure, 25-1 and 25-3, did not separate in the sonicator. The silicon wafer, 25-3, broke into 3 pieces along the crystal planes when manually separated, and is shown in Figure 7-17.

7.1l Wafer Bonding Experiment 26

Due to the minimal bonding with light pressure and glass plates for clamping, Experiment 26 would replicate the glass plates and heavy pressure clamping from the previous experiment. Si(100) four inch wafers were again used with ¼ pieces of a six inch 1000Å thermal oxide wafer. There were two bond pairs. All specimens underwent their respective cleans and 24 hour, 200°C anneal. There was some adhesion, but one pair separated in the sonicator and the other separated using medium manual pressure. The conclusion from this is that the c-clamp mechanism is the most effective method for applying pressure to the wafer pair.

7.2 Conclusions from the Wafer Bonding Experiments

These experiments showed several steps that were needed to go from a process that provided some adhesion for Si(100) wafers and SiO_2 wafers. It was seen that the wafer-to-wafer contact needed to be minimized to be successful. The lack of humidity provided by a dry glove box did not play an important role in bonding of the wafers. An important point was to make certain that the SC2 chemical bath was not at a elevated temperature for a long period before processing the wafers through this step, due to the chemicals reacting and therefore minimizing there impact in the cleaning process. With these parameters optimized, the hydroaffinity of each wafer type was consistent across the surface to be bonded and lead to immediate adherence when the two surfaces came in contact. Using the c-clamp for the clamping mechanism and a 24 hour, 200°C anneal produced the most favorable and repeatable results.

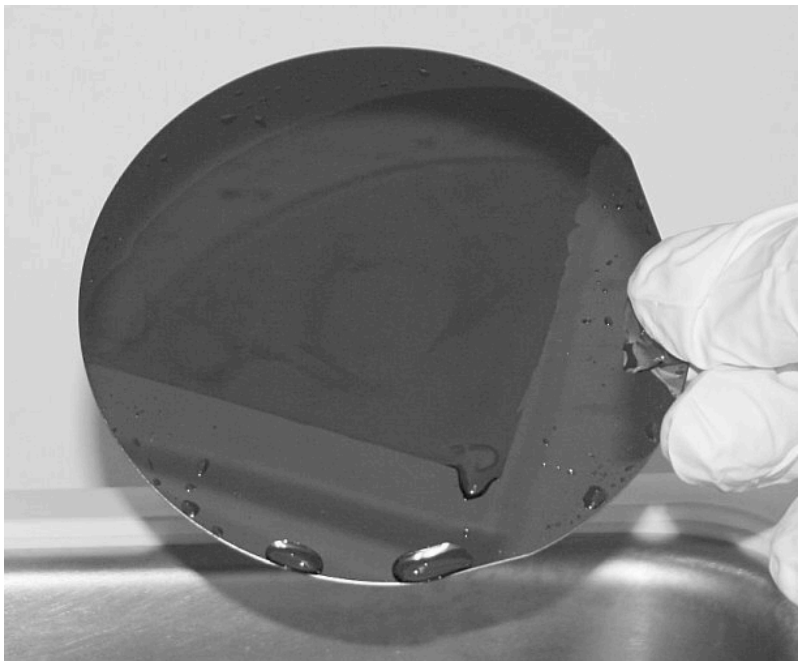

Figure 7-16: Wafer 25-4, which is half of the light clamping pressure bond pair, showed a hydrophilic area that was identical to the area where the thermal oxide wafer bonded to it.

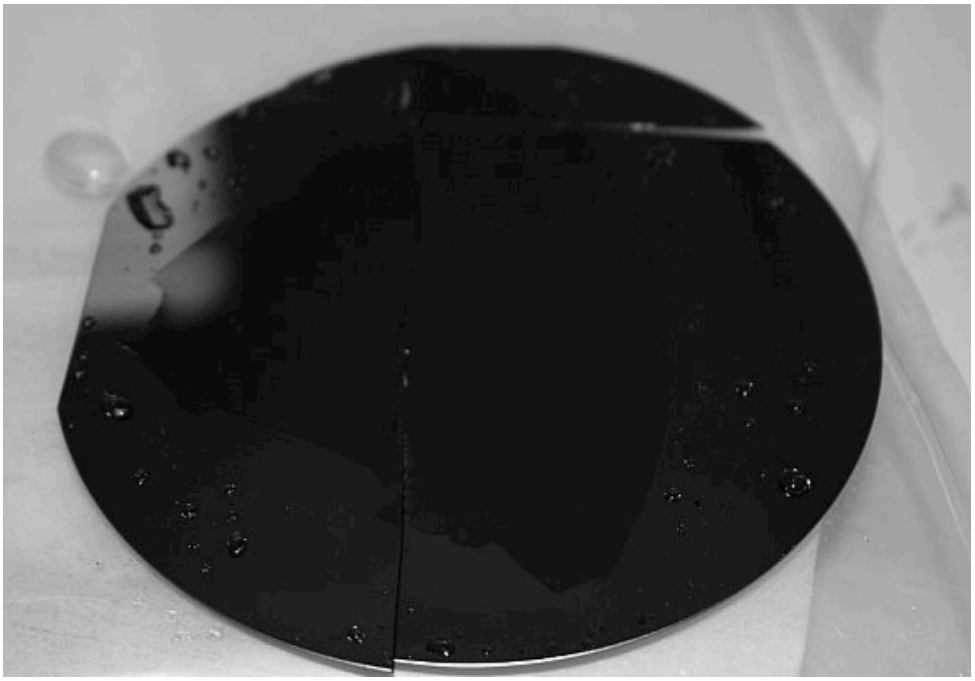

Figure 7-17: Silicon wafer, 25-3, which is half of the bonded pair with heavy clamping pressure, did not separate in the sonicator. It broke into 3 pieces along the crystal planes when manually separated.

7.3 TMAFM Analysis

7.3a TMAFM Analysis of H-A cleaned Si(100) Wafer

A 100mm Si(100) wafer was cleaned with the complete H-A method. This sample saw no further processing. A 2 cm X 2 cm piece of this wafer was apportioned to AFM analysis. The emphasis will be primarily on the 100 nm roughness, as in other chapters due to the particles in the larger AFM scan sizes. Table 7-1 presents the RMS Roughness measurements calculated from AFM scans at three positions on the H-A Cleaned Si(100) sample. Figure 7-18 is a 10 μm AFM image of the H-A Cleaned Si(100). This sample is a small, square portion that was cut from a larger wafer, therefore the particles on this sample may be due to the scribing and removal of this sample from the rest of the cleaned wafer. The 100 nm AFM scan is shown in Figure 7-19 and the surface appears to have waves on the order of 1 nm in height.

The 2D Power Spectral Density of the H-A Cleaned Si(100) sample for 100nm scan size is presented in Figure 7-20. The PSDs have a gradual fall-off and at a wavelength of approximately 0.03 μm, all three become interlaced. This peak is consistant with the cross sectional TEM data.

AFM Scan Size	Position 1 RMS Roughness (nm)	Position 2 RMS Roughness (nm)	Position 3 RMS Roughness (nm)	Average RMS Roughness	Standard Deviation
10 um	0.226	0.185	0.139	0.183	0.043
1 um	0.235	0.219	0.164	0.206	0.037
100 nm	**0.072**	**0.097**	**0.094**	**0.088**	**0.014**

Table 7-1: RMS Roughness calculated from AFM scans at three positions on the H-A Cleaned Si(100) sample.

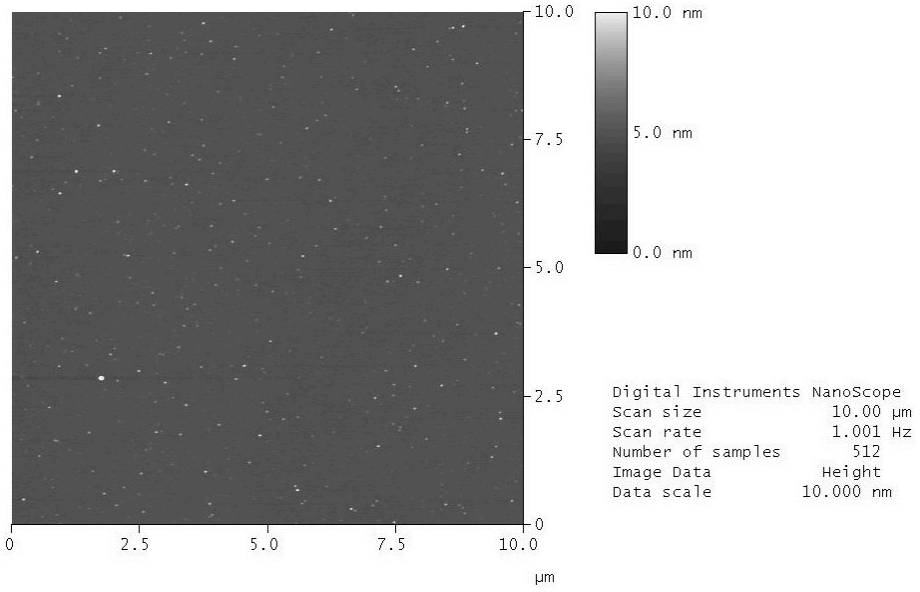

Figure 7-18: A 10 mm top view AFM image of H-A cleaned Si(100) sample. The particle size is small. This sample is also a portion of a wafer, so there could be particles on the surface due to the scribing and removal of this sample from the rest of the Si wafer.

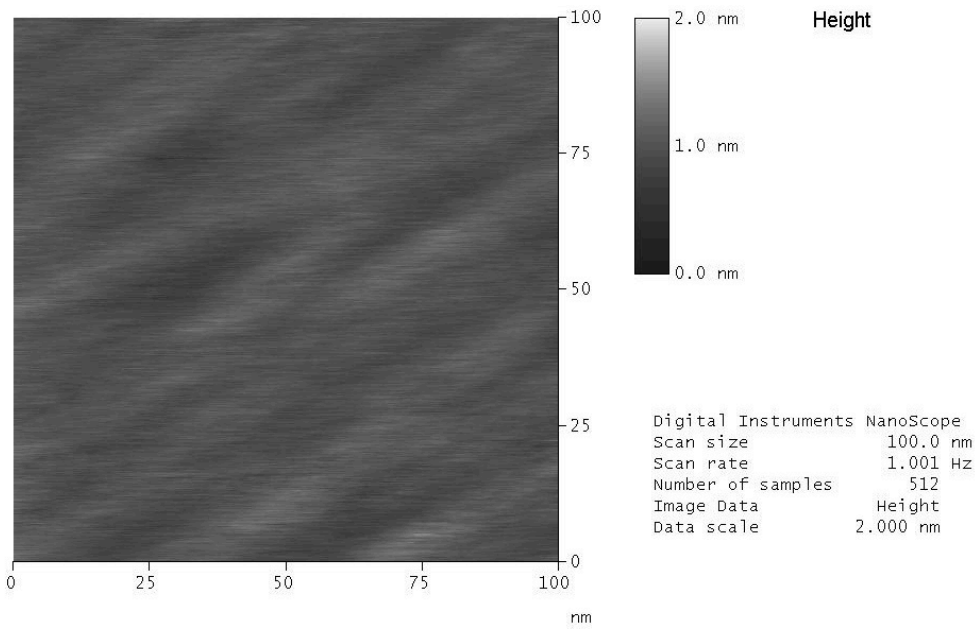

Figure 7-19: A 100 nm top view AFM image of H-A cleaned Si(100) sample. The surface has waves on the order of 1 nm in height.

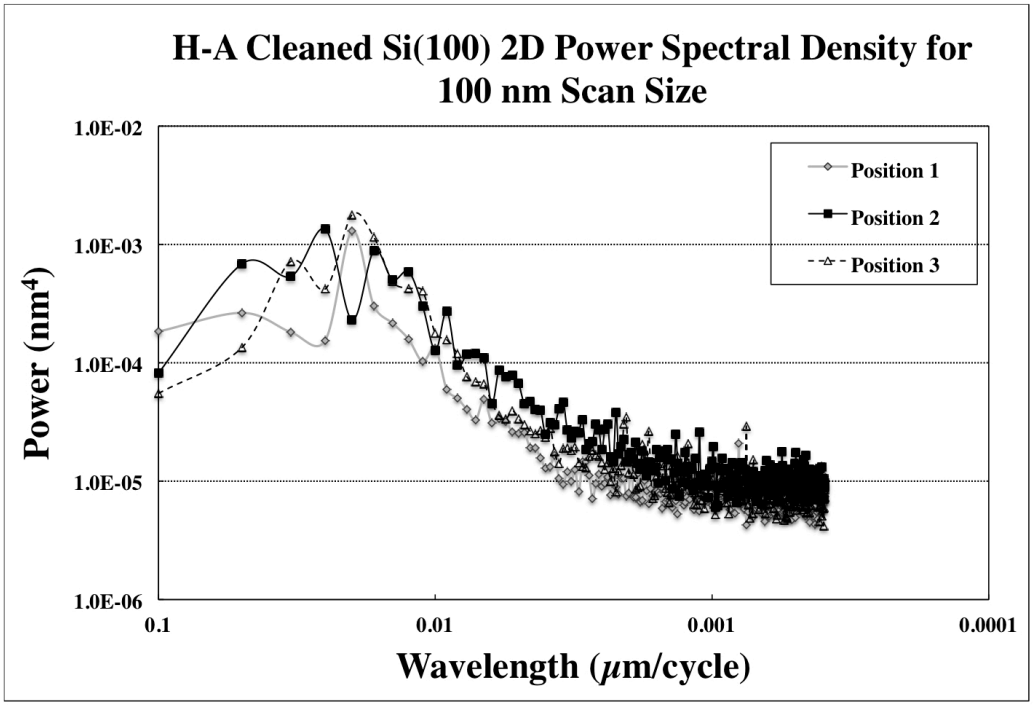

Figure 7-20: 2D Power Spectral Density of the H-A Cleaned Si(100) wafer for 100nm scan size. The PSDs have a gradual fall-off and at a wavelength of approximately 0.03 μm, all three become interlaced. The maximums for the positions are : Position 1 (0.02 μm, 1.30×10^{-3} nm^4), Position 2 (0.025 μm, 1.34×10^{-3} nm^4), Position 3 (0.02 μm, 1.77×10^{-3} nm^4)

7.3b TMAFM Analysis of Witness Si(100) Wafer and Spin-Etch Clean Si(100) Sample

The two wafers described in this section were from a 25 wafer lot that was partially processed in an experiment at Entrepix, Inc. in Tempe, AZ. Wafer 1 is the witness wafer and therefore was not processed during the experiment. For this reason, it will be referred to as the "Witness Si(100)" wafer. Table 7-2 shows the processing of the Baseline and Witness wafer groups, which includes the Witness Si(100) wafer.

Wafer 8 is shown with the other group D wafers in Table 7-3. Wafer 8 underwent the complete clean which included processing by Entrepix engineers in their Bernoulli chuck, single-wafer clean system. The SC1 rinse time was 10 minutes, the HF rinse was 1 minute, and the SC2 rinse was 2 minutes. This wafer was placed back into a clean wafer transfer box and transported to the Herbots Group clean room, where the process was completed using a HF:Methanol dip for 1 minute and a Methanol dip for 1 minute. Due to this processing, the wafer will be referred to as the "H-A Spin Etch Clean" wafer. The wafer dewetted evenly, had few spots as it dried, and showed no residue from the Methanol. The H-A Spin Etch Clean wafer underwent the cleaning sequence that should remove the most particles and smooth the surface, since it is the wafer with the longest exposure to each chemical in each step. Therefore, it represents the wafer with the largest possibility for differentiation from the unprocessed Witness Si(100) sample.

The RMS roughness is shown for the Witness Si(100) in the Table 7-4. The AFM images were collected at three positions on a portion of each sample with 10 μm, 1 μm, and 100 nm scan size images at each position. Again, it is particularly important to compare the 100 nm scan size roughness, due to the particles that lie on the surface of the wafers. At 100 nm, imaging is only done of the Si surface and allows a comparison of the roughness of the substrates. The Witness Si(100) sample has a large amount of particles, which are shown in the 10 μm AFM scan in Figure 7-21. These particles contribute largely to the 10 μm and 1 μm RMS roughness. The high particle density show that either the wafer came from the manufacturer in a contaminated state, the wafer or sample was handled incorrectly, the cutting of the wafer to acquire this sample portion created particles, or a combination of these reasons. Figure 7-22 presents a 100 nm top view AFM image of the Witness Si(100) sample**.** The scan has undulations that are observable at 2 nm height scale.

Figure 7-23 shows the 2D Power Spectral Density (PSD) for the Witness Si(100) sample using the 100nm scan size. The three scan positions on sample each appear on the graph with a separate PSD. The position 1 PSD has a maximum power in the $2x10^{-3}$ nm^4 range, while that of the Position 2 PSD is in the $1.1x10^{-2}$ nm^4 region. This PSD set all have steep fall-offs and minimize at or below a power of $1.0x10^{-5}$ nm^4.

Table 7-5 presents the RMS Roughness for the H-A Spin Etch clean sample. The average roughness at all three AFM scan sizes for this sample are significantly lower than those for the Witness Si(100) sample. The 100 nm RMS

measurement average for the H-A Spin etch clean samples nearly 60% lower than that of the Witness Si(100) sample.

A top view image of the 10 μm AFM scan of the H-A Spin Etch Clean sample is shown in Figure 7-24. It can be discerned that the sample has a lower number of larger particles, compared to the Witness Si(100) , which lowers significantly the roughness in the 10 μm and 1 μm images. Figure 7-25 shows a 100nm top view AFM image of the H-A Spin Etch clean sample. The surface is extremely smooth, even with a 2 nm height data scale.

The 2D Power Spectral Density (PSD) for the H-A Spin Etch Clean sample using the 100nm scan size in presented in Figure 7-26. The PSDs of the three scan positions on this sample have a more moderate fall-off than the Witness Si(100), due to a lower average maximum. This accounts for the lower RMS value at the 100 nm scan size.

Figure 7-27 shows the 2D PSDs for both wafers, calculated by averaging each wavelength for the three scan positions. The average of the H-A Spin Etch clean sample has lower power at all wavelengths. At the maximum for each PSD, located at 0.033 μm wavelength, the Witness Si(100) sample has a power of 6.32×10^{-3} and the H-A Spin Etch Clean sample has a power of 6.58×10^{-4} nm^4. This shows that the peak of the Spin etch is 10 nm or more above the step width seen on H-A processed Si(100), which suggests that the step width has increased.

Group	Wafer #	SC1/HF/SC2 (minutes)	HF:Meth (minutes)	Methanol Dip (minutes)	Observations
Done at Entrepix			Done at ASU lab		
Baseline	22	10/0.5/10	1	1	Initially wet, uneven drying, medium residue, 45 seconds for residue to disappear, medium spotting at bottom
	23	10/0.5/10	1	1	
	24	10/1/10	1	1	Initially wet, even drying, streaking, residue was strong, 45 seconds for residue to disappear, wafer 25 touched by wafer 24
	25	10/1/10	1	1	
Witness	1	No Processing			Not Processed

Table 7-2: Processing Matrix for the Baseline and Witness groups of wafers partially processed at Entrepix.

Group	Wafer #	SC1/HF/SC2 (minutes)	HF:Meth (minutes)	Methanol Dip (minutes)	Observations
Done at Entrepix			Done at ASU lab		
D	6	10/0.5/2	1	1	'"Some" spots, "some" residue: disappears within 30 seconds, wet initially, Wafer 7 was dropped onto wipe (backside)
	7	10/0.5/2	1	1	
	8	10/1/02	1	1	Wet initially, spot at tweezer site, more even dewetting (than 6,7 above), a few spots, no residue
	9	10/1/02	1	1	

Table 7-3: Processing Matrix for the D group of wafers partially processed at Entrepix.

AFM Scan Size	Position 1 RMS Roughness (nm)	Position 2 RMS Roughness (nm)	Position 3 RMS Roughness (nm)	Average RMS Roughness	Standard Deviation
10 um	3.28	3.10	3.53	3.30	0.214
1 um	2.34	2.55	1.72	2.20	0.429
100 nm	**0.12**	**0.17**	**0.15**	**0.15**	**0.029**

Table 7-4: RMS Roughness in nanometers for Witness Si(100) sample. The sample has a large amount of particles, which contribute largely to the 10 μm and 1 μm RMS roughness.

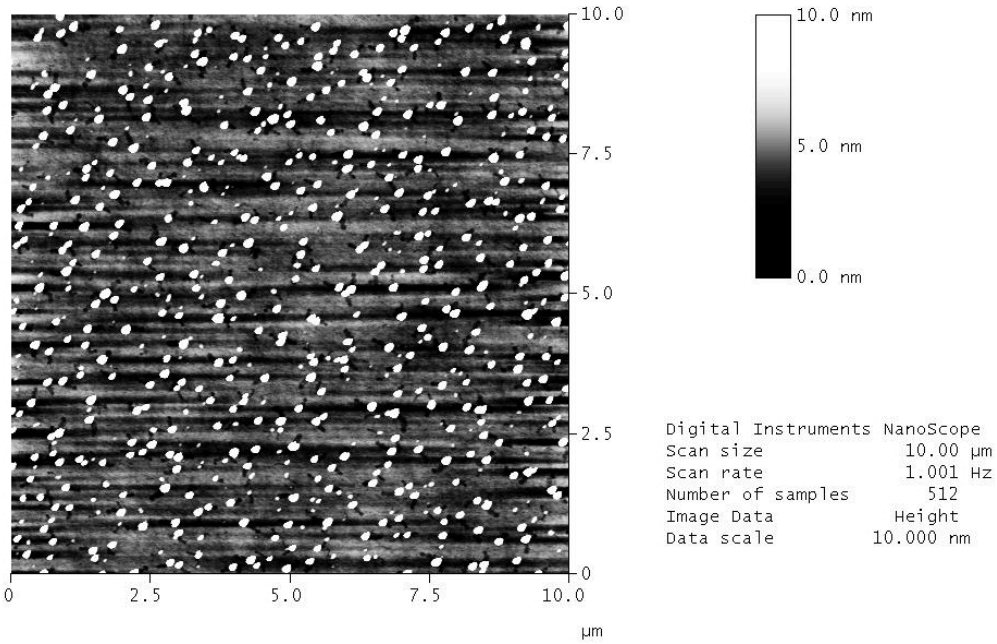

Figure 7-21: 10 µm top view AFM image of Witness Si(100) sample. The scan shows a large amount of particles, which contribute to the 10 µm and 1 µm RMS roughness. The high particle density show that either the wafer came from the manufacturer in a contaminated state, the wafer or sample was handled incorrectly, the cutting of the wafer to acquire this sample portion created particles, or a combination of these reasons.

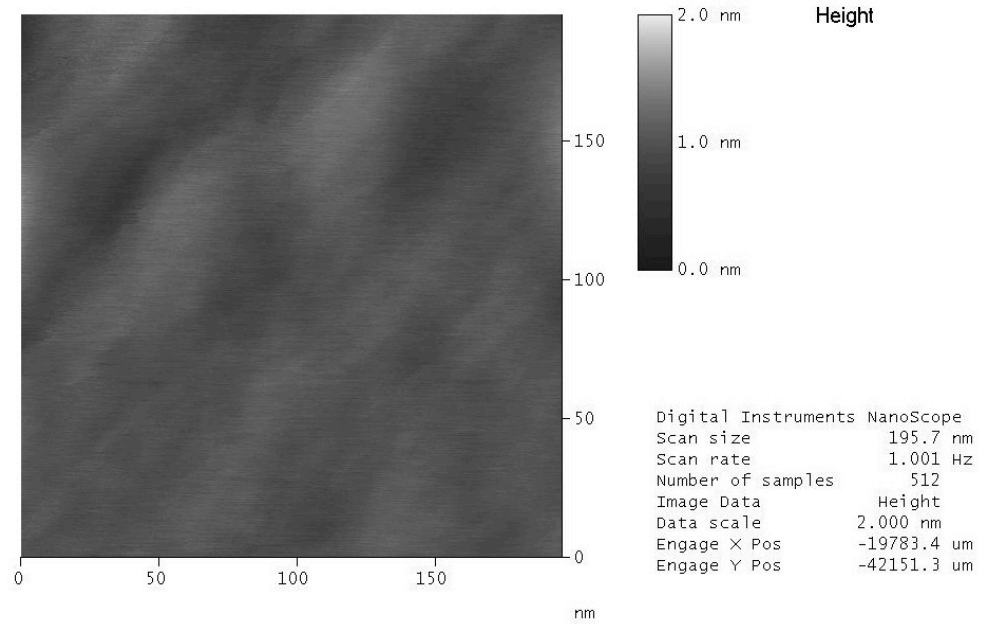

Figure 7-22: A 100 nm top view AFM image of the Witness Si(100) sample**.** The scan has undulations that are observable at 2 nm height scale

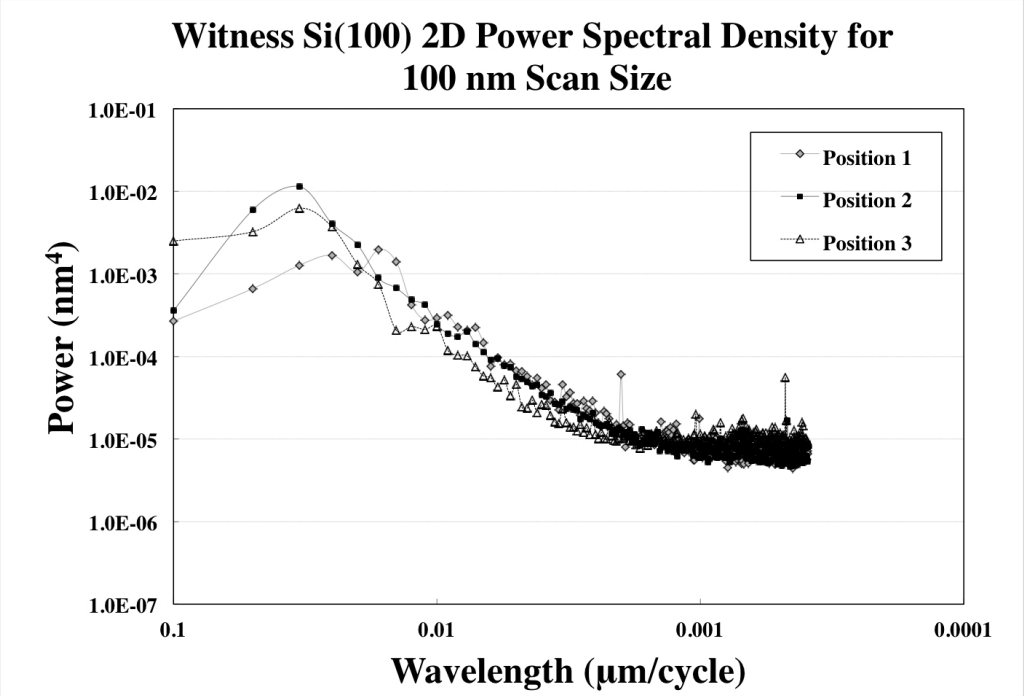

Figure 7-23: 2D Power Spectral Density of Witness Si(100) sample for 100nm scan size. This PSD set all have steep fall-offs and minimize at or below a power of $1.0x10^{-5}$ nm^4. The maximums for the positions are : Position 1 (0.0167 µm, $1.97x10^{-3}$ nm^4), Position 2 (0.033 µm, $1.14x10^{-2}$ nm^4), Position 3 (0.033 µm, $6.26x10^{-3}$ nm^4)

AFM Scan Size	Position 1 RMS Roughness (nm)	Position 2 RMS Roughness (nm)	Position 3 RMS Roughness (nm)	Average RMS Roughness	Standard Deviation
10 um	1.031	0.65	0.67	0.78	0.215
1 um	0.314	0.02	0.11	0.16	0.135
100 nm	**0.08**	**0.05**	**0.057**	**0.06**	**0.017**

7-5: RMS Roughness in nanometers for H-A Spin Etch clean sample. The average roughness at all three AFM scan sizes for this sample are significantly lower than those for the Witness Si(100) sample. The 100 nm RMS measurement average for the H-A Spin etch clean samples nearly 60% lower than that of the Witness Si(100) sample.

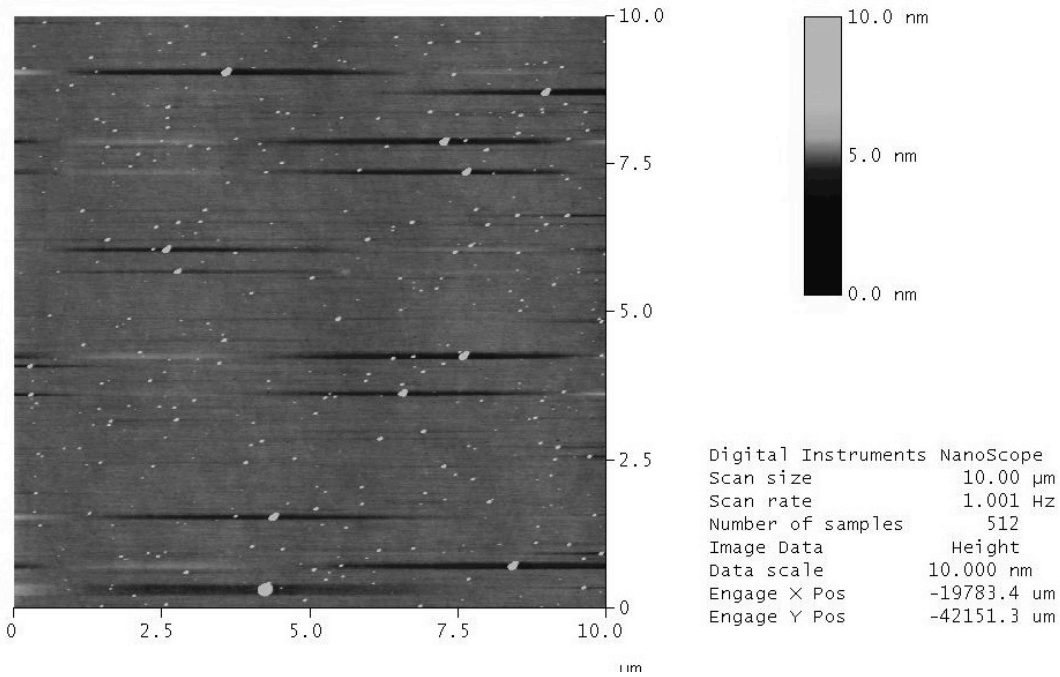

Figure 7-24: 10um top view AFM image of the H-A Spin Etch clean sample. It can be discerned that the sample has a lower number of larger particles, compared to the Witness Si(100) sample , which lowers significantly the roughness in the 10 µm and 1 µm images.

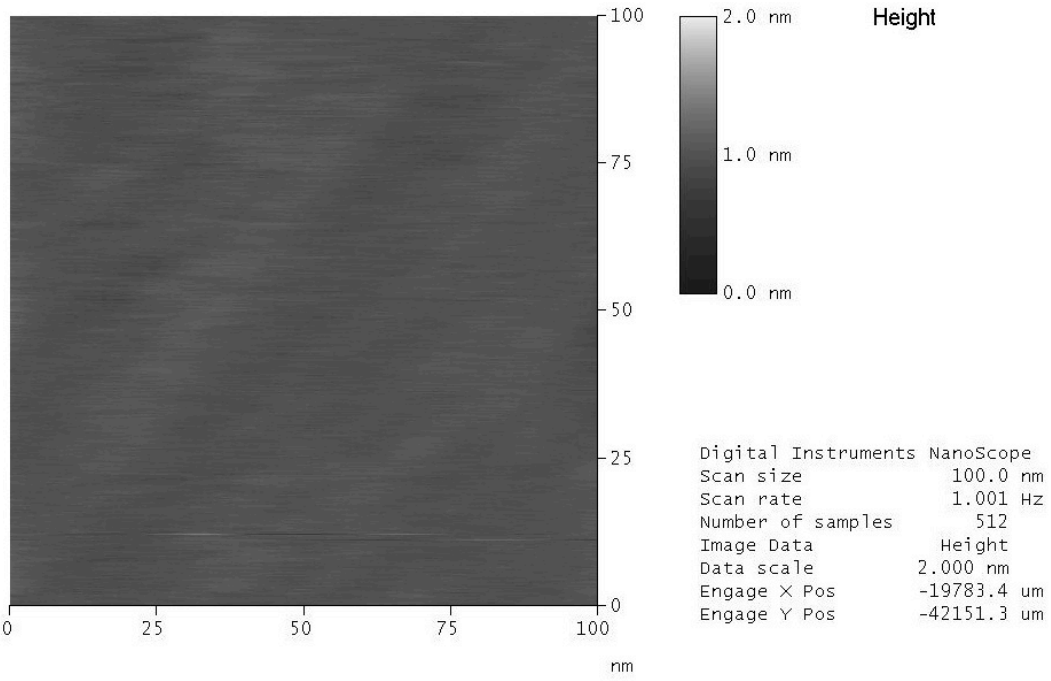

Figure 7-25: A 100nm top view AFM image of the H-A Spin Etch clean sample. The surface is extremely smooth, even with a 2 nm height data scale.

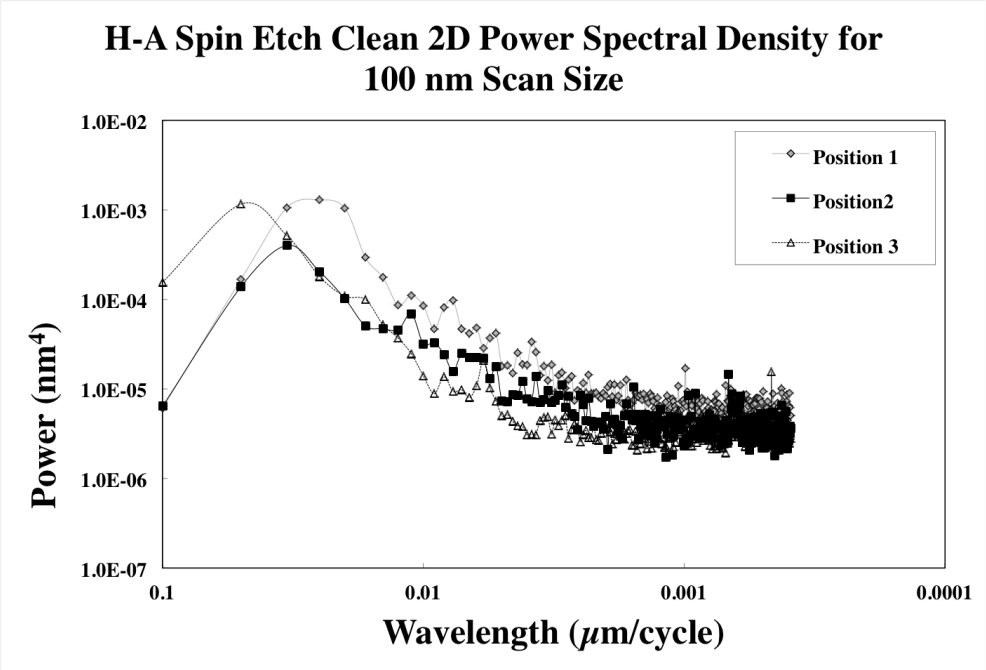

Figure 7-26: 2D Power Spectral Density of The H-A Spin Etch clean sample for 100nm Scan size. The PSDs of the three scan positions on this sample have a more moderate fall-off than Witness Si(100), due to a lower average maximum. This accounts for the lower RMS value at the 100 nm scan size. The maximums for the positions are : Position 1 (0.025 μm, 1.29×10^{-3} nm^4), Position 2 (0.033 μm, 4.02×10^{-4} nm^4), Position 3 (0.05 μm, 1.15×10^{-3} nm^4)

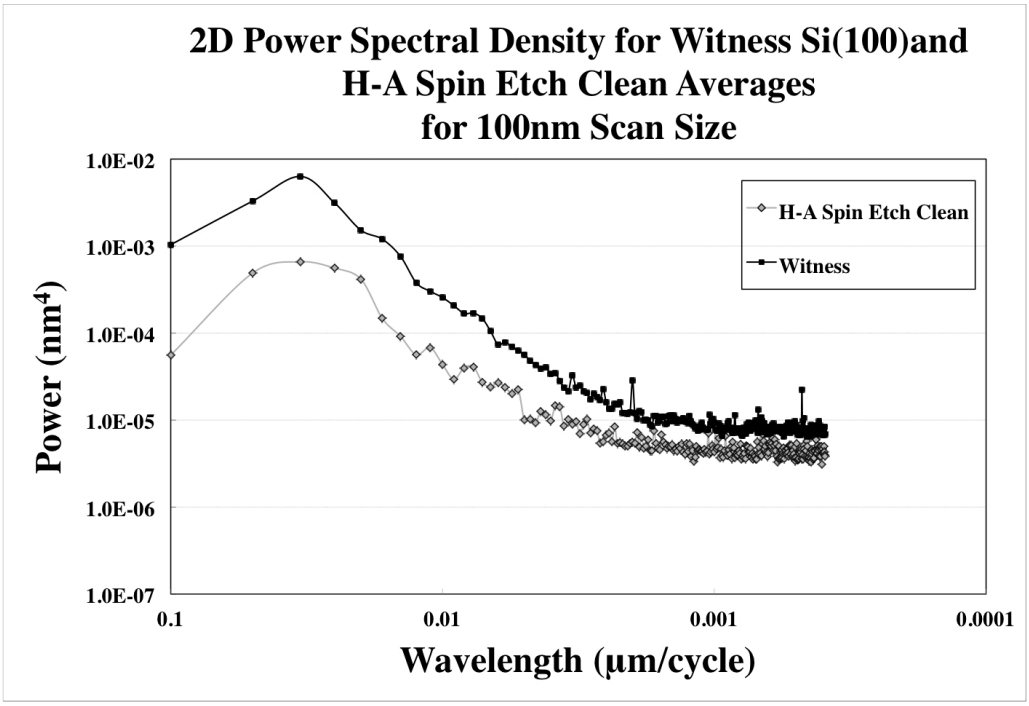

Figure 7-27: 2D PSDs for Witness Si(100) sample and The H-A Spin Etch clean sample at the 100 nm scan size. These were calculated by averaging each wavelength for the three scan positions. The average of the H-A Spin Etch Clean sample has lower power at all wavelengths. The maximum for the Witness Si(100) sample average is located at (0.033 µm, 6.32×10^{-3} nm^4) and the maximum for The H-A Spin Etch clean sample average is located at (0.033 µm, 6.58×10^{-4} nm^4).

7.3c TMAFM Analysis of Bonded Wafer Pairs

7.3c (i) AFM Analysis of Si(100) Substrates Before Processing, After leaning and Annealing, and After Debonding

For this section, a Si(100) wafer was needed that had seen the same conditions as the bonding wafers, but had not been processed. A 100 mm wafer was selected to undergo AFM analysis and will be noted as the "As Received Si(100)" wafer. Table 7-6 shows the RMS roughness for the three positions that were scanned at 10 μm, 1 μm and 100 nm. The RMS roughness measurements for all scan sizes were at the lower end of all RMS data that is in this thesis, especially those for 1 μm and 100 nm, since both are below 0.1 nm. In this chapter, the focus will be primarily on the 100 nm roughness. This is due to the fact that the larger scan sizes have multiple particles in the images. In capturing the 100 nm scans, these particles were avoided so that only the actual surface topography was imaged. Figure 7-28 shows the As-Received Si(100) wafer. The image shows a smooth surface that has a low RMS roughness measurement. The wafer has a small number of particles, showing that the sample was handled correctly and that there were not cuts to the wafer to obtain samples. A 100nm scan from the As-Received Si(100) wafer is shown in Figure 7-29. The surface is extremely smooth, even with a 2 nm height data scale. Figure 7-30 shows the three 100 nm scan size Power Spectral Densities (PSD). All of the PSDs rise marginally at the longer wavelengths and then minimize at a power near 1×10^{-5} nm^4. The flatness of the graphs account for the low RMS values.

Figure 7-31 shows the Si(100) wafer from Bonding Experiment 22 under a bright light. While this experiment is discussed in detail earlier in this chapter, a brief overview is that this experiment showed successful bonding on a portion of the wafer. This Si wafer was manually separated, or debonded, from the 5000Å thermal oxide on Si(100) wafer, since the bonded wafer pair did not separate during six minutes of sonication. There are areas in 2 corners, which and encompassed by gray lines, which are the portions of the wafer which did not contact the thermal oxide wafer during bonding and annealing. Therefore, these regions are used for the AFM scans of Si(100) after H-A clean and 180ºC annealing. The substrate showed discoloration in the bond area and a difference of hydroaffinity inside and outside of the bond area. This area is surrounded by a white oval in the figure and was used for the AFM study of the debonded Si(100).

Table 7-7 shows the RMS roughness of the 10 μm, 1 μm, and 100 nm scan sizes for the Si(100) sample after the H-A clean and 180°C anneal. This sample has RMS roughness measurements that are higher at all scan sizes in comparison to the As-Received Si(100) wafer. The primary factor for the increase in the 10 μm and 1 μm scans is due to the increase in particles, which is obvious in the 10 μm scan that is shown in Figure 7-32. The 100 nm scan has 60% higher average roughness with three times the variation in measurements. The 100 nm scan is shown in Figure 7-33 and some small undulations are apparent. The PSDs for all 100 nm scans are shown in Figure 7-34. There is a greater fall-off for all PSDs for this sample then those of the As-Received Si(100) wafer. This accounts for a portion of the higher RMS roughness seen in this sample, but the Position 1

and 3 PSDs power above 1 x 10^{-3} nm^4 for some of the longer wavelengths, which is higher than the As-Received Si(100) wafer.

The largest change comes from the debonding process. The RMS roughness is shown in Table 7-8 and has increased at all scan sizes compared to the As Received Si(100) and the cleaned and annealed Si(100) samples. The 10 μm scan in Figure 7-35 shows topography with hundreds of sub-micrometer depressions and raised areas. This suggests that the surface reacted in areas where bonding took place and that physical bridging with the SiO_2 surface that was part of the bonding pair may have taken place and this was broken when the pair were debonded. Figure 7-36 shows the 100 nm scan of the surface. The greater height of the undulations is apparent and are higher than those in the As Received Si(100) wafer topography, which agrees with the RMS data. The PSDs for the 100 nm scan size, Figure 7-37, have various fall-offs, both steep and shallow. The standard deviation of three measurements are more than ten times the amounts of those associated with the average RMS for the As Received Si(100) and H-A cleaned and 180ºC annealed Si(100) samples.

The averaged PSDs for the 100 nm scan size for the three Si(100) samples, shown in Figure 7-38, presents more detail on the comparison roughness of these substrates. The H-A process and annealed sample has a peak at 20 nm, which matches the step width seen in HRTEM. The debonded PSD has greater power than the others at every point above 0.001 μm. This denotes that the surface has roughened at all scales measurable by AFM.

AFM Scan Size	Position 1 RMS Roughness (nm)	Position 2 RMS Roughness (nm)	Position 3 RMS Roughness (nm)	Average RMS Roughness	Standard Deviation
10 um	0.19	0.24	0.50	0.31	0.167
1 um	0.09	0.10	0.08	0.09	0.014
100 nm	**0.09**	**0.08**	**0.07**	**0.08**	**0.012**

7-6: RMS Roughness calculated from AFM scans at three positions on the As Received Si(100) wafer. These measurements serve as a reference for all Si(100) roughness measurements.

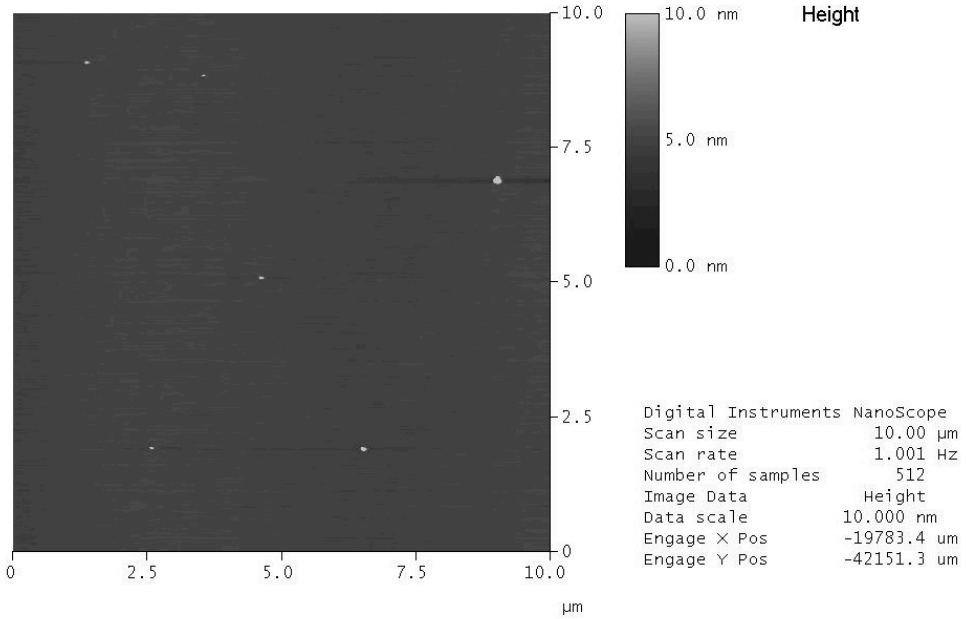

Figure 7-28: A 10 µm top view AFM image of As Received Si(100) wafer. The image shows a smooth surface that has a low RMS roughness measurement. The wafer has a small number of particles, showing that the sample was handled correctly and that there were not cuts to the wafer to obtain samples.

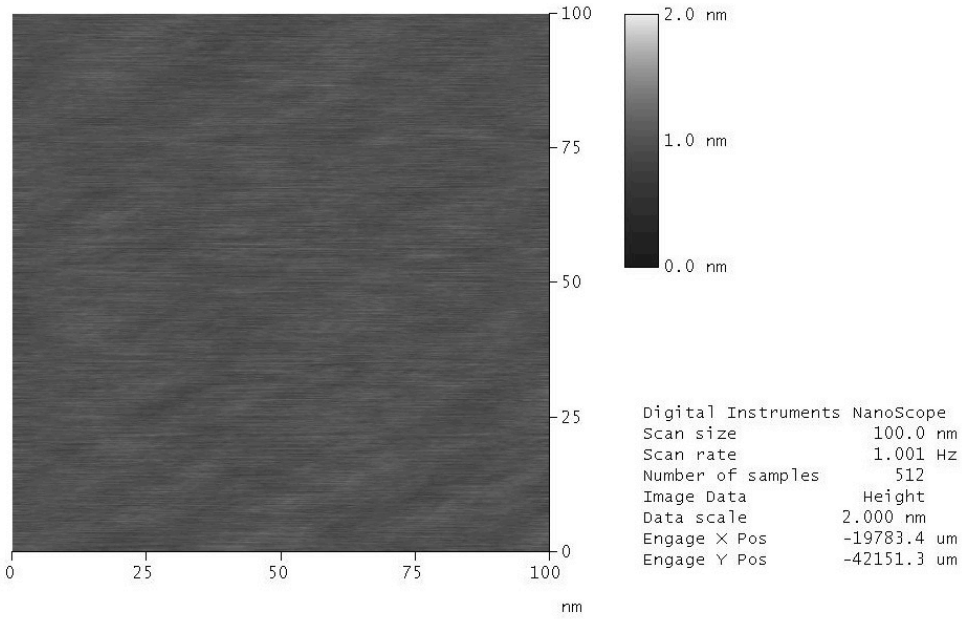

Figure 7-29: A 100nm top view AFM image of As Received Si(100) wafer. The surface is extremely smooth, even with a 2 nm height data scale.

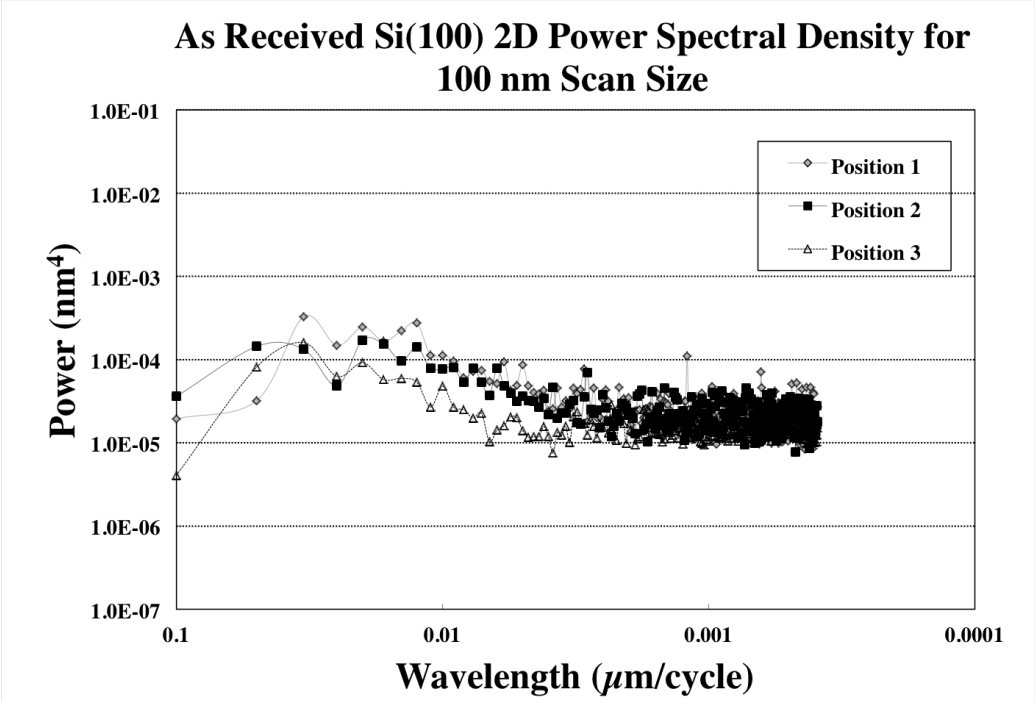

Figure 7-30: 2D Power Spectral Density of the As Received Si(100) wafer for 100nm scan size All of the PSDs rise marginally at the longer wavelengths and then minimize at a power near 1 x 10^{-5} nm^4. The flatness of the graphs account for the low RMS values. The maximums for the positions are : Position 1 (0.033 μm, $3.26x10^{-4}$ nm^4), Position 2 (0.02 μm, $1.71x10^{-4}$ nm^4), Position 3 (0.033 μm, $1.61x10^{-4}$ nm^4)

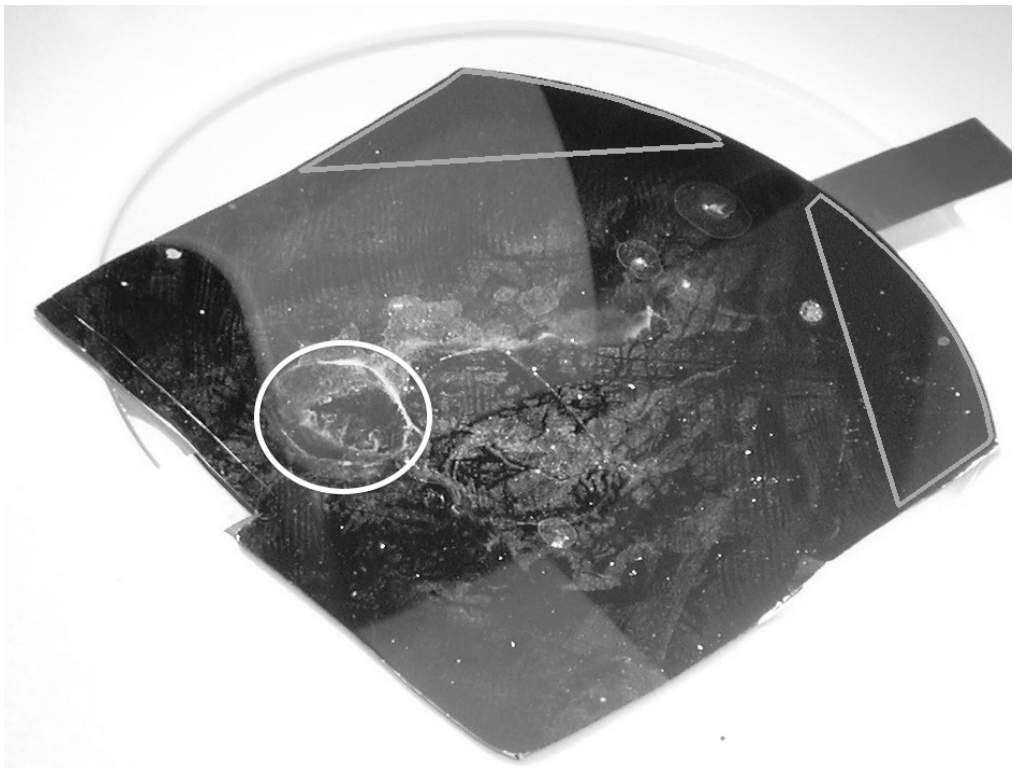

Figure 7-31: Processed Si(100) wafer from bonding Experiment 22. The areas inside the gray lines are the portions of the wafe, which did not contact the thermal oxide wafer during bonding and annealing. Therefore, these regions are used for the AFM scans of Si(100) after H-A clean and 180ºC annealing. The area inside the white oval is the portion where bonding with the thermal oxide wafer occurred, which is used for the AFM study of the debonded Si(100).

AFM Scan Size	Position 1 RMS Roughness (nm)	Position 2 RMS Roughness (nm)	Position 3 RMS Roughness (nm)	Average RMS Roughness	Standard Deviation
10 um	0.517	1.276	1.145	0.979	0.406
1 um	0.314	0.445	0.591	0.450	0.139
100 nm	**0.122**	**0.167**	**0.106**	**0.132**	**0.032**

Table 7-7: RMS Roughness calculated from AFM scans at three positions on Si(100) Cleaned and Annealed sample. These roughness measurements are higher at all scan sizes in comparison to the As Received Si(100) wafer. The primary factor for the decrease in the 10 µm and 1 µm scans is due to the increase in particles. The 100 nm scan has 60% higher average roughness with three times the variation in measurements.

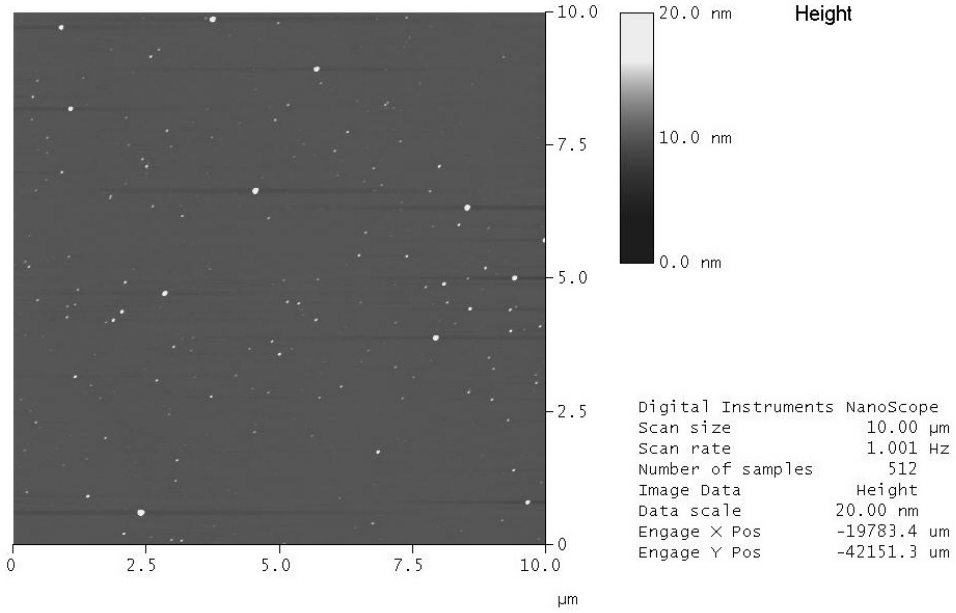

Figure 7-32: A 10 µm top view AFM image of Si(100) Cleaned and Annealed sample. It is evident that the particle density has somewhat increased due to processing, which could include sample cutting or handling.

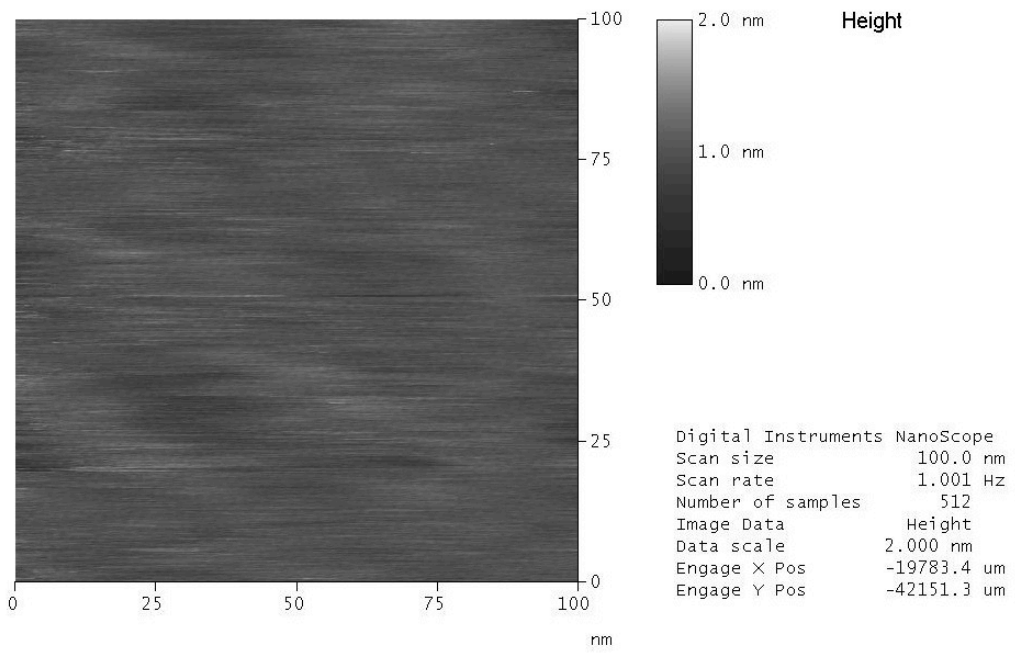

Figure 7-33: A 100 nm top view AFM image of Si(100) Cleaned and Annealed sample. Some small undulations are apparent in the image.

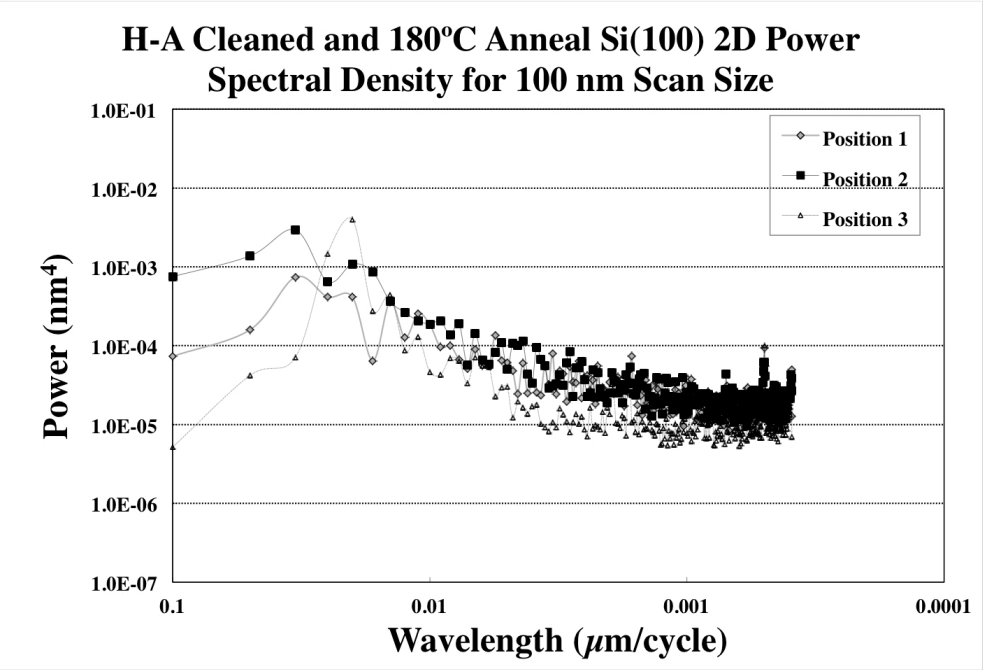

Figure 7-34: 2D Power Spectral Density of the H-A cleaned and 180ºC annealed Si(100) wafer for 100nm scan size. There is a greater fall-off then that of the As Received Si(100) wafer. This accounts for a portion of the higher RMS roughness seen in this sample, but the Position 1 and 3 PSDs power above 1 x 10^{-3} nm^4 for some of the longer wavelengths, which is higher than the As Received Si(100) wafer. The maximums for the positions are : Position 1 (0.033 μm, $7.38x10^{-4}$ nm^4), Position 2 (0.033 μm, $2.93x10^{-3}$ nm^4), Position 3 (0.02 μm, $3.98x10^{-3}$ nm^4)

AFM Scan Size	Position 1 RMS Roughness (nm)	Position 2 RMS Roughness (nm)	Position 3 RMS Roughness (nm)	Average RMS Roughness	Standard Deviation
10 um	3.07	2.04	2.58	2.56	0.519
1 um	1.98	0.57	1.42	1.32	0.709
100 nm	**0.87**	**0.10**	**0.38**	**0.45**	**0.390**

Table 7-8: RMS Roughness calculated from AFM scans at three positions on Si(100) Debonded sample. The roughness as has increased at all scan sizes compared to both the As Received Si(100) and the cleaned and annealed Si(100) sample.

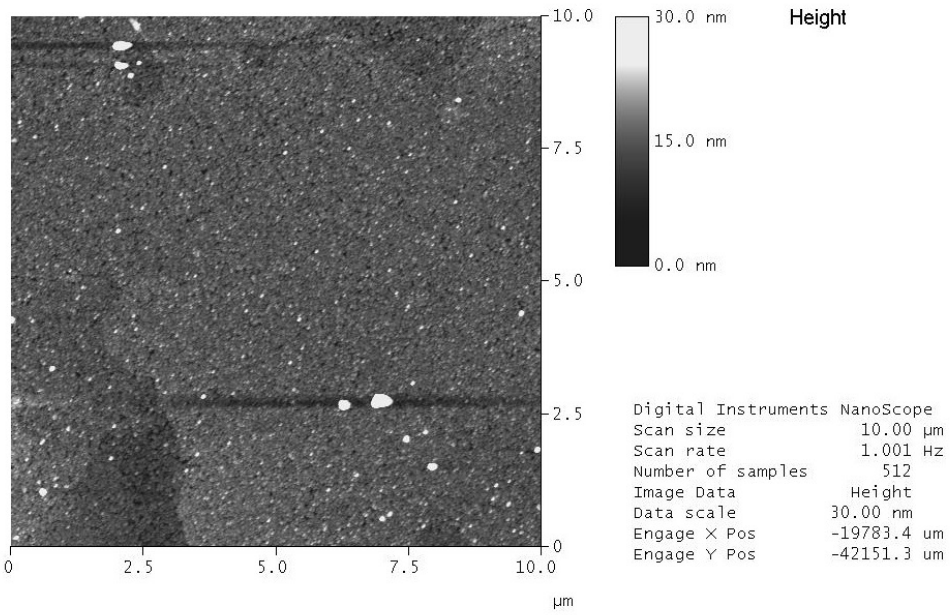

Figure 7-35: A 10 µm top view AFM image of Si(100) Debonded sample. This scan shows a topography with hundreds of sub-micrometer depressions and raised areas, suggesting that the surface reacted in areas where bonding took place and that physical bridging with the SiO_2 surface that was part of the bonding pair may have taken place and this was broken when the pair were debonded.

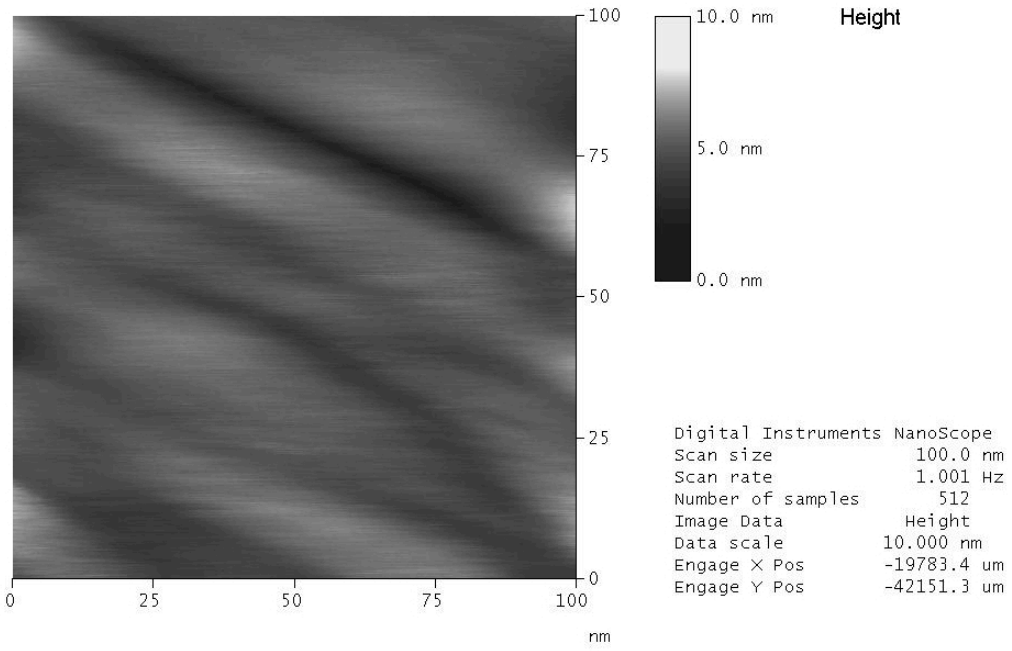

Figure 7-36: A 100 nm top view AFM image of Si(100) Debonded sample**.** The scan has undulations that are higher than those in the As Received Si(100) wafer topography, which agrees with the RMS roughness data.

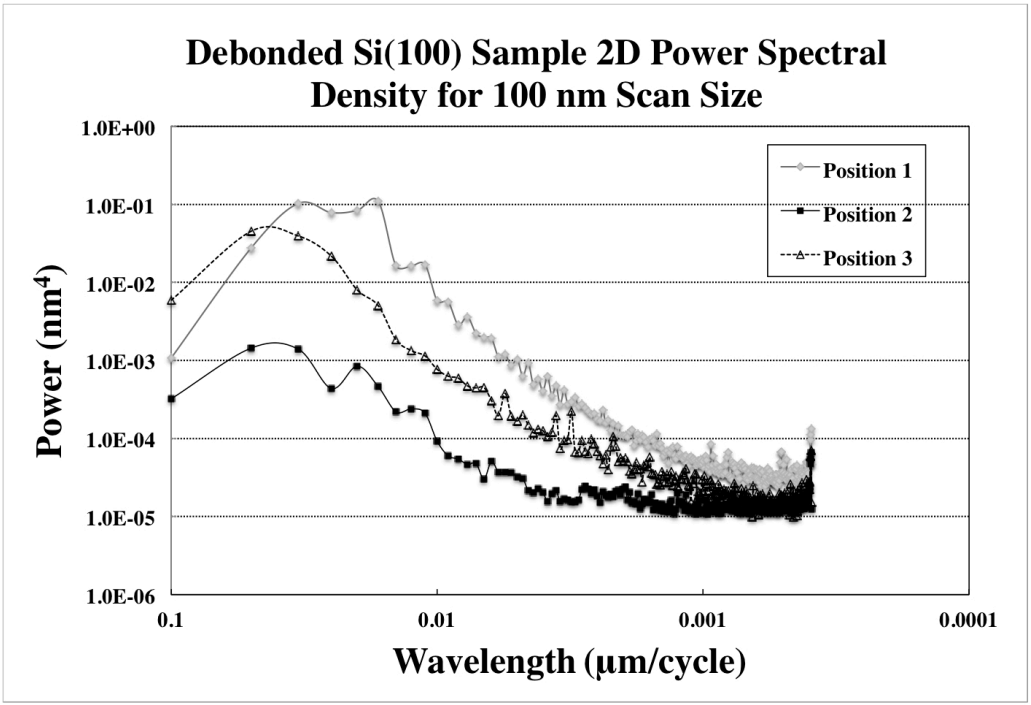

Figure 7-37: 2D Power Spectral Density of the Debonded Si(100) wafer for 100nm scan size. The PSDs have various fall-offs, both steep and shallow. The standard deviation of three measurements are ten times the amounts of those associated with the As Received Si(100) and H-A cleaned and 180ºC annealed Si(100) samples. The maximums for the positions are : Position 1 (0.017 µm, 1.10 $x10^{-1}$ nm^4), Position 2 (0.05 µm, 1.42$x10^{-3}$ nm^4), Position 3 (0.05 µm, 4.53$x10^{-2}$ nm^4)

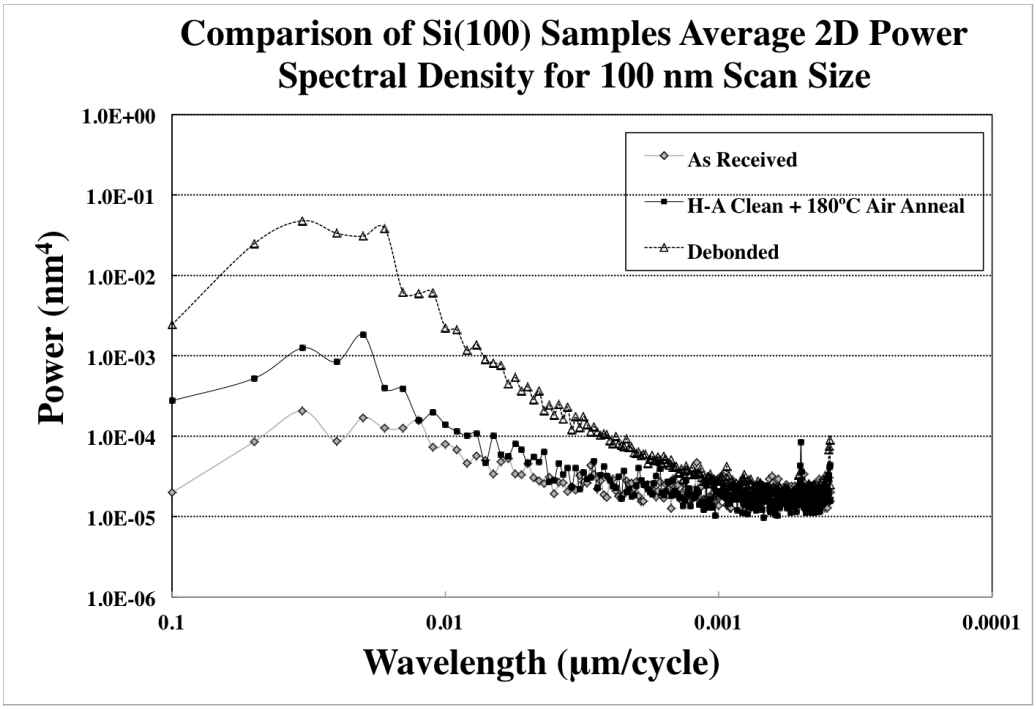

Figure 7-38: Average 2D Power Spectral Density of the As Received, H-A cleaned and 180ºC annealed, and Debonded Si(100) samples for 100nm scan size. The PSDs have differing fall-offs, both steep and shallow. The Debonded Si(100) PSD has greater power than the others at every point above 0.001um. This indicates that the surface has roughened at all scales measurable by AFM. The maximums for the samples are : As Received Si(100) (0.033 µm, 6.32×10^{-4} nm^4), H-A cleaned and 180ºC annealed Si(100) (0.02 µm, 1.82×10^{-3} nm^4), Debonded Si(100) (0.033 µm, 4.78×10^{-2} nm^4).

7.3c (ii) TMAFM Analysis of 5000Å Thermal Oxide on Si(100) substrates before processing, after cleaning and annealing, and after debonding

The first 5000Å Thermal Oxide on Si(100) substrate that underwent AFM imaging was a portion of a wafer As-Received from the manufacturer. This 0.5 μm thermal oxide films will conform to the underlying topography of the Si(100) substrate, but will smooth lateral and horizontal differences. The RMS of this substrate is shown in Table 7-9 and the 100 nm scan has a 9% lower RMS roughness than that of the As-Received Si(100) wafer presented earlier in this chapter. Figure 7-39 shows an AFM image of the As Received Thermal Oxide sample, which has a smooth surface with multiple particles as the main surface feature. Figure 7-40 is a 100 nm scan and has some height differences across the image. The PSDs for this sample, Figure 7-41 all have a rapid fall-off, which minimizes the RMS roughness.

Figure 7-42 is the 5000Å thermal oxide on Si(100) wafer from bonding Experiment 22 after debonding. The portion of the wafer which did not contact the Si(100) wafer during bonding or annealing are outlined with gray lines in the image. These regions are used for the AFM scans of 5000Å thermal oxide on Si(100) after H2BWSC clean and 180ºC annealing. A white oval circles the portion of the sample where bonding with the Si(100) wafer occurred, which is used for the AFM study of the debonded 5000Å thermal oxide on Si(100).

The RMS roughness for the 5000Å Thermal Oxide on Si(100) substrate after H2BWSC cleaning and anneal are shown in Table 7-10. The 10 μm roughness is nearly the same as the Thermal Oxide As-Received sample at the

same scan size, even though the sample has smaller particles. This denotes that the surface has been modified by the HF etching. There is a 25% increase in the 100 nm RMS roughness against that of the as received thermal oxide wafer. The 10 μm AFM image in Figure 7-43 clearly shows how the sample topography has been changed. There are a large number of sub-micron shallow pits in the surface. The shallowness of the pits, only a few nanometers deep, allow for the topology to appear quite different, but the roughness to only increase by a fourth. Figure 7-44 presents the 100 nm AFM of this sample, which has height differences, which are visible on the 2 nm height scale.

The PSDs, shown in Figure 7-45, have a substantial difference compared to those of the as received thermal oxide. The falloff is less steep and there are repeated crests in the functions which signify a surface feature that has a reiterated size or spacing in the AFM scan. This would be the smaller pits, which appear of uniform size in the 10 μm image.

Table 7-11 is the RMS Roughness in nanometers for the Debonded 5000Å Thermal Oxide on Si(100) sample. The average RMS roughness measurements are greater than those of the Thermal Oxide As Received and Thermal Oxide Cleaned and Annealed samples at all scan sizes. The average 100 nm RMS in this table is over 30% greater than the Thermal Oxide Cleaned and Annealed sample average for the same scan size. This surface has become more rough due to the debonding. Figure 7-46 is the 10 μm top view AFM image of the Debonded 5000Å Thermal Oxide on Si(100) sample. There are high and low spots evident in the scan. The high spots average 21.4 nm ± 3.02 nm above the surrounding area,

while the pits average 18.2 nm ± 4.27 nm are below their surrounding area. This suggests that the bonding extended 20 nm below the sample surface of each the two substrates. The 100nm AFM image of this sample is shown in Figure 7-47 and the undulations are more pronounced than any of the other Thermal Oxide samples at this scan size.

Figure 7-48 is the PSDs of the Debonded 5000Å Thermal Oxide on Si(100) sample for 100nm scan size. The three positional PSDs are higher in power than those for the H2BWSC cleaned and Annealed Thermal Oxide in the 0.033 μm – 0.01 μm range. This accounts for the 30% higher RMS roughness. Positions 1 and 3 have repeated crests which signify a surface feature that has a reiterated size or spacing.

Figure 7-49 presents the Average 2D Power Spectral Density of the As Received, H2BWSC cleaned and 180ºC annealed, and Debonded 5000Å Thermal Oxide on Si(100) samples for 100nm scan size. The As-Received Thermal Oxide PSD has steep and rapid fall-off, which accounts for the smoothness of the sample. The H2BWSC cleaned and 180ºC annealed Thermal Oxide PSD has repeated crests in these functions, which signify a surface feature that has a reiterated size or spacing. The graph also confirms the cleaning etches the oxide and increases the intensity of the PSD below wavelengths of 0.02 μm, compared to the As Received Thermal oxide sample. The Debonded Thermal Oxide PSD has greater power than the others in the range of .033 μm to .007 μm. This indicates a rougher surface and reflects what is seen in the 10 μm scan and the RMS measurements. Also, it should be noted that the H2BWSC processed and

annealed sample has a peak at 20 nm as does the Debonded thermal oxide, suggesting that the roughness has a 20 nm width, similar to that seen in the Si(100) samples that underwent H-A processing and HRTEM.

AFM Scan Size	Position 1 RMS Roughness (nm)	Position 2 RMS Roughness (nm)	Position 3 RMS Roughness (nm)	Average RMS Roughness	Standard Deviation
10 um	1.15	1.43	1.44	1.34	0.168
1 um	0.20	0.12	0.17	0.16	0.039
100 nm	**0.06**	**0.08**	**0.07**	**0.07**	**0.009**

Table 7-9: RMS Roughness calculated from AFM scans at three positions on 5000Å Thermal Oxide on As Received Si(100) wafer. The average for the 100 nm scan size has a 9% lower RMS roughness than that of the As Received Si(100) wafer.

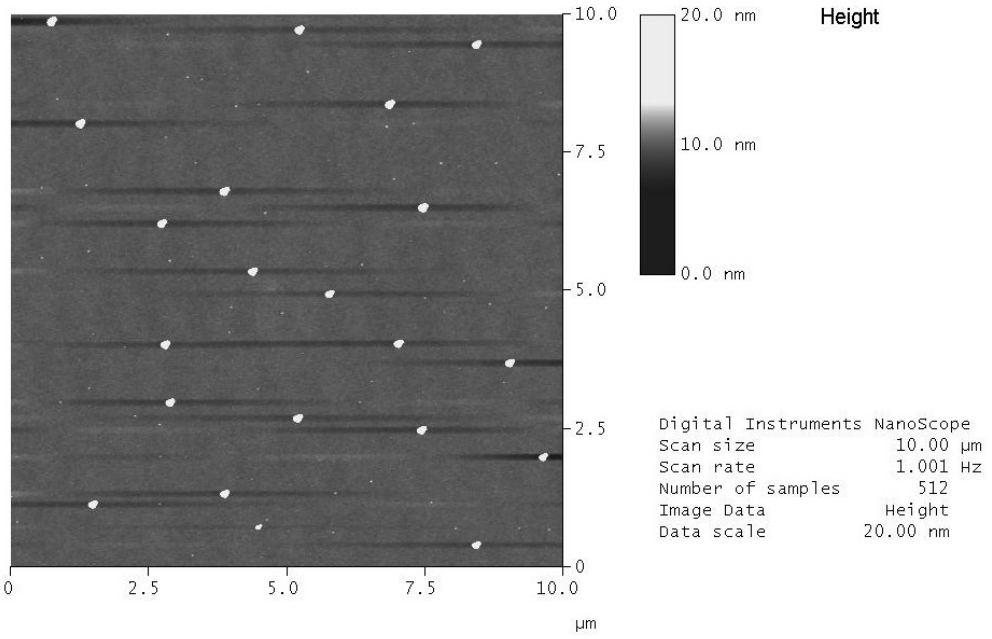

Figure 7-39: A 10 µm top view AFM image of 5000Å Thermal Oxide on As Received Si(100) wafer. The scan displays a smooth surface with multiple particles as the main surface feature. This substrate is lower in particulates than the Si(100) As Received wafer.

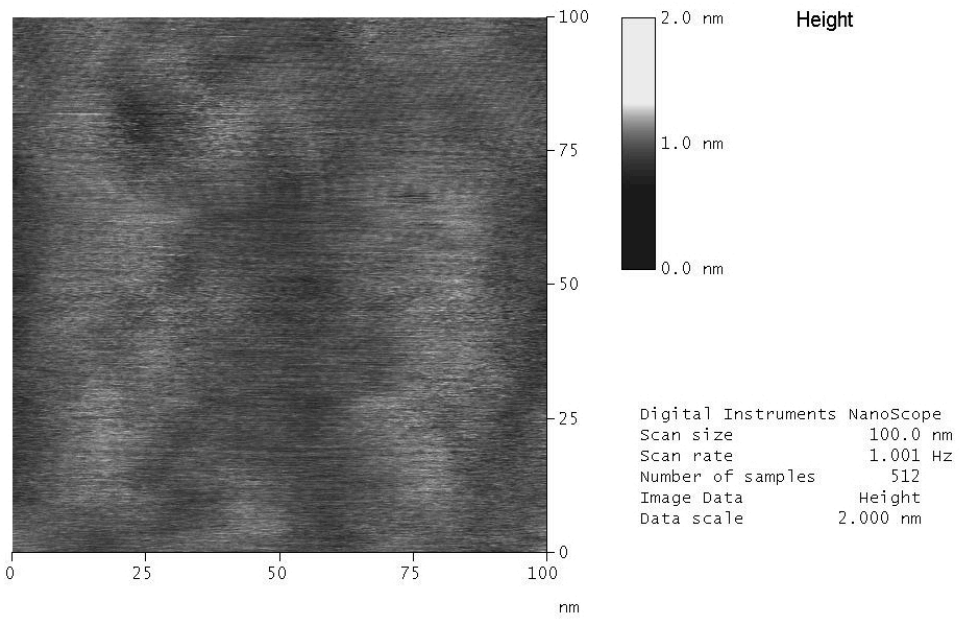

Figure 7-40: A 100 nm top view AFM image of 5000Å Thermal Oxide on As Received Si(100) wafer. There are some minor height differences across the scan.

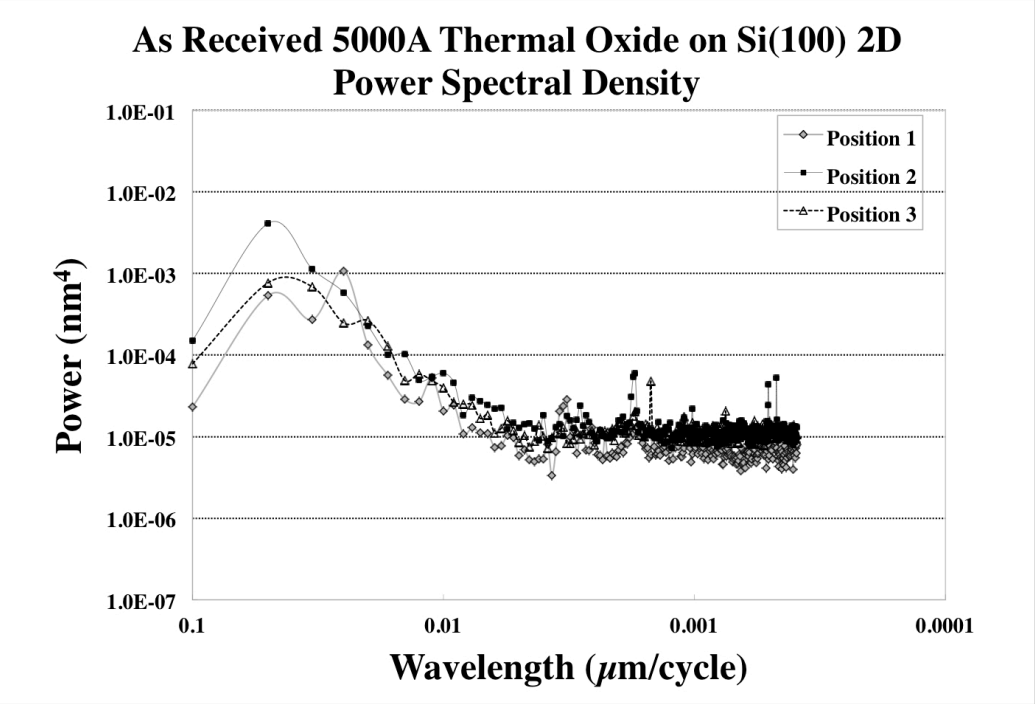

Figure 7-41: 2D Power Spectral Density of the 5000Å Thermal Oxide on Si(100) sample for 100nm scan size. All three PSDs have a rapid fall-off and minimize at a power of $1x10^{-5}$ nm^4, which minimizes the RMS roughness. The maximums for the positions are : Position 1 (0.025 µm, $1.07\ x10^{-3}$ nm^4), Position 2 (0.05 µm, $7.68x10^{-4}$ nm^4), Position 3 (0.05 µm, $4.11x10^{-3}$ nm^4)

Figure 7-42: The 5000Å thermal oxide on Si(100) wafer from bonding Experiment 22 after debonding. The areas inside the gray lines are the portion of the wafer which did not contact the Si(100) wafer during bonding or annealing. These regions are used for the AFM scans of 5000Å thermal oxide on Si(100) after H2BWSC clean and 180ºC annealing. The area inside the white oval is the portion where bonding with the Si(100) wafer occurred, which is used for the AFM study of the debonded 5000Å thermal oxide on Si(100).

AFM Scan Size	Position 1 RMS Roughness (nm)	Position 2 RMS Roughness (nm)	Position 3 RMS Roughness (nm)	Average RMS Roughness	Standard Deviation
10 um	0.77	0.27	3.02	1.35	1.464
1 um	0.64	0.15	0.23	0.34	0.263
100 nm	**0.12**	**0.08**	**0.09**	**0.10**	**0.023**

Table 7-10: RMS Roughness calculated from AFM scans at three positions on 5000Å Thermal Oxide on Si(100) Cleaned and Annealed sample. The 10 µm roughness is nearly the same as the Thermal Oxide As Received sample at the same scan size, even though the sample has smaller particles. This denotes that the surface has been modified by the HF etching. There is a 25% increase in the 100 nm RMS roughness against that of the Thermal Oxide As Received sample.

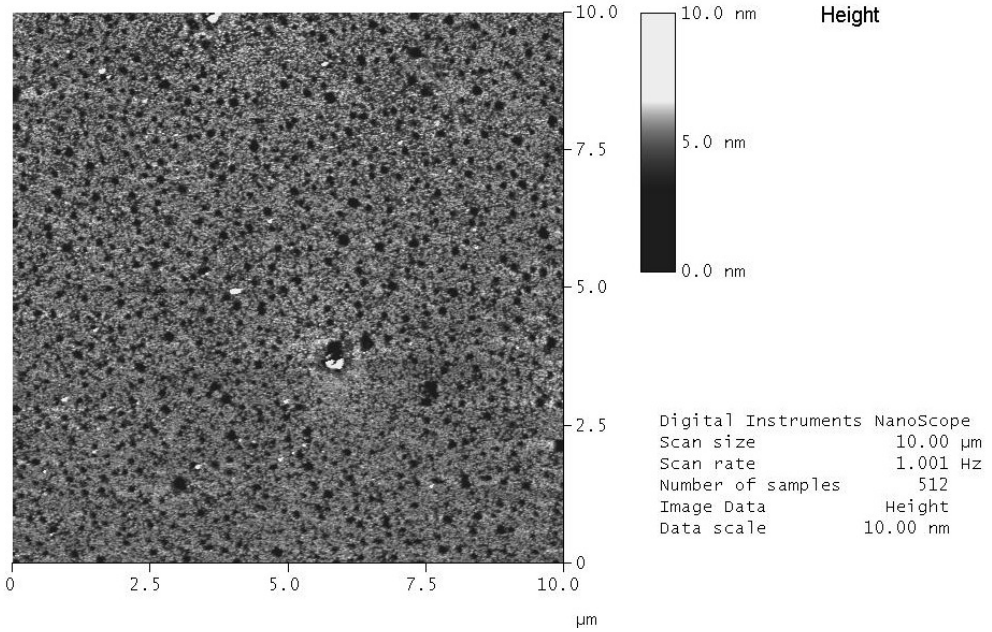

Figure 7-43: A 10 µm top view AFM image of 5000Å Thermal Oxide on Si(100) after H2BWSC Clean and Annealing sample. The scan clearly shows how the sample topography has been changed. A large number of sub-micron shallow pits appear in the scan.

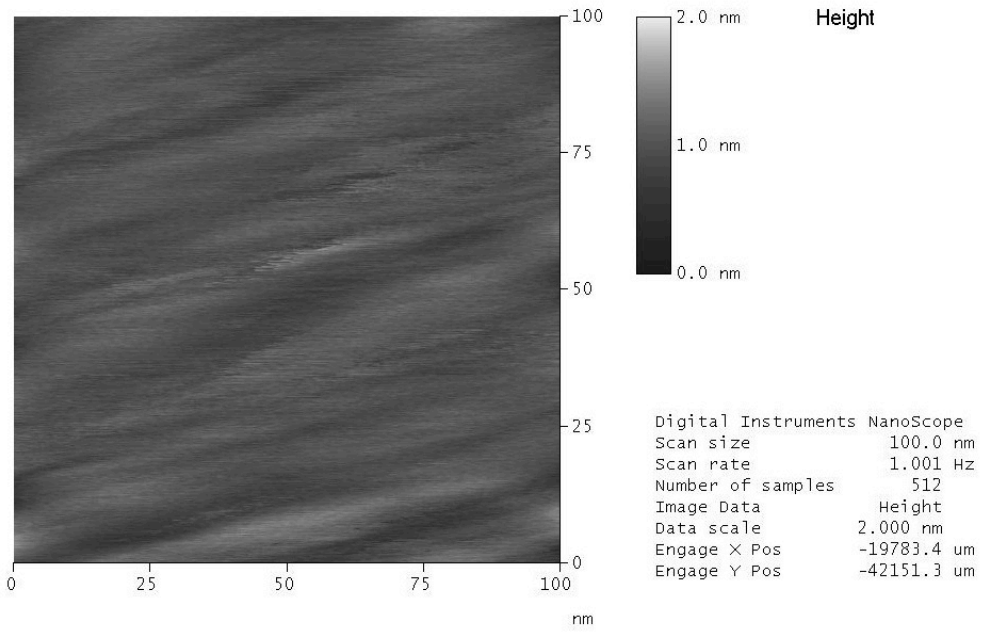

Figure 7-44: A 100 nm top view AFM image of 5000Å Thermal Oxide on Si(100) after H2BWSC Clean and Annealing sample. The topography has height differences, which are visible on the 2 nm height scale.

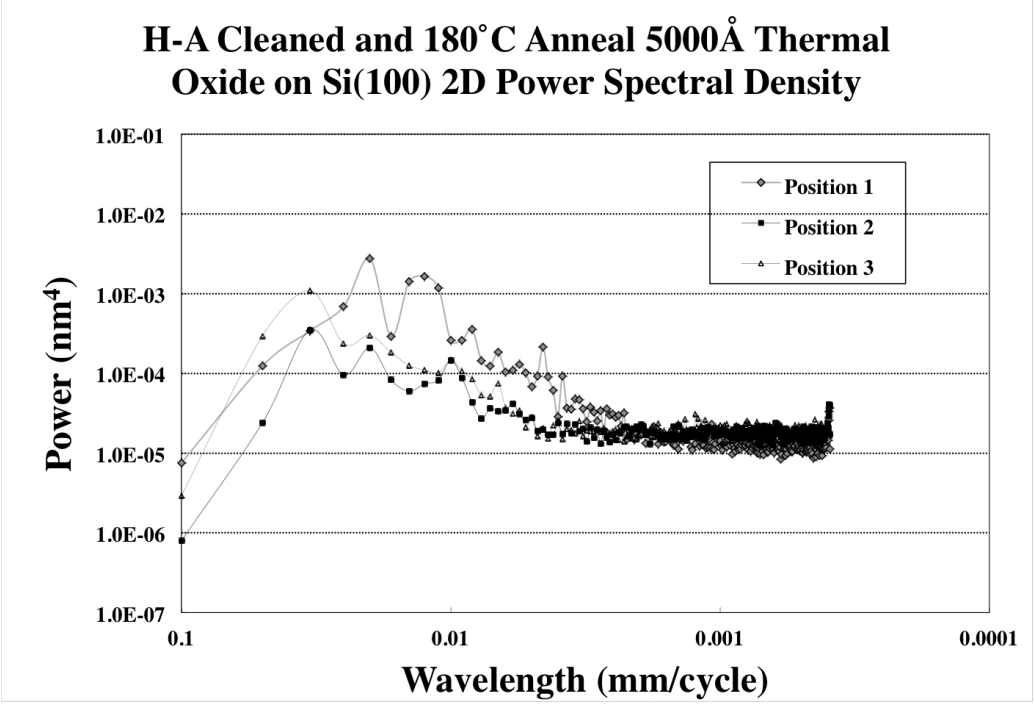

Figure 7-45: 2D Power Spectral Density of the H2BWSC cleaned and Annealed 5000Å Thermal Oxide on Si(100) sample for 100nm scan size. The PSDs have a substantial difference compared to those of the As Received thermal oxide sample. The falloff is less steep and there are repeated crests in these functions which signify a surface feature that has a reiterated size or spacing in the AFM scan. The maximums for the positions are: Position 1 (0.02 μm, 2.75×10^{-3} nm^4), Position 2 (0.033 μm, 3.50×10^{-4} nm^4), Position 3 (0.033 μm, 1.09×10^{-3} nm^4)

AFM Scan Size	Position 1 RMS Roughness (nm)	Position 2 RMS Roughness (nm)	Position 3 RMS Roughness (nm)	Average RMS Roughness	Standard Deviation
10 um	3.38	2.01	1.63	2.34	0.918
1 um	3.04	1.196	0.78	1.67	1.204
100 nm	**0.14**	**0.17**	**0.08**	**0.13**	**0.046**

Table 7-11: RMS Roughness calculated from AFM scans at three positions on the Debonded 5000Å Thermal Oxide on Si(100) sample. The average RMS roughness measurements are greater than those of the Thermal Oxide As Received and Thermal Oxide Cleaned and Annealed samples at all scan sizes. The average 100 nm RMS in this table is over 30% greater than the Thermal Oxide Cleaned and Annealed sample average for the same scan size. This surface has increased roughness due to the debonding.

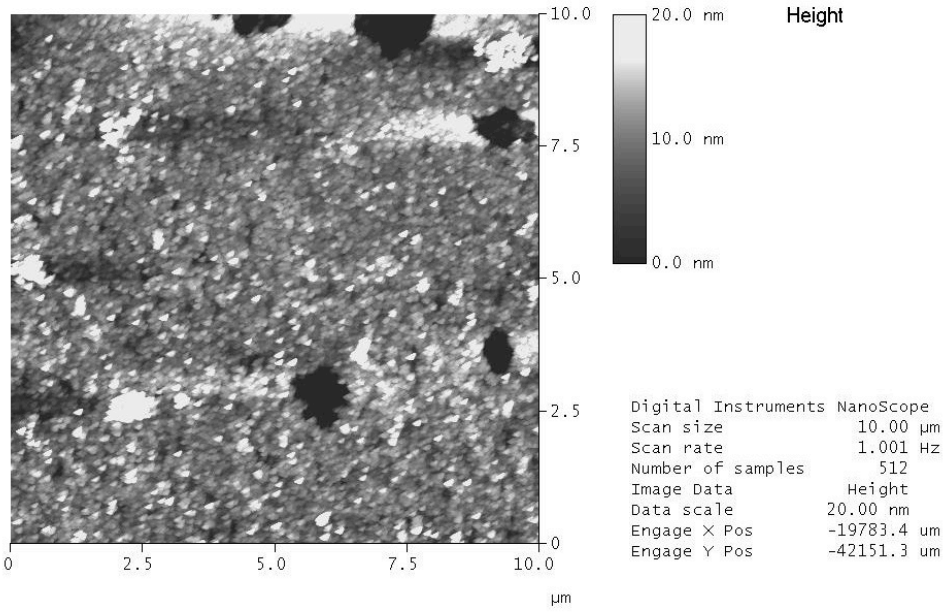

Figure 7-46: A 10 µm top view AFM image of the Debonded 5000Å Thermal Oxide on Si(100) sample. There are high and low spots evident in the scan. The high spots average 21.44 nm ± 3.02 nm above the surrounding area, while the pits average 18.16 nm ± 4.27 nm are below their surrounding area. This suggests that the bonding extended 20 nm below the sample surface of each the two substrates.

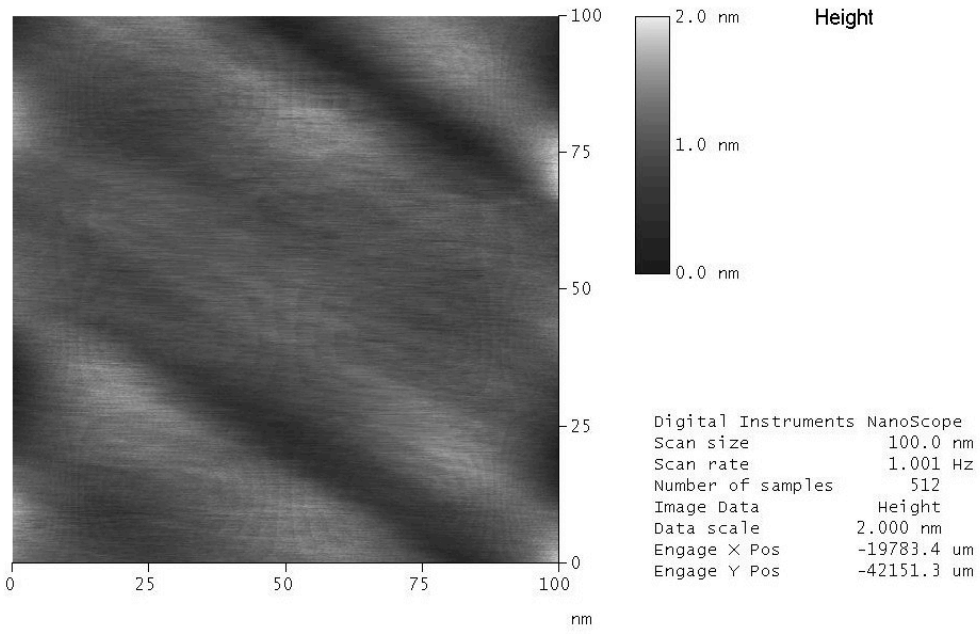

Figure 7-47: A 100 nm top view AFM image of the Debonded 5000Å Thermal Oxide on Si(100) sample. The undulations in this image are more pronounced than any of the other Thermal Oxide samples at this scan size.

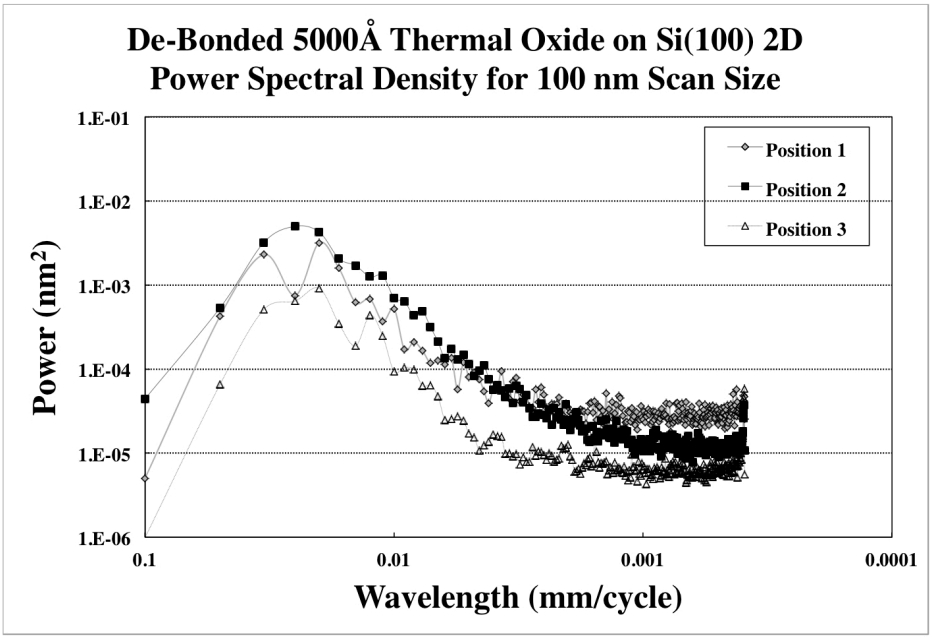

Figure 7-48: 2D Power Spectral Density of the Debonded 5000Å Thermal Oxide on Si(100) sample for 100nm scan size. These PSDs are higher in power than those for the H2BWSC cleaned and Annealed Thermal Oxide in the 0.033 μm – 0.01 μm range. This accounts for the 30% higher RMS roughness. Positions 1 and 3 have repeated crests which signify a surface feature that has a reiterated size or spacing. The maximums for the positions are: Position 1 (0.02 μm, 3.18×10^{-3} nm^4), Position 2 (0.025 μm, 4.98×10^{-3} nm^4), Position 3 (0.02 μm, 9.14×10^{-4} nm^4).

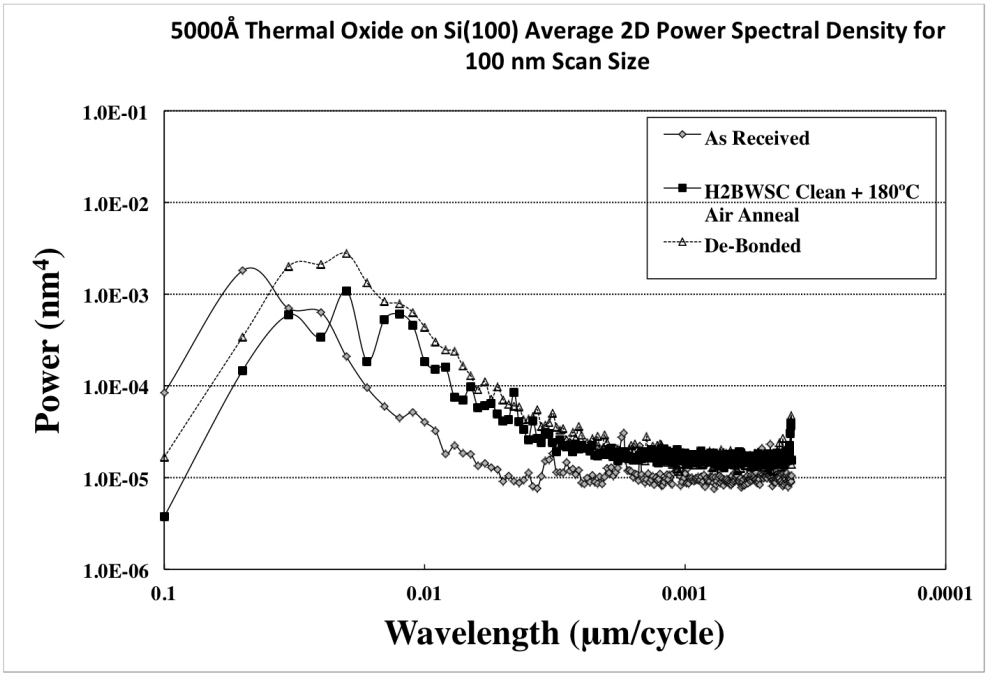

Figure 7-49: Average 2D Power Spectral Density of the As Received, H2BWSC cleaned and 180ºC annealed, and Debonded 5000Å Thermal Oxide on Si(100) samples for 100nm scan size. The As Received Thermal Oxide PSD has steep and rapid fall-off, which accounts for the smoothness of the sample. The H2BWSC cleaned and 180ºC annealed Thermal Oxide PSD has repeated crests in these functions, which signify a surface feature that has a reiterated size or spacing. The graph also confirms the cleaning etches the oxide and increases the intensity of the PSD below wavelengths of 0.02 mm, compared to the As Received Thermal oxide sample. The Debonded Thermal Oxide PSD has greater power than the others in the range of .033 µm to .007 µm. This indicates a rougher surface and reflects what is seen in the 10 µm scan and the RMS measurements. The maximums for the samples are : As Received Thermal Oxide on Si(100) (0.05 µm, 1.81×10^{-3} nm^4), H2BWSC cleaned and 180ºC annealed Thermal Oxide on Si(100) (0.02 µm, 1.09×10^{-3} nm^4), Debonded Thermal Oxide on Si(100) (0.02 µm, 2.79×10^{-3} nm^4).

Chapter 8: Modeling of β-cristobalite on Si(100) as a precursor phase for a silica nano-bonding interphase on Si(100)

8.1 Introduction

In this chapter, a model for the inter-phase that occurs at the Si(100)/SiO2 interface after the Si(100) surface was processed using the H-A clean will be presented in detail. The selection of the silica polymorph will be presented

8.1a Selection of Silica Polymorph for Modeling a Precursor Phase for a Silica Nano-Bonding Interphase on Si(100)

Using the results from Dr. J. D. Bradley's thesis [1], which were presented in Chapter 3, the inter-phase was modeled using β-cristobalite. Several steps were needed to create the structure. The first was to set up the Cartesian coordinates for each atom in Si(100) and β-cristobalite, both are presented in Appendix A. The simulated β-cristobalite that had been fitted to a Si(100) base and then elongated an additional 100%, normal to the Si interface therefore these Cartesian coordinates were needed as well. To fit the β-cristobalite to the Si(100) base, there was a contraction from 7.166Å in (001) and (010) directions to 5.43 Å, while keeping a constant volume. This required the (100) direction of the crystal to be extended to 12.48 Å. This expansion was then doubled, keeping the same ratio of spacing in the (100) direction between the atoms.

Figure 8-1 shows a (100) view of the CrystalMaker model of two layers of Si(100) with two layers 100% elongated β-cristobalite, with each layer being two unit cells wide.

8.1b Selection of β-cristobalite(110) for Calculations

The elongated β-cristobalite crystal structure from Dr. Bradley's work is a model that has large distortions in all three axes with high stress. Simulations on this model were unlikely produce results. The β-cristobalite was therefore rotated at a 45° angle about the (001) axis. This produced a "β-cristobalite(110)" crystal with a base of 5.067Å in both width and length and a height of 7.166 Å. The Cartesian coordinates for the crystal are presented in Appendix A. The β-cristobalite(110) crystal is shown from multiple angles in Figure 8-2. The β-cristobalite(110) crystal is similar to both Si(100) and β-cristobalite, in that all corners have a Si atom present. Also, a Si atom is present at the center of the *x* and *y* axes in four of the faces, but only ¼ of the *z* height versus ½ *z* height in Si(100) and β-cristobalite(100).

When fitting the area of the base of the β-cristobalite(110) crystal to the Si(100) crystal dimensions, the base area has to increase by 13% to fit Si(100), which contrasts with the 74% decrease using the β-cristobalite crystal. These percentages are the same amounts that the height of the two crystal change when fitting them to the underlying Si(100), when total volume is conserved for each structure, where the β-cristobalite height increases to 12.48 Å and the β-cristobalite(110) height decreases to 6.24 Å. The higher percentage deformation

represents a high stress in the structure of the density conserved β-cristobalite crystal. Finally, the density-conserved β-cristobalite(110) crystal fitted to Si(100) has a 120º angle between two oxygen atoms bonded to a Si atoms, where the density-conserved β-cristobalite crystal now has 63.3º. This can be compared to the original 109.5º bond angle between two oxygen atoms bonded to a Si atom

8.1c Creation of β-cristobalite(110) on Si(100) Structure for Calculations

Once the β-cristobalite(110) model was completed, a model of this crystal on a Si(100) layer was needed. Figure 8-3 shows the CrystalMaker model of two layers of Si(100) with two layers β-cristobalite(110), with each layer being two unit cells wide, where the β-cristobalite(110) base is fitted to the Si cell.

8.1d Creation of Amorphous Silica Structure for Calculations

The model from Dr. Bradley's thesis has only a few unit cells of β-cristobalite along the *z* direction in the oxide before the layer became amorphous. Therefore, the structure needed an amorphous silica layer. Dr. Michael Thorpe and his graduate student Adam de Graff had generated a $3x10^5$-atom amorphous silica layer and provided the Cartesian coordinates of this layer to me. A portion of this set was used as a layer that was put on top of the β-cristobalite(110) on a Si(100) structure. This Si(100)- β-cristobalite(110)-amorphous silica structure was used in a simulation software to relax the entire structure and determine the overall energy.

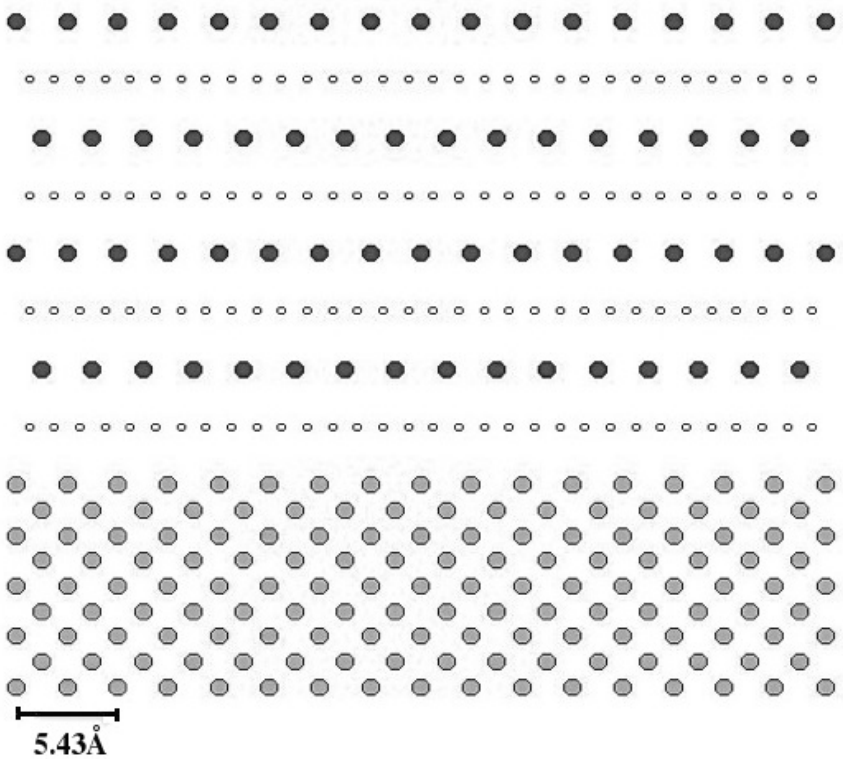

Figure 8-1: (100) view of the CrystalMaker model of 2 layers of Si(100) with 2 layers 100% elongated β-cristobalite, with each layer being two unit cells wide. The β-cristobalite base is fitted to the Si(100) cell. Si(100) atoms are presented as light gray, oxygen atoms as white, and the β-cristobalite Si atoms are dark gray.

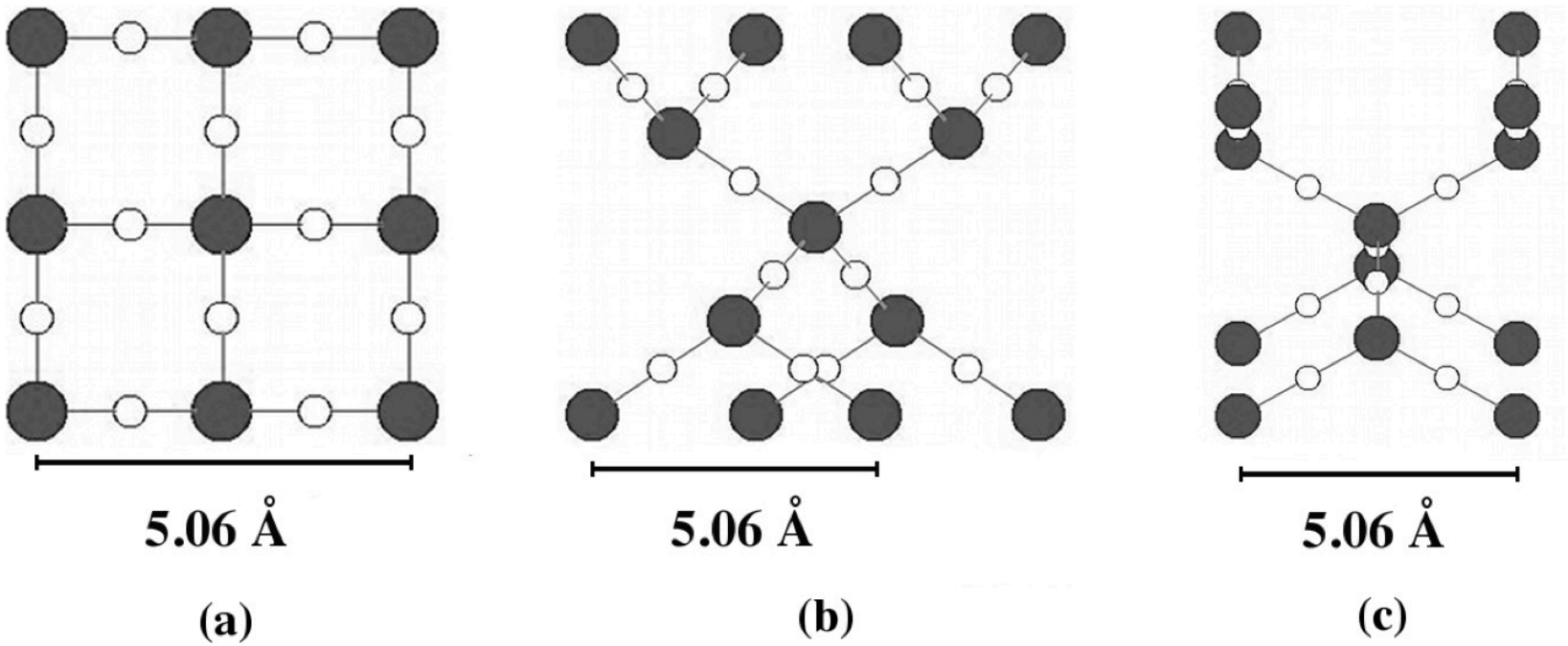

Figure 8-2: CrystalMaker model of the β-cristobalite(110) crystal (a) top view, (b) and (c) side views. The β-cristobalite Si atoms are light gray and oxygen atoms are white.

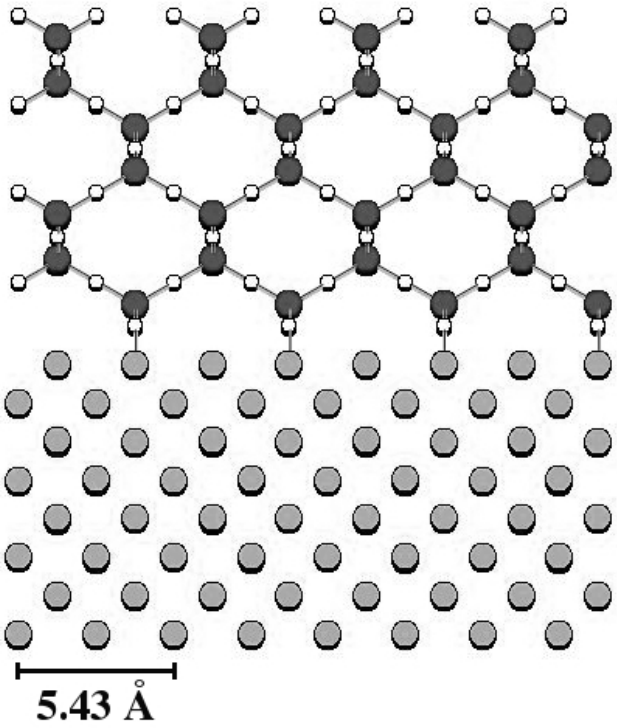

Figure 8-3: (100) view of the CrystalMaker model of two layers of Si(100) with two layers β-cristobalite(110), with each layer being two unit cells wide. The β-cristobalite(110) base is fitted to the Si(100) cell. Si(100) atoms are presented as light gray, oxygen atoms as white, and the β-cristobalite Si atoms are dark gray.

8.2 Analytical Calculation Software and Methods

8.2a Vienna Ab-initio Simulation Package (VASP)

A discussion will be presented about topics that related to the Vienna *Ab-initio* Simulation Package (VASP) software and the methods it employs. It was employed to obtain the relaxed structures.

Since VASP employs *ab-initio* (first principal) calculations, it should be noted that these are a type of processes require no parameters or input other than the atomic number [2].

8.2b Density Functional Theory (DFT)

Density functional theory (DFT) is the base that VASP software is built upon. DFT is a quantum mechanical theory used to study the electronic structure in many-body systems [3]. The first DFT is the method proposed independently by both Thomas and Fermi [4,8-5]. The Thomas-Fermi (TF) method approximated the kinetic energy of the electrons using a function of the density. The electrons were treated as a homogeneous gas of non-interacting particles with the density set to the local density at any point. Both Thomas and Fermi did not attempt to account for the exchange nor the correlation between electrons. The local approximation for exchange was added in 1928 by P.A.M. Dirac [6]. This lead to the energy for an electron in a external potential, $V_{ext}(r)$ [3]:

$$E_{TF} = C_1 \int d^3r \cdot n(\vec{r})^{5/3} + \int d^3r \cdot V_{eff}(\vec{r}) \cdot n(\vec{r}) + C_2 \int d^3r \cdot n(\vec{r})^{4/3} + \qquad \text{(Eq. 8-1)}$$

$$\frac{1}{2} \int d^3r \cdot d^3r' \cdot \frac{n(\vec{r}) \cdot n(\vec{r'})}{\left|\vec{r} - \vec{r'}\right|}$$

where the local approximation to the kinetic energy is the first term with:

$$C_1 = \frac{3}{10}\left(3\pi^2\right)^{2/3} \qquad \text{(Eq. 8-2)}$$

The third term is the local exchange with:

$$C_2 = \frac{3}{4}\left(\frac{3}{\pi}\right)^{1/3} \qquad \text{(Eq. 8-3)}$$

The final term is the classical electrostatic Hartree energy. By minimizing $E_{TF}[n]$, the ground state energy and density can be found by letting the ***n(r)*** be constrained by the total number of electrons, *N*. Using Lagarange multipliers, a solution can be found [3]:

$$\Omega_{TF}[n] = E_{TF}[n] - \mu\left[\int d^3r \cdot n(\vec{r}) - N\right] \qquad \text{(Eq. 8-4)}$$

where μ is the Fermi energy.

Hohenberg and Kohn then created a DFT with two theorems that was an exact theory of many-body systems, using a Hamiltonian of a system of particles in an external potential:

$$\widehat{H} = -\frac{\hbar^2}{2m_e}\sum_i \nabla_i^2 + \sum_i V_{ext}(\vec{r}_i) + \frac{1}{2}\sum_{i\neq j}\frac{e^2}{\left|\vec{r}_i - \vec{r}_j\right|} \qquad \text{(Eq. 8-5)}$$

The first theorem states the ground state electron density determines the ground state properties of an interacting system of particles in an external potential [3]. The second theorem states that a universal functional for the energy can be defined in terms of the density for any external potential and that the exact

ground state density minimizes the universal functional and is a global minimum for the functional.

8.2c Kohn and Sham (KS) Method

The work of Kohn and Sham (KS) [7] shows a method, which replaces the difficult interacting many-body system with a different system that can be solved more easily. The KS method presupposes that the both systems have equal ground state densities. The second system will have non-interacting particles so that independent particle equations can be obtained which are solvable via numerical analysis. The KS approach calculates the exact density and energy ground state by solving a set of Schrödinger-like equations for the independent particles and checking if the condition that the effective potential and density are consistent [3]. The force for the KS approach can be evaluated using the Hellman-Feynmann theorem [8, 9].

8.2d Car-Parrinello (CP) Approach

Car and Parrinello [10] conducted the first quantum dynamics simulations. The Car-Parrinello (CP) approach uses the total energy based on both the classical position variables for ions and the quantum wavelength variable for electrons. CP considers both of these as one single problem. Using the Born-Oppenheimer (adiabatic) approximation, this problem is solved by minimizing the electron energy and finding the nuclei motion simultaneously. This is applied to structure relaxation and thermal simulations of solids. The CP approach uses the total KS energy as the potential energy. This potential energy is a function of the nuclei

positions. Using forces from this energy is the essential principle for all forms of *ab-initio* molecular dynamics, of which VASP is one.

8.2e Plane waves and Pseudopotential

VASP uses plane waves and pseudopotentials in its calculations. Plane waves are typically used since they are a complete and orthonormal basis set and allow for uncomplicated analytical force evaluation. If we look at the Schrödinger-like equation, such as the KS equation, for an electron moving in an effective potential, $V_{eff}(\mathbf{r})$, the eigenstates must satisfy [3]:

$$\widehat{H}_{eff}(\vec{r})\cdot\psi(\vec{r})=\left[-\frac{\hbar^2}{2m_e}\nabla_i^2+V_{eff}(\vec{r}_i)\right]\cdot\psi(\vec{r})=\varepsilon_i\cdot\psi(\vec{r}) \qquad \text{(Eq. 8-6)}$$

In a solid, it is typical to require the states to be to be normalized and have periodic boundary conditions. Then the eigenfunctions, which must be periodic, can be written as a complete set of Fourier components [3]:

$$\psi_i(\vec{r})=\sum_{\vec{q}}c_{i,\vec{q}}\times\frac{1}{\sqrt{\Omega}}\exp(-i\vec{q'}\cdot\vec{r})\equiv\sum_{\vec{q}}c_{i,\vec{q}}\times\left|\vec{q}\right\rangle \qquad \text{(Eq. 8-7)}$$

where W is the volume and $c_{i,\mathbf{q}}$ are the expansion coefficients of the wavefunction is a plane wave basis, where

$$\left\langle\vec{q'}\middle|\vec{q}\right\rangle=\delta_{\vec{q},\vec{q'}} \qquad \text{(Eq. 8-8)}$$

Combining Eq.8-6 and 8-7 gives

$$\sum_{\vec{q}}\widehat{H}_{eff}(\vec{r})\cdot c_{i,\vec{q}}\times\left|\vec{q}\right\rangle \qquad \text{(Eq. 8-9)}$$

If we multiply by $\langle \vec{q}' |$ on the left, we get the Schrödinger equation in Fourier space

$$\sum_{\vec{q}} \langle \vec{q}' | \hat{H}_{eff} | \vec{q} \rangle \cdot c_{i,\vec{q}} = \sum_{\vec{q}} \varepsilon_i \langle \vec{q}' | \vec{q} \rangle \cdot c_{i,\vec{q}} = \varepsilon_i \cdot c_{i,\vec{q}} \quad \text{(Eq.8-10)}$$

Therefore the plane wave basis set allows Fourier space calculations that are straightforward to use in numerical calculations. Plane waves also allow for the wave function to exist in the same configuration in a crystal that has units that repeat.

Pseudopotentials are used in all VASP calculations, since in most cases the core electrons are tightly bound and do not effectively react to valance electron motion. Thus, these electrons can be considered to be at a fixed position [11]. Therefore the core potential is replaced by a pseudopotential, as shown in Figure 8-4, which removes nodes within the core.

8.2f UltraSoft Potentials (USP) and Projector Augmented Wave (PAW) Method

Pseudopotentials are constructed so that the real wavefunction and the pseudo-wavefunctions generate the same charge density outside the core. By achieving this equality, pseudpotentials are said to be norm-conserving. Ultrasoft Potentials have a valence wave function that is not norm-conserving and have smoother (softer) pseudo-wavefunctions that are easier to use in solving for the forces in a system. Projector Augmented Wave (PAW) method is an approach to solving electronic structures. PAW retains the core electron functions, which are

left out of pseudopotentials, and adds them to a smooth summation of the valence wavefunctions [3]. PAW also has easily calculated forces, like USP.

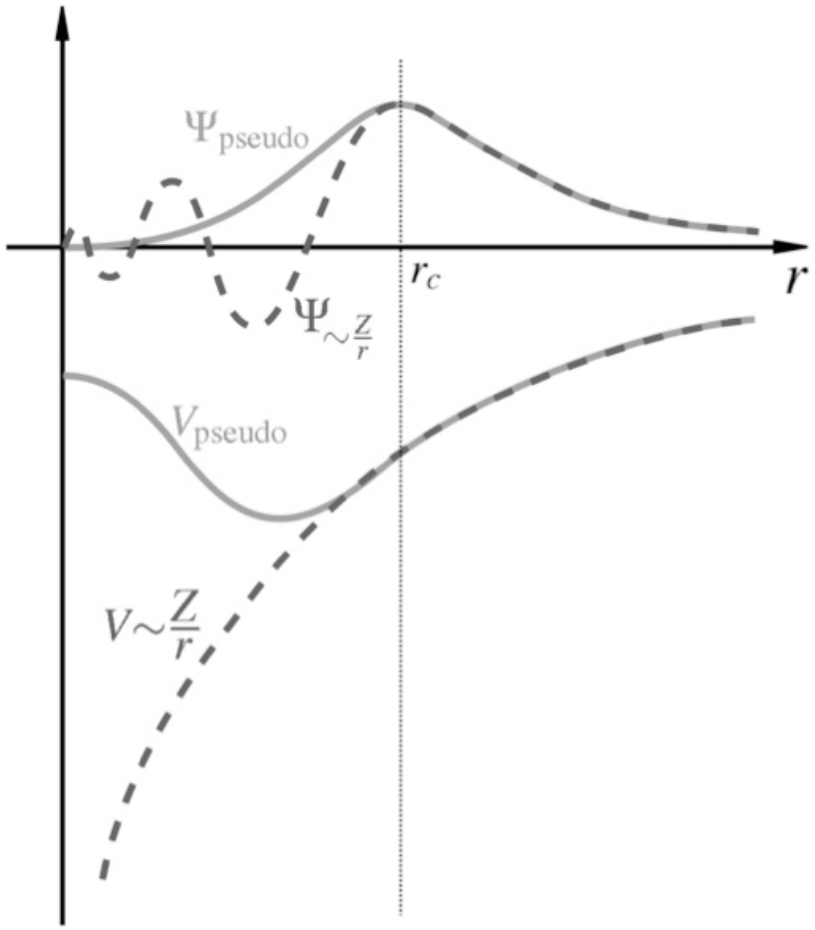

Figure 8-4: A Coulomb potential for a nucleus, in dark gray, is compared to the pseudopotential, in light gray. The real and pseudo wavefunction are shown at the top. Both the pseudo and real wavefunction, as well as the actual potential and pseudopotential match beyond a cutoff radius, r_c [12].

8.2g Local Density Approximation (LDA) and Generalized-Gradient Approximation (GGA)

The Kohn-Sham method, mentioned above, uses an exchange-correlation function of the density, E_{xc} , which incorporates all the many-body terms from the independent particle equations [3]. This is a complex function that can be approximated. The Local Density Approximation (LDA) uses an exchange-correlation function that is based on the exchange-correlation energy. LDA assumes that at each point in the space being considered, that the exchange-correlation density is constant. Each point represents an infinitesimal volume of the region. Integrating over all points in space gives the exchange-correlation energy and therefore the E_{xc}. The Generalized-Gradient Approximation (GGA), seeks to improve the exchange-correlation function by allowing the density in each point to have a gradient to the density inside the volume that it represents. In this way, it can be considered an improvement over LDA.

8.3 Conducting the Simulation

8.3a ASU High Performance Computing Initative's Saguaro Cluster System

The VASP calculations were run on the ASU High Performance Computing Initative's Saguaro cluster system. Saguaro has 4560 processing cores used in parallel computing. Two structures were designed to be relaxed via VASP calculation.

8.3b Configuration of Si(100)- β-cristobalite(110)-Amorphous Silica and Si(100)-Amorphous Silica Structures

The first was a configuration with a Si(100) base with a β-cristobalite(110) and amorphous silica. The Silicon base was two units cells wide, two units cells wide deep, and three unit cells high. The β-cristobalite(110) was two unit cells in all three directions. The amorphous silica was placed above the β-cristobalite(110) and was 10.6Å thick. The CrystalMaker representation of this structure in shown in Figure 8-5. The second model consisted of an identical Si(100) base, but with a 26.4 Å thick amorphous silica on top. This silica thickness was created so that both structure had identical total numbers of silicon and oxygen atoms. This arrangement is shown in Figure 8-6. A comparison of the structures is shown in Figure 8-7.

8.3c Relaxation of Si(100)-β-cristobalite(110)-Amorphous Silica and Si(100)-Amorphous Silica Structures

Both structures were relaxed in VASP using USP with LDA (USP-LDA), USP with GGA (USP-GGA), PAW with LDA (PAW-LDA), and PAW with GGA (PAW-GGA). The initial VASP relaxation runs were done allowing all atoms in the two structures to freely move. When the Si(100) base with β-cristobalite(110) and 10.6Å thick amorphous silica configuration was brought into CrystalMaker after relaxing using PAW-GGA, it was seen that an oxygen atom had migrated into the Si(100) structure., as shown in Figure 8-8. The oxygen atom was located multiple angstroms into the Si(100) portion of the structure and had distorted the

positions of the Si atoms surrounding it. Since these relaxations have no temperature effects, the oxygen atom would not realistically diffuse into the Si surface. It was concluded that these results would not be used to determine how the Si(100) with β-cristobalite(110) and amorphous silica structure would relax and the final energy would not be compared to the energy of the relaxed Si(100) with amorphous silica. To mitigate this from occurring, some of the Si atoms in the Si(100) structure were fixed in their positions at the beginning of the VASP run. Two variations were used. The first fixed the positions of the unit cell of the center layer in the Si(100), while the second fixed the two layers of Si atoms in the Si(100) structure.

Several VASP relaxation runs were completed using the four calculation types and with configurations with fixed Si atoms or all atoms free to move. As a representation of the various calculations, the two structures before and after relaxation of the PAW-GGA with the middle unit cell layer of the Si(100) with fixed positions are shown in figures 8-8 and 8-9.

Figure 8-9 shows the Si(100) base with a β-cristobalite(100) and amorphous silica structure prior to and after using PAW-GGA in VASP to relaxed the formation. There is movement in both the non-fixed position Si(100) atoms and of all atoms in the β-cristobalite(100). The distortions are at the atom positions at the Si(100)- β-cristobalite(100) interface, the β-cristobalite(100) is no longer crystalline, and there is change of the overall structure to a parallelepiped from a rectangular cuboid. The final energy of the relaxed structure is –1842.3 eV.

In Figure 8-10, the Si(100) with amorphous silica shows movement in both the Si(100) atoms which were not in fixed positions and of all of the atoms in the silica, after VASP relaxation using PAW-GGA. The distortions are at the atom positions at the Si(100)-silica interface and the change of the overall structure to a parallelepiped from a rectangular cuboid. The final energy of the relaxed structure is –1838.3 eV, which is higher than that for the Si(100) base with a β-cristobalite(100) and amorphous silica.

Table 8-1 presents the abbreviations used in the energy calculations that are in this section. Although these terms are presented in the text, this brief list will serve as assistance to many readers.

Table 8-2 presents the energies for the two structures with the various calculation types and with fixed or non-fixed Si atoms. The data shows that in a majority of the calculations, the energy of the Si(100) with β-cristobalite(110) and amorphous silica structure is the lower of the two formations. The PAW-LDA run with the middle unit cell of Si(100) fixed shows the energies within 0.5 eV, but with the Si(100) and amorphous silica structure at this slightly lower energy. This data permits the conclusion that on a qualitative basis, the Si(100) with β-cristobalite(110) and amorphous silica structure is the lower energy formation at near room temperatures. This data does not allow for a quantitative calculation of the amount of energy difference, nor does it necessarily hold that this condition exists at higher temperatures.

Finally, there is distortion in the Si(100) lattice that is three unit cells into the bulk. Because both models have the same number of Si and O atoms, they can be compared.

8.3d Calculation of Interfacial Energies in Si(100)-β-cristobalite(110)-Amorphous Silica and Si(100)-Amorphous Silica Structures

For the interfacial energy to be calculated, the energies of both Si(100), β-cristobalite(110) and Amorphous Silica would need to be calculated. By subtracting these energies from the total energy calculated by VASP, the interfacial energy can be determined This requires taking each portion of the structure separately and using PAW-GGA in VASP to calculate the relaxed structure's final energy. Therefore, Si(100) and β-cristobalite(110) were quickly computed. An issue with the total force on Si atoms appeared with the amorphous silica. In relaxed structures, the total force in the three Cartesian directions are below 0.1 eV/Å. The silica calculation would complete and there where total forces on several atoms in the range of 1-3 eV/Å. The first attempt to try to mitigate the high total force was to elongate one of the three axes of the silica by 10%. This would expand the distances of the atoms along one axis so that they may find lower force positions. This did not lead to low total force for any of the axes, nor did expanding all three axes by 10% simultaneously. The final option that was tried included expanding all three axes by 10% concurrently and altering the positions of high force atoms slightly, then running the relaxation calculation again. The expansion would allow the atoms to move to alternate locations, while

the displacement of high force atoms would force VASP to calculate lower force positions. This did not lower the total force on several of the atoms and even increased some forces.

The main issue that is occurring is that while the amorphous silica is a collection of 76 atoms, 49 oxygen and 27 silicon atoms, in a volume that is approximately 11Å by 11Å by 10Å, the calculation repeats this block on atoms in the three orthonormal directions, creating interfaces. Using an analogy to a rectangular block in space, any atom on the $+z$ face is a neighbor to atoms on the $-z$ face that have similar position with respect to x and y. This is the case for +x and –x faces with similar y and z coordinates, as well as the +y and –y faces with similar x and z coordinates. This does not cause an issue in a crystal, since they generally replicate in the three directions, but an amorphous glass does not. The complex nature of the replication would most likely involve two items in attempting to create a silica that would relax in simulations. First, a large number of atoms in the rectangular block, using hundreds of atoms would need to be constructed There would also need to precise placement of the atoms near the edges and faces of the block, creating a quasi-amorphous silica with nearly crystal-like atomic positions near the boundaries. This simulation would need to be a separate experiment with tens of thousands, or more, hours of computing processing.

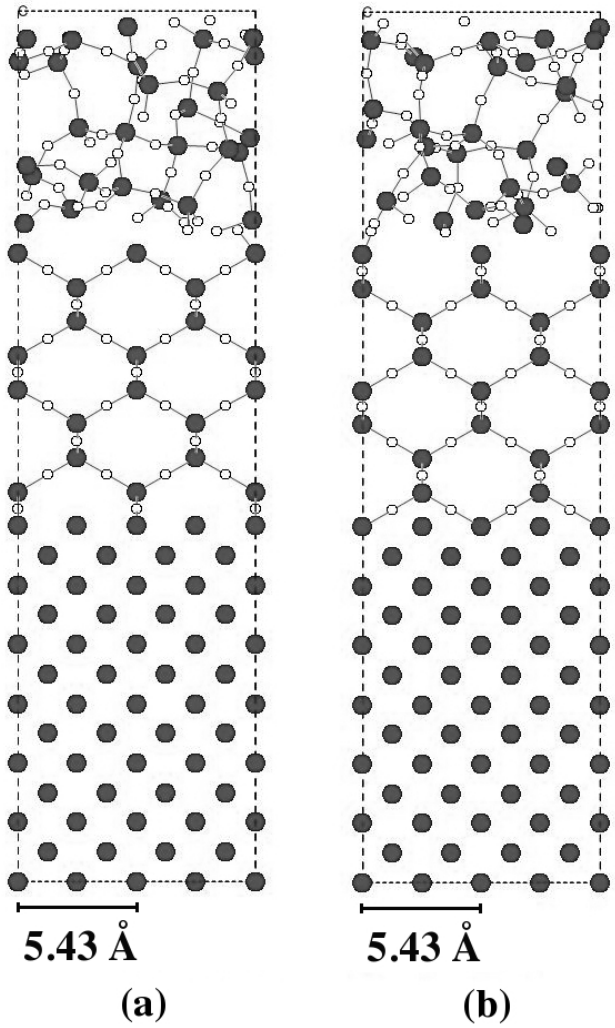

Figure 8-5: CrystalMaker model of the structures for: (a) Si(100) base (two units cells wide, two units cells wide deep, and 3 unit cells high) with a β-cristobalite(110) (two unit cells in all three directions) and 10.6Å thick amorphous silica (b) the same crystal rotated 90º about the vertical axis. The dotted line represents that edge of the cell in VASP. The Si atoms are in dark gray and the oxygen atoms are white.

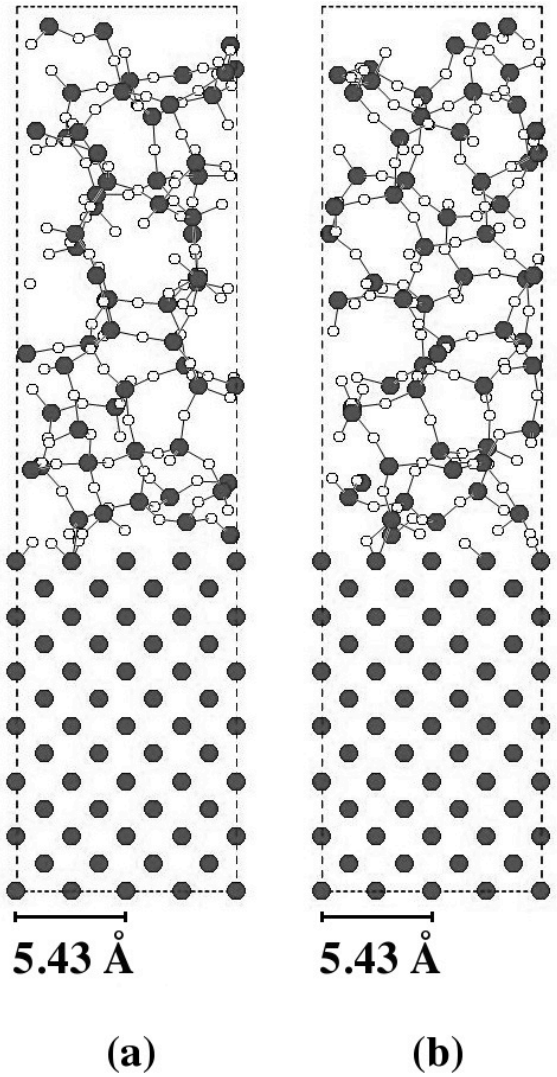

Figure 8-6: CrystalMaker model of the structures for: (a) Si(100) base (two units cells wide, two units cells wide deep, and three unit cells high) with a 26.4 Å thick amorphous silica on top (b) the same crystal rotated 90º about the vertical axis. The dotted line represents that edge of the cell in VASP. The Si atoms are in dark gray and the oxygen atoms are white.

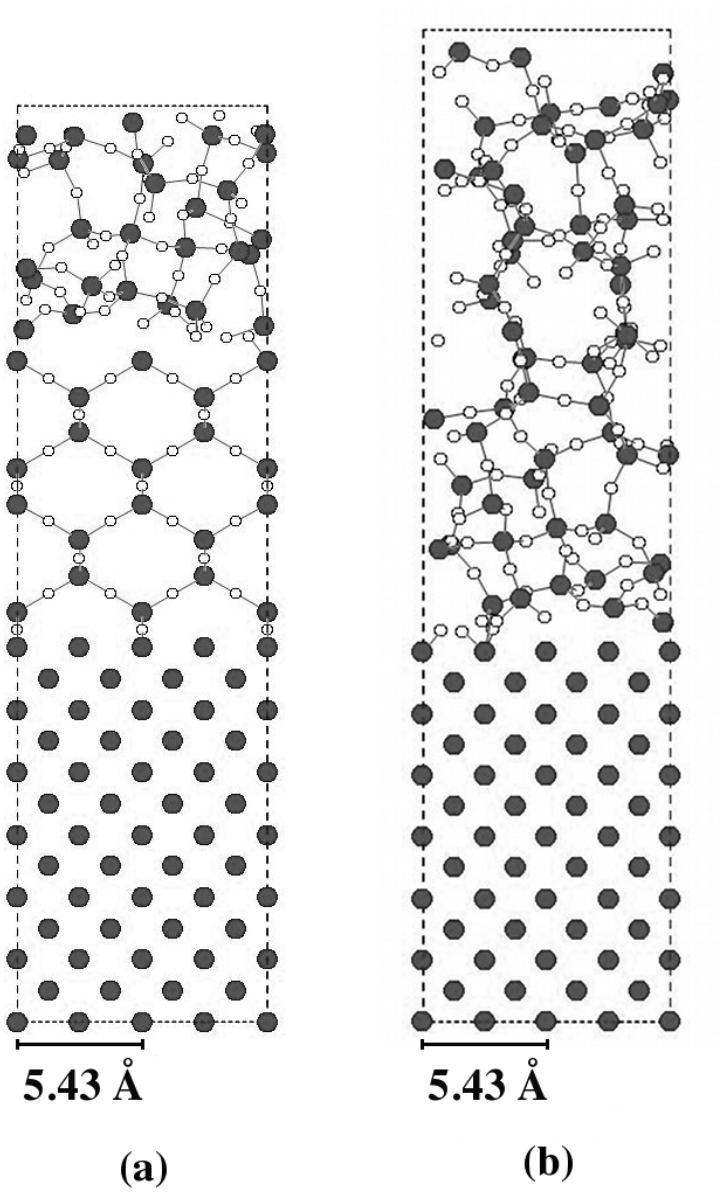

Figure 8-7: CrystalMaker model comparing the structures of: (a) Si(100) base (two units cells wide, two units cells wide deep, and three unit cells high) with a β-cristobalite(110) (two unit cells in all three directions) and 10.6Å thick amorphous silica (b) an identical Si(100) base with a 26.4 Å thick amorphous silica on top. The dotted line represents that edge of the cell in VASP. The Si atoms are in dark gray and the oxygen atoms are white.

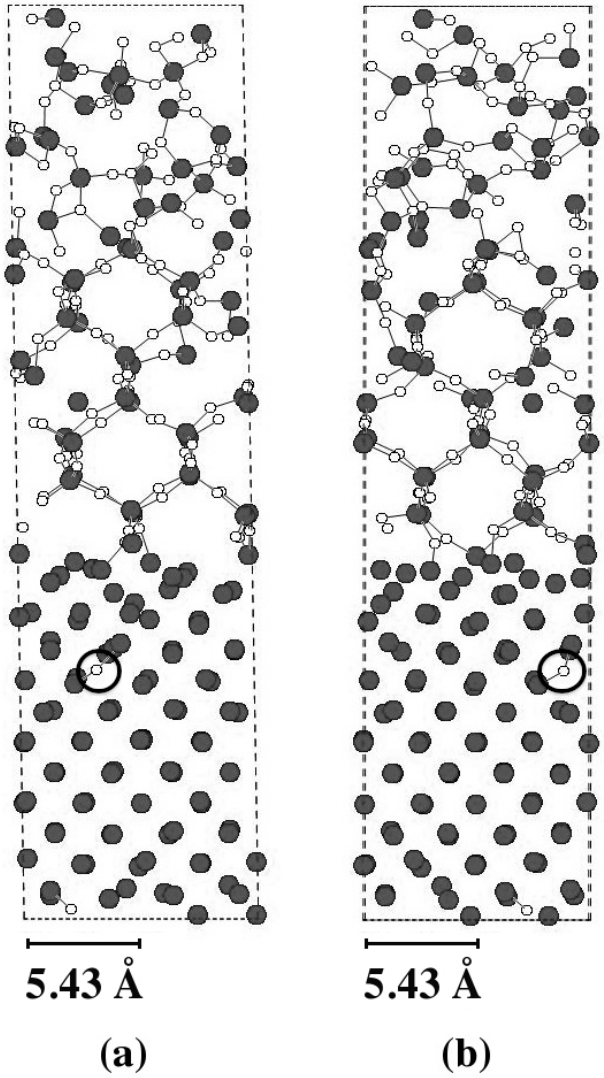

Figure 8-8: CrystalMaker model of the structures for: (a) Si(100) base (two units cells wide, two units cells wide deep, and three unit cells high) with a β-cristobalite(110) (two unit cells in all three directions) and 10.6Å thick amorphous silica after using PAW-GGA in VASP to relaxed the structure. (b) the same crystal rotated 90º about the vertical axis. A white circle encompasses a oxygen atom which has migrated into the Si(100) crystal, distorting the structure. Therefore, the data from this structure is not valid. The dotted line represents that edge of the cell in VASP. The Si atoms are in dark gray and the oxygen atoms are white.

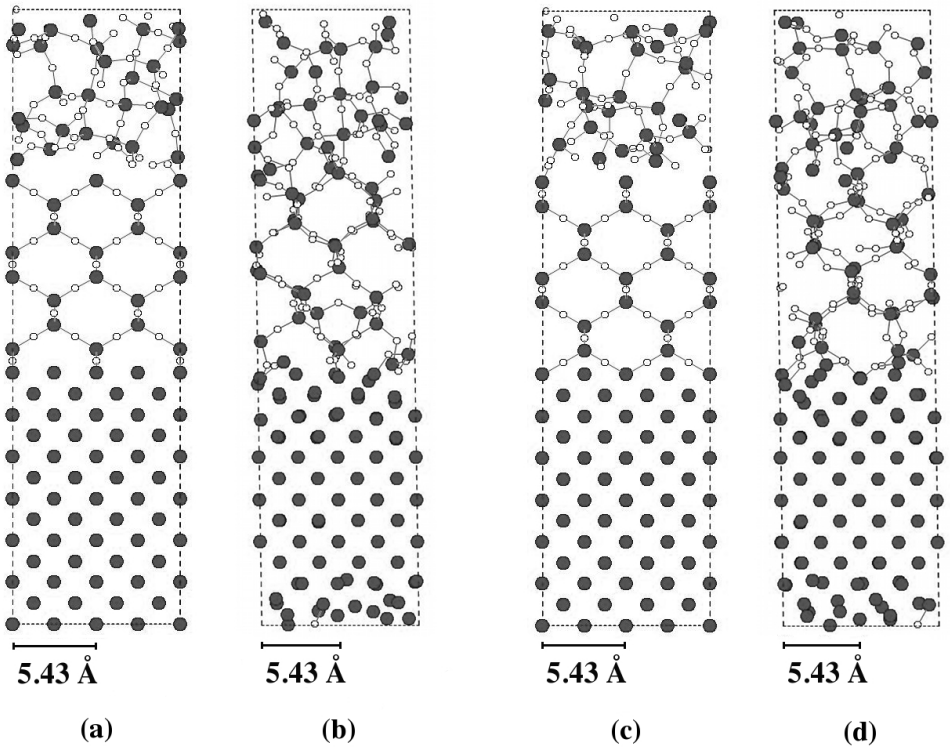

Figure 8-9: CrystalMaker model of (a) Si(100) base with a β-cristobalite(100) and 10.6Å thick amorphous silica; (b) the structure after using PAW-GGA in VASP to relaxed the structure; (c) is the (a) structure rotated 90º about the vertical axis; (d) is the (b) structure rotated 90º about the vertical axis . The middle unit cell layer of the Si(100) crystal was held in a fixed position in this simulation. There is movement in both the non-fixed position Si(100) atoms and of all atoms in the β-cristobalite(100). The obvious distortions are at the atom positions at the Si(100)-β-cristobalite(100) interface, the β-cristobalite(100) is no longer crystalline, and there is change of the overall structure to a parallelepiped from a rectangular cuboid. The Si atoms are in dark gray and the oxygen atoms are white.

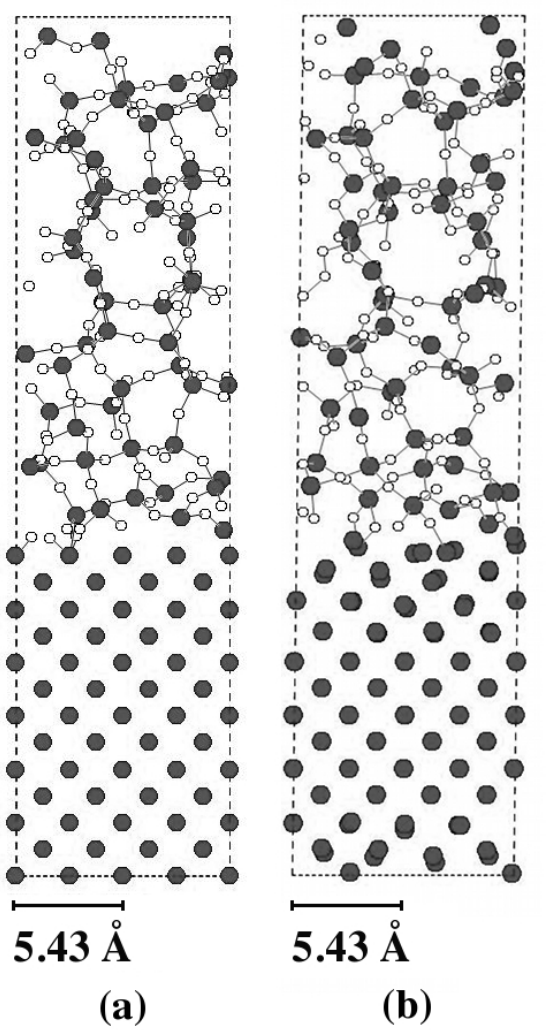

Figure 8-10: CrystalMaker model of: (a) the Si(100) base with a 26.4 Å thick amorphous silica (b) the structure after using PAW-GGA in VASP to relaxed the structure. The middle unit cell layer of the Si(100) crystal was held in a fixed position in this simulation. There is movement in both the non-fixed position Si(100) atoms and of all atoms in the silica. The obvious distortions are at the atom positions at the Si(100)-silica interface and the slight change of the overall structure to a parallelepiped from a rectangular cuboid. The Si atoms are in dark gray and the oxygen atoms are white.

Abbreviation	
LDA	Local Density Approximation
GGA	Generalized-Gradient Approximation
USP	UltraSoft Potentials
PAW	Projector Augmented Wave

Table 8-1: List of Abbreviations used in the calculation types

Electronic Approximation and Atomic Potential used in Calculation	Number of Fixed Atoms in Si(100) "substrate"	Layered Nano-Bonding Phase Cell Type	Final Total Energy (eV)	Energy Difference between the Si(100)/a-SiO2 and Si(100)/ β-c SiO2/a-SiO_2 (eV)
USP-LDA	No Fixed Atoms	Si(100)/β-c SiO2/a-SiO_2	-2030.12	-2.40
USP-LDA	No Fixed Atoms	Si(100)/ a-SiO_2	-2027.72	
USP-LDA	1 Unit Cell Fixed	Si(100)/β-c SiO2/a-SiO_2	-2013.48	-6.44
USP-LDA	1 Unit Cell Fixed	Si(100))/a-SiO_2	-2007.04	
USP-LDA	2 Layers Fixed	Si(100)/β-c SiO2/a-SiO_2	-2014.88	-3.89
USP-LDA	2 Layers Fixed	Si(100)/ a-SiO_2	-2010.99	
PAW-LDA	No Fixed Atoms	Si(100)/β-c SiO2/a-SiO_2	-2037.32	-2.82
PAW-LDA	No Fixed Atoms	Si(100)/a-SiO_2	-2034.50	
PAW-LDA	1 Unit Cell Fixed	Si(100)/β-c SiO2/a-SiO_2	-2015.74	0.42
PAW-LDA	1 Unit Cell Fixed	Si(100)/a-SiO_2	-2016.16	
PAW-GGA	1 Unit Cell Fixed	Si(100)/β-c SiO2/a-SiO_2	-1842.33	-4.03
PAW-GGA	1 Unit Cell Fixed	Si(100)/a-SiO_2	-1838.30	
USP-GGA	No Fixed Atoms	Si(100)/β-c SiO2/a-SiO_2	-1808.750	**Migrating Oxygen**
USP-GGA	No Fixed Atoms	Si(100)/a-SiO_2	-1847.695	
USP-GGA	1 Unit Cell Fixed	Si(100)/β-c SiO2/a-SiO_2	-1836.47	-3.34
USP-GGA	1 Unit Cell Fixed	Si(100)/a-SiO_2	-1833.13	

Table 8-2: The data from the VASP relaxation runs. It shows that in a majority of the calculations, the energy of the Si(100) with β-cristobalite(110) and amorphous silica structure is the lower of the two formations.

8.4 Multi-slice for Transmission Electron Microscopy (TEM) Simulation

To simulate a structure undergoing Transmission Electron Microscopy (TEM), a calculation technique termed multi-slice was developed. This computation entails taking the formation that will undergo TEM simulation and slicing it into multiple layers, or slices. Then an electron wavefunction impinges upon the first slice and is transmitted through this slice. The outgoing wavefunction then propagates to the next slice, where this process is repeated until the wavefunction has been transmitted through the final slice. This is a general overview of the computation.

To understand the physics of the multi-slice calculation, we will first look at the time-independent Schrödinger equation in *x, y*,and *z* for the full wave function in an electrostatic potential *V(x,y,z)* [13]:

$$\left[-\frac{\hbar^2}{2m}\nabla^2 - eV(x,y,z)\right]\psi_{full}(x,y,z) = E\psi_{full}(x,y,z) \qquad \text{(Eq. 8-11)}$$

where $m=\gamma m_0$ and *e* is the charge of an electron. If we let the electron move predominately in the z directions, the full wavefunction can be written as two factor, a $\psi(x,y,z)$ that varies slowly with z position and a plane wave traveling in z.

$$\psi_{full}(x,y,z) = \psi(x,y,z)\exp\left(\frac{2\pi i z}{\lambda}\right) \qquad \text{(Eq. 8-12)}$$

The ∇^2 of the wavefunction. This requires taking the first and second derivatives of the full wavefunction with respect to *z* and allowing the *x* and *y* portions of the Laplacian to remain as an operator, then [13]:

$$\nabla^2 \psi_{full}(x,y,z) = \left[\nabla_{xy}^2 + \frac{\partial^2}{\partial z^2} \right] \psi_{full}(x,y,z) \qquad \text{(Eq. 8-13)}$$

which simplifies to:

$$\nabla^2 \psi_{full}(x,y,z) = \exp\left(\frac{2\pi i z}{\lambda} \right) \left[\nabla_{xy}^2 + \frac{\partial^2}{\partial z^2} + \frac{4\pi i}{\lambda} \frac{\partial}{\partial z} \right] \psi(x,y,z) - \frac{4\pi^2}{\lambda^2} \psi_{full}(x,y,z) \qquad \text{(Eq. 8-14)}$$

Since:

$$E = \frac{4\pi^2 \hbar^2}{2m\lambda^2} \qquad \text{(Eq. 8-15)}$$

when Eq.8-14 is substituted into Eq.8-11, the energy on the right side cancel out the last term of Eq. 8-14 and the following is obtained:

$$-\frac{\hbar^2}{2m} \left\{ \exp\left(\frac{2\pi i z}{\lambda} \right) \left[\nabla_{xy}^2 + \frac{\partial^2}{\partial z^2} + \frac{4\pi i}{\lambda} \frac{\partial}{\partial z} \right] \psi(x,y,z) \right\} - eV(x,y,z) \left[\exp\left(\frac{2\pi i z}{\lambda} \right) \psi(x,y,z) \right] = 0 \qquad \text{(Eq. 8-16)}$$

Dividing by $\exp(2\pi i z/\lambda)$ and simplifying, the following is obtained:

$$-\frac{\hbar^2}{2m} \left[\nabla_{xy}^2 + \frac{\partial^2}{\partial z^2} + \frac{4\pi i}{\lambda} \frac{\partial}{\partial z} + \frac{2meV(x,y,z)}{\hbar^2} \right] \psi(x,y,z) = 0 \qquad \text{(Eq. 8-17)}$$

Since the electrons are moving in the z direction, y changes slowly with z [13]. Also, the wavelength of the electron, λ, is small, so:

$$\left| \frac{\partial^2 \psi}{\partial z^2} \right| << \left| \frac{1}{\lambda} \frac{\partial \psi}{\partial z} \right| \qquad \text{(Eq. 8-18)}$$

so Eq. 8-17 reduces to

$$-\frac{\hbar^2}{2m}\left[\nabla_{xy}^2+\frac{4\pi i}{\lambda}\frac{\partial}{\partial z}+\frac{2meV(x,y,z)}{\hbar^2}\right]\psi(x,y,z)=0 \qquad \text{(Eq. 8-19)}$$

This may be re-written as a first order differential equation [13]:

$$\frac{\partial\psi(x,y,z)}{\partial z}=\left[\frac{i\lambda}{4\pi}\nabla_{xy}^2+\frac{2mei\lambda V(x,y,z)}{4\pi\hbar^2}\right]\psi(x,y,z) \qquad \text{(Eq. 8-20)}$$

Letting

$$\sigma=\frac{2mei\lambda}{4\pi\hbar^2} \qquad \text{(Eq. 8-21)}$$

then Eq. 8-20 becomes

$$\frac{\partial\psi(x,y,z)}{\partial z}=\left[\frac{i\lambda}{4\pi}\nabla_{xy}^2+\sigma V(x,y,z)\right]\psi(x,y,z) \qquad \text{(Eq. 8-22)}$$

If *A* and *B* are non-commuting operators, then Eq.8-22 can be written as [13]:

$$\frac{\partial\psi(x,y,z)}{\partial z}=[A+B]\psi(x,y,z) \qquad \text{(Eq.8-23)}$$

Eq.8-23 has a solution of:

$$\psi(x,y,z)=\exp\left[\int_0^z[A(z')+B(z')]dz'\right]\psi(x,y,0) \qquad \text{(Eq. 8-24)}$$

If we let the difference between zero and *z* be *Δz*, then we can let the lower limit be *z* and the upper limit be *z+Δz*. This gives [13]:

$$\psi(x,y,z+\Delta z)=\exp\left[\int_z^{z+\Delta z}[A(z')+B(z')]dz'\right]\psi(x,y,z) \qquad \text{(Eq. 8-25)}$$

Replacing the A and B operators with their operations [13]:

$$\psi(x,y,z+\Delta z)=\exp\left[\int_{z}^{z+\Delta z}\left[\frac{i\lambda}{4\pi}\nabla_{xy}^{2}+\sigma V(x,y,z')\right]dz'\right]\psi(x,y,z) \quad \text{(Eq. 8-26)}$$

Part of the point of this derivation is to create multiple sections, or slices, a sample so that one can look at the electron wavefunction as it travel through the sample. By defining Δz as a small slice and setting the projected potential between z and $z+\Delta z$ as $v_{\Delta z}$, we obtain [13]:

$$\psi(x,y,z+\Delta z)=\exp\left[\frac{i\lambda}{4\pi}\Delta z\nabla_{xy}^{2}+i\sigma v_{\Delta z}(x,y,z')\right]\psi(x,y,z) \quad \text{(Eq. 8-27)}$$

This has the form of:

$$\psi(x,y,z+\Delta z)=\exp\left[A\Delta z+B\Delta z\right]\psi(x,y,z) \quad \text{(Eq. 8-28)}$$

The exponential can be simplified as [13]

$$\exp\left[A\Delta z+B\Delta z\right]=\exp(A\Delta z)\exp(B\Delta z)+\frac{1}{2}\left[B,A\right](\Delta z)^{2}+\mathrm{O}\left[(\Delta z)^{3}\right] \quad \text{(Eq. 8-29)}$$

Placing Eq. 8-29 into Eq. 8-27, it simplifies to [13]:

$$\psi(x,y,z+\Delta z)=\exp\left(\frac{i\lambda}{4\pi}\Delta z\nabla_{xy}^{2}\right)\exp\left[i\sigma v_{\Delta z}(x,y,z)\right]\psi(x,y,z)+\mathrm{O}\left[(\Delta z)^{2}\right] \quad \text{(Eq. 8-30)}$$

If we let

$$t(x,y,z)=\exp\left[i\sigma v_{\Delta z}(x,y,z)\right] \quad \text{(Eq. 8-31)}$$

Then Eq. 8-30 becomes

$$\psi(x,y,z+\Delta z)=\exp\left(\frac{i\lambda}{4\pi}\Delta z\nabla_{xy}^{2}\right)t(x,y,z)\psi(x,y,z)+\mathrm{O}\left[(\Delta z)^{2}\right] \quad \text{(Eq. 8-32)}$$

$t(x,y,z)$ is the transmission function in the specimen slice between z and Δz [13].

Now we want to look at the right hand side of Eq. 8-32 and ignore the function that is to the second power in Δz. The way to evaluate this portion of the equation is to use transform to allow the equation to be evaluated. We will use the Fourier transform to go from *x*,*y*,*z*-space to *k*-space [13].

$$\iint \exp\left(\frac{i\lambda}{4\pi}\Delta z\nabla_{xy}^2\right)t(x,y,z)\psi(x,y,z)\exp\left(2\pi i(k_x x+k_y y)\right)dxdy =$$

$$\iint\left[\exp\left(\frac{i\lambda}{4\pi}\Delta z\frac{\partial^2}{\partial x^2}\right)\exp\left(\frac{i\lambda}{4\pi}\Delta z\frac{\partial^2}{\partial y^2}\right)\right]t(x,y,z)\psi(x,y,z)\times \quad \text{(Eq. 8-33)}$$

$$\exp\left(2\pi i(k_x x+k_y y)\right)dxdy$$

Now the exponential can be power series expanded using

$$\exp\left(\alpha\frac{\partial^2}{\partial\beta^2}\right)=\sum_{n=0}^{\infty}\frac{1}{n!}\left(\alpha\frac{\partial^2}{\partial\beta^2}\right)^n \quad \text{(Eq. 8-34)}$$

So Eq.8-33 becomes [13]:

$$\iint\sum_{n=0}^{\infty}\frac{1}{n!}\left(\frac{i\lambda}{4\pi}\Delta z\frac{\partial^2}{\partial x^2}\right)^n\sum_{n=0}^{\infty}\frac{1}{n!}\left(\frac{i\lambda}{4\pi}\Delta z\frac{\partial^2}{\partial y^2}\right)^n t(x,y,z)\psi(x,y,z)\times \quad \text{(Eq. 8-35)}$$

$$\exp\left(2\pi i(k_x x+k_y y)\right)dxdy$$

Now, by integrating by parts and $t(x,y,z)y(x,y,z)$ goes to zero at infinity or obeys periodic boundary conditions [13], Eq.8-35 simplifies to:

$$\sum_{n=0}^{\infty}\frac{1}{n!}\left(-i\pi\lambda\Delta z k_x^2\right)^n\sum_{n=0}^{\infty}\frac{1}{n!}\left(-i\pi\lambda\Delta z k_y^2\right)^n\times \quad \text{(Eq.8-36)}$$

$$\iint t(x,y,z)\psi(x,y,z)\exp\left(2\pi i(k_x x+k_y y)\right)dxdy$$

Since, the second portion of equation 8-36 is a Fourier transform (FT)

$$\iint t(x,y,z)\psi(x,y,z)\exp\left(2\pi i(k_x x + k_y y)\right)dxdy = FT\left[t(x,y,z)\psi(x,y,z)\right] \quad \text{(Eq. 8-37)}$$

So Eq.8-36 simplifies to [13]:

$$\exp\left[-i\pi\lambda\Delta x(k_x^2 + k_y^2)\right]FT\left[t(x,y,z)\psi(x,y,z)\right] = P(k,\Delta z)FT\left[t(x,y,z)\psi(x,y,z)\right] \quad \text{(Eq. 8-38)}$$

where $P(k,\Delta z)$ is the propagator function and $k^2=k_x^2+k_y^2$. The multiplication is Fourier space is a convolution operation in real space. So the operator becomes [13]:

$$\exp\left(\frac{i\lambda}{4\pi}\Delta z\nabla_{xy}^2\right) = p(x,y)\otimes \quad \text{(Eq. 8-39)}$$

and Eq.8-32 becomes

$$\psi(x,y,z+\Delta z) = p(x,y)\otimes t(x,y,z)\psi(x,y,z) + \mathrm{O}\left[(\Delta z)^2\right] \quad \text{(Eq. 8-40)}$$

This is one way of obtaining the result in Eq.8-40. Cowley and Moodie [14] obtained the same result by slicing a specimen into many thin slices and using a physical optics viewpoint. The propagator function was linked to the Fresnel diffraction over Dz and the transmission function was seen as the phase grating approximation of a thin layer between z and $z+\Delta z$. The wavefunction would hit the specimen face at $z=0$ and be transmitted through the slices and propagate in the vacuum between slices.

To use numerical computation to carry out multi-slice calculations, we want to look at the Eq.8-40 at various slices. If we let $n=0,1,2,3\ldots$, the the wavefunction $y_n(x,y)$ approaches a slice, is transmitted, $t_n(x,y)$, and propagated, $p_n(x,y,\Delta z)$, such that [13]

$$\psi_{n+1}(x,y) = p_n(x,y,\Delta z_n) \otimes t_n(x,y)\psi_n(x,y) + \mathrm{O}\left[(\Delta z)^2\right] \quad \text{(Eq. 8-41)}$$

This can calculated using fast Fourier transforms (FFT), as first shown by Ishizuka and Uyeda [15]. Since convolution can be represented by Fourier transforms and inverse Fourier transforms (FT^{-1})

$$g(x,y) \otimes h(x,y) = FT^{-1}\left\{FT\left[G(k_x,k_y)\right]FT\left[H(k_x,k_y)\right]\right\} \quad \text{(Eq. 8-42)}$$

So, Eq.8-32 becomes:

$$\psi_{n+1}(x,y) = FT^{-1}\left\{P_n(k_x,k_y,\Delta z_n)FT\left[t_n(x,y)\psi_n(x,y)\right]\right\} + \mathrm{O}\left[(\Delta z)^2\right] \quad \text{(Eq. 8-43)}$$

This means that the multi-slice solution can be calculated using FT, inverse FT, the wavefunction, the transmission function and the propagation function. Since FFT can be substituted for the FT, as can the inverse function, this calculation can be carried out quickly using computation by a computer.

8.5 High Resolution Transmission Electron Microscopy (HRTEM) Simulation

8.5a High Resolution Electron Microscopy image simulation programs (xHREM)

xHREM is a collection of simulation programs that was developed based on the High Resolution Electron Microscopy (HREM) image simulation programs that use FFT multi-slice technique and wave-optics developed by Ishizuka [15 - 18]. One portion of xHREM was developed to simulate High Resolution Transmission Electron Microscopy (HRTEM) images.

The first step in performing HRTEM simulation was to take the crystal structure from the VASP simulations and manipulate it so that one face of crystal aligns with the (110) direction of the Si(100). This is done because the HRTEM

scans of the Si(100) surfaces after H-A cleaning and oxidation were imaged using the (110) orientation, as was shown in Chapter 3 in figure 3-4, 3-5, and 3-6. Many of the relaxed crystals are similar in nature, therefore the Si(100) with a β-cristobalite(100) and 10.6Å thick amorphous silica relaxed using PAW-GGA in VASP would be used in the TEM simulations. Using the coordinates of the structure relaxed using PAW-GGA in VASP, the crystal was rotated by 45º about the central vertical axis. The CrystalMaker image is shown in figure 8-11. The Si(100) structure that was held in fixed positions, which occurs one unit cell from the bottom of the structure, clear shows the Si(110) atomic orientation.

Since the simulation would be compared to the HRTEM data seen in Figures 3-4 through 3-6, the same energy and conditions would be necessary. The data from the H-A clean samples had been taken at 400 keV. To calculate the wavelength of the electron, the total energy is needed (Eq. 8-44)

$$E_{Total}^2 = (m_0c^2 + eV)^2 = p^2c^2 + m_0^2c^4 \qquad \text{(Eq. 8-44)}$$

where m_0 is the rest mass of the electron, c is the speed of light in a vacuum, p is the momentum of the electron, e is the charge of an electron, and V is the potential that the electron is accelerated through [13].

Since the de-Broglie wavelength λ of an electron is:

$$\lambda = h / p \qquad \text{(Eq. 8-45)}$$

where h is Planck's constant.

Substituting Eq. 8-45 into Eq. 8-44,

$$(m_0c^2 + eV)^2 = \frac{h^2c^2}{\lambda^2} + m_0^2c^4 \qquad \text{(Eq.8-46)}$$

which simplifies to:

$$\lambda = \frac{hc}{\sqrt{(m_0c^2 + eV)^2 - m_0^2c^4}} \quad \text{(Eq. 8-47)}$$

where m_0c^2 = 511 keV and hc= 12.398 keV-Å. Therefore at 400 keV, the electrons in the beam will have a wavelength of 0.0164Å.

The H-A cleaned samples had HRTEM data taken at the Scherzer focus, which is defined as [13]:

$$\Delta f_{Scherzer} = 1.22\sqrt{C_s\lambda} \quad \text{(Eq. 8-48)}$$

Using the wavelength of the 400 keV electrons and the C_s, the spherical aberration, of the HRTEM, which was 1mm, a $\Delta f_{Scherzer}$ of 486 Å is obtained.

8.5b Simulation Data from xHREM

To more fully understand the data from xHREM, the data for a Si(110) crystals was inputted into the simulation program. Both a single cell of Si(110) and a larger two unit cells by two unit cells of Si(110) were simulated. The Si(110) single unit cell was divided into four slices, which yields a thickness of 1.902 Å per slice. The larger crystal structure was cut into 8 slices, which gave the same 1.902 Å per slice. The data was obtained using a 400 keV beam energy with a 486 Å focus, as is all data in this section.

The xHREM software produced a simulated the intensity of the diffracted beams versus slice for both Si(110) crystals at (000) and (111). Since 200 slices were requested, which is more than either initial structure contained, the program replicates the structure over and over in the three Cartesian coordinate directions.

The data was transformed into intensity versus depth in Ångstroms by multiplying the number of slices by 1.902 Å and is shown in Figure 8-12. The data show that the diffracted beam intensity at (000) and (111) for the Si(110) crystal oscillates over 142.65 Å. The intensity oscillation leads to an inversion of contrast in the image

The Si(100) base with a β-cristobalite(100) and amorphous silica structure which was relaxed using PAW-GGA in VASP is used as a representative of all relaxed structure of this type, This assembly has a 2 unit cells by 2 unit cells of Si(100) in fixed positions in the middle layer of the Si(100) base. Therefore, when the structure is rotated to the (110) direction for xHREM simulation, the data in Figure 8-12 should closely correspond to the fixed Si(100) unit cells and this portion of the structure should reverse contrast over approximately 140 Å difference in depth.

The positions of all atoms of PAW-GGA relaxed structure rotated to the (110) direction were entered into xHREM. This structure is slightly wider than a two unit cells by two unit cells of Si(110), so while it was divided into eight slices, each slice was 1.92 Å. Figure 8-13 presents the CrystalMaker model of the PAW-GGA relaxed structure and the simulated images at depths of 38.1 Å, 70.4 Å, 108.5 Å. Figure 8-14 presents the same CrystalMaker model with the simulated images at 142.7 Å, 180.8 Å, 213.1 Å. Finally, Figure 8-54 shows the CrystalMaker model and the simulated images at depths of 285.5 Å, and 353.9 Å.

The data shows a strong, discernable pattern at smaller depths, but the images becomes less delineated at greater depths. This implies that the simulation images are only applicable for very thin samples of this structure. The change in intensity in the PAW-GGA relaxed structure also makes it difficult to detect a contrast reversal in the fixed Si atoms portion between the 38.1 Å and the 180.8 Å simulated images, even though they have a 142 Å depth difference. Therefore, no conclusions can be made about the TEM simulation data.

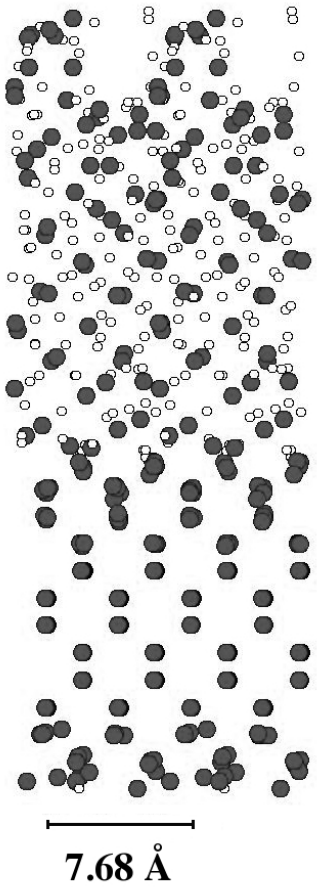

Figure 8-11: The (110) orientation of a CrystalMaker model of Si(100) base with a β-cristobalite(100) and 10.6Å thick amorphous silica, after using PAW-GGA in VASP to relaxed the structure. The middle unit cell layer of the Si(100) crystal was held in a fixed position in this simulation. The Si atoms are in dark gray and the oxygen atoms are white.

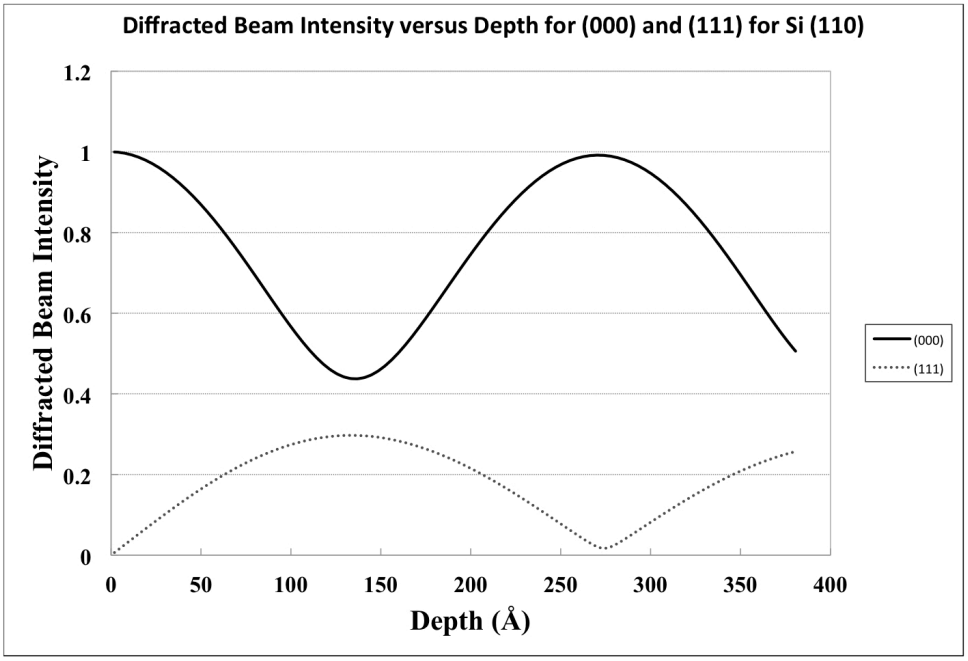

Figure 8-12: The data produced from xHREM software of a simulated the diffracted beam intensity versus depth for Si(110) crystals for the (000) and (111). This data show that the intensity for both for the Si(110) crystal inverts over 143 Å.

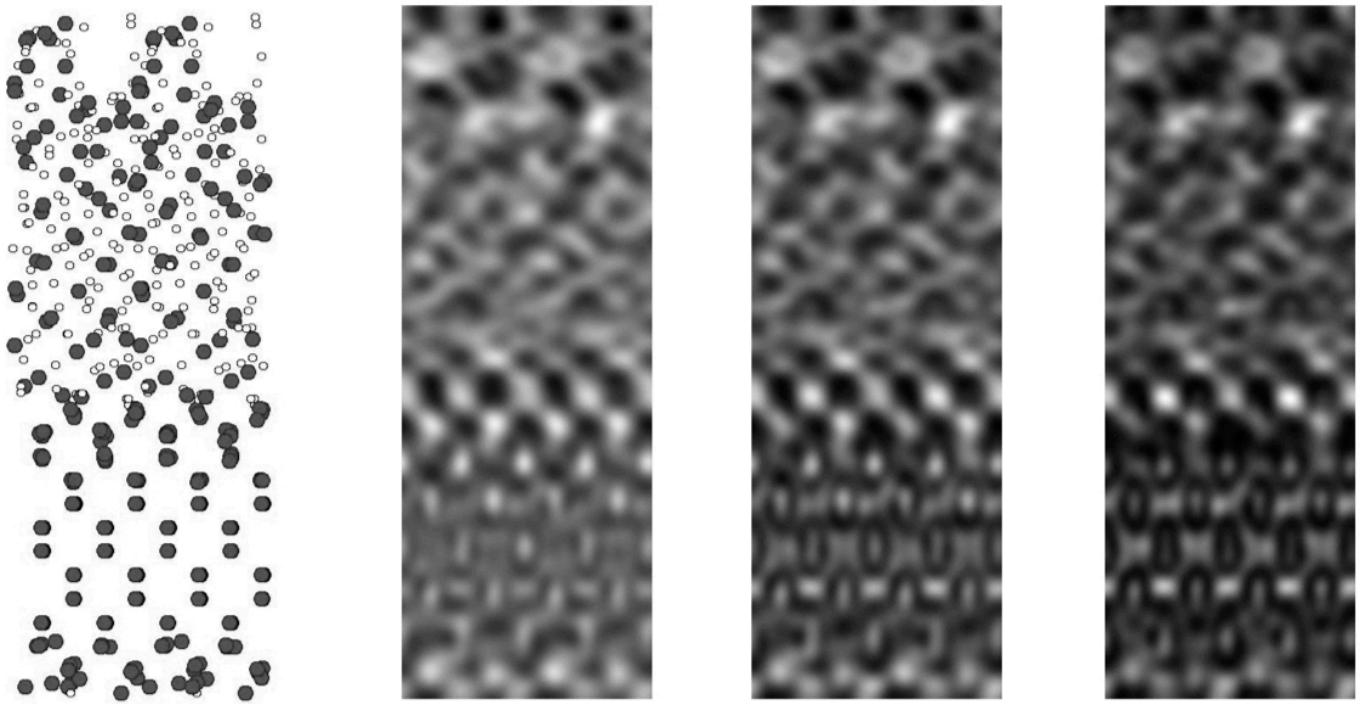

Figure 8-13: The images of: (a) the CrystalMaker model of Si(100) base with a β-cristobalite(100) and 10.6Å thick amorphous silica, after using PAW-GGA in VASP to relaxed the structure the PAW-GGA rotated to the (110) direction; (b) the xHREM produced simulated images at depths of 38.1 Å; (c) 70.4 Å; (d) 108.5 Å.

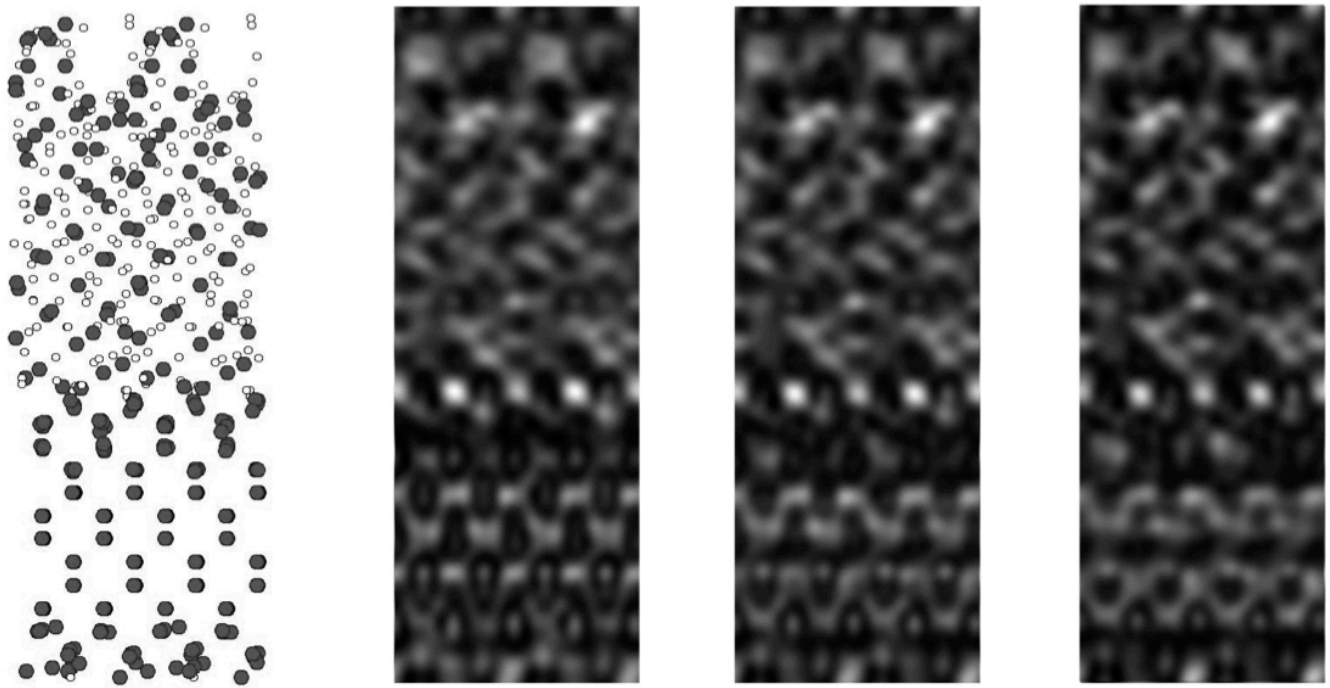

Figure 8-14: The images of: (a) the CrystalMaker model of Si(100) base with a β-cristobalite(100) and 10.6Å thick amorphous silica, after using PAW-GGA in VASP to relaxed the structure the PAW-GGA rotated to the (110) direction; (b) the xHREM produced simulated images at depths of 142.7 Å; (c) 180.8 Å; (d) 213.1 Å.

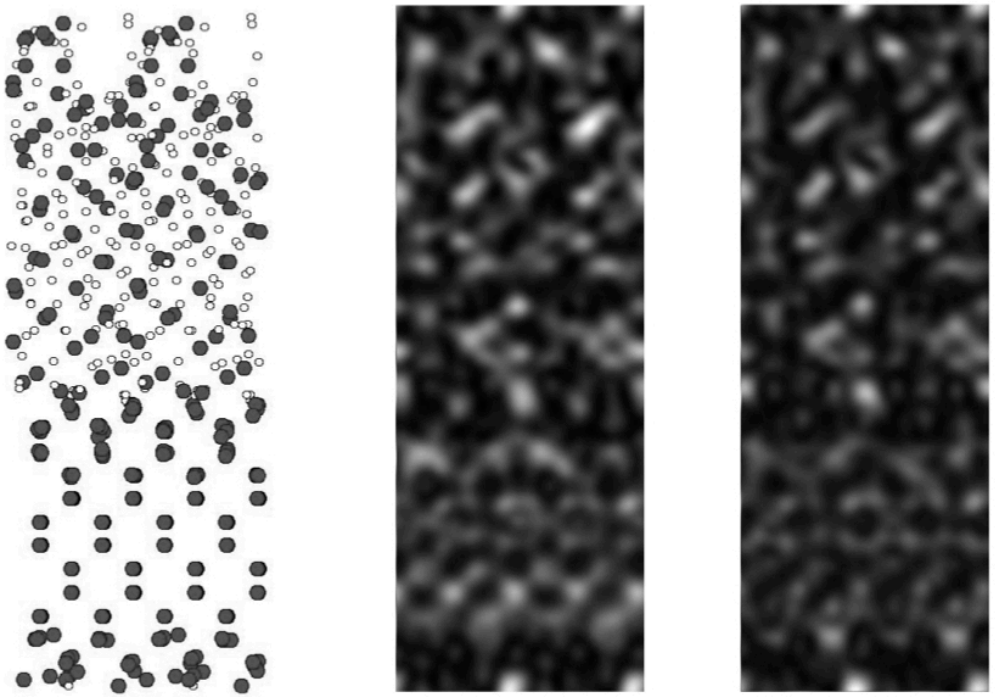

Figure 8-15: The images of: (a) the CrystalMaker model of Si(100) base with a β-cristobalite(100) and 10.6Å thick amorphous silica, after using PAW-GGA in VASP to relaxed the structure the PAW-GGA rotated to the (110) direction; (b) the xHREM produced simulated images at depths of (b) 285.5 Å; (c) 353.9 Å

Chapter 8 References

[1] J.D. Bradley, *A new heteroepitaxial silicon dioxide nanophase on OH-(1X1) silicon (100) identified via 3.05 MEV ion channeling and the new 3-D multistring code*, Arizona State University, Ph. D. Thesis 2006

[2] G. Kresse, J. Furthmiiller, *Comput. Mater. Sci*. **6**, 1, 15-50 (1996)

[3] R. M. Martin, *Electronic Structure: Basic Theory and Practical Methods*, Cambridge University Press (2004)

[4] L.H. Thomas, *Proc. Camb. Phil. Soc*. **23**, 542-548 (1927)

[5] E. Fermi, *Rend. Accad. Naz. Lincei* **6**, 602–607 (1927)

[6] Dirac, P. A. M, *Proc. Cambridge Philos. Soc*. **26**, 376-385 (1930)

[7] W. Kohn , L. J. Sham, *Phys. Rev*. **140**, A1133–A1138 (1965)

[8] G. Kresse, J. Furthmiiller, *Phys. Rev. B* **54**, 11169–11186 (1996)

[9] R. P. Feynman, *Phys. Rev*. **56**, 340–343 (1939)

[10] R. Car, M. Parrinello, *Phys. Rev. Lett*. **55**, 2471–2474 (1985)

[11] D J Singh, *Planewaves, pseudopotentials, and the LAPW method*, Kluwer Academic Publishers (1994)

[12] http://en.wikipedia.org/wiki/Pseudopotential, Oct. 21, 2010. Public Domain image

[13] E.J. Kirkland , *Advanced Computing in Electron Microscopy*, Springer (1998)

[14] J. M. Cowley, A. F. Moodie, *Acta Cryst*. **10**, 609-619 (1957)

[15] K. Ishizuka, N. Uyeda, Acta Crystallogr., *Sect. A: Found. Crystallogr*. **33**, 5, 687–862 (1977)

[16] K. Ishizuka, *Ultramicroscopy* **5**, 55-65 (1980)

[17] K. Ishizuka, *Acta Cryst*. **A38**, 773-779 (1982)

[18] K. Ishizuka, *Ultramicroscopy* **90**, 71-83 (2001)

Chapter 9: Comparison of Various Heteroepitaxial Alignment of β-cristobalite(110) on Si(100)

In this chapter, three versions of β-cristobalite are placed on Si(100). All three structures align with the Si(100) atoms along the <100> direction with respect to the Si(100) substrate and would produce IBA data that would show no disorder at the interface. So, it is the goal of the chapter to evaluate the models in the <110> and <111> direction with respect to the Si(100) substrate and calculate the shadow cones for the silicon in the three β-cristobalite types to determine if shadowing is possible of the silicon in the Si(100) which would possibly produce IBA results similar to those shown in Chapter 3. Since this requires a large number of calculations, the only data that will be shown in this chapter is for those β-cristobalite Si atoms that shadow Si(100) atoms that are near the interface. All other data will be placed in Appendix B, so that it may be used as a reference by other researchers.

9.1 Structure of β-cristobalite(110) on Si(100) in the <110> and <111> Directions

9.1a Structure of β-cristobalite(110) on Si(100) in the <110> Direction

As presented in Chapter 8, a structure was designed which has the β-cristobalite rotated and has been designated β-cristobalite(110), along with amorphous oxide on Si(100). In this section, the amorphous oxide will be disregarded and only the crystalline configuration will be discussed, since the silica has no effect on the IBA data that this configuration is being compared to. Figure 9-1 shows the arrangement from a side view. The Si in the β-

cristobalite(110) are shown in dark gray, the oxygen are white, and the Si(100) atoms are light gray. By rotating the crystal structure the perspective is through the β-cristobalite(110) to the underlying Si(100), as shown in Figure 9-2. This is the <100> orientation of the model. The correspondence of all of the various silicon atoms is apparent. The model is then rotated by 45° about the (100) plane, which is shown in Figure 9-3. This places the <110> direction pointing out of the page, or the <110> orientation, and the Si(100) atoms in a <110> configuration. Figure 9-3 gives a complex view of this arrangement. Because of the rectangular cubic nature of the structure, this rotation give a perspective where there are exposed Si(100) atoms at the bottom of the figure, an overlap of the β-cristobalite(110) above the Si(100) in the center, and β-cristobalite(110) at the top of the figure. This is the area that will be analyzed.

In his thesis, Hurst [4] showed that due to the low atomic mass, oxygen in a crystal structure will vibrate at room temperature such that they will not shadow underlying silicon atoms in IBA. Since previous IBA data is the primary reasons for the current examination of this structure, the oxygen can be removed and an arrangement of only silicon atoms can be shown. This is presented in Figure 9-4. While this is still complicated structure, the middle area has a repeating characteristic. Figure 9-5 shows the same arrangement, but with a black box surrounding a small area in the middle section of the figure. The box contains what is the basic cell of the area. It can be seen that the assembly with in the box is repeated to the left, right, and above. An enlargement of the box is shown in

Figure 9-6. This figure shows 4 distinct groups from left to right. The first set is a single Si(100) atom, which will have identical atoms behind it, or into the page. The second set is a Single Si(100) atoms, which has identical atoms behind it, along with a string of three β-cristobalite(110) Si atoms. The third set is identical to the first set, but located in a different position. The last set, set four, is several β-cristobalite(110) Si atoms which obscure a Si(100) atom, which again will have repeated Si(100) atoms behind it.

The individual sets and provide data on the location of the atoms within the set will be evaluated. Since each individual set is along the same plane, then each set can be presented using only relative y and z coordinates. The position of the lowest atoms designates where z is equal to zero and the atom with the smallest y value is set to zero.

Since sets 1 and 3 are silicon atoms in the Si(100), there is no shadowing from β-cristobalite(110) that can occur. The information on the relative coordinates is presented in Appendix B.

Set 2 has a more complicated arrangement, but the calculations indicate that there is no possible shadowing of the Si(100) atoms by the β-cristobalite(110) Si atoms. The relative coordinates, visual representation, and the calculations of shadowcone radii for a 3.05 MeV He^{++} atom interacting with each β-cristobalite(110) Si atom with the other atoms in the set along the <110> direction is presented in Appendix B.

A visual arrangement of Set 4 is shown in Figure 9-7, where each atom is labeled. Table 9-1 is the relative coordinates of the Set 4 atoms, using relative y and z coordinates. This allows the horizontal and vertical distances to be known, since they are necessary for shadow cone calculations. Of the four β-cristobalite(110) Si atoms, only the atom labeled B has shadow cone radii which could shadow atoms in the substrate that are near the interface. Table 9-2 shows the absolute distance along the <110> axis between atom B and the other atoms in the set.

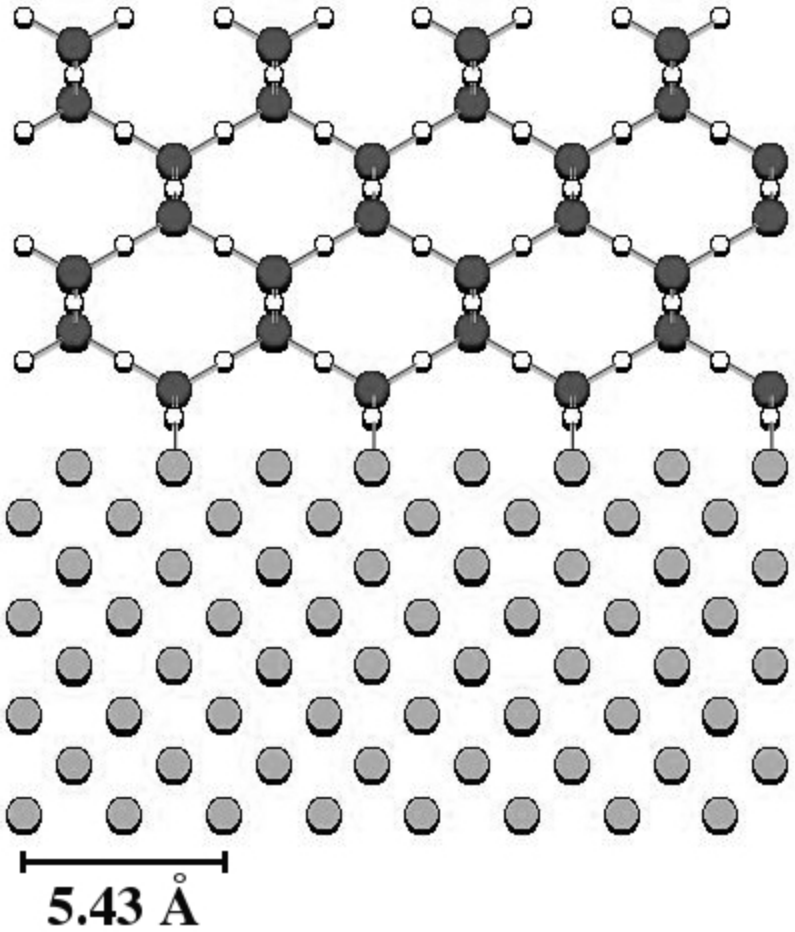

Figure 9-1: The arrangement of β-cristobalite(110) on Si(100) from a side view. The Si in the β-cristobalite(110) are shown in dark gray, the oxygen are white, and the Si(100) atoms are light gray.

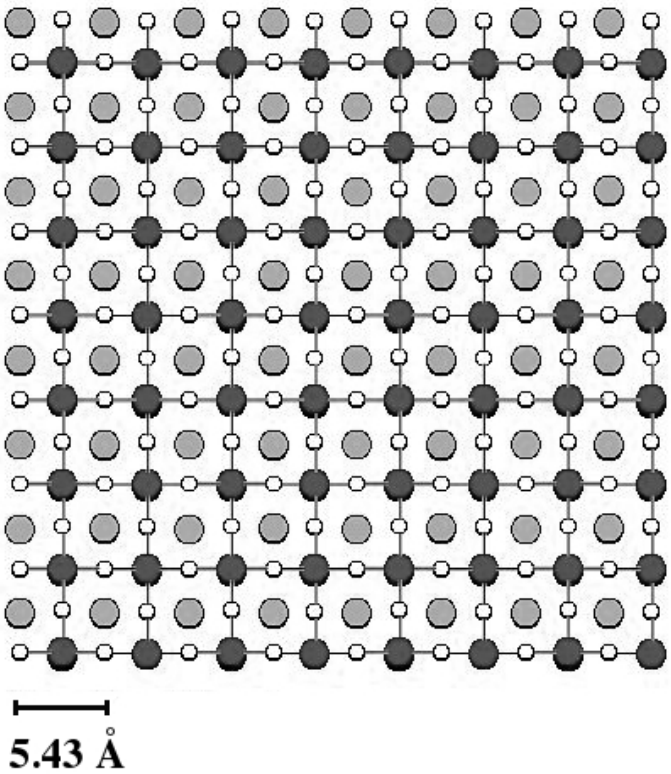

Figure 9-2: The arrangement of β-cristobalite(110) on Si(100) from the <100> orientation. The Si in the β-cristobalite(110) are shown in dark gray, the oxygen are white, and the Si(100) atoms are light gray.

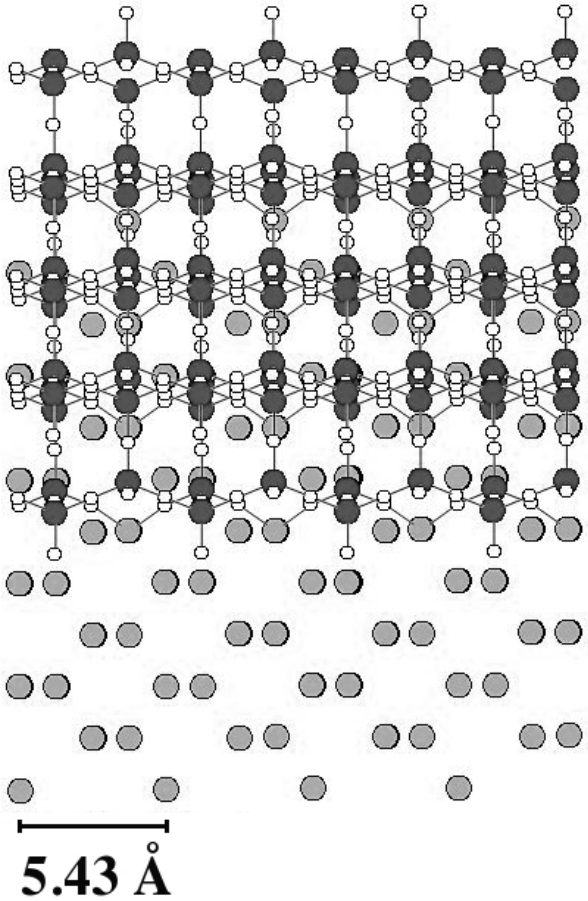

Figure 9-3: The arrangement of β-cristobalite(110) on Si(100) in the <110> orientation. The Si in the β-cristobalite(110) are shown in dark gray, the oxygen are white, and the Si(100) atoms are light gray.

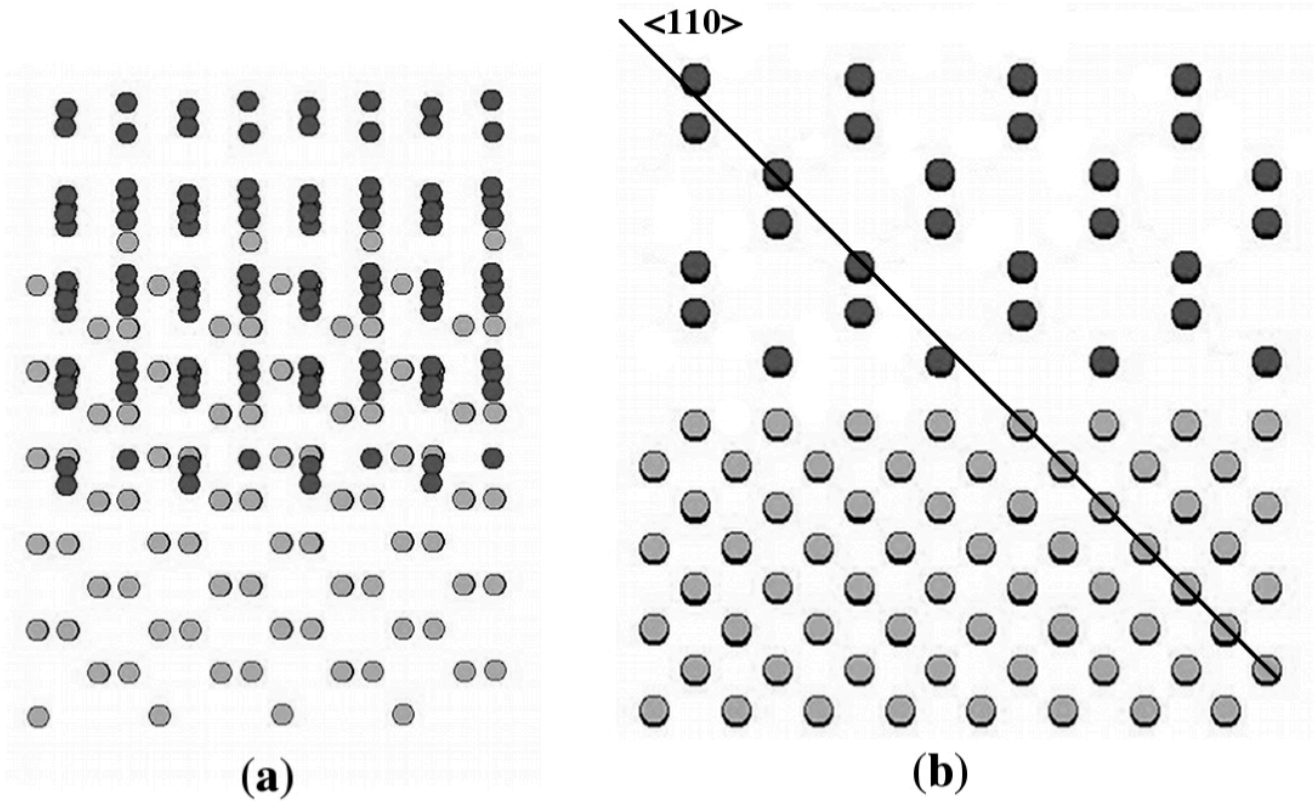

Figure 9-4: (a) The arrangement of β-cristobalite(110) on Si(100) in the <110> orientation, without oxygen and (b) the side view of the structure with a black line signifying the current <110> perspective . The Si in the β-cristobalite(110) are shown in dark gray and the Si(100) atoms are light gray.

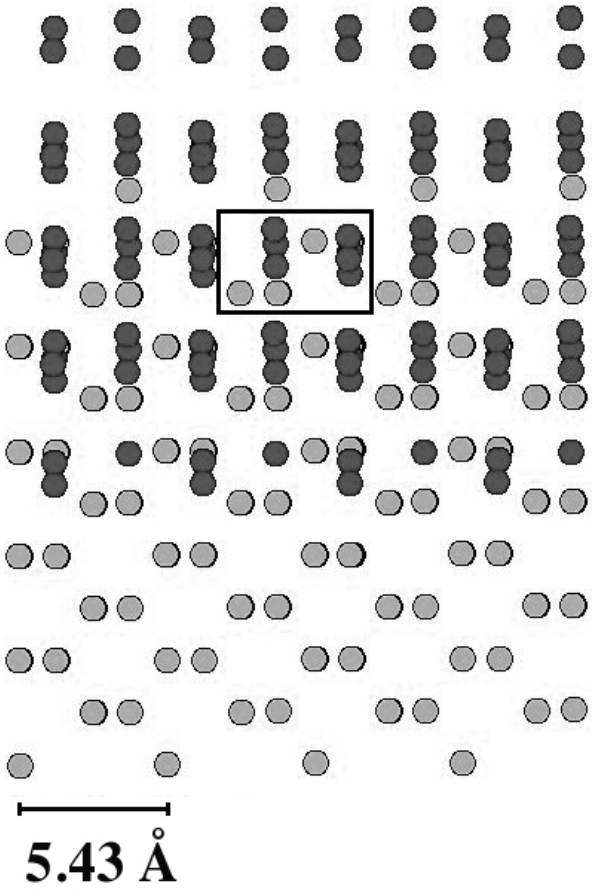

Figure 9-5: The arrangement of β-cristobalite(110) on Si(100) in the <110> orientation, without oxygen. A black box, containing the basic cell of the area, surrounds a small area in the middle section of the figure. The Si in the β-cristobalite(110) are shown in dark gray and the Si(100) atoms are light gray.

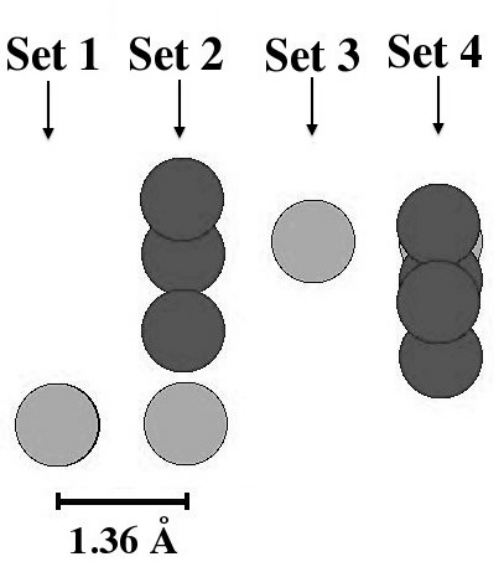

Figure 9-6: An enlargement of the basic cell of the area from the arrangement of β-cristobalite(110) on Si(100) rotated 45˚ about the horizontal without oxygen. The Si in the β-cristobalite(110) are shown in dark gray and the Si(100) atoms are light gray.

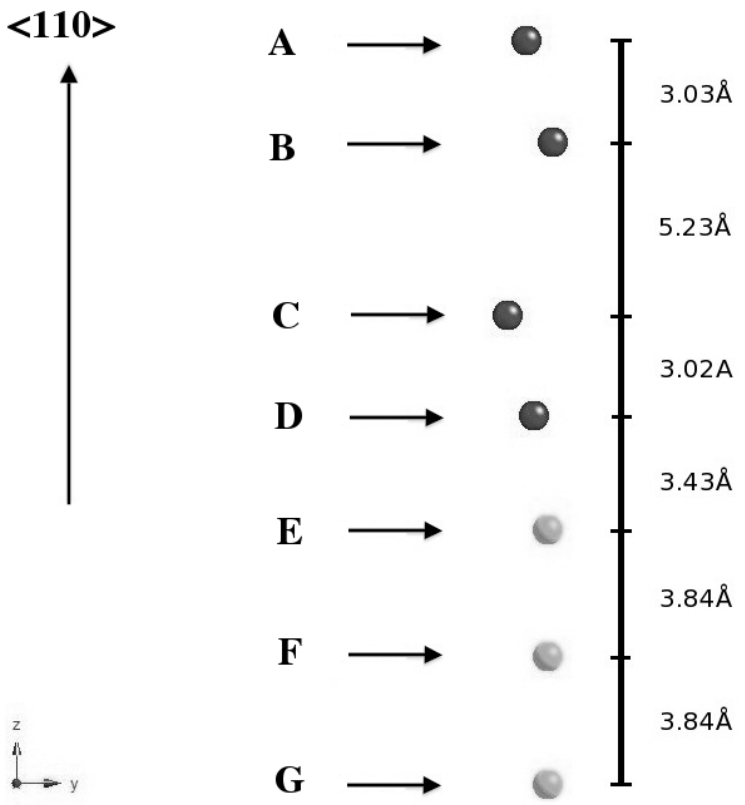

Figure 9-7: Visual representation of Set 4 of the <110> direction. The Si in the β-cristobalite(110) are shown in dark gray and the Si(100) atoms are light gray. The z direction is along the <110> direction.

Atom	y (Å)	z (Å)
(A) β-cristobalite(110) Si	0.57	22.39
(B) β-cristobalite(110) Si	1.39	19.36
(C) β-cristobalite(110) Si	0.00	14.13
(D) β-cristobalite(110) Si	0.82	11.11
(E) Si(100)	1.23	7.68
(F) Si(100)	1.23	3.84
(G) Si(100)	1.23	0.00

Table 9-1: Set 4 of the <110> direction relative coordinates, in Angstroms.

Atom Type	Absolute Distance along <110> axis (Å)	Shadow cone Radius (Å)	Horizontal Distance (Å)
(B) β-cristobalite(110) Si	0.00	0.00	----
(C) β-cristobalite(110) Si	5.25	0.05	1.39
(D) β-cristobalite(110) Si	8.27	0.07	0.57
(E) Si(100)	11.70	0.08	0.16
(F) Si(100)	15.54	0.09	0.16
(G) Si(100)	19.38	0.10	0.16

Table 9-2: Shadow cone Radii for distances along the <110> direction for a 3.05 MeV He^{++} atom interacting with the (B) β-cristobalite(110) Si atom of Set 4. The absolute distances are from (B).

9.1b Structure of β-cristobalite (110) on Si(100) in the <111> Direction

To obtain the <111> direction for the Si(100) in the model, the crystal structure is aligned so that the perspective is through the β-cristobalite(110) to the underlying Si(100) , which is the same as was done in the last section and was shown in Figure 9-2. The model is then rotated by 45° about the (001) plane, which is shown in Figure 9-8. Finally, the structure is rotated 55° about the (100) plane. The result is shown in Figure 9-9 with the model in the <111> orientation. Figure 9-10 shows the same arrangement without the oxygen atoms. Again, the rectangular cubic nature of the crystal, this rotation give a viewpoint where there is uncovered Si(100) atoms at the bottom of the figure, an overlap of the β-cristobalite(110) on top of the Si(100) in the center, and β-cristobalite(110) at the top of the figure. This overlapping, middle section will be analyzed here.

There is a repeating portion in the central section of the model. Figure 9-11 shows a black ellipse around a portion of the model. Figure 9-12 is an enlargement of the area in the ellipse. There are three sets in the repeating portion, which are labeled numerically from left to right. The first is an individual Si(100) atom, which has repeating Si(100) atoms beneath it. The second set has Si(100) atoms has two visible Si(100) atoms and three β-cristobalite(110) Si atoms. As with the first set, the Si(100) atoms in the second set will have repeating beneath. The third set is four β-cristobalite(110) Si atoms which obscure a Si(100) atom. As with the block in the <110> direction, each individual set has the same plane and can be presented using only the y and z coordinates.

Set 1 is only Si(100) atoms, so shadowing from β-cristobalite(110) Si atoms is not possible. The relative coordinates and visual representation are shown in Appendix B

Shadow cone calculations for Set 2 show no possible shadowing. The relative coordinates, visual representation, and the calculations for the shadowcone radii for the three β-cristobalite(110) Si atoms when interacting with a 3.05 MeV He^{++} atom are presented in Appendix B for reference.

The visual representation for set 3 is shown in Figure 9-13. The relative coordinate data is presented in Table 9-3. The shadow cone calculations show that only β-cristobalite(110) Si atom labeled C is able to shadow Si(100) near the interface and these calculations are shown in table 9-4, all other shadow cone calculation for this set are presented in Appendix B.

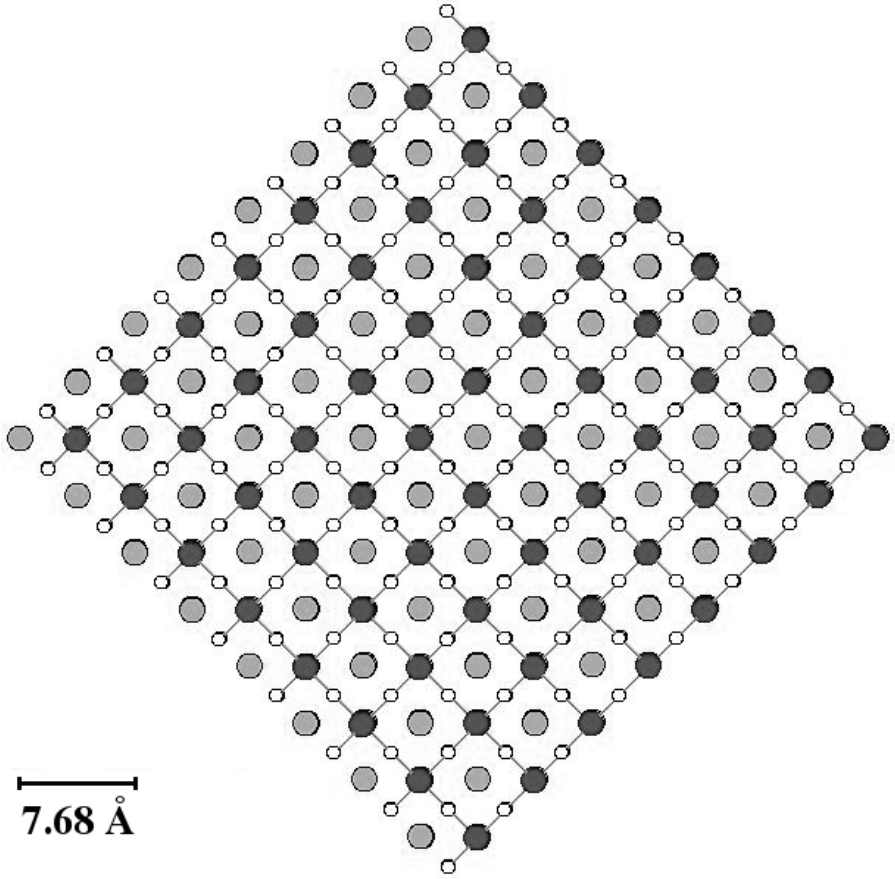

Figure 9-8: The arrangement of β-cristobalite(110) on Si(100), in a top view, rotated by 45° about the (001) plane. The Si in the β-cristobalite(110) are shown in dark gray, the oxygen are white, and the Si(100) atoms are light gray.

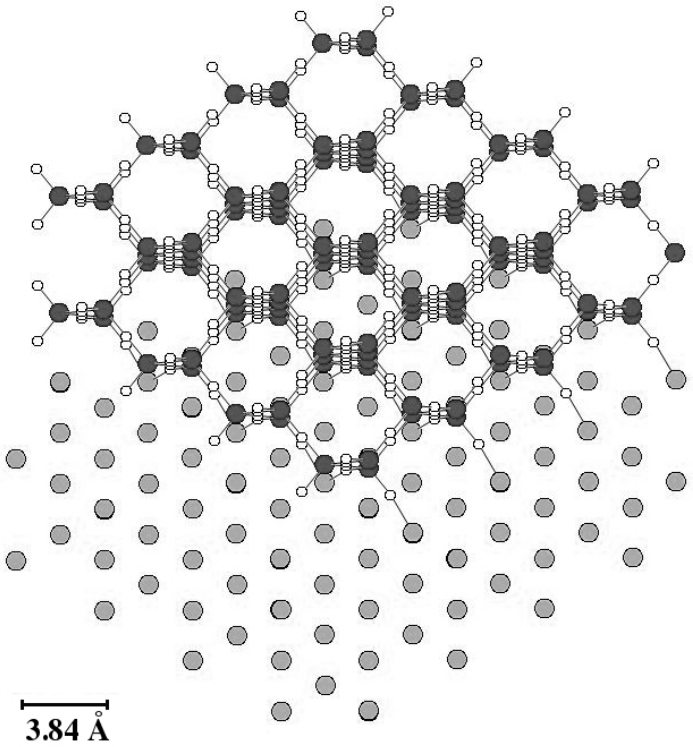

Figure 9-9: The arrangement of β-cristobalite(110) on Si(100), rotated by 45° about the (001) plane and the rotated 55º about the (100) plane. The Si in the β-cristobalite(110) are shown in dark gray, the oxygen are white, and the Si(100) atoms are light gray.

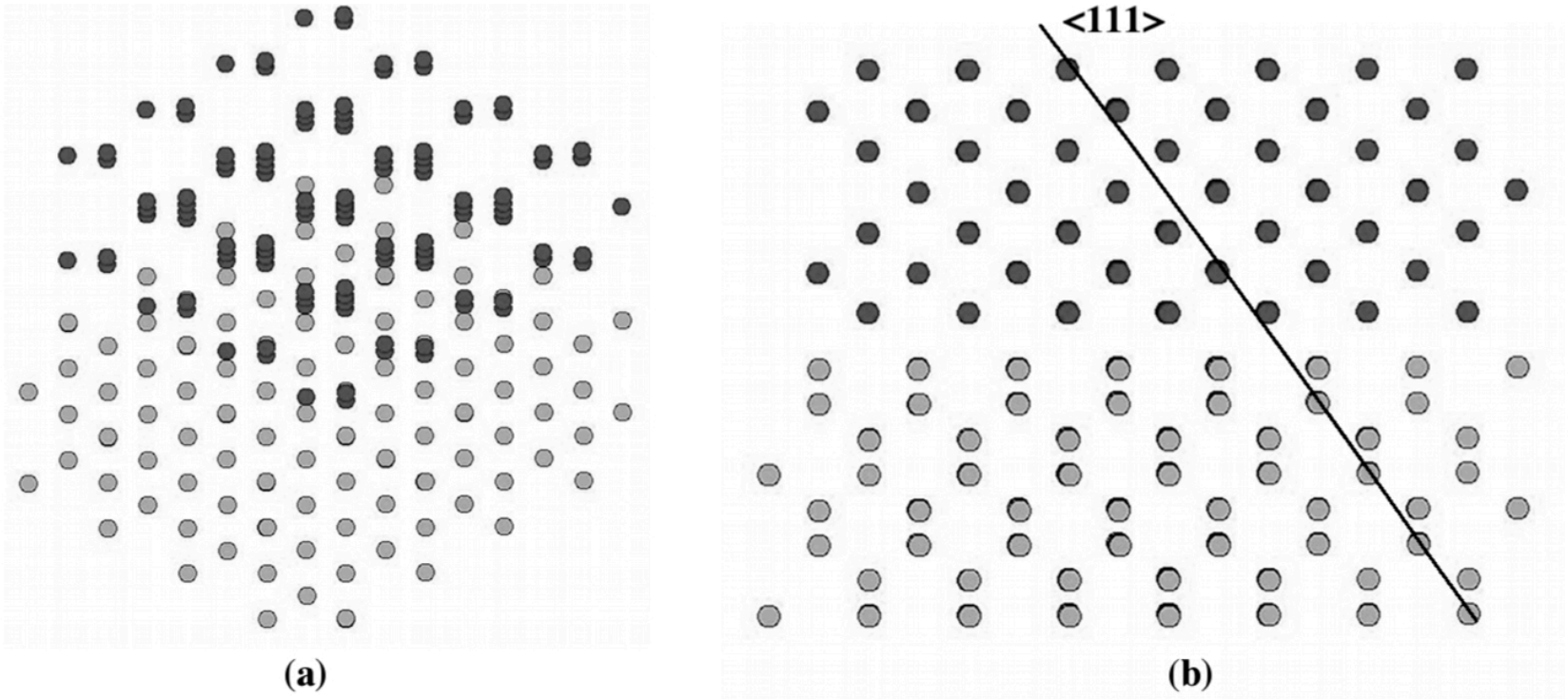

Figure 9-10: (a) The arrangement of β-cristobalite(110) on Si(100), rotated by 45˚ about the (001) plane and the rotated 55˚ about the (100) plane., without oxygen atoms and (b) the side view of the structure, rotated 45˚, with a black line signifying the current <111> perspective. The Si in the β-cristobalite(110) are shown in dark gray and the Si(100) atoms are light gray.

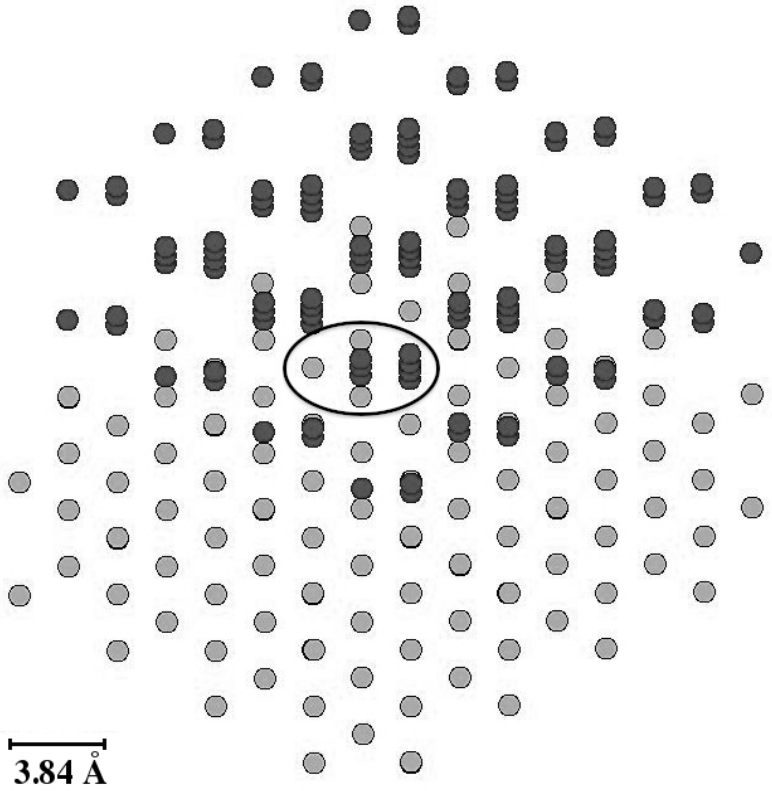

Figure 9-11: The arrangement of β-cristobalite(110) on Si(100) in the <111> orientation, without oxygen atoms. A black ellipse, containing the basic cell of the area, surrounds a small area in the middle section of the figure. The Si in the β-cristobalite(110) are shown in dark gray and the Si(100) atoms are light gray.

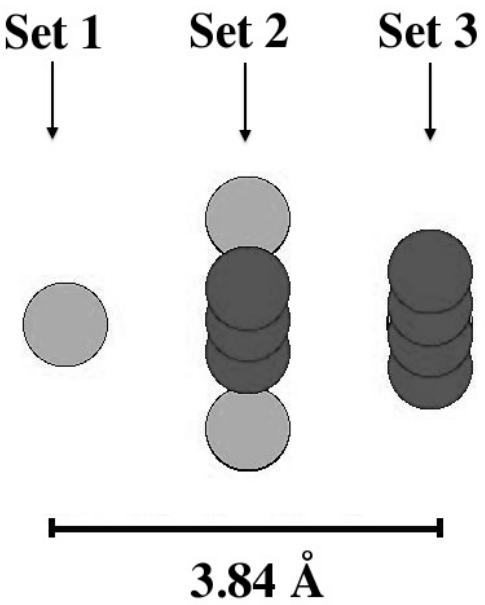

Figure 9-12: An enlargement of the basic cell of the area from the arrangement of β-cristobalite(110) on Si(100) in the <111> orientation, without oxygen atoms. The Si in the β-cristobalite(110) are shown in dark gray and the Si(100) atoms are light gray.

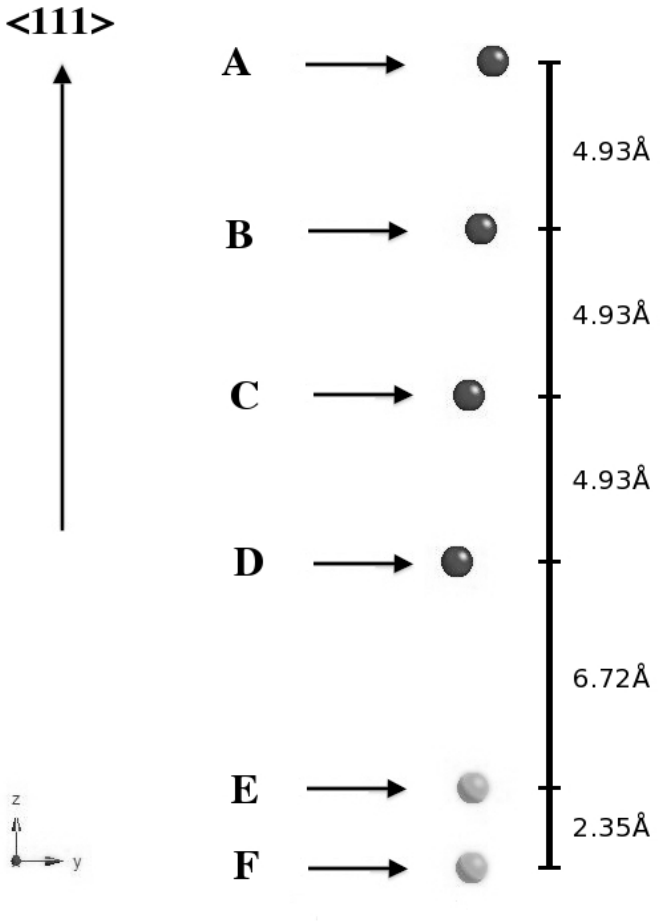

Figure 9-13: Visual representation of Set 3 of the <111> direction. The Si in the β-cristobalite(110) are shown in dark gray and the Si(100) atoms are light gray. The z direction is the <111> direction.

Atom	y (Å)	z (Å)
(A) β-cristobalite(110) Si	1.06	23.88
(B) β-cristobalite(110) Si	0.71	18.94
(C) β-cristobalite(110) Si	0.35	14.01
(D) β-cristobalite(110) Si	0.00	9.07
(E) Si(100)	0.44	2.35
(F) Si(100)	0.43	0.00

Table 9-3: Set 3 for <111> direction relative coordinates, in Angstroms.

Atom Type	Absolute Distance along <111> axis(Å)	Shadow cone Radius (Å)	Horizontal Distance (Å)
(C) β-cristobalite(110) Si	0.00	0.00	----
(D) β-cristobalite(110) Si	4.94	0.05	-0.35
(E) Si(100)	11.66	0.07	0.09
(F) Si(100)	14.01	0.09	0.08

Table 9-4: Shadowcone Radii for z distances, which is the <111> direction, for a 3.05 MeV He^{++} atom interacting with (C) β-cristobalite(110) Si atom of Set 3.

9.1c Conclusion of Shadow Cones for with β-cristobalite(110) on Si(100)

In the <100> direction, as seen in Figure 9-2, the model has perfect alignment, so one should get a 0.5 slope for the amorphous oxide and the β-cristobalite(110) with no disorder at the interface, since you have two crystal structures meeting at the surface of the Si(100). This matches the IBA data presented in Figure 9-18 [1].

The <110> direction shows some possible shadowing due to the β-cristobalite(110) Si atoms. The thermal vibration of the Si atoms has an amplitude with a standard deviation of 0.075Å [2], or 0.176Å Full Width at Half Maximum (FWHM). Therefore the vibration is 0.088Å amplitude at half maximum. The vibrations of the Si atoms occur at a rate of $1x10^{13}$ Hz, so each vibration takes $1x10^{-13}$ second. A 3.05 MeV He^{++} will travel the 0.1 Å in approximately $1x10^{-18}$ second. Therefore, each He^{++} will encounter a Si atom that is effectively at a stationary position.

The β-cristobalite(110) Si atom labeled B of Set 3 has a shadow cone which could encompass Si(100) atoms, since they fall within radius of the cone when the FWHM vibration is added. The IBA data in Figure 9-18 for the <110> direction suggests that there may be some missing Si at the surface. The results for the β-cristobalite(110) would produce a 0.5 slope in the oxide and no disorder at the surface and some shadowing.

The <111> direction IBA results show a significant portion on the surface Si in the Si(100) crystal to be shadowed. For the β-cristobalite(110) Si atom of Set 3

labeled C shadows, it is clear the Si(100) atoms near the interface will be shadowed when the thermal vibrations are taken into account. This would lead to IBA data that would show reduced Si atoms at the interface.

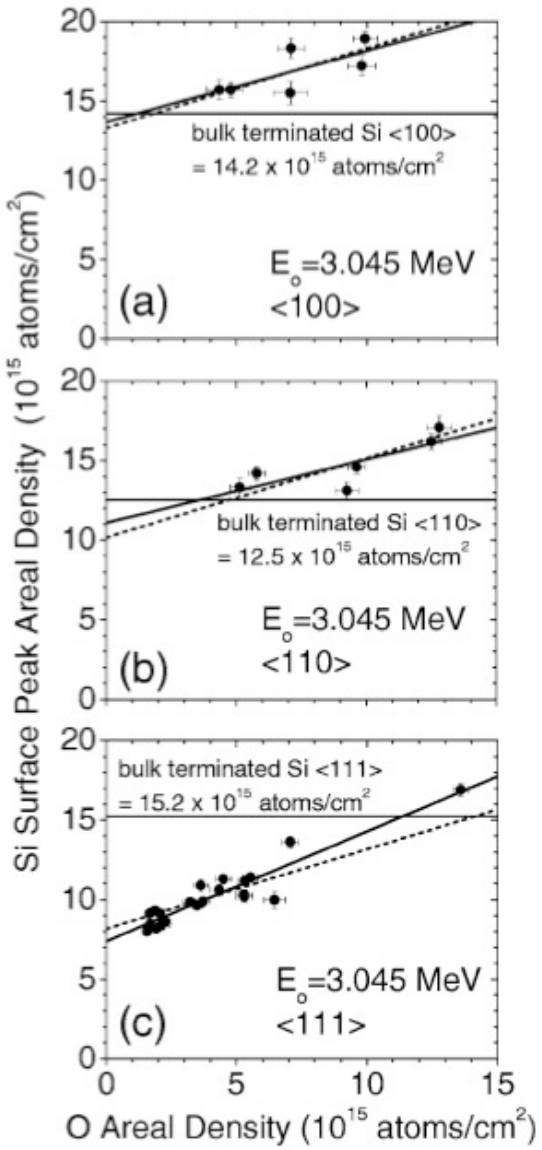

Figure 9-14: These are plots of Si surface peak areal density versus that of O for Si substrates that went through the H-A process and then underwent gate oxidization for the (a) <100>, (b) <110>, and (c) <111> directions. Each plot has a solid regression fit based on the data, as well a dotted line which represents a regression fit with an ideal 0.5 slope. The bulk surface Si amount for each direction is shown in each graph as a horizontal line. [1].

9.2 Structure of 100% Elongated β-cristobalite on Si(100) in the <110> and <111> Directions

9.2a Structure of 100% Elongated β-cristobalite on Si(100) in the <110> Direction

Another structure was created from the data in Dr. J.D. Bradley's thesis, the 100% elongated β-cristobalite on Si(100), where the elongation is along the normal to the Si(100) interface [3]. Figure 9-15 shows the arrangement from a side view. The Si in the elongated β-cristobalite are shown in dark gray, the oxygen are white, and the Si(100) atoms are light gray. By rotating the crystal structure so that the perspective through the elongated β-cristobalite to the underlying Si(100), which is shown in Figure 9-16. This top view is the <100> orientation of the model. The correspondence of all of the various silicon atoms is apparent. This model is then rotated by 45° about (100) plane to the <110> orientation, which is shown in Figure 9-17. This places the <110> direction to be pointing out of the page. Because of the rectangular cubic nature of the structure, this rotation give a perspective where there is exposed Si(100) atoms at the bottom of the figure, an overlap of elongated β-cristobalite above the Si(100) in the center, and elongated β-cristobalite at the top of the figure. The middle section will be used in the analysis.

As in the last chapter, the oxygen can be removed and an arrangement of only silicon atoms can be shown, since low atomic mass oxygen in a crystal structure will vibrate at room temperature such that they will not shadow

underlying silicon atoms in IBA. This is presented in Figure 9-18. This model has a repeating characteristic in the middle area. Figure 9-19 shows an enlargement of the middle section of the model, with a black line surrounding an area in the middle section of the figure. It contains what is the basic cell of the model. It can be seen that the assembly with in the box is repeated all around the enclosed area. A further enlargement of the box is shown in Figure 9-20, with all other atoms outside the parallelogram removed. This figure shows 2 distinct groups. The first set is two β-cristobalite Si atoms and a Si(100) atom, which will have identical atoms behind it, or into the page. The second set is a Si(100) atom, which has identical atoms behind it, along with two β-cristobalite Si atoms. Each individual set is in the same plane and so, these sets can be shown using only relative y and z coordinates. The position of the lowest atoms designates where z is equal to zero and the atom with the smallest y value is set to zero.

The shadow cone calculation show that the β-cristobalite Si atoms from both sets do not shadow the Si(100) atoms. All data and models for these sets are therefore presented in Appendix B for reference.

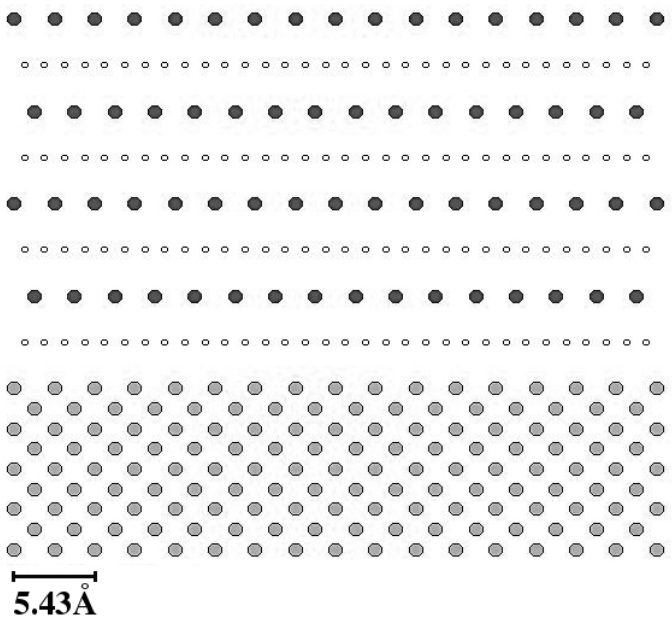

Figure 9-15: The arrangement of elongated β-cristobalite on Si(100) from a side view. The Si in the elongated β-cristobalite are shown in dark gray, the oxygen are white, and the Si(100) atoms are light gray.

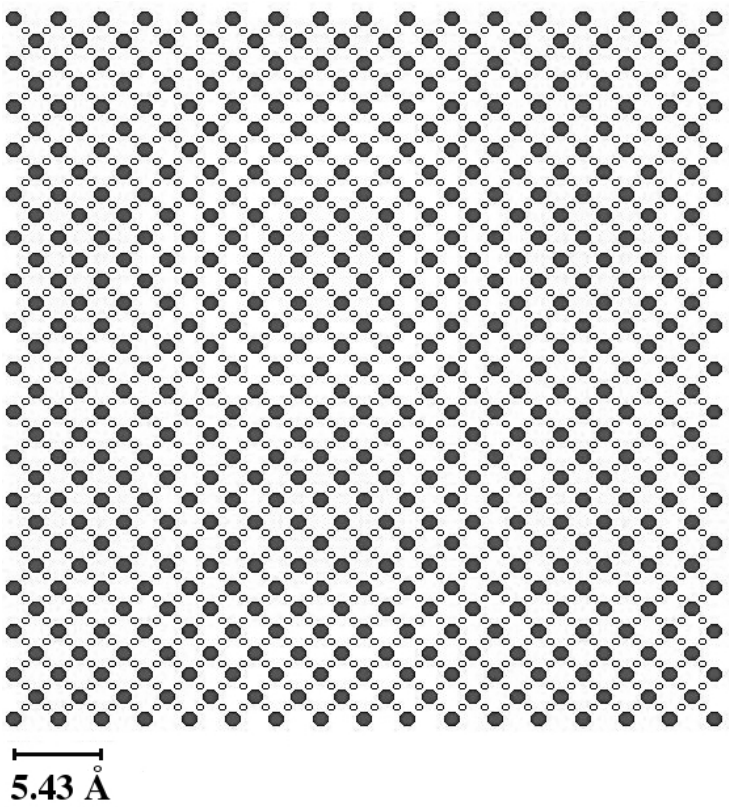

Figure 9-16: The arrangement of elongated β-cristobalite on Si(100) from a top view, or the <100> orientation. The Si in the elongated β-cristobalite are shown in dark gray, the oxygen are white, and the Si(100) atoms are light gray. Due to the correlation of positions of both sets of Si atoms, the Si(100) atoms can not be seen in this orientation.

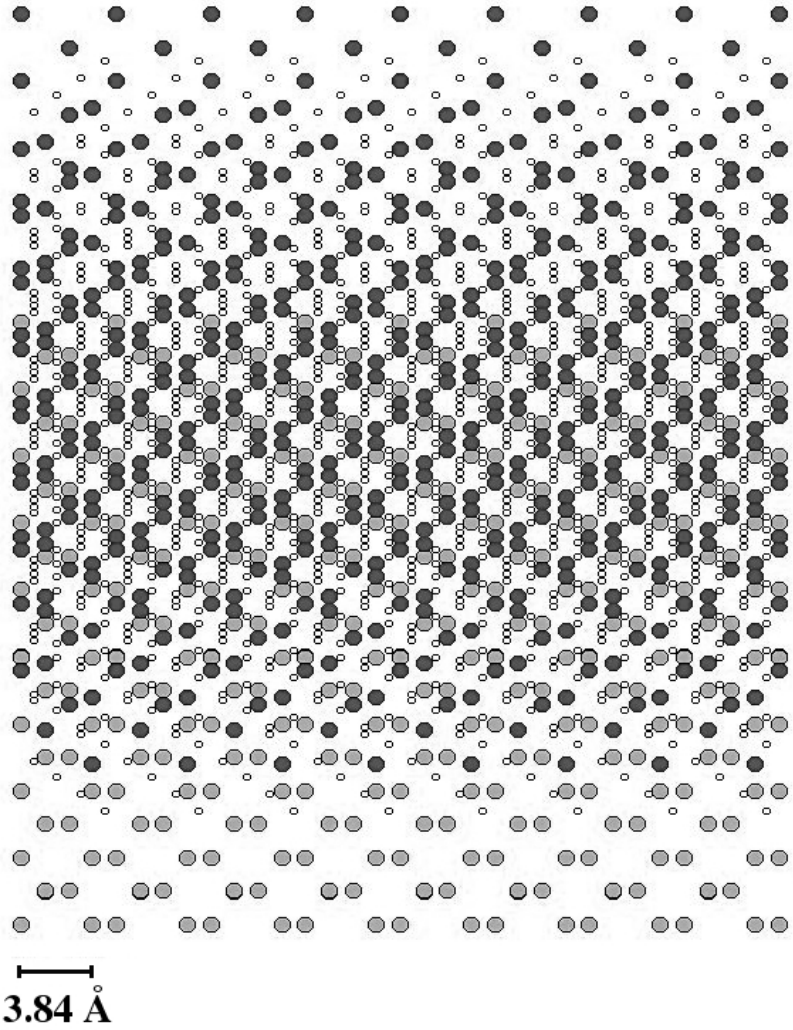

Figure 9-17: The arrangement of elongated β-cristobalite on Si(100) rotated 45˚ in the (100) plane to the <110> orientation. The Si in the elongated β-cristobalite are shown in dark gray, the oxygen are white, and the Si(100) atoms are light gray.

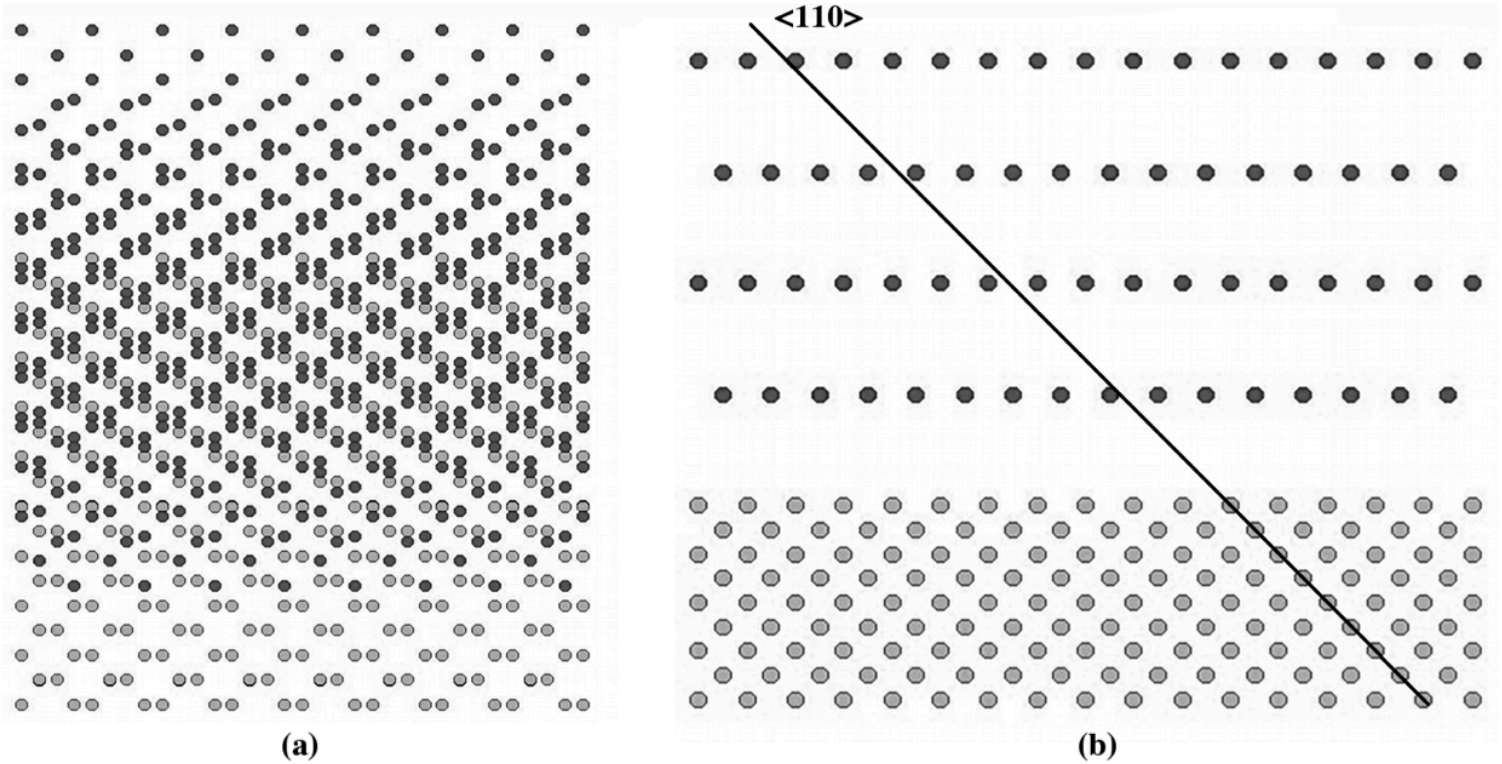

Figure 9-18: The arrangement of elongated β-cristobalite on Si(100) in the <110> orientation, without oxygen and (b) the side view of the structure without oxygen, with a black line signifying the current <110> perspective . The Si in the elongated β-cristobalite are shown in dark gray and the Si(100) atoms are light gray.

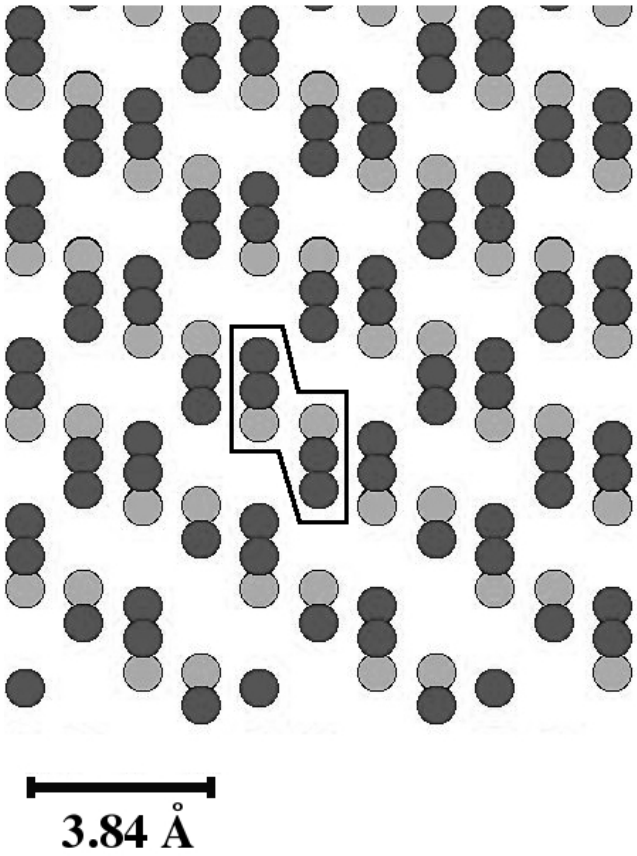

Figure 9-19: An enlargement of the middle section of the arrangement of elongated β-cristobalite on Si(100) in the <110> orientation, without oxygen. A black parallelgram, containing the basic cell of the area, surrounds a small area in the middle section of the figure. The Si in the elongated β-cristobalite are shown in dark gray and the Si(100) atoms are light gray.

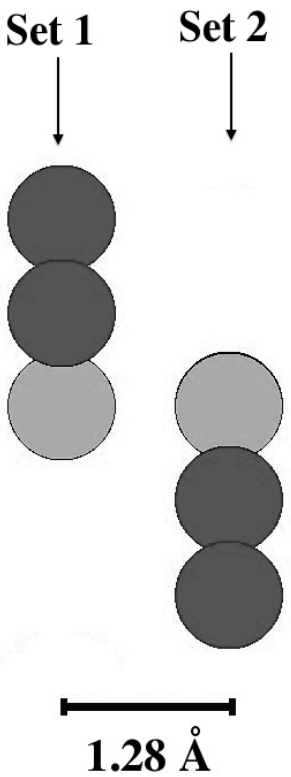

Figure 9-20: A further enlargement of the basic cell of the model of elongated β-cristobalite on Si(100) in the <110> orientation, without oxygen. The Si in the elongated β-cristobalite are shown in dark gray and the Si(100) atoms are light gray.

9.2b Structure of 100% Elongated β-cristobalite on Si(100) in the <111> Direction

To obtain the <111> direction for the Si(100) in the formation, the crystal structure is aligned so that the perspective is through the elongated β-cristobalite to the underlying Si(100). The model is then rotated by 45° about the (001) plane, which is shown in Figure 9-21. The structure is then rotated 55° about the (100) plane. The resulting <111> orientation is shown in Figure 9-22 Figure 9-23 shows the model without the oxygen atoms. Again, the rectangular cubic nature of the model, this rotation give a viewpoint where there is uncovered Si(100) atoms at the bottom of the figure, an overlap of the β-cristobalite(110) above the Si(100) in the center, and β-cristobalite(110) at the top of the figure. This center section will be used in the analysis of the model.

There is a repeating portion in the section as was seen the <110> orientation of the crystal. Figure 9-24 is an enlargement of the middle section and shows a black oval around the portion of the model. This cell repeated above, below, to the left, to the right, and diagonally. Figure 9-25 is a further enlargement of the area in the white line. There are two sets in the repeating portion. The first is a two β-cristobalite Si atoms and a Si(100) atom, which has repeating Si(100) atoms behind it. The second set is similar to the first, with two β-cristobalite Si atoms and a Si(100) atom with repeating atoms behind it. As with the in the <110> direction, each individual set has the same plane and can be presented using only relative y and z coordinates.

The shadow cone calculation show that it is not possible for the β-cristobalite Si atoms in the two sets to shadow the Si(100) atoms along the <111> direction. Therefore all data for these sets are presented in Appendix B.

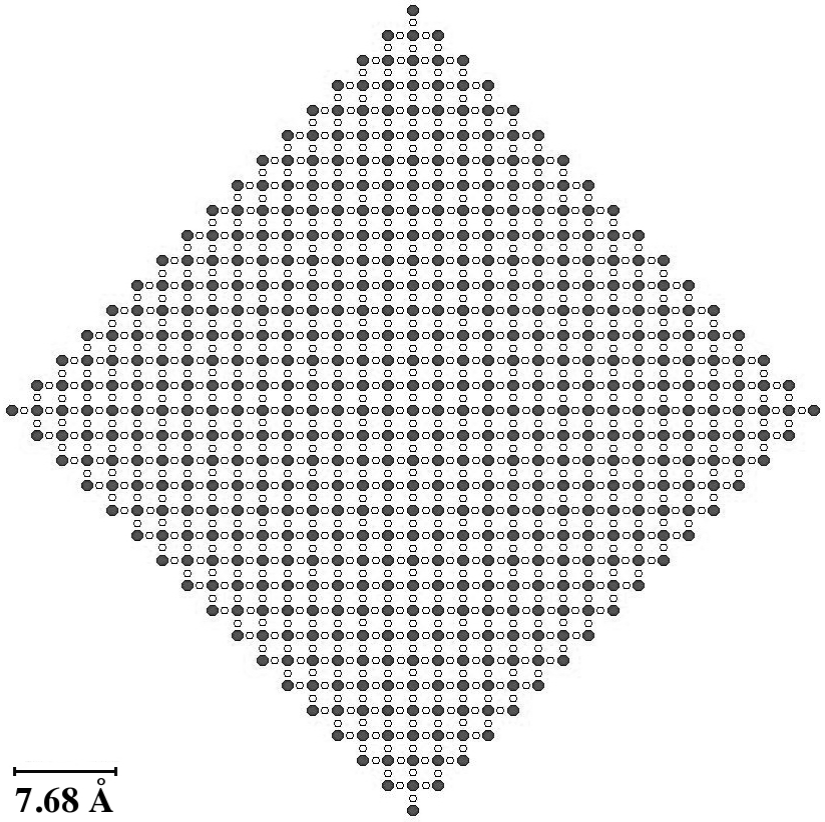

Figure 9-21: The arrangement of elongated β-cristobalite on Si(100), in a top view, rotated by 45° about (001) plane. The Si in the elongated β-cristobalite are shown in dark gray, the oxygen are white.

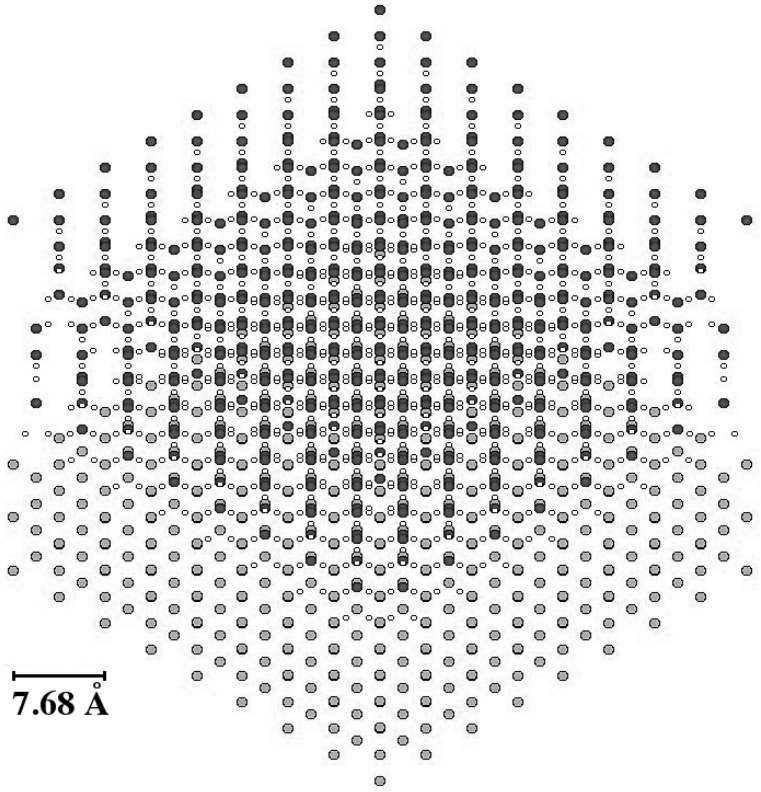

Figure 9-22: The arrangement of elongated β-cristobalite on Si(100) in the <111> orientation. The Si in the elongated β-cristobalite are shown in dark gray, the oxygen are white, and the Si(100) atoms are light gray.

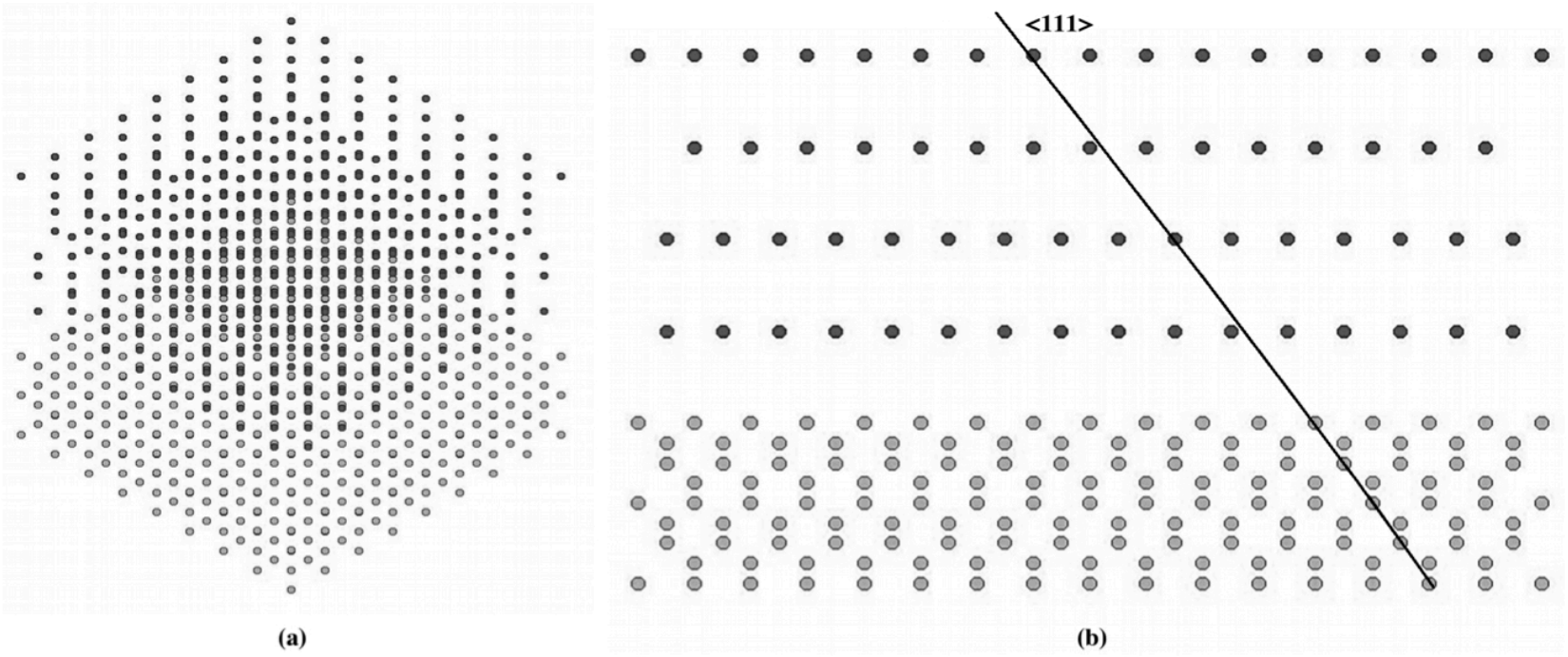

Figure 9-23: The arrangement of elongated β-cristobalite on Si(100) in the <111> orientation, without oxygen atoms and (b) the side view of the structure with a black line signifying the current <111> perspective. The Si in the elongated β-cristobalite are shown in dark gray and the Si(100) atoms are light gray.

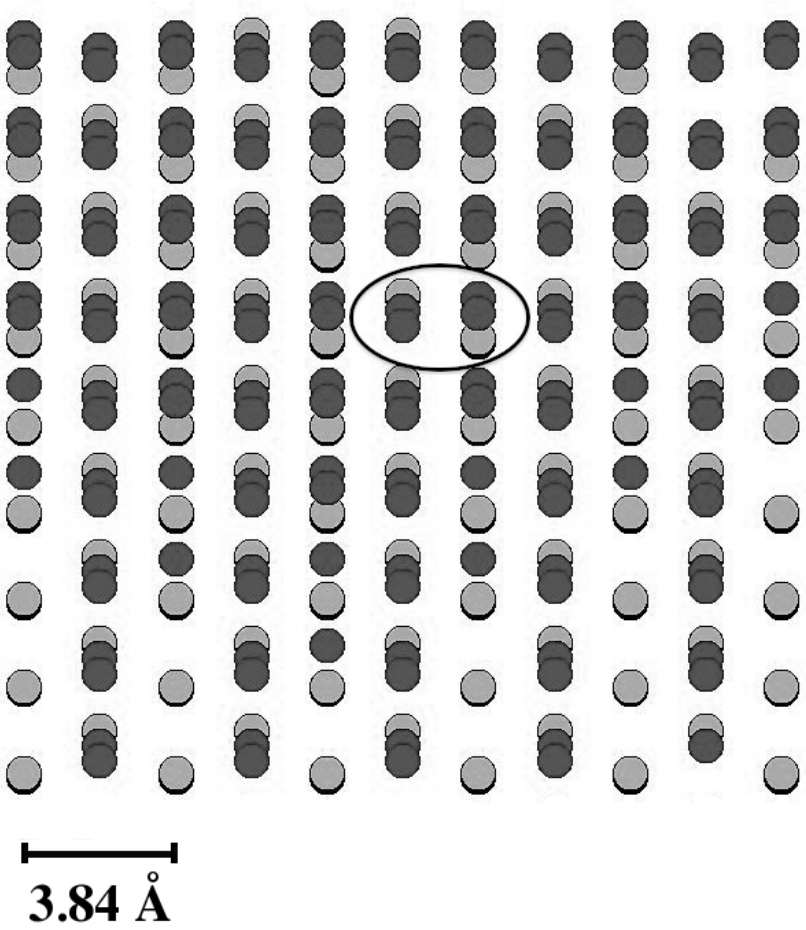

Figure 9-24: The arrangement of elongated β-cristobalite on Si(100) in the <111> orientation, without oxygen atoms. A black oval encloses the basic cell of the area, surrounds a small area in the middle section of the figure. The Si in the elongated β-cristobalite are shown in dark gray and the Si(100) atoms are light gray.

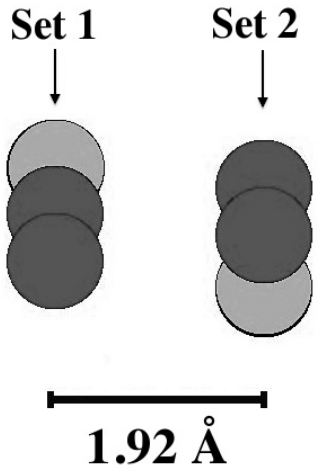

Figure 9-25: An further enlargement of the basic cell of the area from the arrangement of elongated β-cristobalite on Si(100) in the <111> orientation, without oxygen atoms. The Si in the elongated β-cristobalite are shown in dark gray and the Si(100) atoms are light gray.

9.2c Conclusion of Shadow Cones for Elongated β-cristobalite on Si(100)

In the <100> direction, as seen in Figure 9-16, the model has perfect alignment of all silicon atoms, so one should get a 0.5 slope for the amorphous oxide and the elongated β-cristobalite with no disorder at the interface, since you have two crystal structures meeting at the surface of the Si(100). This matches the IBA data presented in Figure 9-14 (a) [1].

The <110> direction shows no shadowing due to the elongated β-cristobalite Si atoms. The thermal vibration of the Si atom is 0.075Å at 293K [2], or 0.176Å FWHM. The horizontal distances are larger than the shadow cone and the Si vibration, so there will be no shadowing. The IBA data in Figure 9-18 (b) for the <110> direction suggests that there may be some amount of missing Si at the surface. The results for the elongated β-cristobalite would produce a 0.5 slope in the oxide and no disorder at the surface. Therefore, there may be some discrepancy between the IBA results in Figure 9-18 (b) and the shadow cone data presented here.

In the <111> direction there is no shadowing, even when accounting for Si thermal vibration. The <111> direction IBA results show a significant portion on the surface Si in the Si(100) crystal to be shadowed. Consequently, this crystal cannot match the IBA results in Figure 9-18 (c).

9.3 Structure of Density Conserved β-cristobalite on Si(100) in the <110> and <111> Directions

9.3a Structure of Density Conserved β-cristobalite on Si(100) in the <110> Direction

Dr. J.D. Bradley also created density conserved β-cristobalite (which will be referred to as simply β-cristobalite for the remainder of the chapter) with amorphous silica on Si(100) in his thesis [3]. That crystalline configuration has been duplicated in this chapter. Figure 9-26 shows the arrangement from a side view. The Si in the β-cristobalite are shown in dark gray, the oxygen are white, and the Si(100) atoms are light gray. By rotating the model to the <100> direction, so that the perspective through the β-cristobalite to the underlying Si(100) is shown in Figure 9-27. There is a correspondence of the positions of all of the silicon atoms in the β-cristobalite and Si(100). This model is then rotated by 45° about the (100) plane, shown in Figure 9-28. This is the <110> orientation and the figure shows Si(100) atoms in a <110> projection. Because of the rectangular cubic nature of the structure, this rotation give a perspective where there are uncovered Si(100) atoms at the bottom of the figure, an overlap of β-cristobalite above the Si(100) in the center, and β-cristobalite at the top of the figure. The middle section will be used for analysis of the shadow cones in this section of the thesis.

As in the last two sections, the oxygen can be removed and an arrangement of only silicon atoms can be shown, since low atomic mass, oxygen

in a crystal structure will vibrate at room temperature such that they will not shadow underlying silicon atoms in IBA. This is presented in Figure 9-29(a). Figure 9-29(b) gives the side view of the structure with a black line signifying the current <110> perspective. This <110> orientation of the model has a repeating characteristic in the middle area, as seen in the previous sections of this chapter. Figure 9-30 shows an enlargement of the same arrangement, but with a black ellipse surrounding an area in the middle section of the figure. The ellipse contains what is the basic cell of the model. It can be seen that the unit within the box is repeated all around the enclosed area. A further enlargement of the cell is shown in Figure 9-31, with all other atoms outside the ellipse removed.

This figure shows four distinct sets. Each individual set is in the same plane and each of these sets can be shown using only the y and z coordinates. This data is presented so that the only the relative y and z coordinates. The position of the lowest atoms designates where z is equal to zero and the atom with the smallest y value is set to zero.

The first set is a single β-cristobalite Si atoms with no Si(100) atoms. Since it is a single atom, and can not shadow Si(100), no visual representation or calculation is offered.

The second set consists of three β-cristobalite Si atoms. There are no Si(100) atoms in the set to shadow, so no shadow cone calculations are presented. The relative positions and a visual representation of the set are presented in Appendix B.

Set 3 in the <110> orientation is a string of three β-cristobalite Si atoms and one Si(100) atom which has repeating Si atoms behind it. The shadow cone calculations show that it is not possible for the β-cristobalite Si atoms to shadow atoms in the Si(100). Therefore, the visual representation, relative positions for the atoms, and the shadow cone data for the three β-cristobalite Si atoms for set 3 is presented in Appendix B.

Set 4 is one β-cristobalite Si atom and a column of Si(100) atoms. Figure 9-32 is a illustration of the set and Table 9-5 shows the relative positions. The shadow cone radius data for the single β-cristobalite Si atom in the set is presented in Table 9-6. This data shows that the β-cristobalite Si atom will shadow several Si(100) atoms near the interface, when thermal vibration is taken into account.

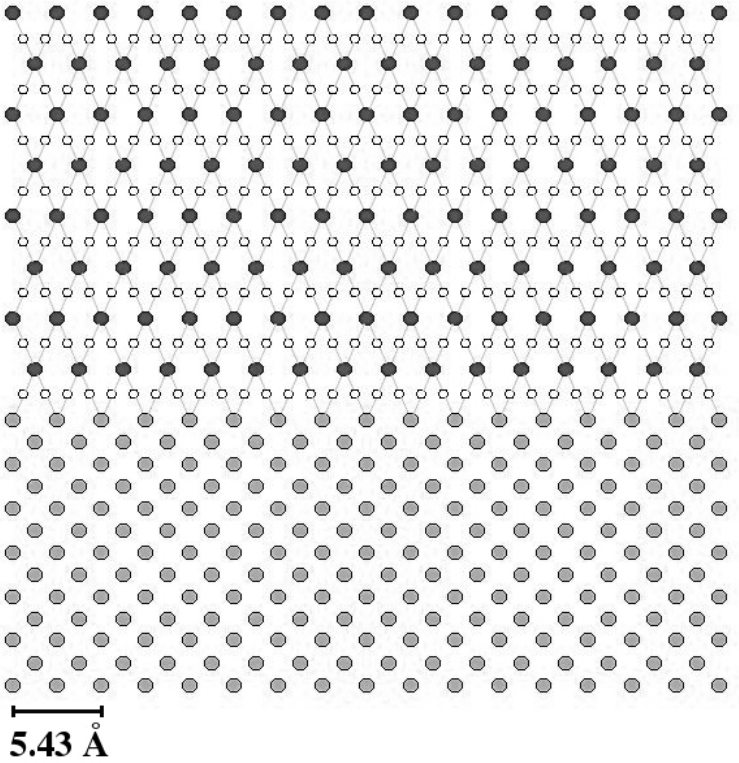

Figure 9-26: The arrangement of β-cristobalite on Si(100) from a side view. The Si in the β-cristobalite are shown as dark gray, the oxygen are white, and the Si(100) atoms are light gray .

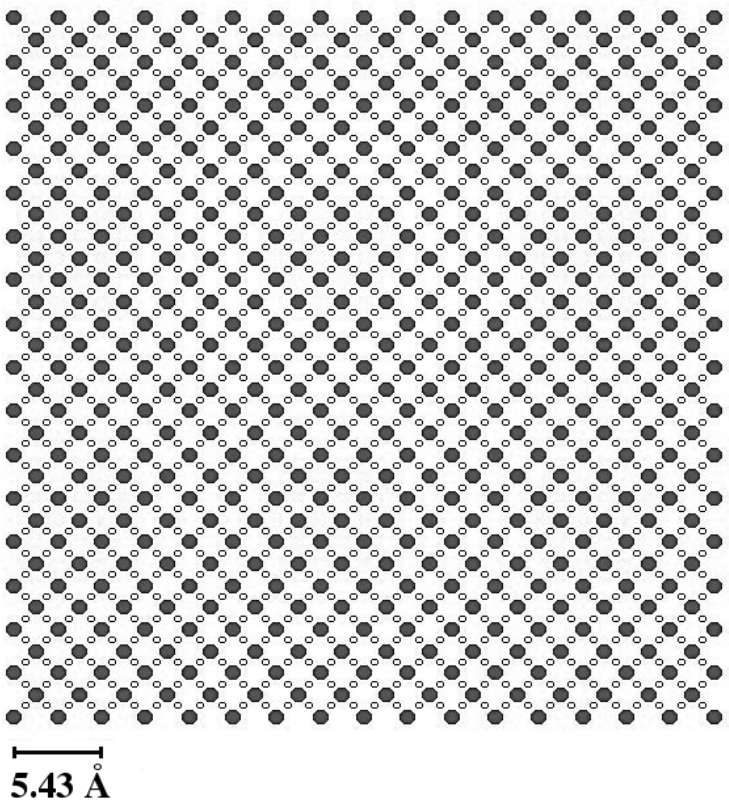

Figure 9-27: The arrangement of β-cristobalite on Si(100) in the <100> direction. The Si in the β-cristobalite are shown in dark gray, the oxygen are white, and the Si(100) atoms are light gray. Due to the position correspondence of the β-cristobalite to the underlying Si(100), no Si(100) appear.

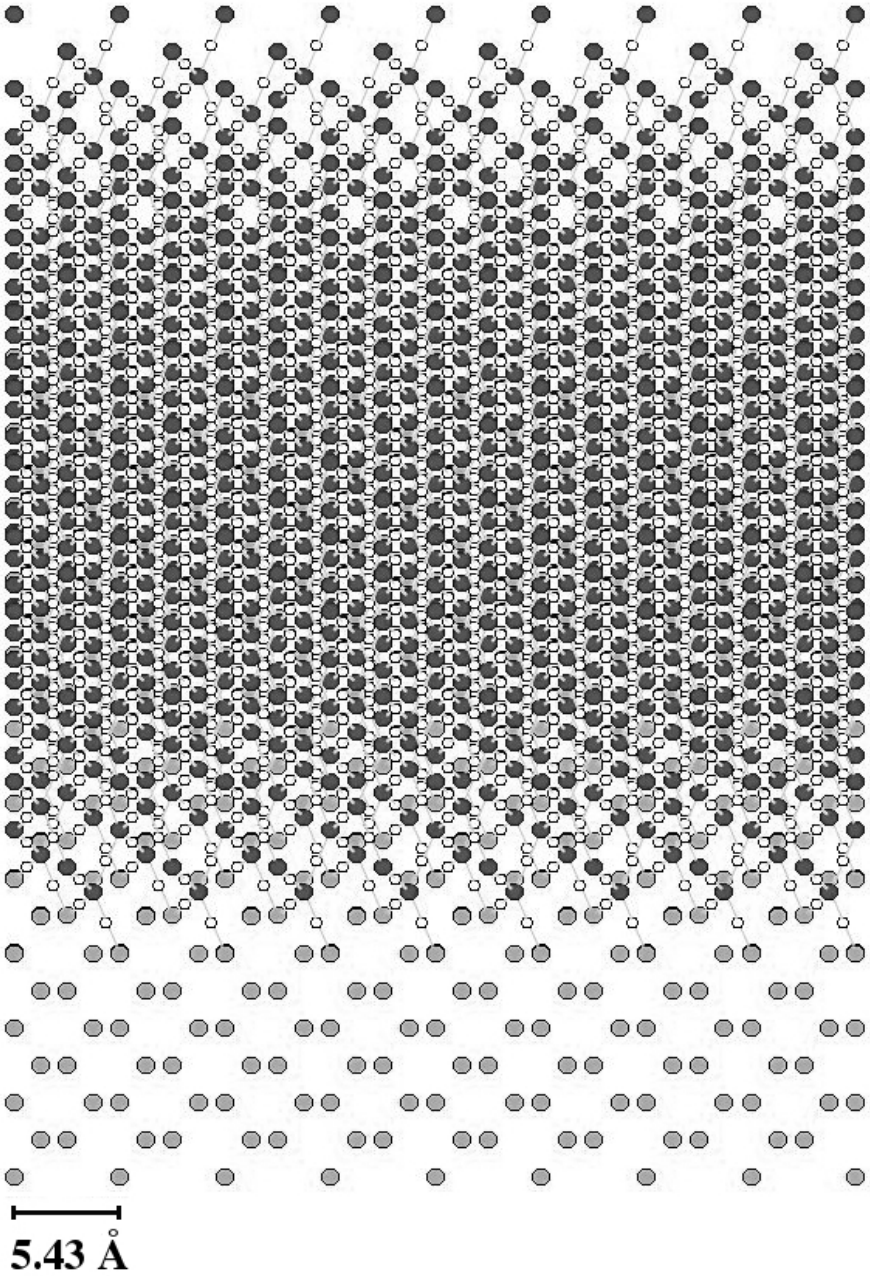

Figure 9-28: The arrangement of β-cristobalite on Si(100) rotated 45˚ about (100) plane. This is the <110> orientation. The Si in the β-cristobalite are shown in dark gray, the oxygen are red, and the Si(100) atoms are light gray.

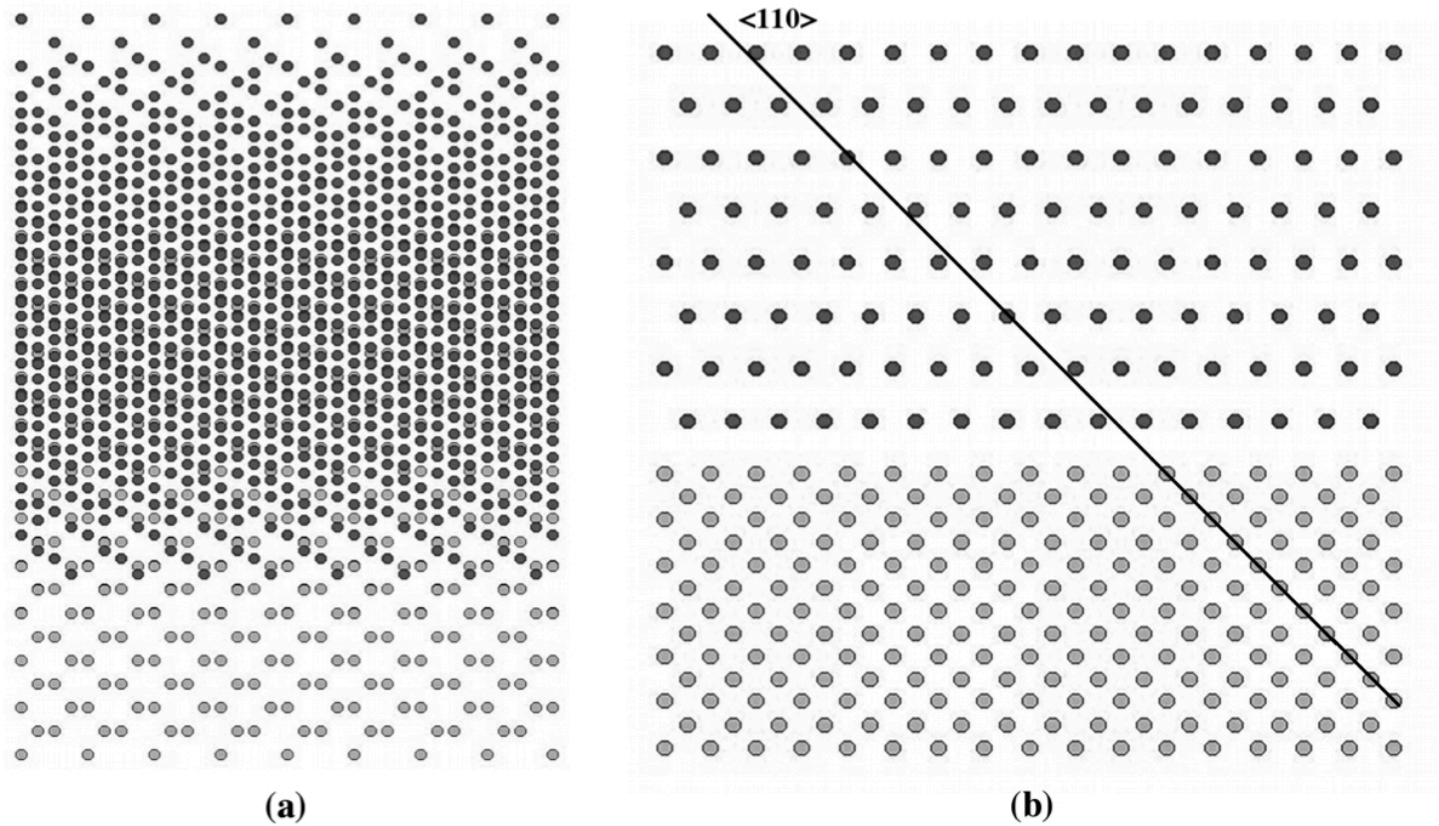

Figure 9-29: The (a) arrangement of β-cristobalite on Si(100) in the <110> orientation, without oxygen and (b) the side view of the structure with a black line signifying the current <110> perspective . The Si in the β-cristobalite are shown in dark gray and the Si(100) atoms are light gray.

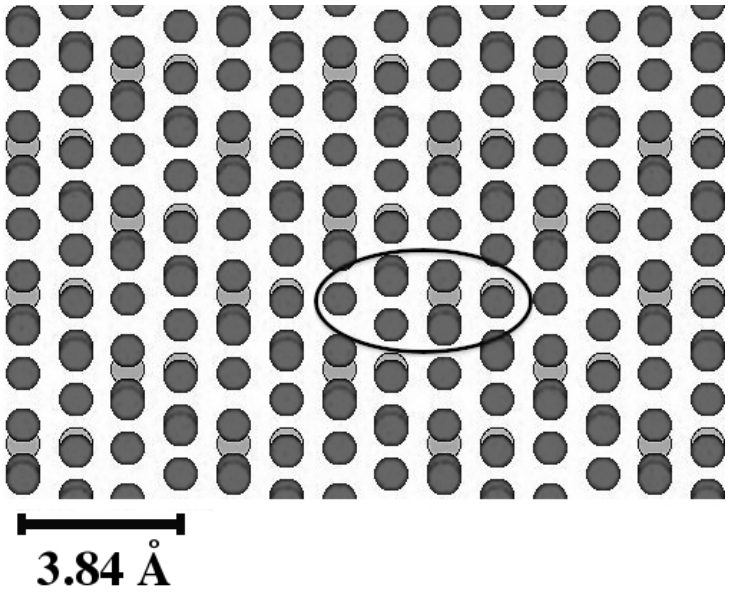

Figure 9-30: An enlargement of the middle section of the arrangement of β-cristobalite on Si(100) in the <110> orientation, without oxygen. A black ellipse, containing the basic cell of the area, surrounds a small area in the middle section of the figure. The Si in the β-cristobalite are shown in dark gray and the Si(100) atoms are light gray.

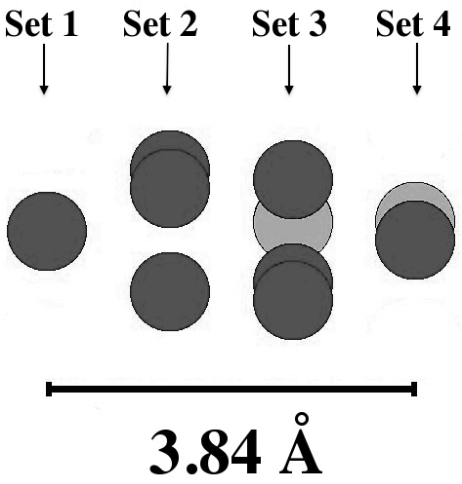

Figure 9-31: A further enlargement of the basic cell of the model from the arrangement of β-cristobalite on Si(100) in the <110> orientation, without oxygen. The Si in the β-cristobalite are shown in dark gray and the Si(100) atoms are light gray.

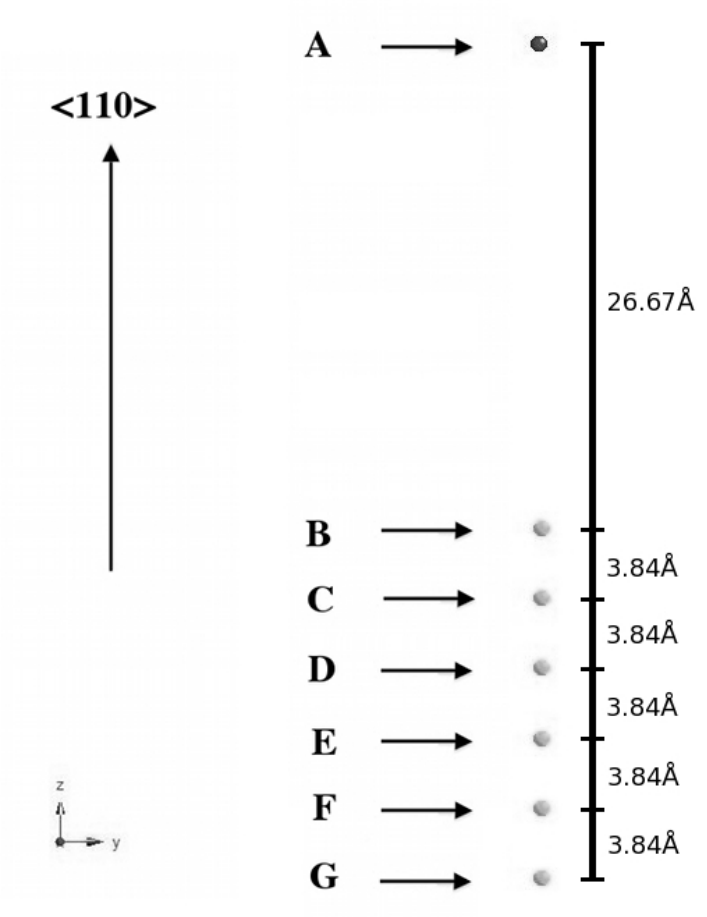

Figure 9-32: Visual representation of Set 4 of the <110> direction. The Si in the β-cristobalite are shown in dark gray and the Si(100) atoms are light gray. The z direction is the <110> direction.

Atom Type	y (Å)	z (Å)
(A) β-cristobalite Si	0.00	45.87
(B) Si(100)	0.20	19.20
(C) Si(100)	0.20	15.36
(D) Si(100)	0.20	11.52
(E) Si(100)	0.20	7.68
(F) Si(100)	0.20	3.84
(G) Si(100)	0.20	0.00

Table 9-5: Set 4 of the <110> direction relative coordinates, in Angstroms.

Atom Type	Absolute Distance along <110> axis(Å)	Shadowcone Radius (Å)	Horizontal Distance (Å)
(A) β-cristobalite Si	0.00	0.00	----
(B) Si(100)	26.67	0.12	0.20
(C) Si(100)	30.51	0.13	0.20
(D) Si(100)	34.35	0.13	0.20
(E) Si(100)	38.19	0.14	0.20
(F) Si(100)	42.03	0.15	0.20
(G) Si(100)	45.87	0.16	0.20

Table 9-6: Shadowcone Radii for z distances, which is the <110> direction, for a 3.05 MeV He^{++} atom interacting with the (A) β-cristobalite Si atom in Set 4.

9.3b Structure of Density Conserved β-cristobalite on Si(100) in the <111> Direction

The <111> direction for the Si(100) in the formation must now be obtained. Therefore, the crystal structure is aligned in the <100> direction which gives the viewpoint through the density conserved β-cristobalite to the Si(100) lying underneath. This is the same procedure was performed in the previous section of this chapter and was shown in Figure 9-34. The model is then rotated by 45° about the (001) plane, which is shown in Figure 9-33. This structure is then rotated 55° about the (100) plane. The result is shown in Figure 9-34 and is the <111> orientation. The Si(100) atoms are in a <111> formation.

Figure 9-35(a) shows the model in the <111> orientation without the oxygen atoms. Figure 9-45(b) shows a side view with the <111> direction marked by a black line. The rectangular cubic nature of the crystal gives this rotation a viewpoint with uncovered Si(100) atoms at the bottom of the figure, an overlap of the β-cristobalite(110) above the Si(100) in the center, and β-cristobalite(110) at the top of the figure. The middle section will be analyzed using shadow cone calculations in this section. Figure 9-46 is an enlargement of the middle section of the model. To determine if a repeating cell exist, in Figure 9-37 the radii of all of the Si atoms have been reduced. The repetitive characteristic of the structure can now be observed. A black line surrounds the basic cell of model in this orientation and this pattern can be seen repeating above, below, and diagonally to the cell.

Figure 9-38 is a further enlargement of the area in the black line, where all outside atoms have been removed. There are two sets in the repeating portion. The first is two clusters of two β-cristobalite Si atoms and a single column Si(100) atoms. The second set is four β-cristobalite Si atoms and a single column Si(100) atoms. As with the cell in the <110> direction, each individual set is in the same plane and can be presented using only the y and z coordinates.

The β-cristobalite Si atoms of this set cannot shadow any Si(100) atoms that are near the interface according to the calculations Therefore all data for this set is presented in Appendix B.

The Set 2 visual representation is presented in Figure 9-39, while the relative coordinates of the set are in Table 9-7. Table 9-8 shows the shadow cone radii for the (B) β-cristobalite Si atoms in set 2 when interacting with a 3.05 MeV He^{++} atom. This data indicates that it will shadow Si(100) atoms that are near the interface. Table 9-9 shows similar data for the (C) β-cristobalite Si atoms in set 2.

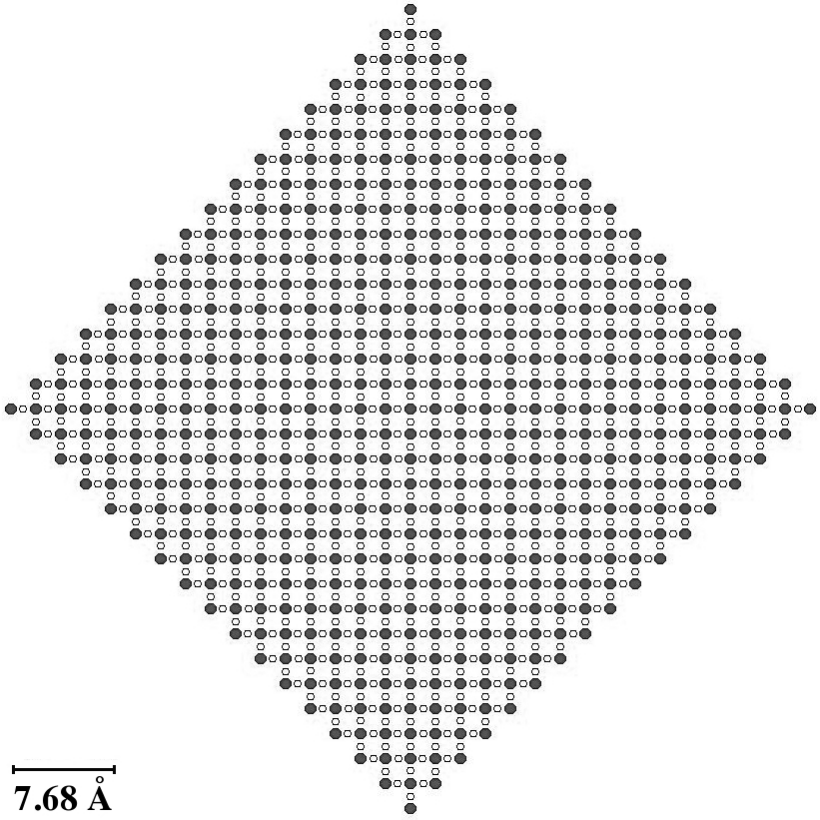

Figure 9-33: The arrangement of β-cristobalite on Si(100), in a top view, rotated by 45° about the (001) plane. The Si in the β-cristobalite are shown in dark gray, the oxygen are white, and the Si(100) atoms are light gray.

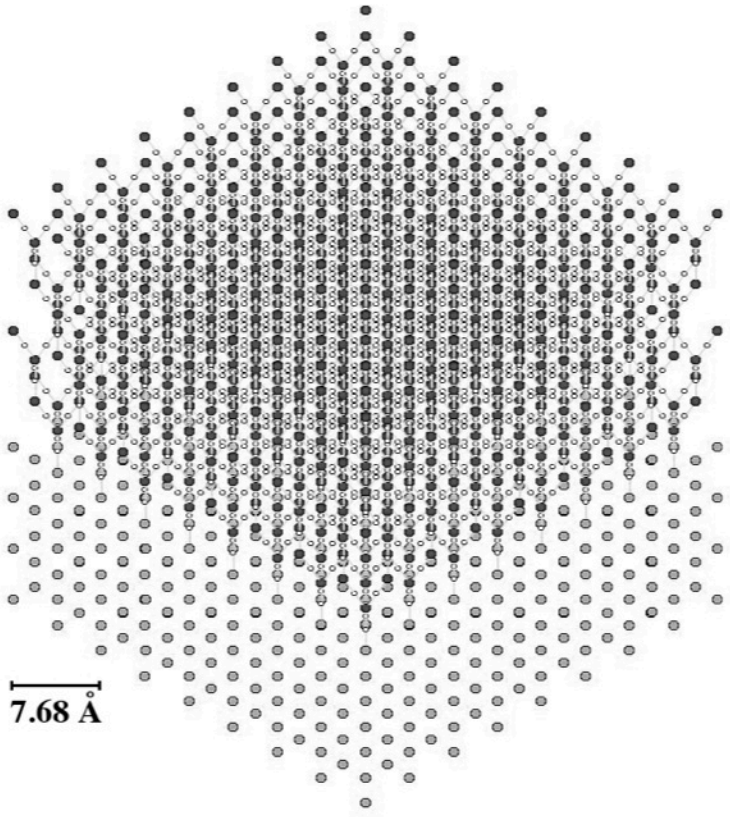

Figure 9-34: The arrangement of β-cristobalite on Si(100), in the <111> orientation. The Si in the β-cristobalite are shown in dark gray, the oxygen are white, and the Si(100) atoms are light gray.

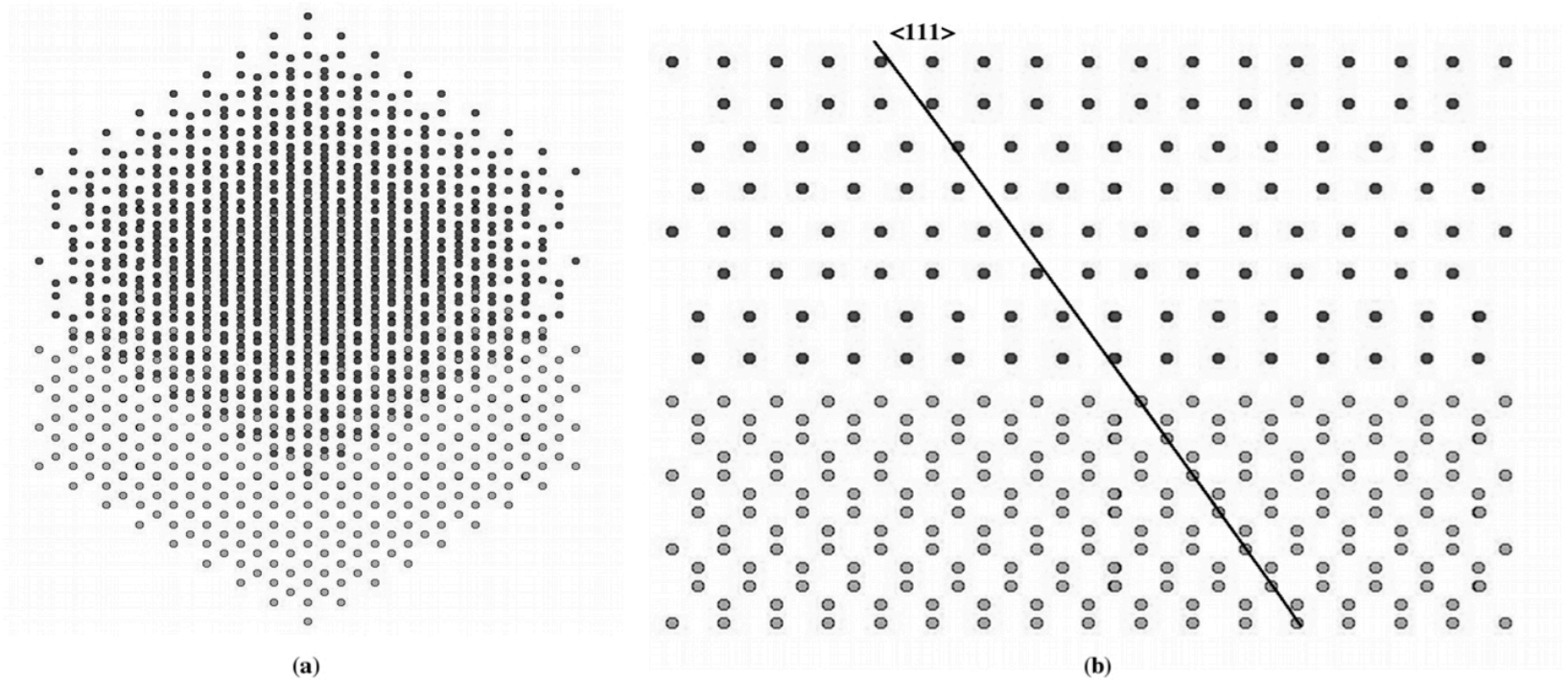

Figure 9-35: The arrangement of β-cristobalite on Si(100) in the <111> orientation, without oxygen atoms and (b) the side view, rotated 45°, of the structure with a black line signifying the current <111> perspective. The Si in the β-cristobalite are shown in dark gray and the Si(100) atoms are light gray.

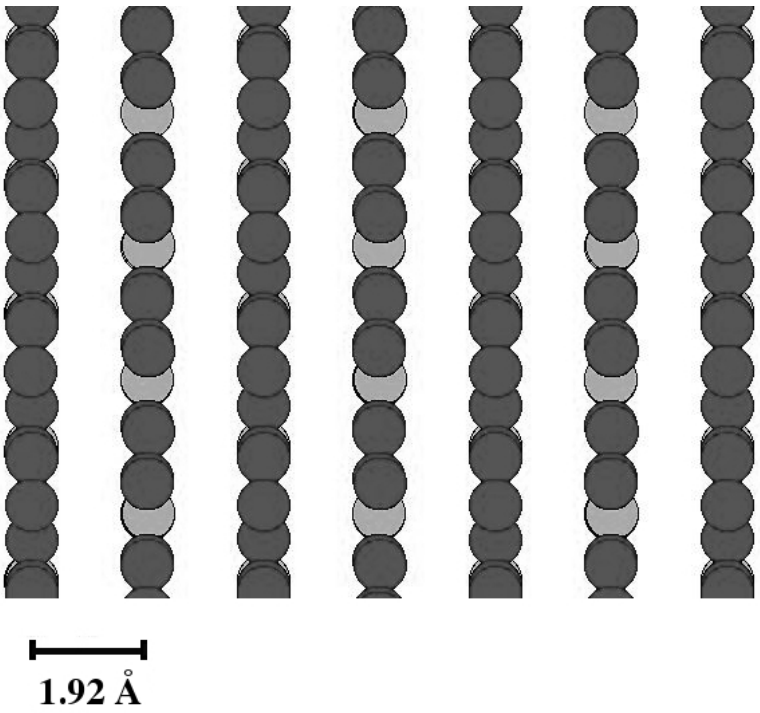

Figure 9-36: An enlargement of the of the area of the arrangement of β-cristobalite on Si(100) in the <111> orientation, without oxygen atoms. The complex nature of this perspective is apparent. The Si in the β-cristobalite are shown in dark gray and the Si(100) atoms are light gray.

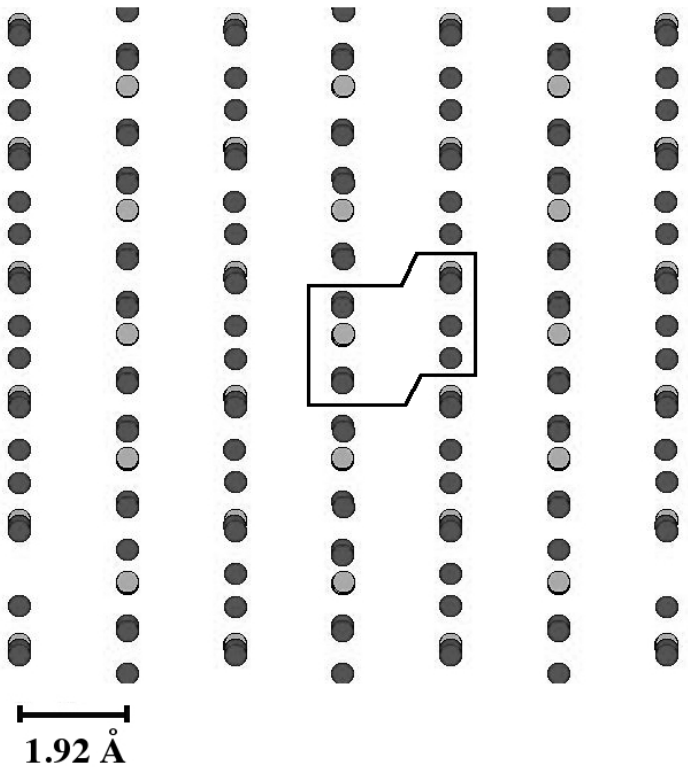

Figure 9-37: An enlargement of the of the area of the arrangement of β-cristobalite on Si(100) in the <111> orientation, without oxygen atoms. The radii of the atoms has been reduced, so that the repetitive characteristic of the structure can be observed. A black line surrounds the basic cell of the area in the middle section of the figure. The Si in the β-cristobalite are shown in dark gray and the Si(100) atoms are light gray.

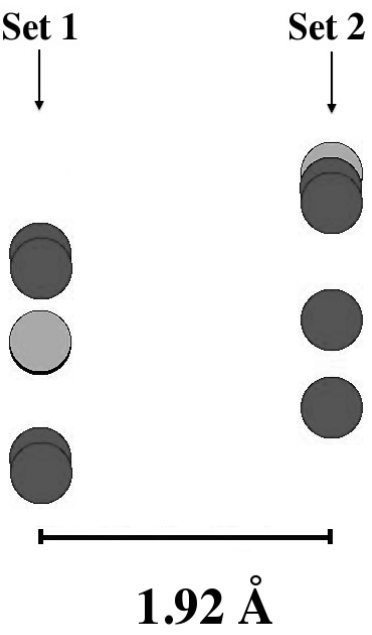

Figure 9-38: An further enlargement of the surrounds the basic cell in the area from the arrangement of β-cristobalite on Si(100) in the <111> orientation, without oxygen atoms. All other atoms have been removed. The Si in the β-cristobalite are shown in dark gray and the Si(100) atoms are light gray.

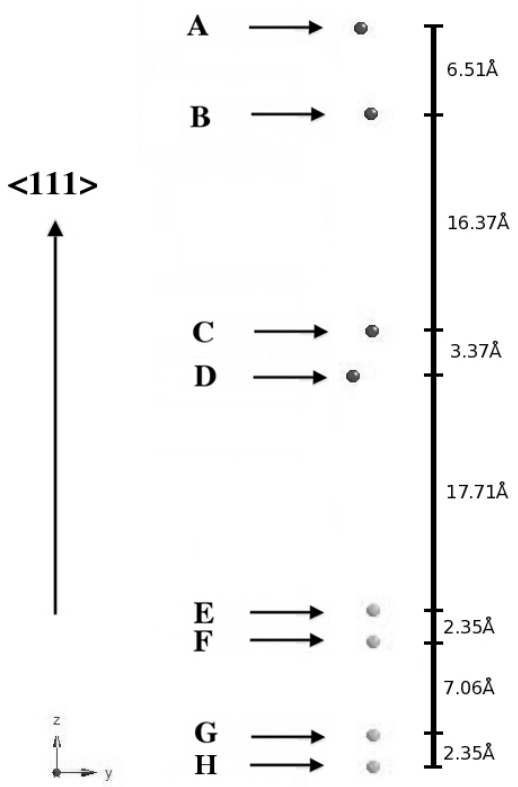

Figure 9-39: Visual representation of Set 2 of the <111> direction. The Si in the β-cristobalite are shown in dark gray and the Si(100) atoms are light gray. The z direction is the <111> direction.

Atom Type	y (Å)	z (Å)
(A) β-cristobalite Si	0.57	55.72
(B) β-cristobalite Si	1.34	49.21
(C) β-cristobalite Si	1.44	32.84
(D) β-cristobalite Si	0.00	29.47
(E) Si(100)	1.54	11.76
(F) Si(100)	1.54	9.41
(G) Si(100)	1.54	2.35
(H) Si(100)	1.54	0.00

Table 9-7: Set 2 for <111> direction relative coordinates, in Angstroms, for β-cristobalite on Si(100) in the <111> orientation.

Atom Type	Absolute Distance along <111> axis(Å)	Shadow cone Radius (Å)	Horizontal Distance (Å)
(B) β-cristobalite Si	0.00	0.00	----
(C) β-cristobalite Si	16.38	0.09	0.10
(D) β-cristobalite Si	19.74	0.10	-1.34
(E) Si(100)	37.46	0.14	0.19
(F) Si(100)	39.81	0.15	0.19
(G) Si(100)	46.86	0.16	0.19
(H) Si(100)	49.21	0.16	0.19

Table 9-8: Shadowcone Radii for z distances, which is the <111> direction, for a 3.05 MeV He^{++} atom interacting with the (B) β-cristobalite Si atom of Set 2.

Atom Type	Absolute Distance along <111> axis(Å)	Shadowcone Radius (Å)	Horizontal Distance (Å)
(C) β-cristobalite Si	0.00	0.00	----
(D) β-cristobalite Si	3.37	0.04	-1.44
(E) Si(100)	21.08	0.11	0.09
(F) Si(100)	23.43	0.11	0.09
(G) Si(100)	30.48	0.13	0.09
(H) Si(100)	32.84	0.13	0.09

Table 9-9: Shadowcone Radii for z distances, which is the <111> direction, for a 3.05 MeV He^{++} atom interacting with the (C) β-cristobalite Si atom of Set 2.

9.3c Conclusion of Shadow Cones for Density Conserved b-cristobalite on Si(100)

The <100> orientation of the density conserved β-cristobalite on Si(100), Figure 9-27, shows a model with perfect Si atom alignment. This means that IBA would obtain a 0.5 slope for the amorphous oxide and the β-cristobalite with no disorder at the interface, since there are two crystal structures meeting at the surface of the Si(100). This matches the IBA data presented in Figure 9-18(a) [1].

The <110> direction shows shadowing of Si(100) atoms near the interface due to the (A) β-cristobalite Si atom of set 4, shown in Table 9-6, when including the thermal vibration of 0.075Å at 293K of the Si atoms. This suggests that the density conserved β-cristobalite may match the IBA data in the <110> direction in Figure 9-18(b).

In the <111> direction there is has shadowing from two β-cristobalite Si atoms in Set 2, shown in Tables 9-8 and 9-9, when accounting for Si thermal vibration. The <111> direction IBA results show a portion on the surface Si in the Si(100) crystal to be shadowed. This suggests that the density conserved β-cristobalite may match the IBA data in the <111> direction in Figure 9-18(c).

9.4 Conclusions of Shadow Cones of Various β-cristobalite Models on Si(100)

As the data has shown, The β-cristobalite(110) and the volume conserved β-cristobalite both have shadowing which is similar what is necessary to produce the IBA data. The β-cristobalite that is elongated does not meet those requirements. Therefore, further study of the β-cristobalite(110) and the volume conserved β-cristobalite is necessary to determine the nature of the ordered oxide at the interface after H-A method processing of Si(100).

Chapter 9 References

[1] J. M. Shaw, N. Herbots, Q. B. Hurst, D. Bradley, R. J. Culbertson, V. Atluri, K. T. Queeney, *J. Appl. Phys*. **100**, 10, 104-109 (2006)

[2] W. K. Chu, J. W. Mayer, M. A. Nicolet, *Backscattering spectrometry*, Academic Press (1978)

[3] J.D. Bradley, *A new heteroepitaxial silicon dioxide nanophase on OH-(1X1) silicon (100) identified via 3.05 MEV ion channeling and the new 3-D multistring code*, Arizona State University, Ph. D. Thesis 2006

[4] Q. B. Hurst , *Ordering at the silicon (001)-silicon dioxide interface as studied by ion beam analysis*, Arizona State University, Ph. D. Thesis 2000

Chapter 10: Mechanism of Si(100) to SiO_x Wafer Bonding

10.1 Previous Work

In the Motivation section of Chapter 1, a basic hypothesis was described for a mechanism of low temperature (T< 200C) bonding between Si(100) and SiOx substrates using wet chemistry. In Chapter 3, the H-A clean of Si(100) and previous published results were presented. These papers and theses demonstrate that the silicon has an ordered oxide at its surface that is of sub-micron thickness. These ordered oxide nano-films exhibit interfaces and surfaces with extended terraces wider by 1 to 2 orders of magnitude when compared to as received wafers. H-A cleaned Si(100) substrates can have a further SiO_2 layer grown on them and IBA results show that there is no disorder at the surface in the <100> direction. The <110> and <111> IBA data give evidence toward the theory that there is shadowing of a crystal SiOx structure. The thesis of J.D Bradley put forth a density conserved β-Cristobalite structure fitted to the underlying Si(100) crystal as a possible candidate for the ordered oxide at the Si interface, as explained in detail in Chapter 3. Chapter 8 described that the β-Cristobalite(110) fitted to underlying Si(100) has shadowing that may achieve the IBA results published by Dr. Herbots *et al*., making it a second possible candidate for the SI interface ordered oxide.

10.2 Work in This Thesis

This section reviews the data that has been presented in this thesis and presents a model of the bonding mechanism based on that data.

10.2a Wafer Bonding Experiments

In the wafer bonding experiments chapter, it was shown that the H-A method leaves the Si(100) surface hydrophobic. The hydrophobic surface can only exist if there are minimal free charges at the surface-water boundary. Experiments that modified the last two cleaning steps, substituting DI H_2O for Methanol, produced a hydrophilic SiO_x surface. The hydrophobic nature of the surface implies that there is free charge at the SiO_x surface, which would be dangling bonds that are created during the HF etch. A series of experiments produce a final bonding process, which minimized the wafer-to-wafer contact time and optimized the steps in the cleaning process. This leads to cleaned SiO_x and Si(100) substrates that were attracted to one another on contact and formed an preliminary bond at room temperature. The bonding pair were placed in the clamping mechanism and annealed at 180º C for 24 hr. Measurement of the bonding of a 150mm Si(100) and 5000Å thermal oxide on Si(100) wafer pair gave a minimum bonding strength of 8 MPa. The bonding test reached 8 MPa, and then the Si(100) delaminated at a crystal plane below the bonding interface, which means the bond did not fail and that the is a minimum bond strength measurement. The strong bonding between the two interfaces suggests that they

are physically connected such that the individual separated interfaces no longer exists in some, or all, of the original bonding plane(s).

10.2b VASP Simulations

The VASP simulations in this thesis used two structures. The first is a β-Cristobalite structure that was rotated to the <110> direction, which has been termed β-cristobalite(110). The β-cristobalite(110), conserving its volume, to a Si(100) base. The Si(100) base is 2 units cells wide, 2 units cells wide deep, and 3 unit cells high. The β-cristobalite(110) is 2 unit cells in all three directions. A 10.6Å thick amorphous silica was placed on top of the structure. The second structure consisted of a same Si(100) base with 26.4 Å thick amorphous silica on top. The VASP simulations provide data that the β-cristobalite(110) crystal structure at the interface between Si(100) and an amorphous silica was lower in energy than Si(100) and amorphous silica structure.

Abbreviation	
LDA	Local Density Approximation
GGA	Generalized-Gradient Approximation
USP	UltraSoft Potentials
PAW	Projector Augmented Wave

Table 10-1: List of Abbreviations used in the calculation types

Electronic Approximation and Atomic Potential used in Calculation	Number of Fixed Atoms in Si(100) "substrate"	Layered Nano-Bonding Phase Cell Type	Final Total Energy (eV)	Energy Difference between the Si(100)/a-SiO2 and Si(100)/ β-c SiO2/a-SiO_2 (eV)
USP-LDA	No Fixed Atoms	Si(100)/β-c SiO2/a-SiO_2	-2030.12	-2.40
USP-LDA	No Fixed Atoms	Si(100)/ a-SiO_2	-2027.72	
USP-LDA	1 Unit Cell Fixed	Si(100)/β-c SiO2/a-SiO_2	-2013.48	-6.44
USP-LDA	1 Unit Cell Fixed	Si(100))/a-SiO_2	-2007.04	
USP-LDA	2 Layers Fixed	Si(100)/β-c SiO2/a-SiO_2	-2014.88	-3.89
USP-LDA	2 Layers Fixed	Si(100)/ a-SiO_2	-2010.99	
PAW-LDA	No Fixed Atoms	Si(100)/β-c SiO2/a-SiO_2	-2037.32	-2.82
PAW-LDA	No Fixed Atoms	Si(100)/a-SiO_2	-2034.50	
PAW-LDA	1 Unit Cell Fixed	Si(100)/β-c SiO2/a-SiO_2	-2015.74	0.42
PAW-LDA	1 Unit Cell Fixed	Si(100)/a-SiO_2	-2016.16	
PAW-GGA	1 Unit Cell Fixed	Si(100)/β-c SiO2/a-SiO_2	-1842.33	-4.03
PAW-GGA	1 Unit Cell Fixed	Si(100)/a-SiO_2	-1838.30	
USP-GGA	No Fixed Atoms	Si(100)/β-c SiO2/a-SiO_2	-1808.75	**Migrating Oxygen**
USP-GGA	No Fixed Atoms	Si(100)/a-SiO_2	-1847.70	
USP-GGA	1 Unit Cell Fixed	Si(100)/β-c SiO2/a-SiO_2	-1836.47	-3.34
USP-GGA	1 Unit Cell Fixed	Si(100)/a-SiO_2	-1833.13	

Table 10-2: The data from the VASP relaxation runs. It shows that in a majority of the calculations, the energy of the Si(100) with β-cristobalite(110) and amorphous silica structure is the lower of the two models

10.2c Shadow Cone Calculations

In Chapter 9, the three structures were investigated and the shadowing during IBA using a 3.05 MeV He^{++} particle were analyzed. The first configuration was the density conserved β-Cristobalite(110) on Si(100). Examination of the alignment of the atoms in the β-Cristobalite(110) showed partial shadowing in the <110> and <111> directions, while no blocking occurs in the <100> direction. IBA data that was taken Si(100) wafers that underwent the H-A method had no blocking in the <100> direction and shadowing in the <110> and <111> directions. Therefore, the density conserved β-Cristobalite(110) on Si(100) is a possible candidate for a crystal SiO_x that exists on a Si(100) after undergoing the H-A method. The second structure consisted of the 100% stretched β-Cristobalite structure, which had no shadowing in the <100>, <110> and <111> directions. Therefore, it is not a possible fit for the IBA data and conflicts with the 3DSTRING analysis of this structure that was presented in J.D. Bradley's thesis. The final arrangement of atoms was the density conserved β-Cristobalite on Si(100). This structure showed no blocking in the <100> direction, and some shadowing of the underlying Si(100) in the <110> and <111> directions using a 3.05 MeV He^{++} particle, which concur with the IBA Data. Therefore, there are at least two possible oxide nano-phases at the Si(100) interface after processing a Si(100) substrate with the H-A method.

10.2d TMAFM Images, RMS Roughness, and PSD

The AFM characterization provided images and roughness data on the topography of the Si(100) and SiO_2 surfaces before cleaning, after cleaning and 180° C anneal, and after manual debonding.

Figure 10-1 presents top and 3-D views of 10 μm AFM height images of the As received Si(100) sample, Si(100) wafer after H-A clean and 180° C anneal sample, and Si(100) after debonding. Table 10-3 are the RMS values of the 100 nm AFM scan size images for these same three samples. Finally, Figure 10-2 shows the Power Spectral Density (PSD) for the three samples

The As Received Si(100) has RMS roughness measurements for all scan sizes that are at the lower end of all RMS data that is in this thesis, especially those for 1 μm and 100 nm scans, since both are below 0.1 nm. The AFM image shows a smooth surface with a small number of particles. This shows that the sample was handled correctly and that there were not cuts to the wafer to obtain samples. (PSD). All of the PSDs are flat, which accounts for the low RMS values.

The Si(100) sample processed with the H-A method and then annealed is smooth with a larger number of small particles. This sample is a portion of a wafer that was bonded to a thermal wafer, so the additional handling after the anneal, which included debonding of the thermal wafer, could add particles**.** The clean has increased the RMS roughness in the 100nm scan size by 60%, but that is only a 0.05 nm increase in the RMS, so the sample is still smooth, as shown in the AFM scans. The averaged PSD of the Si(100) after H-A processing show a more

complex comparison to the As Received Si(100). The processed surface PSD has greater power at wavelengths greater than 0.0067 μm wavelength, but the two PSDs are intertwined at wavelengths below 0.0067μm. The peak of the H-A processed and annealed sample is 02 μm, or 20 nm, which is the same as the step width seen in the HRTEM of H-A processed Si(100) samples.

The AFM images of the Si(100) surface after debonding show a discernable roughened topography. The 100 nm scan size has a RMS roughness that is approximately five and a half times larger than either the as received wafer or the clean substrate. The average PSD of the debonded surface is also has a larger power at every wavelength above 0.001 μm. At smaller wavelengths, it somewhat interlaces with the two other PSDs.

Figure 10-3 presents the top view and 3-D views of 10 μm AFM height images of the As Received 5000Å Thermal Oxide sample, 5000Å Thermal Oxide sample after H2BWSC clean + 180° C Anneal, and a 5000Å Thermal Oxide sample after processing and deboding. Table 10-2 are the RMS values of the 100 nm AFM scan size images for these same three samples. Finally, Figure 10-4 shows the Power Spectral Density (PSD) for the three samples

The scans of the 5000Å Thermal Oxide on Si(100) are somewhat different. The As Received thermal oxide is very smooth, with an RMS roughness that is 9% lower than that of the cleaned Si(100). This is expected, since the thermal

oxide is conformal. There are multiple particulates on the surface, somewhat higher than what is seen on the Si(100) As Received wafer.

When the thermal oxide wafer is cleaned using the H2BWSC process and annealed, the surface roughness increases. The RMS roughness is 32% higher for the cleaned sample versus the thermal oxide as received. Comparing the average PSDs of the thermal oxide as received and after clean, it is seen that cleaned surface has higher power, in general, for wavelengths below 0.02 mm. This shows that the surface is roughening overall, but has less long range features, which coincides with the 10 mm image showing a large amount of shallow depressions. These depressions are about 5 nm deep. The debonded thermal oxide shows another increase of approximately 30% in RMS roughness. The average PSD of the debonded sample is the highest of the thermal oxide samples between wavelengths of 0.0333 μm to 0.0056 μm, where it entwined with the average PSD of the cleaned wafer. The 10 μm image shows a surface with multiple protrusions that are higher than those seen on the cleaned thermal oxide surface.

Figure 10-5 presents the AFM 10 μm scans of Si(100) samples which underwent H-A clean + 180º C Anneal, H-A clean, and H-A Spin Etch clean. All the samples appear smooth at this scan size with varying particle sizes and counts. Table 10-5 are the RMS values of the 100 nm AFM scan size images for these Si(100) samples. This data shows that the H-A clean produces a smooth surface with a RMS $\leq$ 0.1 nm for 100 nm scan size. This is only 13% higher than the As Received sample. The 180º C anneal increases the roughness after the H-A clean

by approximately 30%. The H-A Spin etch clean reduces the Si RMS roughness by 30% versus the H-A clean, showing that is an improvement using this metric.

Figure 10-6 presents the PSD graphs for Si(100) processed with the H-A Spin Etch Clean, the H-A Clean and 180º C Anneal, and the H-A clean . This data show the same trends as the RMS roughness data, but it reveals that the H-A Spin Etch is lower in power at nearly all wavelengths. Both the H-A process sample and the H-A process and annealed sample peak at 20 nm, the same as the step width of H-A processed Si(100) observed via HRTEM. The H-A Spin Etch sample peak is at 30 nm, which suggests that the Spin Etch process not only smooths the surface, but also increase the step width from 20 nm to 30 nm.

The TMAFM data shows that the H-A cleaned surface is smooth, RMS $\leq$ 0.1 nm, and that debonding roughens the surface. The thermal oxide surface is roughened by the cleaning process and the surface has more defects after debonding, with a higher RMS roughness. The roughening of both debonded surfaces suggests that each interface had a physical link that was disrupted during the debonding. The bonding experiments produce the data that the Si(100) is hydrophobic after clean, the thermal oxide is hydrophilic once processed, and the two interfaces are attracted to one another when they are put into contact. This is in line with the proposal that the thermal oxide dangling bonds partially polarize the Si(100) surface and an attractive force occurs. The two possible β-Cristobalite structures offer a basis upon which a bridge could be built between the interfaces.

10.3 Data from Herbots' Group Members

The following section presents data taken by several members of the Herbots' Group. The analysis presented here is a novel combination of all of the data and is the first time it is evaluate with respect to nano-bonding.

10.3a Contact Angle Measurements and Surface Free Energy

In section 6.4d, a detailed the background of contact angle and Surface Free Energy is presented. That derivation of the calculation of the Surface Free Energy was used to obtain the data presented in this section.

Tables 10-4 through 10-7 presents data from contact angle measurements for three liquids on Si(100) that either have not received processing, the As Received Si(100), or have undergone various process steps. The tables contain the contact angles, θ, that were measured with two polar liquids, 2MΩ DI water and the hygroscopic glycerin ($C_3H_8O_3$), and the non-polar liquid, a-bromo-naphathalene, to isolate the three free energy components. Using Eq. 10-7 with these contact angles, the Si(100) solid surface γ^{LW}, γ^{+}, and γ^{-} can be calculated, since the γ^{LW}, γ^{+}, and γ^{-} for each of the three liquids are known.

Table 10-6 presents the contact angle measurements with three liquids, 2 MΩ DI Water , Glyercin, and α-Bromonaphtalene, for two As Received Si(100) surfaces measured by memebrs of the Herbots' Group.. Also shown are the resulting experimental values of the total surface free energy (a.k.a Surface tension) in mJ/m^2 derived from the data. Finally, a Total Surface Free Energy of a cut Si(100) wafer published by Faibish et al [2] is presented. In general, the two

Si(100) studied by the Herbots' Group have the same measurements for the three contact angles and therefore have the same Total Free Surface Energy. This measurement is more than 25% lower than the Faibish measurement.

Table 10-7 presents the contact angle measurements with the three different liquids for Si(100) surfaces after H-A method and other processing. There is a large difference in the Contact Angle between α-Bromonaphtalene and Si(100) Surface when comparing the uncut and cut wafer after H-A method processing. The anneal has also increased all of the contact angles and therefore there is a large decrease in the Total Surface Free Energy.

The contact angle measurements with three different liquids for two As Received Si(100) samples that underwent Ion Beam Modification of Materials surfaces (IBMM) during IBA are shown in Table 10-8. IBMM entails repeated IBA of the surface. The averages of the two samples are also shown in the table. The contact angles, all three components of the Free energy, and the Total Surface Free Energy are the same for the two samples, within the experimental error. The 45.0 ± 1.0 mJ/m^2 average Total Free Surface Energy is approximately 22% lower than the same type of measurements on the As Received Si(100) before IBMM. The difference is primarily accounted for by the lowering of both the Electron Donor Component of the Surface Free Energy and the Electron Acceptor Component of the Surface Free Energy. This suggest that the IBMM is affecting the bonds near the surface so that the bonds are changed in the lattice such that the

acceptor and donor atoms are bonding and removing free electroms, and holes, from the crystal structure.

Table 10-9 shows the contact angle measurements with three different liquids for Si(100) surfaces for two samples, H-A method after IBMM and H-A Method and 180º C Anneal after IBMM. The H-A method after IBMM sample can be compared to the two H-A method samples in Table 10-2. The IBMM sample has higher contact angles for the 2 MΩ DI Water and Glyercin, but lower for the α-Bromonaphtalene than those of the samples without IBMM. This primarily changes γ^{LW}, where the IBMM sample has nearly 41 mJ/m^2, where the two samples without IBMM in Table 10-2 are at approximately 31 mJ/m^2 and 39 mJ/m^2. This causes the sample with IBMM to have a higher Total Surface Free Energy than those samples without IBMM. The higher γ^{LW} means that the IBMM has created more dipoles at the surface of a sample that has been processed with the H-A method. The H-A method and anneal sample with IBMM can be compared to the H-A method sample from Table 10-4. The IBMM sample has lower contact angles for the 2 MΩ DI Water, Glyercin and α-Bromonaphtalene. The IBMM increases the Lifshitz-Van der Waals and Electron Donor components of the Surface Free Energy and therefore the Total Surface Free Energy.

Table 10-10 presents the contact angle measurements with three different liquids for As-Received Si(100) surfaces, both cut and uncut. Also presented is the difference between the contact angle, components of the Surface Free Energy, and the Total Surface Free Energy. The contact angles for Glyercin and α-

Bromonaphtalene, all three components of the Free energy, and the Total Surface Free Energy are the same for the two As Received samples, within the experimental error. The difference between the 2 MΩ DI Water is significant, but is not large enough to deviate the Total Surface Free Energy difference outside the error of the measurements.

The contact angle measurements with three different liquids for Si(100) surfaces after H-A method processing, both cut and uncut, and the difference between the contact angle, components of the Surface Free Energy, and the Total Surface Free Energy are shown in Table 10-11. The α-Bromonaphtalene contact angle shows a large deviation that is significant, while the 2 MΩ DI Water, Electron Donor Component of the surface free energy, Lifshitz-Van der Waals Component of the surface free energy, and the Total Surface Free Energy all show significant, but smaller, deviations. This suggest that cutting the sample may change the Total Free Surface Energy.

The data from Table 10-10 shows that the average Total Free Surface Energy of the cut and uncut As Received Si(100) is 57. ±1. mJ/m^2. The Total Free Surface Energy of Si(100) after processing by the H-A method can not be averaged due to the a large difference in the contact angle between α-Bromonaphtalene and the Si(100) Surface when comparing the uncut and cut wafer. But, the 39 ± 2. mJ/m^2 for the cut wafer and the 42.4 ± 0.6 mJ/m^2 for the uncut wafer show a reduction of at least 25%. The H-A Method and 180º C Anneal in Air is a reduction of approximately 55% from the Total Free Surface

Energy of the As Received Si(100) and is at least a 30% reduction from that of the H-A method processed wafer. This is showing that the H-A method reduces the surface energy and the anneal reduces it further due to the densification of oxidation in a dry ambient. This progression follows the hypothesis made of a more ordered Si surface. There is also a large difference between the Acceptor Component of the Surface Free Energy in the As Received Si(100) samples, which average 32 ± 2 mJ/m^2, and Si(100) samples, which average 13. ± 1.4 mJ/m^2. Since the initial wafers for both of these sample types were p-type, this indicates that near surface acceptor compounds are being removed and/or saturation of unsaturated bonds during the H-A method processing.

The difference in the cut and uncut samples processed by the H-A method suggest that these surfaces are exhibiting a statistical significant difference the two, which translates into a difference of approaching 10% for total surface energy values. These results translates into wafers surfaces yielding about 10% more hydrophilic values than cut pieces

10.3b Steam Nano-bonding and Surface Free Energy

During the last few month, Dr. Herbots and several of her students have begun experiments in a new type of nano-bonding. These investigations use Si(100) wafer that have undergone H-A method processing in the past and 5000 Å thermal oxide wafers that are briefly exposed to a HF:H_2O bath. This HF etch is to deplete oxygen at the surface of the oxide wafer.

The Si(100) substrate are contacted with sections of 5000 Å thermal oxide wafers and then placed in a stainless steel pressure vessel. Teflon insert are used to hold the edges of the samples in the container. At this point, water is heated to boiling and introduced into the vessel via a Teflon gas line. The steam that enters into the container both enables the reaction between the surfaces and also provides a system to provide contact of the two substrates with even pressure. This has proved to be a promising possibility to produce nano-bonding and is called "Steam Nano-bonding". Several experiments have been performed and contact angle data has been obtained on a few samples to determine the Surface Free Energy.

Table 10-12 shows two portions of a Si(100) that previously was processed with the Spin-Etch H-A Method and then underwent 180° C Steam Nano-Bonding Anneal. One portion, the uncovered, had no oxide placed on top in these are where contact angle measurements were taken. The second had an oxide wafer in contact in the area, but no bonding occurred. They show that the Total Surface Free Energy is approximately the same as the H-A method processed wafers, all of which are very close to 40 mJ/m^2. But, the Electron Donor and Electron Acceptor Components of the Surface Free Energy have changed. The electron donor contribution increases from near 0 mJ/m^2 to 30 mJ/m^2, which means the surface is dramatically enriched in negative charge carriers, such as OH^-. The electron acceptor component goes to 0 mJ/m^2, which is expected if Boron acceptors are oxidized, as happens more easily in steam oxidation.

10.4 Poisson's Ratio

Poisson's ratio, υ, for a material is a the proportion of lateral strain, ε', to the axial strain, ε, as show in Eq. 10-9 [7].

$$\nu = -\frac{lateral\ strain}{axial\ strain} = -\frac{\varepsilon'}{\varepsilon} \qquad \text{(Eq.10-9)}$$

The negative sign in the equation compensates for the fact that lateral strain and axial strain typically have opposite signs.

10.4a Poisson's Ratio in Bulk Phase β-cristobalite Crystals

In a paper, Tomakova calculated stereographic projections of the Poisson ratio for a series of crystals, which included bulk phase β-cristobalite [8]. Figure 10-7 approximately replicates a portion of a figure from that paper, which is the stereographic projection of the Poisson's ratio for β-cristobalite in the bulk phase. It shows the Poisson ratio for compression and expansion in both the [100] direction, which is shown on the x-axis, and in the [010] direction, shown in the y-axis. Each axis is a portion of the compression up to 40%, which is shown on the graph as -0.4 , and the expansion up to 40%, shown as 0.4. The center of the graph is at a Poisson ratio of 0.106. The ratio increases along the lateral and horizontal, but decreases in the four diagonal directions. Each line is a difference of approximately 0.35.

The Poisson ratio for β-cristobalite fitted to Si(100) requires compression of the crystal along the x and y axes of the crystal from 7.166 Å to 5.43 Å, which is a 24% compression, or -0.24 for this graph, in both direction.

Using Figure 10-7, this shows a ratio of 0.106, which means that the β-cristobalite elongates only 10.6% of the distance necessary to conserve volume from its original height of 7.166 Å as it is compressed to fit Si(100). Therefore, the β-cristobalite expands an additional 5.31 Å when fitting to Si(100) and conserving volume. Using this data, the expansion is 0.563 Å, resulting in a crystal that has a height of 7.73 Å.

For the β-cristobalite(110), the two base axes are expanded from 5.067 Å to 5.43 Å. Since this crystal has been rotated 45º from the original orientation, this expands the original x and y axes from 7.166 Å to 7.616 Å. This is a 7% expansion, or 0.07 for the graph, in each direction, resulting 0.106 Poisson ratio, according to the graph. So the β-cristobalite(110) contracts 10.6% of the distance necessary to conserve volume from its original height of 7.166 Å. So, the β-cristobalite(110) contracts approximately 0.1 Å in height when the base is fitted to Si(100). This results in a crystal with a height of 7.068 Å.

It should be noted that these Poisson ratios are calculated based on data from the bulk phase of β-cristobalite. Since this thesis deals with a nano-phase of this material, these ratios may or may not hold. What can be noted is that the final crystal heights created by fitting the β-cristobalite base to Si(100) could be calculated and used in a simulation to compare to previous results, along with the density conserved models created in this thesis.

10.5 Proposed Bonding Mechanism

Using these conclusions from the analysis of the data presented in this thesis, a mechanism for the bonding of Si(100) surface with a silicate. When a -OH or –H terminated ordered silicate nano-phase on Si(100) are put into contact with an oxygen-deficient silicate phase, they may drive an interface facilitated chemical reactions between the two substrates in an oxidizing ambient when the correct conditions occurs. Interface controlled chemical reactions can nucleate and grow a cross-bonding inter-phase between the two substrates that achieves nano-bonding between pairs of wafers or substrates of Si and silica. The term inter-phase means a phase of a material between the two phases of the materials that have been bonded. It is a spatial arrangement of bound molecules in a specific geometry constrained in space by two other materials phases. In other words, an inter-phase has no free surface, unlike a thin film, and is not an interface whose definition is simply the geometric location of a boundary between two materials phases.

The ordered silicate on Si(100) is a inter-phase at room temperature and above. Interphases are synthesized sequentially in the form of molecular (two-dimensional) sheets with a thickness ranging between 0.5 nm to approximately 40 nm. The nano-bonding forms cross-bonding molecules, which condense into a continuous macroscopic phase across the two surfaces when they are put into direct mechanical contact. This leads to a continuous, hermetic two-dimensional inter-phase that grows over more than hundreds of inter-atomic distances along

the geometric interface as well as a few interatomic distances bridging between the two wafer surfaces.

At the microscopic scale, atomic steps are typically found every 2 nm on Si wafers with mis-cuts < 0.025° off the crystal axis. By extending the atomic terraces widths by an order of magnitude using the H-A method, such steps average of 20 nm wide, as shown in Chapter 3. Therefore, discontinuities in the cross-bonding phase that typically occur every 4 to 5 inter-atomic distances decrease to one every 45 interatomic distances. In other words, the cross-bond density in the two-dimensional nano-phase increases by two orders of magnitude. The nano-phase is now truly two-dimensional as continuous, ordered arrays of bonds form in surface domains of the order of 20 nm in diameter instead of approximately 2 nm.

The interphase thickness can vary form one to tens of interatomic distances or molecules, but whose aspect ratio, width/thickness, is clearly > 4. In order words, contains more than 4 molecular cross-bridges at a location where the phase may be only intermolecular layer thick. A non-2-D interphase may have aspect ratio equal to 1, which would be considerably weaker a bond.

Given that the cross-bonding nano-phase thickness can vary from 2 nm up to greater than 10 nm or more, only domains at least 20 nm in lateral extension can be described as a two-dimensional layer in contrast to the scattered three-dimensional phase of coalescing bonds found with rougher substrates.

Bonding of substrates surfaces smoothed at the nano-scale with low particulate densities can result in a bonding strength larger than 8 MPa/cm^2, as measured by mechanical bond pull tests. At such bonding strengths, wafer breakage within the bulk of both Si and silicate substrates is observed before interface delamination ever takes place. The bond strength of the inter-phase is expected to increase with the square of the atomic terrace width, resulting in a two order of magnitude increase compared to bonding with conventionally processed substrates. This has been shown in this thesis that this is indeed observed experimentally.

The bonding experiments described in this thesis placed a -OH or –H terminated ordered silicate nano-phase on Si(100) in direct mechanical contact with an oxygen-deficient silicate phase at both the macroscopic and the microscopic scale in an oxidizing ambient at $\leq$ 200°C. This allowed a local chemical reaction can be initiated between the ordered Si oxides on Si(100) and oxygen deficient SiO_2. The result is the nucleation and growth of a two-dimensional inter-phase between the two substrates.

Oxidation rates on Si(100) surfaces are isotropic and are orders of magnitude larger along the surface as compared to oxidation bulk. The large lateral oxidation rate acts like an atomic-scale tsunami smoothing obstacles in its wake and progressive flattening of the surface as the oxidation progresses. For thick (> 10 μm) oxide films and silica substrates, the final surface is more akin to

a smooth liquid surface due to the vitreous nature of thermal oxides and amorphous silica, and its atomic-scale smoothness is unparalleled.

The final etch steps of the H2BWSC process on silica depletes oxygen and makes the silica surface more reactive at low temperatures ($120°C \leq T \leq 180°$ C). This increased reactivity drives the nucleation and growth of the nano-bonding inter-phase between the two substrates by re-oxidizing the silica and creating cross-bonding silica bridges between the SiO_2 and the -OH or –H terminated ordered silicate nano-phase on Si(100).

Figure 10-8 shows three structures. The first is Si(100) with density conserved β-cristobalite –OH terminated, O_2 and H_2O molecules, and amorphous silica with dangling bonds on Si(100). The second is nearly identical to the first, but having β-cristobalite –H terminated. The third structure is Si(100) with density conserved β-cristobalite bonded to amorphous silica on Si(100).

Figure 10-9 is similar to the previous figure, but with β-cristobalite(110) instead of β-cristobalite. These two figures are a visual representation of the bonding mechanism discussed in this section of the thesis.

Figure 10-10 presents that bonded structures from Figure 10-8 and 10-9. This allows comparison of the two models. As can be seen in the figures, the two layers of β-cristobalite(110), at 12.48 Å, is ½ the height of the two layers of β-cristobalite. There is FTIR data, which was initially presented in Chapter 3, which is shown Figure 10-11, which compares the longitudinal-optic (LO) and transverse-optic (TO) peak frequencies as a function of film thickness for the H-A

cleaned substrate and the RCA cleaned substrates. The TO frequencies are show a narrow band of frequencies as the oxide on the H-A method processed wafer at and below 10 Å thickness. This points to an ordered oxide on the surface that is approximately 10 Å thick, which is what has been modeled by the β-cristobalite(110) in this thesis.

In final analysis, the present thesis has produced a detailed structural understanding of nano-bonding interphases mechanism of nucleation, formation and growth during the process of Si-based wafer nano-bonding. We have modeled the arrangement of the four phases found to be involved: Si(100), beta-cristobalite, cross-bridging SiO_2, amorphous SiO_2. By carefully analyzing and combining structure and phase information from previous IBA and IR with our TMAFM analysis, nano-bonding experiments, shadowcone calculations, and surface energy measurements.

The final figure of this work, Figure 10-12, depicts one of the structural arrangements we have established for nano-bonding, for the case of beta-cristobalite(110). This shows a smooth Si(100) base that has wide terraces that are 20 nm in width, as aspected from a H-A processed Si(100) substrate. The top Si(100) has an amorphous silica initially grown on it. Since the Si(100) wafers with silica that were received from manufacturers in this thesis were not process with the H-A method before silica was grown, this silicon substrate is shown with the 2nm step width that would be expected. The nano-bonding process proceeds in a lateral direction and is shown as an incomplete bonding on the right hand

side. This may continue, or it may stop at this point, due to the kinetics of the bridging.

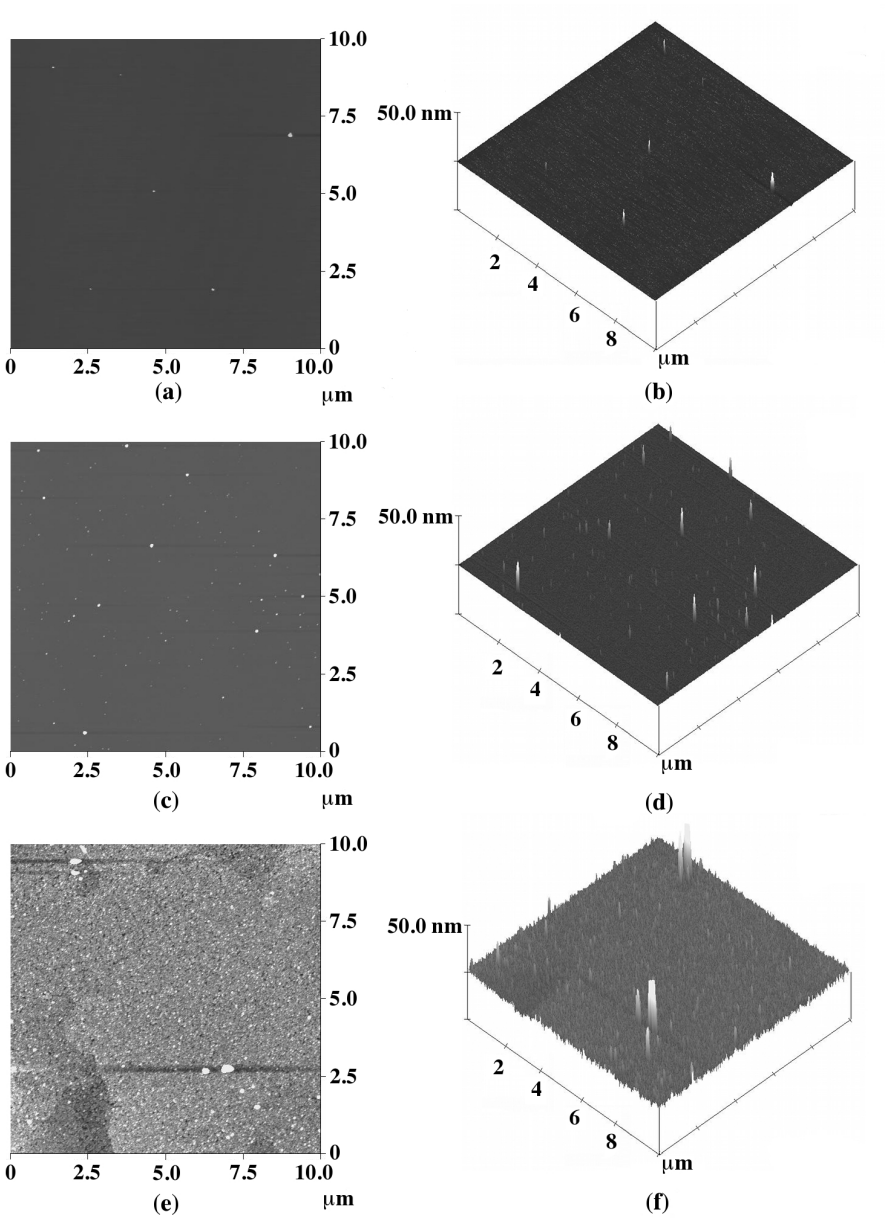

Figure 10-1: Top View and 3-D views of 10 μm AFM height images of three Si(100) wafer samples. The As Received Si wafer images (a-b) have a smooth surface. The images of a Si wafer after H-A clean and 180° C anneal (c-d) shows a small increase in particulates and a smooth surface. The AFM scans of a Si(100) after debonding (e-f) demonstrate that the surface has been roughened and transformed by the debonding process.

Si(100) Wafer Processing Step	RMS (nm) Position 1	RMS (nm) Position 2	RMS (nm) Position 3	Average RMS (nm) ± Std Dev.	Relative Change to As Received ± Fluctuation
As Received	0.09	0.08	0.07	0.08 ± 0.01	1.0 ± 0.1
H-A processed + 180° C Nano-Bonding Anneal (> 2 hrs)	0.12	0.17	0.11	0.13 ± 0.03	1.6 ± 0.3 (60 % rougher, 300% more fluctuation)
After Mechanical Debonding	0.87	0.100	0.38	0.45 ± 0.4	5.6 ± 4.0 (560 % rougher,4000% more fluctuation)

Table 10-3: The RMS values of the 100 nm AFM scan size images for Si(100) at each key Nano-bonding step. The 100 nm scan size is used to compare the Si roughness of images collected between large particulates. The table numerically confirms that the Si(100) wafer becomes smoother after the combination of H-A method and 180º C anneal. The de-bonded wafer is roughened substantially to a level that is three times the As Received wafer and suggests that the surface has been modified by the debonding.

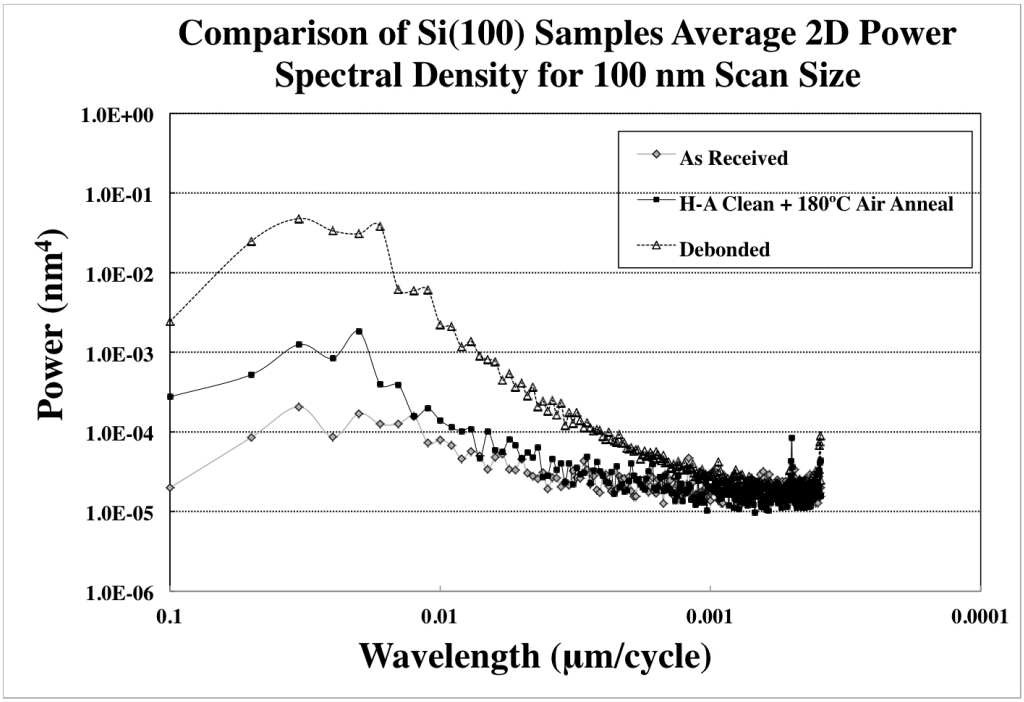

Figure 10-2: The two dimensional Power Spectral Density (2D PSD) graphs of the As Received Si(100) wafer , Si(100) wafer after H-A clean and 180° C anneal, and Si(100) after Debonding. Each PSD is an average of three AFM images collected for the separate sample types. The graph plainly indicates that the Si in the de-bonded sample has been roughened at all wavelengths, indicated by higher power, above 0.002 µm. This indicates a change the topography of the sample.

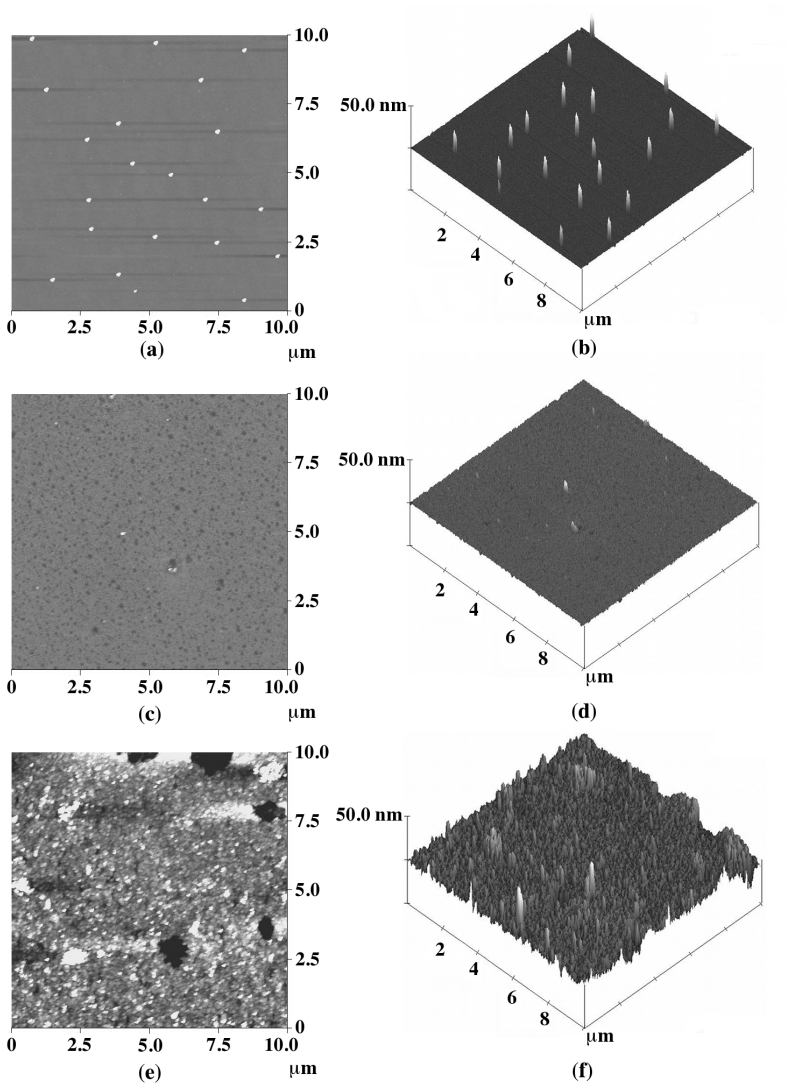

Figure 10-3: Top view and 3-D views of 10 μm AFM height images of various 5000Å Thermal Oxide samples. The As Received Oxide images (a-b) are a smooth surface with some particles. An Oxide wafer after H2BWSC clean + 180**°** C Anneal (c-d) becomes somewhat roughen due to HF etch. After Debonding (e-f), the topography of the Oxide wafer is entirely changed, with pits and raised areas, indicating that the surface has undergone a extensive modification due to the mechanical reversal of the bonding.

SiO_2 Thermal Oxide Processing Step	RMS (nm) Position 1	RMS (nm) Position 2	RMS (nm) Position 3	Average RMS (nm) ± Std Dev.	Relative Change to As Received ± Fluctuation
As Received	0.06	0.08	0.07	0.07 ± 0.01	1.0 ± 0.1
H2BWSC processed + 180º C Nano-Bonding Anneal (> 2 hrs)	0.12	0.08	0.09	0.1 ± 0.02	1.4 ± 0.2 (140 % rougher, 200% more fluctuation)
After Mechanical Debonding	0.14	0.17	0.37	0.23 ± 0.13	3.3 ± 0.7 (330 % rougher, 1300% more fluctuation)

Table 10-4: RMS values of the 100 nm AFM scan size images for the 5000Å Thermal Oxide at major Nano-bonding steps. The table shows a low RMS for the As Received Oxide wafer, which has a RMS value that is 12% less than that of the Si(100) As Received wafer. The HF etch and subsequent anneal produce samples that are 40% rougher, but still maintain an RMS less than the Si(100) As Received sample. The Mechanical de-bonding radically changes the surface topology and produces a three times rougher surface with an extremely high fluctuation.

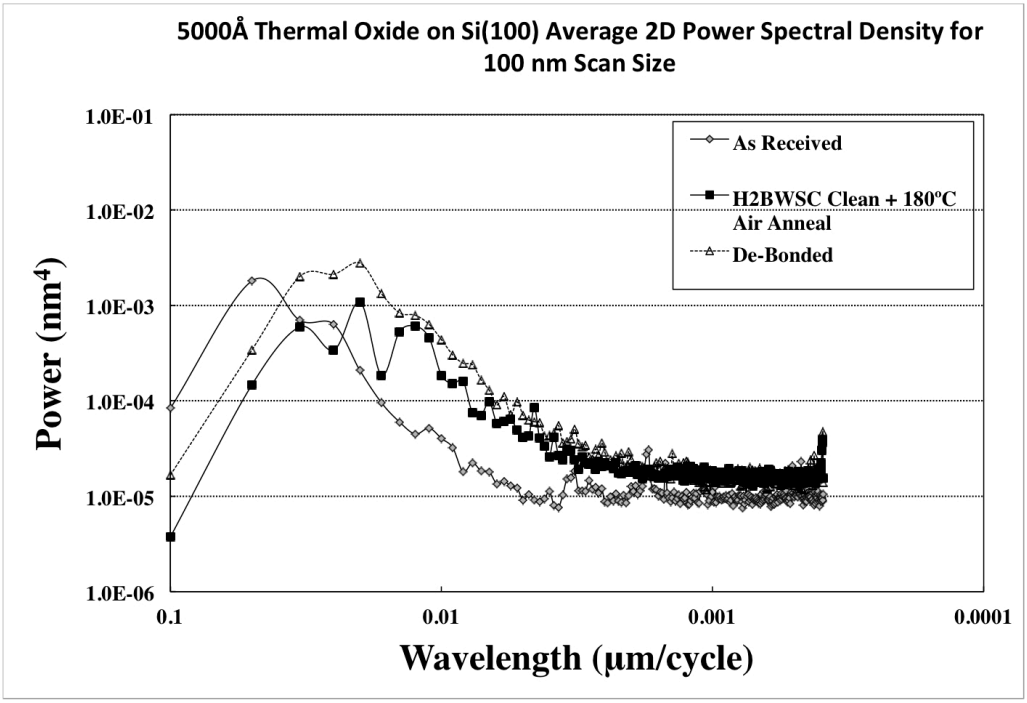

Figure 10-4: The 2D PSD graphs for 5000Å Thermal Oxide wafers As Received, after H2BWSC Clean and 180º C Anneal, and after Debonding. Each PSD is an average of three AFM scans. The graph indicates that each step is increasing the roughness at all wavelengths.

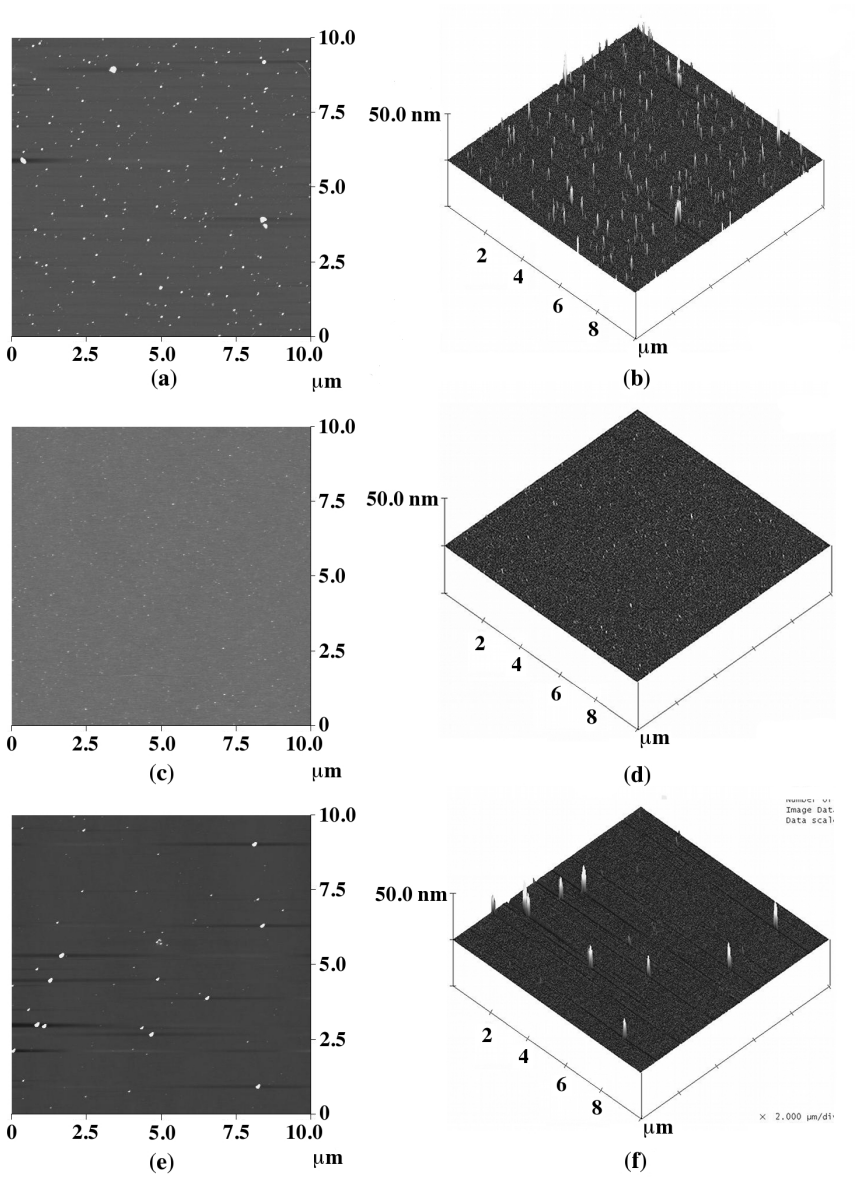

Figure 10-5: Top view and 3-D views of 10 μm AFM height images of three Si(100) samples which underwent different processing: (a-b) after H-A clean + 180º C Anneal, (c-d) after H-A clean, and (e-f) after H-A Spin Etch clean. At the 10 μm scan size, all samples appear as relatively smooth surfaces that primarily differ with respect to the particle count and size.

Si(100) Wafer Processing Step	RMS (nm) Position 1	RMS (nm) Position 2	RMS (nm) Position 3	Average RMS (nm) ± Std Dev.
H-A Clean	0.10	0.07	0.09	0.09 ± 0.01
H-A Clean + 180º C Nano-Bonding Anneal (> 2 hrs)	0.12	0.17	0.11	0.13 ± 0.03
H-A Spin Etch Clean	0.08	0.05	0.06	0.06 ± 0.02

Table 10-5: RMS values of the 100 nm AFM scan size images for three Si(100) wafers, each processed with a distinct method. This data shows that the 180º C anneal increases the roughness after the H-A clean by approximately 30%. The H-A Spin etch clean reduces the Si RMS roughness by 30% versus the H-A clean, showing that is an improvement using this metric.

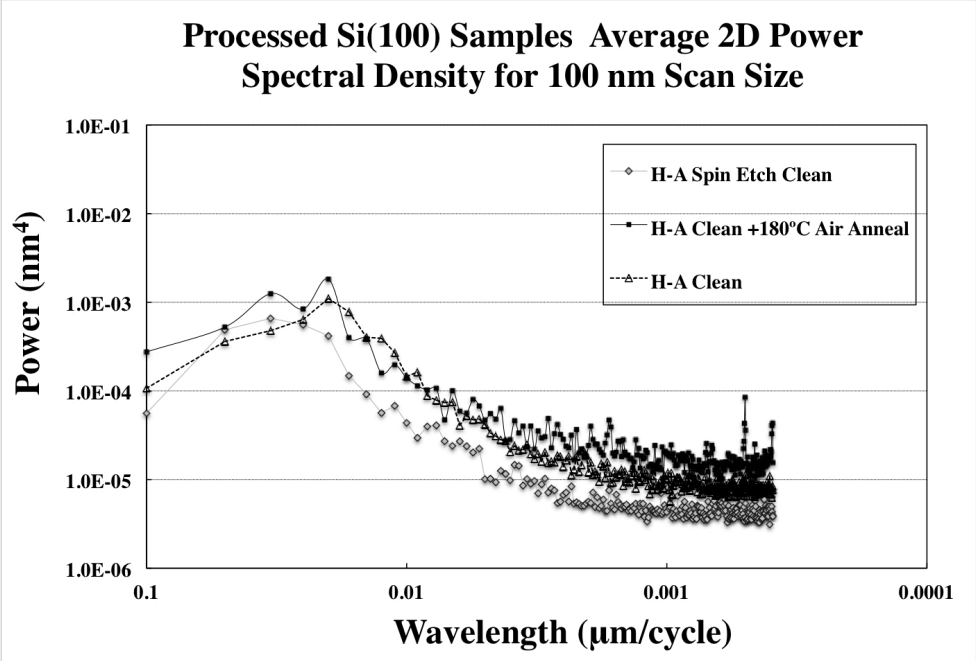

Figure 10-6: The 2D PSD graphs for Si(100) separately processed with the H-A Spin Etch Clean, the H-A Clean and 180º C Anneal, and the H-A clean . This data show the same trends as the RMS roughness data, but it reveals that the H-A Spin Etch is lower in power at nearly all wavelengths. Each PSD is an average of three AFM scans.

Processing step (s) Undergone by Si-Based Material Surfaces prior to Contact Angle Measurement	Contact Angle between 2 MΩ DI Water and Si or SiO_2 $\theta_{2M\Omega\ DI\ Water}$ (degrees)	Contact Angle between Glycerin and Si(100) Surface $\theta_{Glycerin}$ (degrees)	Contact Angle between α-Bromonaphtalene and Si(100) Surface $\theta_{\alpha\text{-}Bromo\text{-}naphthalene}$ (degrees)	Lifshitz-Van der Waals Compon-ent of the Surface Free Energy γ^{LW} (mJ/m^2)	Lewis Acid or Electron Donor Compon-ent of the Surface Free Energy γ^{+} (mJ/m^2)	Lewis Base or Electron Acceptor Compon-ent of the Surface Free Energy γ^{-} (mJ/m^2)	Total Surface Free Energy γ^{Total} (mJ/m^2)	Ref.
Reference As Received Si(100) cut into 1" x 1" samples							78.7	[2]
As Received Si(100) Wafer cut into 1" x 1" samples	38 ± 0.80	31 ± 0.50	19.9 ± 0.50	41.8 ± 0.5	2 ± 0.4	30 ± 3.4	57± 1.9	[5]
As Received Si(100) uncut Wafer	34 ± 0.60	31 ± 2.6	18 ± 1.6	42 ± 0.84	1.8 ± 0.32	33 ± 1.1	57 ± 1.4	[6]

Table 10-6: Contact angle measurements with three different liquids for As Received Si(100) surfaces and resulting experimental value of the total surface free energy (a.k.a Surface tension) in mJ/m^2 derived from the data.

Processing step (s) Undergone by Si-Based Material Surfaces prior to Contact Angle Measurement	Contact Angle between 2 MΩ DI Water and Si or SiO2 $\theta_{2M\Omega\ DI\ Water}$ (degrees)	Contact Angle between Glycerin and Si(100) Surface $\theta_{Glycerin}$ (degrees)	Contact Angle between α-Bromonaphtalene and Si(100) Surface $\theta_{\alpha\text{-}Bromo\text{-}naphthalene}$ (degrees)	Lifshitz-Van der Waals Component of the Surface Free Energy γ^{LW} (mJ/m^2)	Lewis Acid or Electron Donor Component of the Surface Free Energy γ^{+} (mJ/m^2)	Lewis Base or Electron Acceptor Component of the Surface Free Energy γ^{-} (mJ/m^2)	Total Surface Free Energy γ^{Total} (mJ/m^2)	Ref.
After H-A Method, cut & Intermediate Processing	69 ± 0.5	61 ± 0.6	47 ± 0.8	31 ± 1.3	1 ± 0.5	13 ± 2.5	39 ± 2.3	[5]
After H-A Method, uncut wafer, extended non-controlled environment storage	67 ± 1.9	62 ± 1.6	28.9 ± 1.35	39 ± 0.5	0.2 ± 0.03	13.8 ± 1.1	42 ± 0.6	[6]
After H-A Method & 180° C Anneal in Air	100 ± 0.7	92 ± 0.4	59 ± 0.6	26 ± 1.3	0.03 ± 0.1	2.1 ± 1.4	26.0 ± 1.51	[5]

Table 10-7: Contact angle measurements with three different liquids for Si(100) surfaces after H-A method and other processing. The resulting experimental value of the total surface free energy (a.k.a Surface tension) in mJ/m^2. There is a large difference in the Contact Angle between α-Bromonaphtalene and Si(100) Surface when comparing the uncut and cut wafer after H-A method processing. The anneal has also increased all of the contact angles and therefore decreased the Total Surface Free Energy.

Processing step (s) Undergone by Si-Based Material Surfaces prior to Contact Angle Measurement	Contact Angle between 2 MΩ DI Water and Si or SiO2 $\theta_{2M\Omega\ DI\ Water}$ (degrees)	Contact Angle between Glycerin and Si(100) Surface $\theta_{Glycerin}$ (degrees)	Contact Angle between α-Bromonaphtalene and Si(100) Surface $\theta_{\alpha\text{-}Bromo\text{-}naphthalene}$ (degrees)	Lifshitz-Van der Waals Compon-ent of the Surface Free Energy γ^{LW} (mJ/m^2)	Lewis Acid or Electron Donor Compon-ent of the Surface Free Energy γ^{+} (mJ/m^2)	Lewis Base or Electron Acceptor Compon-ent of the Surface Free Energy γ^{-} (mJ/m^2)	Total Surface Free Energy γ^{Total} (mJ/m^2)	Ref.
As Received Wafer-1 after IBMM	79 ± 0.6	78 ± 0.8	23 ± 0.5	41 ± 0.4	0.4 ± 0.2	11 ± 1.9	45 ± 1.2	[5]
As Received Wafer-2 after IBMM	80 ± 1.1	78 ± 1.0	24 ± 0.4	41 ± 0.3	0.4 ± 0.3	9.9 ± 3.1	45 ± 1.7	[5]
Average Values of two As Received Wafers after IBMM	80 ± 0.6	78± 0.6	24 ± 0.3	41 ± 0.3	0.4 ± 0.2	10 ± 1.8	45 ± 1.0	----

Table 10-8: Contact angle measurements with three different liquids for As Received Si(100) surfaces that underwent Ion Beam Modification of Materials surfaces (IBMM) during IBA. The resulting experimental value of the total surface free energy (a.k.a Surface tension) in mJ/m^2 . The averages of the two samples are also shown. The contact angles, all three components of the Free energy, and the Total Surface Free Energy are the same for the two samples, within the experimental error.

Processing step (s) Undergone by Si-Based Material Surfaces prior to Contact Angle Measurement	Contact Angle between 2 MΩ DI Water and Si or SiO2 $\theta_{2M\Omega\ DI\ Water}$ (degrees)	Contact Angle between Glycerin and Si(100) Surface $\theta_{Glycerin}$ (degrees)	Contact Angle between α-Bromonaphtalene and Si(100) Surface $\theta_{\alpha\text{-}Bromo\text{-}naphthalene}$ (degrees)	Lifshitz-Van der Waals Component of the Surface Free Energy γ^{LW} (mJ/m^2)	Lewis Acid or Electron Donor Component of the Surface Free Energy γ^{+} (mJ/m^2)	Lewis Base or Electron Acceptor Component of the Surface Free Energy γ^{-} (mJ/m^2)	Total Surface Free Energy γ^{Total} (mJ/m^2)	Ref.
H-A Method-1 after IBMM	75 ± 1.1	75 ± 0.9	24 ± 0.9	41 ± 0.7	0.3 ± 0.3	14 ± 4.4	44.9 ± 2.25	[5]
H-A Method and 180° C Anneal-1 in air after IBMM	69 ± 0.7	72 ± 0.7	29 ± 1.0	39 ± 1.0	0.2 ± 0.2	20 ± 3.5	42.9 ± 2.26	[5]

Table 10-9: Contact angle measurements with three different liquids for Si(100) surfaces after H-A method and other processing. They then underwent Ion Beam Modification of Materials surfaces (IBMM) during IBA. The resulting experimental value of the total surface free energy (a.k.a Surface tension) in mJ/m^2 .

Processing step (s) Undergone by Si-Based Material Surfaces prior to Contact Angle Measurement	Contact Angle between 2 MΩ DI Water and Si or SiO2 $\theta_{2M\Omega\ DI\ Water}$ (degrees)	Contact Angle between Glycerin and Si(100) Surface $\theta_{Glycerin}$ (degrees)	Contact Angle between α-Bromonaphtalene and Si(100) Surface $\theta_{\alpha\text{-}Bromo\text{-}naphthalene}$ (degrees)	Lifshitz-Van der Waals Compon-ent of the Surface Free Energy γ^{LW} (mJ/m^2)	Lewis Acid or Electron Donor Compon-ent of the Surface Free Energy γ^{+} (mJ/m^2)	Lewis Base or Electron Acceptor Compon-ent of the Surface Free Energy γ^{-} (mJ/m^2)	Total Surface Free Energy γ^{Total} (mJ/m^2)	Ref.
As Received Si(100) Wafer cut into 1" x 1" samples	38 ± 0.8	31 ± 0.5	20 ± 0.5	42 ± 0.5	2 ± 0.4	30 ± 3.4	57 ± 1.9	[5]
As Received Si(100) uncut Wafer	34 ± 0.6	32 ± 2.6	19 ± 1.6	42 ± 0.8	2 ± 0.3	33 ± 1.1	58 ± 1.4	[6]
Difference between Cut 1" x 1" samples and 4" or 6" uncut wafers	3.8 ± 1.0	0.3 ± 2.7	1.2 ± 1.7	0.2 ± 0.9	0.2 ± 0.5	3.3 ± 3.6	0.2 ± 2.3	----

Table 10-10: Contact angle measurements with three different liquids for As Received Si(100) surfaces, both cut and uncut, and resulting experimental value of the total surface free energy (a.k.a Surface tension) in mJ/m^2. Also presented is the difference between the contact angle, components of the Surface Free Energy, and the Total Surface Free Energy. The contact angles for Glyercin and α-Bromonaphtalene, all three components of the Free energy, and the Total Surface Free Energy are the same for the two As Received samples, within the experimental error. The difference between the 2 MΩ DI Water is significant, but is not large enough to deviate the Total Surface Free Energy difference outside the error of the measurements.

Processing step (s) Undergone by Si-Based Material Surfaces prior to Contact Angle Measurement	Contact Angle between 2 MΩ DI Water and Si or SiO2 $\theta_{2M\Omega\ DI\ Water}$ (degrees)	Contact Angle between Glycerin and Si(100) Surface $\theta_{Glycerin}$ (degrees)	Contact Angle between α-Bromonaphtalene and Si(100) Surface $\theta_{\alpha\text{-}Bromo\text{-}naphthalene}$ (degrees)	Lifshitz-Van der Waals Component of the Surface Free Energy γ^{LW} (mJ/m^2)	Lewis Acid or Electron Donor Component of the Surface Free Energy γ^{+} (mJ/m^2)	Lewis Base or Electron Acceptor Compon-ent of the Surface Free Energy γ^{-} (mJ/m^2)	Total Surface Free Energy γ^{Total} (mJ/m^2)	Ref.
After H-A Method, cut & Intermediate Processing	69 ± 0.5	61 ± 0.6	47 ± 0.8	31 ± 1.3	1 ± 0.5	12 ± 2.5	39 ± 2.3	[5]
After H-A Method, wafer, extended non-controlled environment storage	67 ± 1.9	62 ± 1.6	28.9 ± 1.35	39 ± 0.5	0.2 ± 0.03	14 ± 1.1	42 ± 0.6	[6]
Difference between Cut 1" x 1" samples and 4" or 6" uncut wafers	2.2 ± 2.0	0.8 ± 1.7	18 ± 1.6	7.7 ± 1.4	0.9 ± 0.5	1.3 ± 2.7	3.7 ± 2.3	---

Table 10-11: Contact angle measurements with three different liquids for Si(100) surfaces after H-A Method processing, both cut and uncut, and resulting experimental value of the total surface free energy (a.k.a Surface tension) in mJ/m^2. Also presented is the difference between the contact angle, components of the Surface Free Energy, and the Total Surface Free Energy. The α-Bromonaphtalene contact angle shows a large deviation that is significant, while the 2 MΩ DI Water, Electron Donor Component of the surface free energy, Lifshitz-Van der Waals Component of the surface free energy, and the Total Surface Free Energy all show smaller, significant deviations.

Processing step (s) Undergone by Si-Based Material Surfaces prior to Contact Angle Measurement	Contact Angle between 2 MΩ DI Water and Si or SiO2 $\theta_{2M\Omega\ DI\ Water}$ (degrees)	Contact Angle between Glycerin and Si(100) Surface $\theta_{Glycerin}$ (degrees)	Contact Angle between α-Bromonaphtalene and Si(100) Surface $\theta_{\alpha\text{-}Bromo\text{-}naphthalene}$ (degrees)	Lifshitz-Van der Waals Component of the Surface Free Energy γ^{LW} (mJ/m^2)	Lewis Acid or Electron Donor Component of the Surface Free Energy γ^{+} (mJ/m^2)	Lewis Base or Electron Acceptor Compon-ent of the Surface Free Energy γ^{-} (mJ/m^2)	Total Surface Free Energy γ^{Total} (mJ/m^2)	Ref.
After Spin-Etch H-A Method and 180° C Steam Nano-Bonding Anneal, covered	51 ± 2.5	55 ± 0.3	30 ± 1.3	39 ± 0.1	31 ± 0.3	0.1 ± 0.1	43 ± 1.4	[6]
After Spin-Etch H-A Method, and 180° C Steam Nano-Bonding Anneal, uncovered	60 ± 1.8	61 ± 1.1	22 ± 1.6	41 ± 0.5	24 ± 1.6	0.0 ± 0.0	42 ± 0.5	[6]

Table 10-12: Two portions of a Si(100) that previously was processed with the Spin-Etch H-A Method and then underwent 180° C Steam Nano-Bonding Anneal. One portion, the uncovered, had no oxide placed on top in these are where contact angle measurements were taken. The second had a oxide wafer in contact in the area, but no bonding occurred. They show that the Total Surface Free Energy is approximately the same as the H-A method processed wafers, but the Electron Donor and Electron Acceptor Components of the Surface Free Energy have changed. The electron donor contribution increases from near 0 mJ/m^2 to 30 mJ/m^2, which means the surface is dramatically enriched in negative charge carriers, such as OH^-. The electron acceptor component goes to 0 mJ/m^2, which is expected if Boron acceptors are oxidized, as happens more easily in steam oxidation.

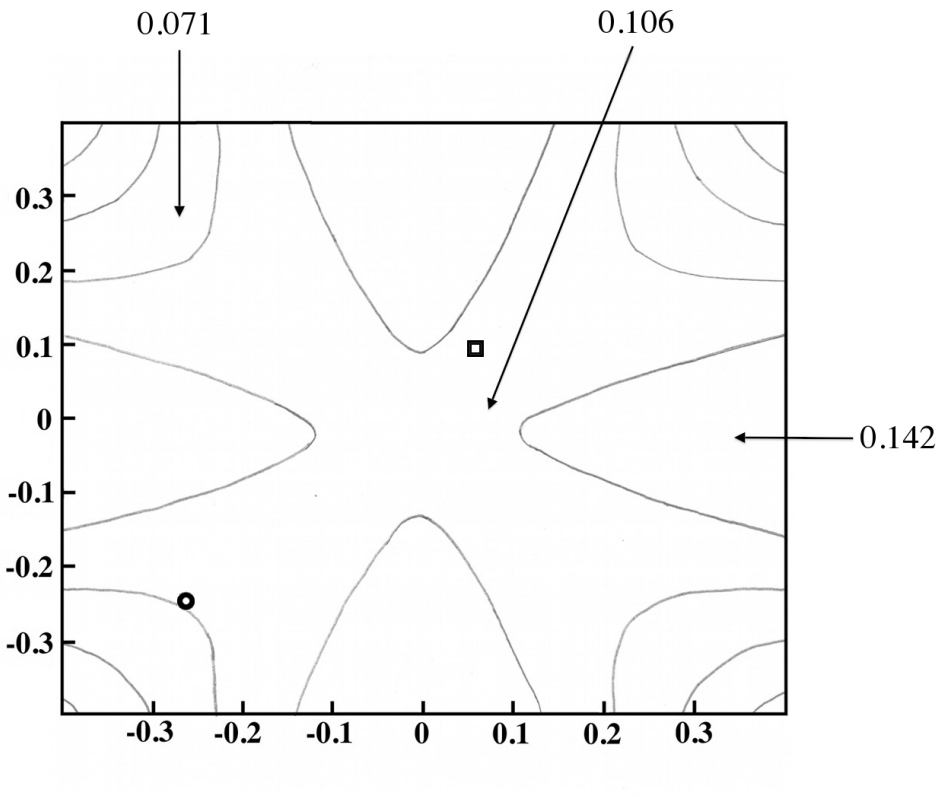

Figure 10-7: An approximate replication of a portion of the stereographic projection figure of the Poisson Ratio for bulk phase β-cristobalite from a paper by P. S. Tomakova [8]. It shows the Poisson ratio for compression and expansion in both the [100], which is shown on the x-axis, and in the [010] direction, shown in the y-axis. Each axis is a portion of the compression up to 40%, which is shown on the graph as -0.4 , and the expansion up to 40%, shown as 0.4. The center of the graph is at a Poisson ratio of 0.106. The ratio increases along the lateral and horizontal, but decreases in the four diagonal directions. Each line is a difference of approximately 0.35. Both the Poisson ratio of bulk phase β-cristobalite contracted 24% (○) in each direction, corresponding to the β-cristobalite crystal fitted to Si(100) , and expanded 7% (□), corresponding to the β-cristobalite(110) crystal fitted to Si(100) .

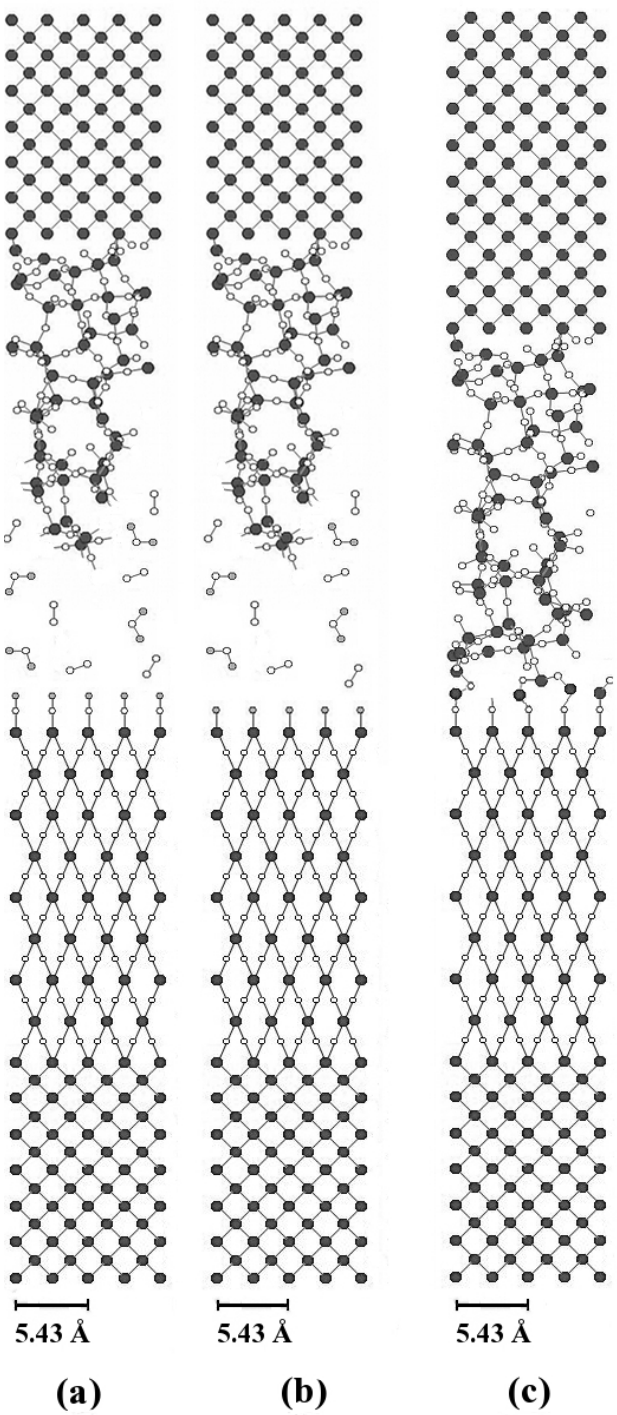

Figure 10-8: The structures are: (a) Si(100) with density conserved β-cristobalite –OH terminated, O_2 and H_2O molecules, amorphous silica with dangling bonds on Si(100); (b) Identical to (a), but having β-cristobalite –H terminated; (c) Si(100) with density conserved β-cristobalite bonded to amorphous silica on Si(100). The Si atoms are dark gray, the O atoms are white, and the H atoms are light gray.

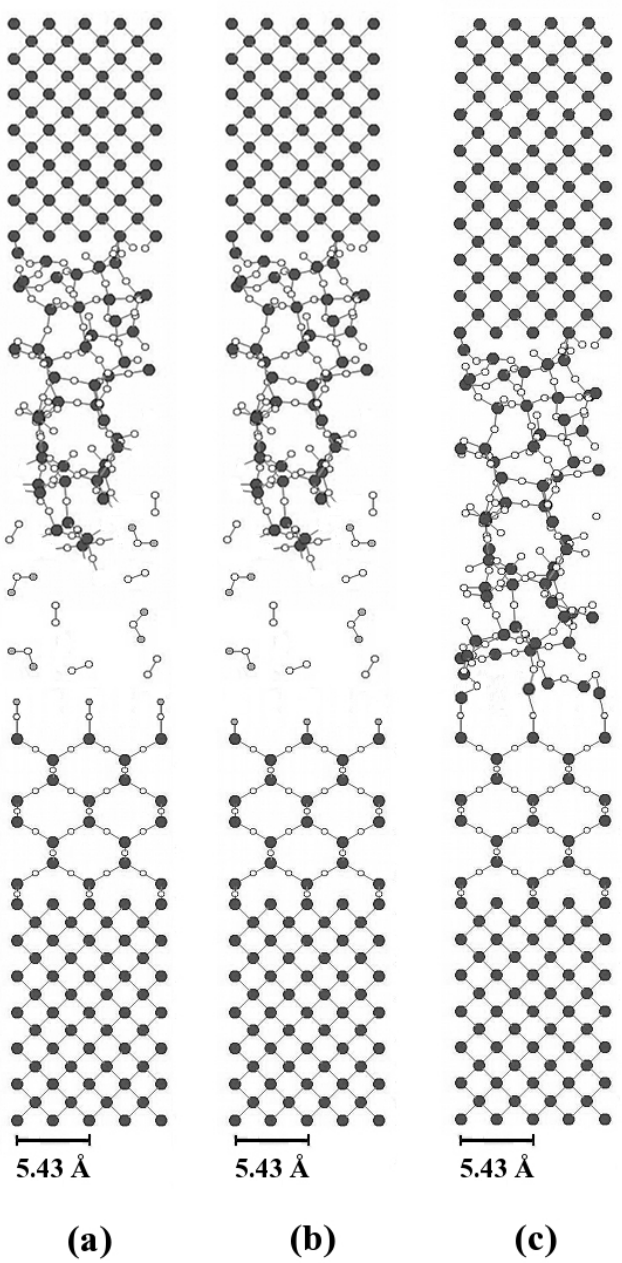

Figure 10-9: The structures are: (a) Si(100) with density conserved β-cristobalite(110) –OH terminated, O_2 and H_2O molecules, amorphous silica with dangling bonds on Si(100); (b) Identical to (a), but having β-cristobalite(110) –H terminated; (c) Si(100) with density conserved β-cristobalite(110) bonded to amorphous silica on Si(100). The Si atoms are dark gray, the O atoms are white, and the H atoms are light gray.

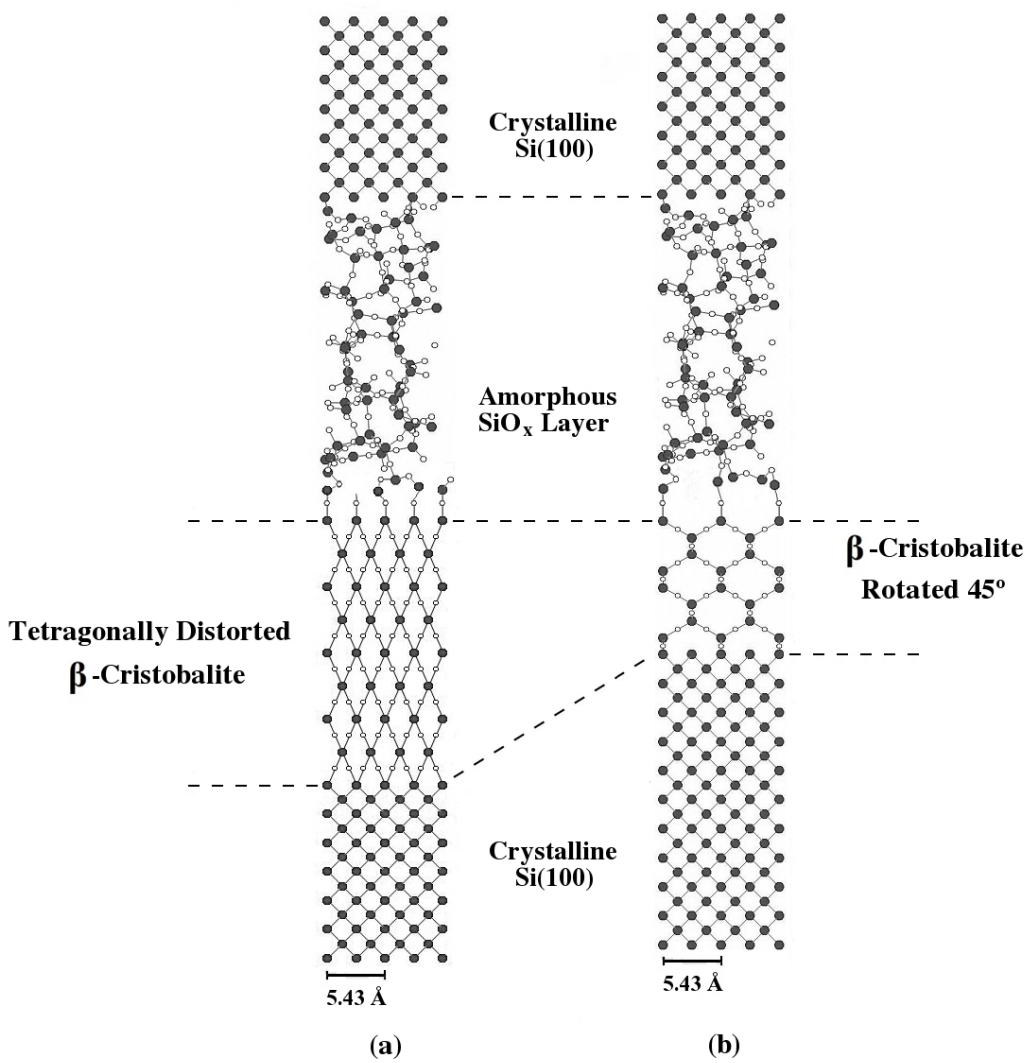

Figure 10-10: The structures are: (a) Si(100) with density conserved β-cristobalite bonded to amorphous silica on Si(100). (b) Si(100) with density conserved β-cristobalite(110) bonded to amorphous silica on Si(100). The Si atoms are dark gray, and the O atoms are white.

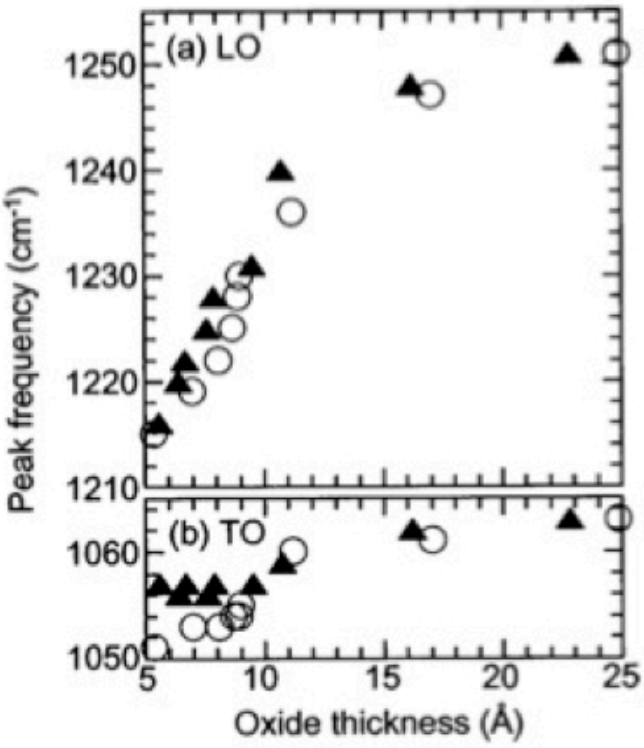

Figure 10-11: The longitudinal-optic (LO) and transverse-optic (TO) peak frequencies as a function of film thickness for the H-A cleaned substrate (▲) and the RCA cleaned substrates (○) [9].

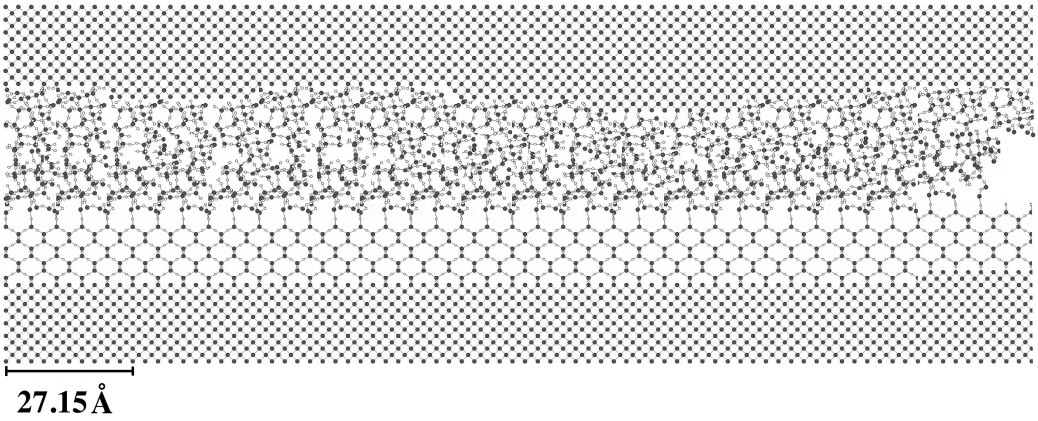

Figure 10-12: The structural arrangements for nano-bonding, for beta-cristobalite(110). This shows a smooth Si(100) base that has wide terraces that are 20 nm in width, as aspected from a H-A processed Si(100) substrate. The top Si(100) has an amorphous silica initially grown on it. Since the Si(100) wafers with silica that were received from manufacturers in this thesis were not process with the H-A method before silica was grown, this silicon substrate is shown with the 2nm step width that would be expected. The nano-bonding process proceeds in a lateral direction and is shown as an incomplete bonding on the right hand side. This may continue, or it may stop at this point, due to the kinetics of the bridging.

Reference Chapter 10

[1] Hans-Jürgen Butt, Michael Kappl, *Surface and Interfacial Forces*, Wiley-VCH (2010)

[2] R S. Faibish, W. Yoshida, Y. Cohen*, J. Colloid Interface Sci*. 256, 2, 341-350 (2002)

[3] C. J. van Oss, R. J. Good, *J. Macromol. Sci. Chem. A* **26**, 1183 (1989)

[4] A. Carre, *J. Adhesion Sci. Technol*. **21**, 10, 961–981 (2007)

[5] N. Herbots, Q. Xing, M. A. Hart, J. D. Bradley, D. A. Sell, R. J. Culbertson, B. J. Wilkens, *Nucl. Instr. and Meth. B* (2011)

[6] R. B. Bennett-Kennett, *Honors thesis*, to be published

[7] James M. Gere, Barry J. Goodno, *Mechanics of Materials*, CL-Engineering (2011)

[8] S. P. Tomakova, *Phys. Stat. Sol B* **242**, 3, 721-729 (2005)

[9] K. T. Queeney, N. Herbots, J. M. Shaw, V. Atluri, V. Y. J. Chabal, *Appl. Phys. Lett*. **84**, 4, 493-496 (2004)

Chapter 11: Future Work

11.1 Future Work in Nano-Bonding

The Steam Nano-bonding is providing a pathway that may achieve similar bonding with a less complex mechanism for providing pressure to bond the wafers together. This technology is in the process of being patented and a company, Solvay, is planning to partner with the CIMD SiO_2 Research Group at ASU to work towards a thin film encapsulation method for photovoltaics using this nano-bonding method.

11.2 Future Work in Nano-phase structure

In the Herbots et a. paper of 2001 [1], it was shown that the critical supersaturation of hydrogen occuring in H-A processed, ordered beta-cristobalite nano-phases is a ratio1:1, which derived from IBA analysis and IR, where the chemical compound SiO_2 was found to contain a 2 nm-thick, far-from-equilibrium 2D heteroepitaxial nanofilm. It is not shown in the images in this thesis, but including hydrogen in the next structure is the logical step in further modeling these new experimental nanophases from a fundamental perspective. The measured stoichiometry by IBA and IR is $SiO_2(Hx)$ where $X = 1 \leq x \leq 2.4$.

11.3 Future Work in VASP Simulation

At the conclusion of the simulations in VASP, two possibilities arose for further, future investigation. The first entailed the fact that the relaxed structures had movement of silicon atoms three layers into the Si(100). To achieve a more accurate representation of the underlying silicon and the reaction of the β–

cristobalite and/or silica, several more layers of Si(100) should be added to the structure and then relaxed using VASP. The second possibility for VASP simulation is to construct a larger block of amorphous silica to attempt to obtain the energy by relaxing the silica. This silica structure will need to be constructed so that it is pseudo-amorphous at the edges, so that the simulation, which replicates the structure along the three Cartesian axes, which causes high forces in the atoms at the edge in strictly amorphous silica structures.

There is also a possibility to refine the initial interface between the crystal β–cristobalite(110) and the amorphous silica to enhance the positions at the boundary between the two phases and minimize any initial dangling bonds.

Finally, including hydrogen in the next beta-cristobalite structure is the next step in simulating these new experimental nanophases.

11.4 Future work in 3DSTRING Simulation

The shadowcone data of β–cristobalite (110) on Si(100) showed that this configuration has the possibility of achieving the results found in the IBA channeling data. The information on the relative positions of the presented in Chapter 9 and the distances between sets in the (110) and (111) directions should allow the construction of the strings necessary to accomplish the simulations. The Poisson ratio data could also be used to create structures that hold to the bulk phase model and could be compared to the results from the models in this thesis. The simulated data can then be compared to the IBA data to draw a more

definitive conclusion on the possibility of the β–cristobalite (110) allowing for enough blocking to match experimental results.

11.5 Future work in Atomic Force Microscopy

There are several samples that were processed using the spin-etch H-A method which have not received AFM analysis. These samples could provide a richer understanding of the process by completing the AFM imaging and comparing the RMS, PSD, and topography to the all the AFM data presented in this thesis.

APPENDIX A

CRYSTAL DATA

Atoms	x	y	z
Si	0	0	0
Si	0	5.43	0
Si	5.43	0	0
Si	5.43	5.43	0
Si	2.715	2.715	0
Si	1.3575	1.3575	1.3575
Si	4.0725	4.0725	1.3575
Si	0	2.715	2.715
Si	2.715	0	2.715
Si	5.43	2.715	2.715
Si	2.715	5.43	2.715
Si	4.0725	1.3575	4.0725
Si	1.3575	4.0725	4.0725
Si	2.715	2.715	5.43
Si	5.43	5.43	5.43
Si	5.43	0	5.43
Si	0	5.43	5.43
Si	0	0	5.43

Table A-1: Cartesian Coordinates for Si(100)

Atom	x	y	z
Si	0	0	0
Si	0	7.166	0
Si	3.583	3.583	0
Si	7.166	0	0
Si	7.166	7.166	0
O	0.89575	6.27025	0.89575
O	2.68725	4.47875	0.89575
O	4.47875	2.68725	0.89575
O	6.27025	0.89575	0.89575
Si	1.7915	5.3745	1.7915
Si	5.3745	1.7915	1.7915
O	0.89575	4.47875	2.68725
O	2.68725	6.27025	2.68725
O	4.47875	0.89575	2.68725
O	6.27025	2.68725	2.68725
Si	0	3.583	3.583
Si	3.583	0	3.583
Si	3.583	7.166	3.583
Si	7.166	3.583	3.583
O	0.89575	2.68725	4.47875
O	2.68725	0.89575	4.47875
O	4.47875	6.27025	4.47875
O	6.27025	4.47875	4.47875
Si	1.7915	1.7915	5.3745
Si	5.3745	5.3745	5.3745
O	0.89575	0.89575	6.27025
O	2.68725	2.68725	6.27025
O	4.47875	4.47875	6.27025
O	6.27025	6.27025	6.27025
Si	0	0	7.166
Si	0	7.166	7.166
Si	3.583	3.583	7.166
Si	7.166	0	7.166
Si	7.166	7.166	7.166

Table A-2: Cartesian Coordinates for ideal β-cristobalite(100)

	x	y	z
Si	0	0	0
Si	0	5.067	0
Si	5.067	0	0
Si	5.067	5.067	0
Si	2.5335	0	1.7915
Si	2.5335	5.067	1.7915
Si	2.5335	2.5335	3.583
Si	0	2.5335	5.3745
Si	5.067	2.5335	5.3745
Si	0	0	7.166
Si	0	5.067	7.166
Si	5.067	0	7.166
Si	5.067	5.067	7.166
O	1.26675	0	0.89575
O	3.80025	0	0.89575
O	1.26675	5.067	0.89575
O	3.80025	5.067	0.89575
O	2.5335	1.26675	2.68725
O	2.5335	3.80025	2.68725
O	1.26675	2.5335	4.47875
O	3.80025	2.5335	4.47875
O	0	1.26675	6.27025
O	0	3.80025	6.27025
O	5.067	1.26675	6.27025
O	5.067	3.80025	6.27025

Table A-3: Cartesian Coordinates for β-cristobablite(110)

APPENDIX B

ADDITIONAL SHADOW CONE DATA

In Chapter 9, there were several sets of β-cristobalite atoms, or even a few atoms in a set, that did not produce shadow cones that enveloped Si(100) atoms. Those sets are presented here.

The sets of β-cristobalite(110) atoms on Si(100) in the <110> and <111> directions that did not shadow will be the first presented in this appendix. For the <110> direction there are two sets, Set 1 and 3, which are identical. Figure B-1 shows the visual representation of the set, which only includes Si(100) atoms. Table B-1 is the relative coordinates for the two sets. This data is presented so that the only the relative y and z coordinates are shown, since the atoms in a set share x coordinates. The position of the lowest atoms designates where z is equal to zero and the atom with the smallest y value is set to zero. Only the surface Si(100) atom and two additional atoms below it are shown, although there will be another Si atom ever 3.84Å thoughout the Si(100) crystal along this z axis. Since these are Si(100) atoms, no shadow cone data was calculated.

Set 2 has a more complicated arrangement. Figure B-2 is a visual representation and Table B-2 is the relative coordinates for the set. Tables B-3 to B-5 are the shadow cone radii for a 3.05 MeV He^{++} atom interacting with each β-cristobalite(110) Si atom along the the <110> direction, in Set 2.

Set 4 also did not have shadowing for the (A), (C), and (D) β-cristobalite(110) Si atoms, so that data appears in Tables B-6 to B-8.

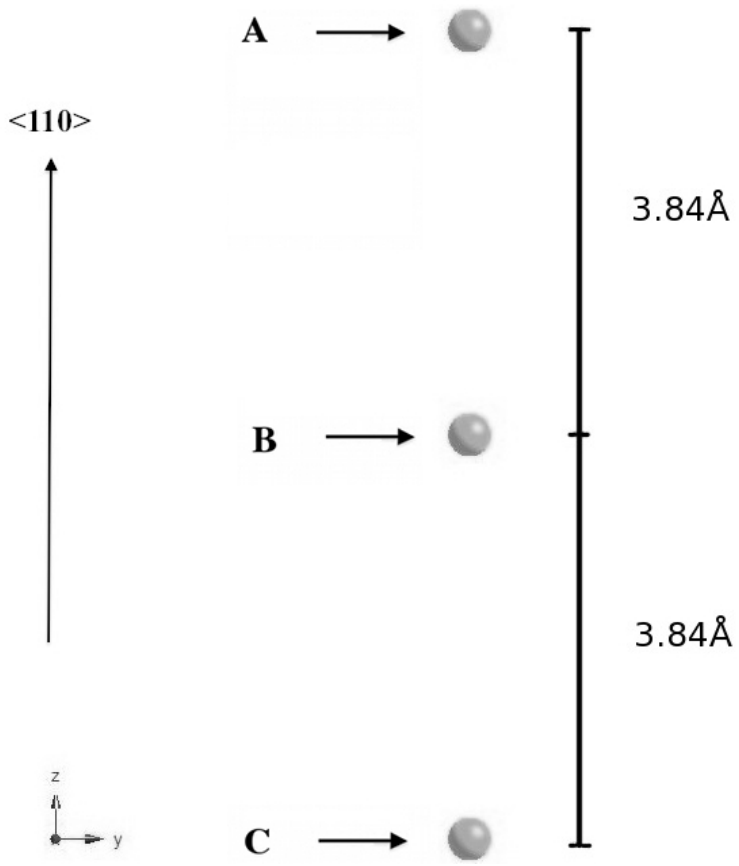

Figure B-1: Visual representation of both Set 1 and 3 of the <110> direction, since the are identical. This is only Si(100) atoms, which are light gray. The z direction is the <110> direction.

Atom Type	y (Å)	z (Å)
(A) Si(100)	0.00	7.68
(B) Si(100)	0.00	3.84
(C) Si(100)	0.00	0.00

Table B-1: Set 1 and 3 of the <110> direction relative coordinates, in Angstroms.

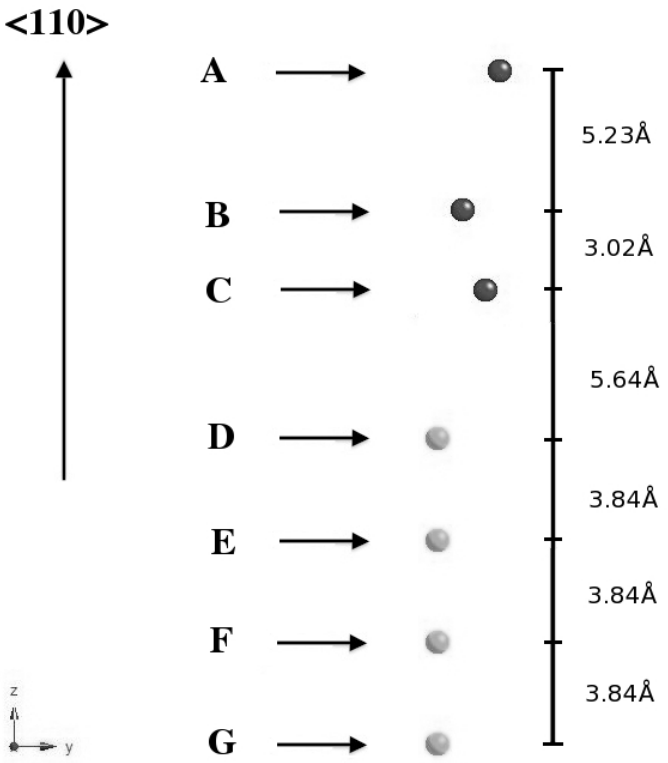

Figure B-2: Visual representation of Set 2 of the <110> direction. The Si in the β-cristobalite(110) are shown in dark gray and the Si(100) atoms are light gray. The z direction is the <110> direction.

Atom	y (Å)	z (Å)
(A) β-cristobalite(110) Si	2.37	25.41
(B) β-cristobalite(110) Si	0.98	20.18
(C) β-cristobalite(110) Si	1.80	17.16
(D) Si(100)	0.00	11.52
(E) Si(100)	0.00	7.68
(F) Si(100)	0.00	3.84
(G) Si(100)	0.00	0.00

Table B-2: Set 2 of the <110> direction relative coordinates, in Angstroms.

Atom Type	Absolute Distance along <110> axis(Å)	Shadow cone Radius (Å)	Horizontal Distance (Å)
(A) β-cristobalite(110) Si	0.00	0.00	----
(B) β-cristobalite(110) Si	5.23	0.05	1.39
(C) β-cristobalite(110) Si	8.25	0.07	0.57
(D) Si(100)	13.89	0.09	2.37
(E) Si(100)	17.73	0.10	2.37
(F) Si(100)	21.57	0.11	2.37
(G) Si(100)	25.41	0.12	2.37

Table B-3: Shadowcone Radii for z distances, which is the <110> direction, for a 3.05 MeV He^{++} atom interacting with the (A) β-cristobalite(110) Si atom of Set 2.

Atom Type	Absolute Distance along <110> axis(Å)	Shadow cone Radius (Å)	Horizontal Distance (Å)
(B) β-cristobalite(110) Si	0.00	0.00	----
(C) β-cristobalite(110) Si	3.02	0.04	-0.82
(D) Si(100)	8.66	0.07	0.98
(E) Si(100)	12.50	0.08	0.98
(F) Si(100)	16.34	0.09	0.98
(G) Si(100)	20.18	0.10	0.98

Table B-4: Shadowcone Radii for z distances, which is the <110> direction, for a 3.05 MeV He^{++} atom interacting with the (B) β-cristobalite(110) Si atom of Set 2.

Atom Type	Distance along z axis(Å)	Shadow cone Radius (Å)	Horizontal Distance (Å)
(C) β-cristobalite(110) Si	0.00	0.00	0.00
(D) Si(100)	5.64	0.05	1.80
(E) Si(100)	9.48	0.07	1.80
(F) Si(100)	13.32	0.08	1.80
(G) Si(100)	17.16	0.10	1.80

Table B-5: Shadowcone Radii for z distances, which is the <110> direction, for a 3.05 MeV He^{++} atom interacting with the (C) β-cristobalite(110) Si atom of Set 2.

Atom Type	Absolute Distance along <110> axis (Å)	Shadow cone Radius (Å)	Horizontal Distance (Å)
(A) β-cristobalite(110) Si	0.00	0.00	----
(B) β-cristobalite(110) Si	3.03	0.04	0.82
(C) β-cristobalite(110) Si	8.26	0.07	-0.57
(D) β-cristobalite(110) Si	11.28	0.08	0.25
(E) Si(100)	14.71	0.09	0.66
(F) Si(100)	18.55	0.10	0.66
(G) Si(100)	22.39	0.11	0.66

Table B-6: Shadowcone Radii for z distances, which is the <110> direction, for a 3.05 MeV He^{++} atom interacting with the (A) β-cristobalite(110) Si atom of Set 4.

Atom Type	Absolute Distance along <110> axis (Å)	Shadow cone Radius (Å)	Horizontal Distance (Å)
(C) β-cristobalite(110) Si	0.00	0.00	----
(D) β-cristobalite(110) Si	3.02	0.04	0.82
(E) Si(100)	6.45	0.06	1.23
(F) Si(100)	10.29	0.07	1.23
(G) Si(100)	14.13	0.09	1.23

Table B-7: Shadowcone Radii for z distances, which is the <110> direction, for a 3.05 MeV He^{++} atom interacting with the (C) β-cristobalite(110) Si atom of Set 4.

Atom Type	Absolute Distance along <110> axis (Å)	Shadow cone Radius (Å)	Horizontal Distance (Å)
(D) β-cristobalite(110) Si	0.00	0.00	----
(E) Si(100)	3.43	0.04	0.41
(F) Si(100)	7.27	0.06	0.41
(G) Si(100)	11.11	0.08	0.41

Table B-8: Shadowcone Radii for z distances, which is the <110> direction, for a 3.05 MeV He^{++} atom interacting with (D) β-cristobalite(110) Si atom of Set 4, located at y= 0.82Å and z= 11.11Å

For β-cristobalite(110) atoms on Si(100) in the <111> direction, there are three sets. Set 1 is all Si(100) atoms, so no shadowing calculations are computed. A visual representation is shown in Figure B-3, along the <111> direction and the relative coordinates are presented in Table B-9.

The Set 2 visual representation along the <111> direction is shown in Figure B-4 and Table B-10 is the relative coordinates for the set. Tables B-11 to B-13 show the shadowcone radii for the three β-cristobalite(110) Si atoms when interacting with a 3.05 MeV He^{++} atom.

For Set 3 of the β-cristobalite(110) in the <111> direction, the (A), (B) and (D) atoms show no shadowing and the shadow cone calculations are presented in Tables B-13 through B-16

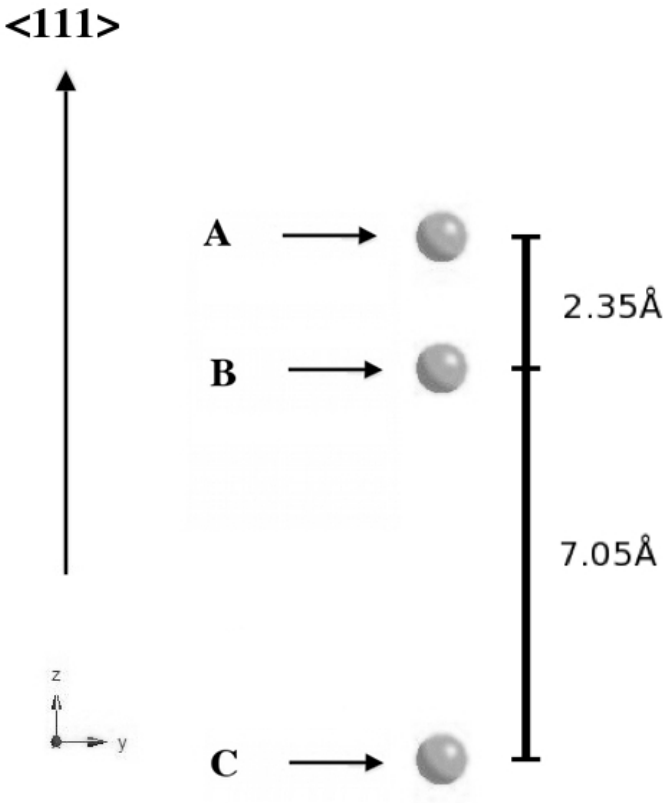

Figure B-3: Visual representation of Set 1 of the <111> direction. The Si in the β-cristobalite(110) are shown in dark gray and the Si(100) atoms are light gray. The z direction is the <111> direction.

Atom Type	y (Å)	z (Å)
(A) Si(100)	0.00	9.40
(B) Si(100)	0.00	7.05
(C) Si(100)	0.00	0.00

Table B-9: Set 1 for <111> direction relative coordinates, in Angstroms.

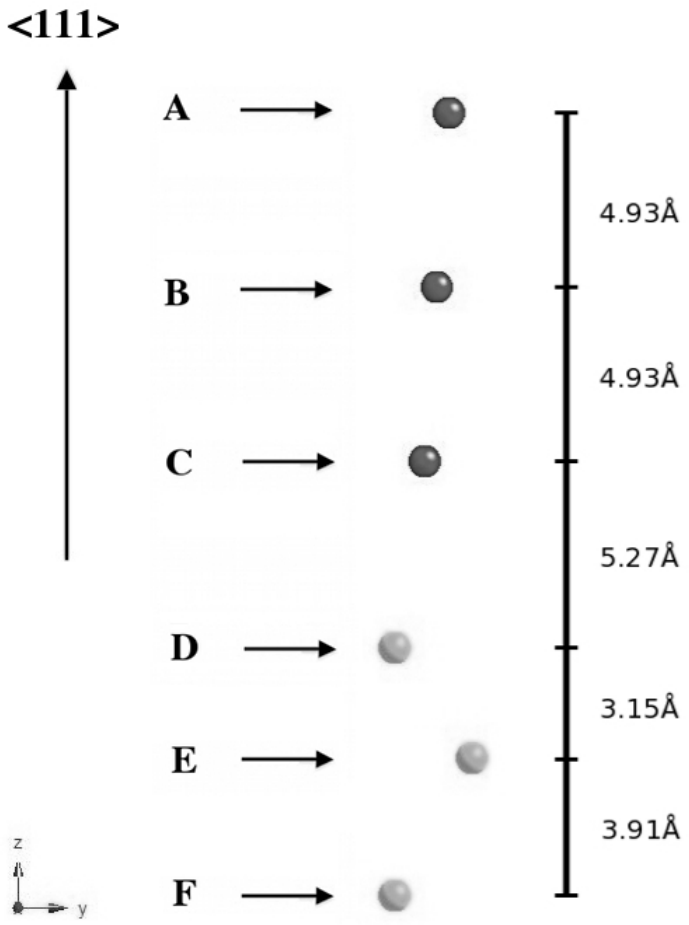

Figure B-4: Visual representation of Set 2 of the <111> direction. The Si in the β-cristobalite(110) are shown in dark gray and the Si(100) atoms are light gray. The z direction is the <111> direction.

Atom Type	y (Å)	z (Å)
(A) β-cristobalite(110) Si	1.57	22.19
(B) β-cristobalite(110) Si	1.21	17.25
(C) β-cristobalite(110) Si	0.86	12.32
(D) Si(100)	0.03	7.05
(E) Si(100)	2.23	3.91
(F) Si(100)	0.00	0.00

Table B-10: Set 2 for <111> direction relative coordinates, in Angstroms.

Atom Type	Absolute Distance along <111> axis (Å)	Shadow cone Radius (Å)	Horizontal Distance (Å)
(A) β-cristobalite(110) Si	0.00	0.00	----
(B) β-cristobalite(110) Si	4.94	0.05	0.36
(C) β-cristobalite(110) Si	9.87	0.07	0.71
(D) Si(100)	15.14	0.09	1.54
(E) Si(100)	18.28	0.10	-0.66
(F) Si(100)	22.19	0.11	1.57

Table B-11: Shadowcone Radii for z distances, which is the <111> direction, for a 3.05 MeV He^{++} atom interacting with the (A) β-cristobalite(110) Si atom of Set 2.

Atom Type	Absolute Distance along <111> axis (Å)	Shadow cone Radius (Å)	Horizontal Distance (Å)
(B) β-cristobalite(110) Si	0.00	0.00	----
(C) β-cristobalite(110) Si	4.93	0.05	0.35
(D) Si(100)	10.20	0.07	1.18
(E) Si(100)	13.34	0.08	-1.02
(F) Si(100)	17.25	0.10	1.21

Table B-12: Shadowcone Radii for z distances, which is the <111> direction, for a 3.05 MeV He^{++} atom interacting with the (B) β-cristobalite(110) Si atom of Set 2.

Atom Type	Absolute Distance along <111> axis (Å)	Shadow cone Radius (Å)	Horizontal Distance (Å)
(C) β-cristobalite(110) Si	0.00	0.00	----
(D) Si(100)	5.27	0.05	0.83
(E) Si(100)	8.41	0.07	-1.37
(F) Si(100)	12.32	0.08	0.86

Table B-13: Shadowcone Radii for z distances, which is the <111> direction, for a 3.05 MeV He^{++} atom interacting with the (C) β-cristobalite(110) Si atom of Set 2.

Atom Type	Absolute Distance along <111> axis (Å)	Shadow cone Radius (Å)	Horizontal Distance (Å)
(A) β-cristobalite(110) Si	0.00	0.00	----
(B) β-cristobalite(110) Si	4.94	0.05	0.35
(C) β-cristobalite(110) Si	9.87	0.07	0.71
(D) β-cristobalite(110) Si	14.81	0.09	1.06
(E) Si(100)	21.53	0.10	0.62
(F) Si(100)	23.88	0.11	0.63

Table B-14: Shadowcone Radii for z distances, which is the <111> direction, for a 3.05 MeV He^{++} atom interacting with the (A) β-cristobalite(110) Si atom of Set 3.

Atom Type	Absolute Distance along <111> axis (Å)	Shadow cone Radius (Å)	Horizontal Distance (Å)
(B) β-cristobalite(110) Si	0.00	0.00	----
(C) β-cristobalite(110) Si	4.93	0.05	0.35
(D) β-cristobalite(110) Si	9.87	0.07	0.71
(E) Si(100)	16.59	0.09	0.27
(F) Si(100)	18.94	0.10	0.28

Table B-15: Shadowcone Radii for z distances, which is the <111> direction, for a 3.05 MeV He^{++} atom interacting with (B) β-cristobalite(110) Si atom of Set 3.

Atom Type	Absolute Distance along <111> axis (Å)	Shadow cone Radius (Å)	Horizontal Distance (Å)
(D) β-cristobalite(110) Si	0.00	0.00	----
(E) Si(100)	6.72	0.06	0.44
(F) Si(100)	9.07	0.07	0.43

Table B-16: Shadowcone Radii for z distances, which is the <111> direction, for a 3.05 MeV He^{++} atom interacting with (D) β-cristobalite(110) Si atom of Set 3, located at y= 0.00Å and z= 9.07Å

The second type of β-cristobalite that was presented in Chapter 9 was the elongated β-cristobalite. In both the <110> and <111>, the shadow cone calculations showed no shadowing.

There two sets in the <110> direction for elongated β-cristobalite. Figure B-5 is a visual representation of the Set 1 and Table B-17 is the relative coordinates. Tables B-18 and B-19 provide the shadow cone radii for a 3.05 MeV He^{++} atom interacting with the (A) and (B) elongate β-cristobalite Si atoms in Set 1. Figure B-6 is a visual representation of Set 2 of elongated β-cristobalite in the <110> direction and Table B-20 is the relative coordinates. Tables B-21 and B-22 are the shadowcone radii for a 3.05 MeV He^{++} atom interacting with the (A) and (B) elongate β-cristobalite Si atoms in the <110> direction for Set 2.

There are also two sets in the <111> direction for elongated β-cristobalite. The visual representation of set 1 in the <111> direction is shown in Figure B-7, with the relative coordinates for this set are presented in Table B-23. The shadowcone Radii for distances along the <111> for a 3.05 MeV He^{++} atom interacting with (A) elongated β-cristobalite Si atom of Set 1 is shown in Table B-24. Table B-25 shows the data for the shadowcone for the (B) elongated β-cristobalite Si atom of Set 1. Figure B-8 shows the visual representation for Set 2 in the <111> direction and the relative coordinates are in Table B-26 and. Tables B-27 and B-28 show the shadowcone radii for the two elongated β-cristobalite Si atoms in set 2 when interacting with a 3.05 MeV He^{++} atom.

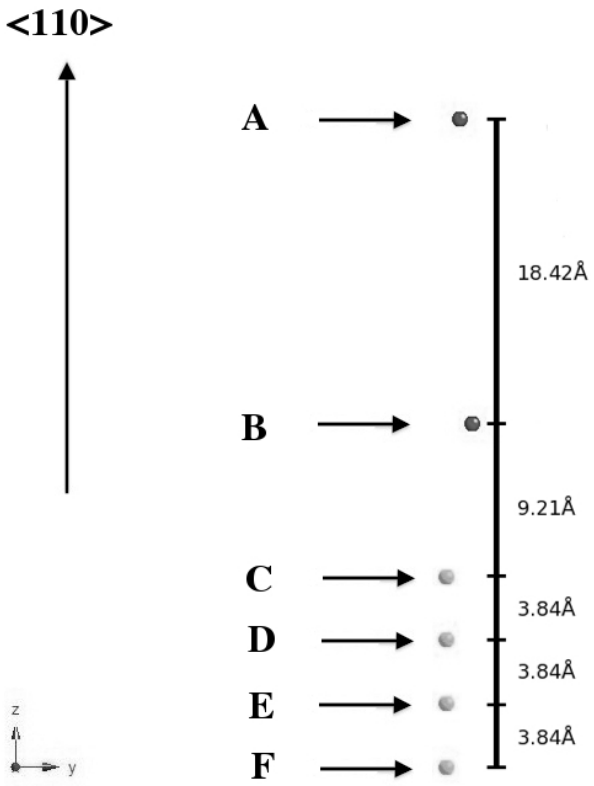

Figure B-5: Visual representation of Set 1 of the <110> direction. The Si in the elongated β-cristobalite are shown in dark gray and the Si(100) atoms are light gray. The z direction is the <110> direction.

Atom Type	y (Å)	z (Å)
(A) Elong. β-cristobalite Si	0.76	39.15
(B) Elong. β-cristobalite Si	1.53	20.73
(C) Si(100)	0.00	11.52
(D) Si(100)	0.00	7.68
(E) Si(100)	0.00	3.84
(F) Si(100)	0.00	0.00

Table B-17: Set 1 of the <110> direction relative coordinates, in Angstroms.

Atom Type	Absolute Distance along <110> axis(Å)	Shadow cone Radius (Å)	Horizontal Distance (Å)
(A) Elong. β-cristobalite Si	0.00	0.00	----
(B) Elong. β-cristobalite Si	18.42	0.10	-0.77
(C) Si(100)	27.63	0.12	0.77
(D) Si(100)	31.47	0.13	0.77
(E) Si(100)	35.31	0.14	0.77
(F) Si(100)	39.15	0.14	0.77

Table B-18: Shadowcone Radii for z distances, which is the <110> direction, for a 3.05 MeV He^{++} atom interacting with the (A) elongated β-cristobalite Si atom of Set 1.

Atom Type	Absolute Distance along <110> axis(Å)	Shadow cone Radius (Å)	Horizontal Distance (Å)
(B) Elong. β-cristobalite Si	0.00	0.00	----
(C) Si(100)	9.21	0.07	1.53
(D) Si(100)	13.05	0.08	1.53
(E) Si(100)	16.89	0.09	1.53
(F) Si(100)	20.73	0.10	1.53

Table B-19: Shadowcone Radii for z distances, which is the <110> direction, for a 3.05 MeV He^{++} atom interacting with the (B) elongated β-cristobalite Si atom of Set 1.

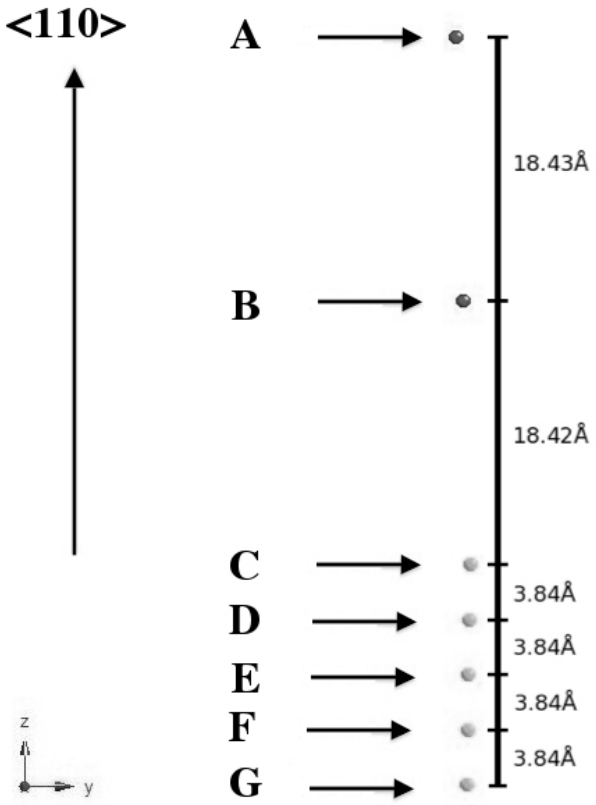

Figure B-6: Visual representation of Set 2 of the <110> direction. The Si in the elongated β-cristobalite are shown in dark gray and the Si(100) atoms are light gray. The z direction is the <110> direction.

Atom Type	y (Å)	z (Å)
(A) Elong. β-cristobalite Si	0.00	52.21
(B) Elong. β-cristobalite Si	0.77	33.78
(C) Si(100)	1.55	15.36
(D) Si(100)	1.55	11.52
(E) Si(100)	1.55	7.68
(F) Si(100)	1.55	3.84
(G) Si(100)	1.55	0.00

Table B-20: Set 2 of the <110> direction relative coordinates, in Angstroms.

Atom Type	Absolute Distance along <110> axis(Å)	Shadow cone Radius (Å)	Horizontal Distance (Å)
(A) Elong. β-cristobalite Si	0.00	0.00	----
(B) Elong. β-cristobalite Si	18.43	0.10	0.77
(C) Si(100)	36.85	0.14	1.55
(D) Si(100)	40.69	0.15	1.55
(E) Si(100)	44.53	0.15	1.55
(F) Si(100)	48.37	0.16	1.55
(G) Si(100)	52.21	0.17	1.55

Table B-21: Shadowcone Radii for z distances, which is the <110> direction, for a 3.05 MeV He^{++} atom interacting with the (A) elongated β-cristobalite Si atom for Set 2.

Atom Type	Absolute Distance along <110> axis(Å)	Shadow cone Radius (Å)	Horizontal Distance (Å)
(B) Elong. β-cristobalite Si	0.00	0.00	----
(C) Si(100)	18.42	0.10	0.78
(D) Si(100)	22.26	0.11	0.78
(E) Si(100)	26.10	0.12	0.78
(F) Si(100)	29.94	0.13	0.78
(G) Si(100)	33.78	0.13	0.78

Table B-22: Shadowcone Radii for z distances, which is the <110> direction, for a 3.05 MeV He^{++} atom interacting with the (B) elongated β-cristobalite Si atom for Set 2.

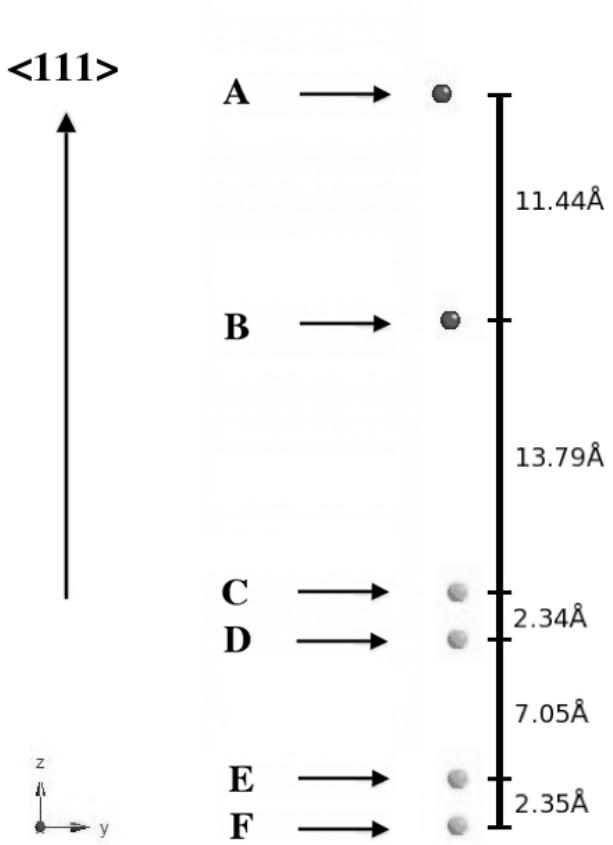

Figure B-7: Visual representation of Set 1 of the <111> direction. The Si in the elongated β-cristobalite are shown in dark gray and the Si(100) atoms are light gray. The z direction is the <111> direction.

Atom Type	y (Å)	z (Å)
(A) Elong. β-cristobalite Si	0.00	36.99
(B) Elong. β-cristobalite Si	0.39	25.55
(C) Si(100)	0.75	11.76
(D) Si(100)	0.75	9.40
(E) Si(100)	0.75	2.35
(F) Si(100)	0.75	0.00

Table B-23: Set 1 for <111> direction relative coordinates, in Angstroms

Atom Type	Absolute Distance along <111> axis(Å)	Shadow cone Radius (Å)	Horizontal Distance (Å)
(A) Elong. β-cristobalite Si	0.00	0.00	----
(B) Elong. β-cristobalite Si	11.44	0.08	0.39
(C) Si(100)	25.24	0.12	0.75
(D) Si(100)	27.59	0.12	0.75
(E) Si(100)	34.64	0.14	0.75
(F) Si(100)	36.99	0.14	0.75

Table B-24: Shadowcone Radii for z distances, which is the <111> direction, for a 3.05 MeV He^{++} atom interacting with the (A) elongated β-cristobalite Si atom of Set 1.

Atom Type	Absolute Distance along <111> axis (Å)	Shadow cone Radius (Å)	Horizontal Distance (Å)
(B) Elong. β-cristobalite Si	0.00	0.00	----
(C) Si(100)	13.79	0.09	0.36
(D) Si(100)	16.14	0.09	0.36
(E) Si(100)	23.20	0.11	0.36
(F) Si(100)	25.55	0.12	0.36

Table B-25: Shadowcone Radii for z distances, which is the <111> direction, for a 3.05 MeV He^{++} atom interacting with the (B) elongated β-cristobalite Si atom of Set 1.

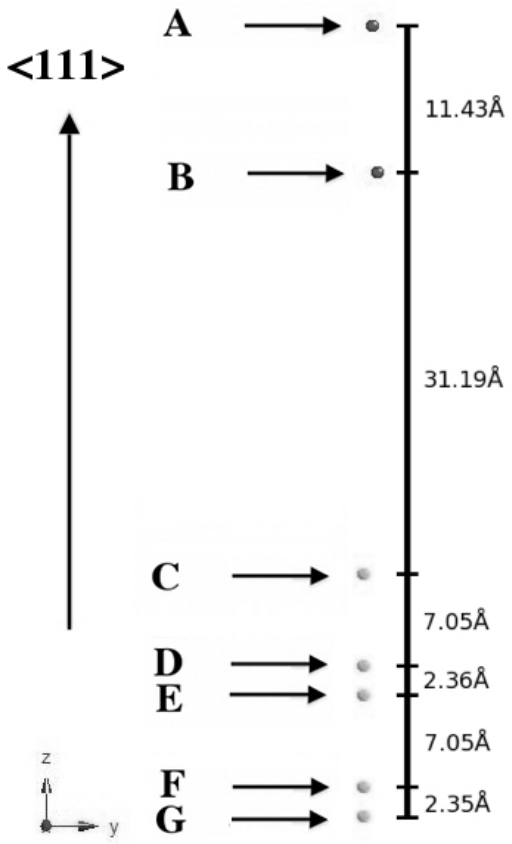

Figure B-8: Visual representation of Set 2 of the <111> direction. The Si in the elongated β-cristobalite are shown in dark gray and the Si(100) atoms are light gray. The z direction is the <111> direction.

Atom Type	y (Å)	z (Å)
(A) Elong. β-cristobalite Si	0.67	61.43
(B) Elong. β-cristobalite Si	1.07	50.00
(C) Si(100)	0.00	18.81
(D) Si(100)	0.00	11.76
(E) Si(100)	0.00	9.40
(F) Si(100)	0.00	2.35
(G) Si(100)	0.00	0.00

Table B-26: Set 2 for <111> direction relative coordinates, in Angstroms.

Atom Type	Absolute Distance along <111> axis (Å)	Shadow cone Radius (Å)	Horizontal Distance (Å)
(A) Elong. β-cristobalite Si	0.00	0.00	----
(B) Elong. β-cristobalite Si	11.44	0.08	-0.39
(C) Si(100)	42.62	0.15	0.67
(D) Si(100)	49.68	0.16	0.67
(E) Si(100)	52.03	0.17	0.67
(F) Si(100)	59.08	0.18	0.67
(G) Si(100)	61.43	0.18	0.67

Table B-27: Shadowcone Radii for z distances, which is the <111> direction, for a 3.05 MeV He^{++} atom interacting with the (A) elongated β-cristobalite Si atom of Set 2.

Atom Type	Absolute Distance along <111> axis (Å)	Shadow cone Radius (Å)	Horizontal Distance (Å)
(B) Elong. β-cristobalite Si	0.00	0.00	----
(C) Si(100)	31.18	0.13	1.07
(D) Si(100)	38.23	0.14	1.07
(E) Si(100)	40.59	0.15	1.07
(F) Si(100)	47.64	0.16	1.07
(G) Si(100)	50.00	0.16	1.07

Table B-28: Shadowcone Radii for z distances, which is the <111> direction, for a 3.05 MeV He^{++} atom interacting with the (B) elongated β-cristobalite Si atom of Set 2.

The third structure in Chapter 9 is β-cristobalite on Si(100). In the <110> direction, there are four sets that make up the structure. The first set is a single β-cristobalite Si atoms with no Si(100) atoms. Since it is a single atom, and can not shadow Si(100), no visual representation or calculation is offered. The second set consists of three β-cristobalite Si atoms with no Si(100) atoms in line with this set. The visual representation of the set are presented in Figure B-9. The relative coordinates are shown in Table B-29. There are no Si(100) atoms in the set to shadow, so no shadow cone calculations are presented**.** The third set has a visual representation presented in Figure B-10 and relative coordinates in Table B-30. The shadow cone calculations for the three β-cristobalite Si atoms are displayed in Tables B-31 through B-33.

β-cristobalite on Si(100) in the <111> direction has two sets that make up the structure. The first set has a visual representation presented in Figure B-11 and relative coordinates in Table B-34. The four β-cristobalite Si atoms do not produce shadow cones that envelop near surface Si(100) atoms, so the shadow cone data is presented in Tables B-35 through B-38. The second set has two β-cristobalite Si atoms do not produce shadow cones that envelop near surface Si(100) atoms and the shadow cone calculation are presented in Tables B39 and B-40.

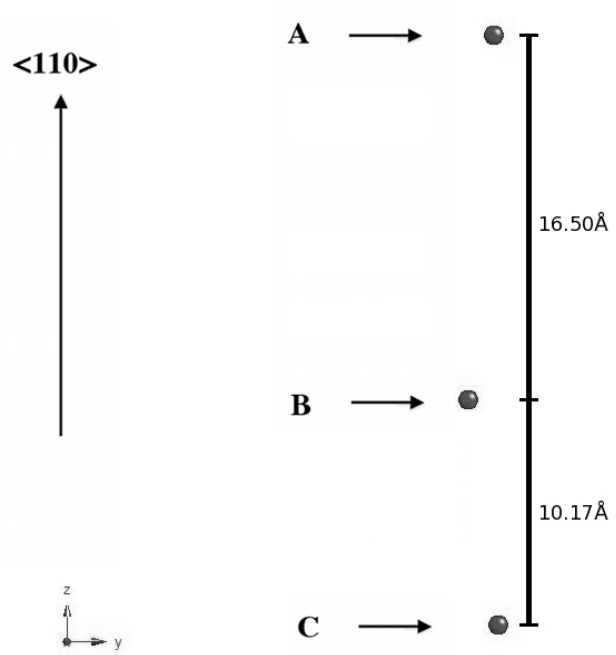

Figure B-9: Visual representation of Set 2 of the <110> direction. The Si in the β-cristobalite are shown in dark gray and the Si(100) atoms are light gray. The z direction is the <110> direction.

Atom Type	y (Å)	z (Å)
(A) β-cristobalite Si	1.14	26.67
(B) β-cristobalite Si	0.00	10.17
(C) β-cristobalite Si	1.35	0.00

Table B-29: Set 2 of the <110> direction relative coordinates, in Angstroms.

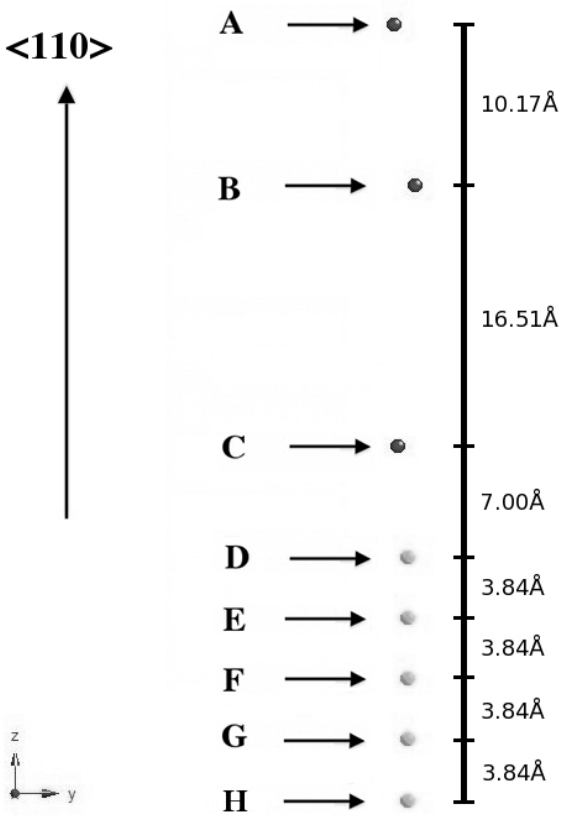

Figure B-10: Visual representation of Set 3 of the <110> direction. The Si in the β-cristobalite are shown in dark gray and the Si(100) atoms are light gray. The z direction is the <110> direction.

Atom Type	y (Å)	z (Å)
(A) β-cristobalite Si	0.00	49.04
(B) β-cristobalite Si	1.35	38.87
(C) β-cristobalite Si	0.20	22.36
(D) Si(100)	0.88	15.36
(E) Si(100)	0.88	11.52
(F) Si(100)	0.88	7.68
(G) Si(100)	0.88	3.84
(H) Si(100)	0.88	0.00

Table B-30: Set 3 of the <110> direction relative coordinates, in Angstroms.

Atom Type	Absolute Distance along <110> axis (Å)	Shadow cone Radius (Å)	Horizontal Distance (Å)
(A) β-cristobalite Si	0.00	0.00	----
(B) β-cristobalite Si	10.17	0.07	1.35
(C) β-cristobalite Si	26.67	0.12	0.20
(D) Si(100)	33.68	0.13	0.88
(E) Si(100)	37.52	0.14	0.88
(F) Si(100)	41.36	0.15	0.88
(G) Si(100)	45.20	0.15	0.88
(H) Si(100)	49.04	0.16	0.88

Table B-31: Shadowcone Radii for z distances, which is the <110> direction, for a 3.05 MeV He^{++} atom interacting with the (A) β-cristobalite Si atom for Set 3.

Atom Type	Absolute Distance along <110> axis (Å)	Shadow cone Radius (Å)	Horizontal Distance (Å)
(B) β-cristobalite Si	0.00	0.00	----
(C) β-cristobalite Si	16.50	0.09	1.14
(D) Si(100)	23.51	0.11	0.47
(E) Si(100)	27.35	0.12	0.47
(F) Si(100)	31.19	0.13	0.47
(G) Si(100)	35.03	0.14	0.47
(H) Si(100)	38.87	0.14	0.47

Table B-32: Shadowcone Radii for z distances, which is the <110> direction, for a 3.05 MeV He^{++} atom interacting with the (B) β-cristobalite Si atom for Set 3.

Atom Type	Absolute Distance along <110> axis (Å)	Shadow cone Radius (Å)	Horizontal Distance (Å)
(C) β-cristobalite Si	0.00	0.00	----
(D) Si(100)	7.01	0.06	0.68
(E) Si(100)	10.85	0.08	0.68
(F) Si(100)	14.69	0.09	0.68
(G) Si(100)	18.53	0.10	0.68
(H) Si(100)	22.37	0.11	0.68

Table B-33: Shadowcone Radii for z distances, which is the <110> direction, for a 3.05 MeV He^{++} atom interacting with the (C) β-cristobalite Si atom for Set 3.

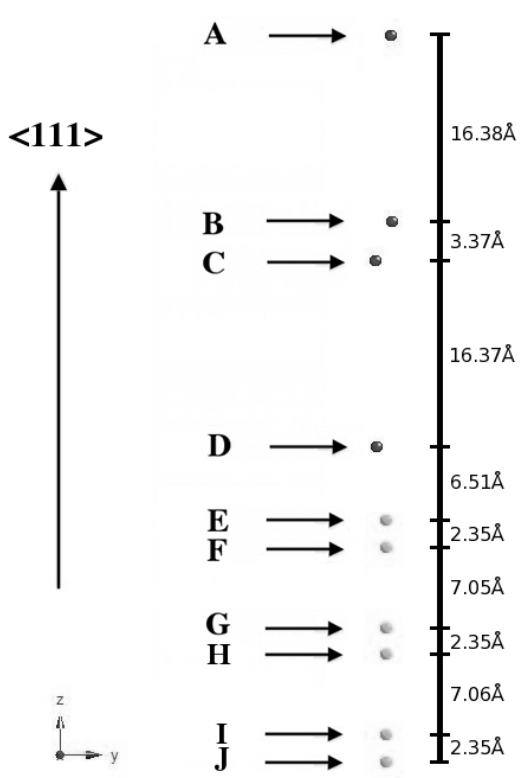

Figure B-11: Visual representation of Set 1 of the <111> direction. The Si in the β-cristobalite are shown in dark gray and the Si(100) atoms are light gray. The z direction is the <111> direction.

Atom Type	y (Å)	z (Å)
(A) β-cristobalite Si	1.34	63.79
(B) β-cristobalite Si	1.44	47.41
(C) β-cristobalite Si	0.00	44.04
(D) β-cristobalite Si	0.10	27.67
(E) Si(100)	0.87	21.16
(F) Si(100)	0.87	18.81
(G) Si(100)	0.87	11.76
(H) Si(100)	0.87	9.41
(I) Si(100)	0.87	2.35
(J) Si(100)	0.87	0.00

Table B-34: Set 1 for <111> direction relative coordinates, in Angstroms.

Atom Type	Absolute Distance along <111> axis (Å)	Shadow cone Radius (Å)	Horizontal Distance (Å)
(A) β-cristobalite Si	0.00	0.00	----
(B) β-cristobalite Si	16.38	0.09	-0.10
(C) β-cristobalite Si	19.74	0.10	1.34
(D) β-cristobalite Si	36.12	0.14	1.25
(E) Si(100)	42.62	0.15	0.48
(F) Si(100)	44.98	0.15	0.48
(G) Si(100)	52.03	0.17	0.48
(H) Si(100)	54.38	0.17	0.48
(I) Si(100)	61.43	0.18	0.48
(J) Si(100)	63.79	0.18	0.48

Table B-35: Shadowcone Radii for z distances, which is the <111> direction, for a 3.05 MeV He^{++} atom interacting with the (A) β-cristobalite Si atom of Set 1.

Atom Type	Absolute Distance along <111> axis (Å)	Shadow cone Radius (Å)	Horizontal Distance (Å)
(B) β-cristobalite Si	0.00	0.00	----
(C) β-cristobalite Si	3.37	0.04	1.44
(D) β-cristobalite Si	19.74	0.10	1.34
(E) Si(100)	26.25	0.12	0.57
(F) Si(100)	28.60	0.12	0.57
(G) Si(100)	35.65	0.14	0.57
(H) Si(100)	38.00	0.14	0.57
(I) Si(100)	45.06	0.15	0.57
(J) Si(100)	47.41	0.16	0.57

Table B-36: Shadowcone Radii for z distances, which is the <111> direction, for a 3.05 MeV He^{++} atom interacting with the (B) β-cristobalite Si atom of Set 1.

Atom Type	Absolute Distance along <111> axis (Å)	Shadow cone Radius (Å)	Horizontal Distance (Å)
(C) β-cristobalite Si	0.00	0.00	----
(D) β-cristobalite Si	16.38	0.09	0.10
(E) Si(100)	22.88	0.11	0.87
(F) Si(100)	25.23	0.12	0.87
(G) Si(100)	32.29	0.13	0.87
(H) Si(100)	34.64	0.14	0.87
(I) Si(100)	41.69	0.15	0.87
(J) Si(100)	44.04	0.15	0.87

Table B-37: Shadowcone Radii for z distances, which is the <111> direction, for a 3.05 MeV He^{++} atom interacting with the (C) β-cristobalite Si atom of Set 1.

Atom Type	Absolute Distance along <111> axis (Å)	Shadow cone Radius (Å)	Horizontal Distance (Å)
(D) β-cristobalite Si	0.00	0.00	----
(E) Si(100)	6.50	0.06	0.77
(F) Si(100)	8.86	0.07	0.77
(G) Si(100)	15.91	0.09	0.77
(H) Si(100)	18.26	0.10	0.77
(I) Si(100)	25.31	0.12	0.77
(J) Si(100)	27.67	0.12	0.77

Table B-38: Shadowcone Radii for z distances, which is the <111> direction, for a 3.05 MeV He^{++} atom interacting with the (D) β-cristobalite Si atom of Set 1.

Atom Type	Absolute Distance along <111> axis (Å)	Shadow cone Radius (Å)	Horizontal Distance (Å)
(A) β-cristobalite Si	0.00	0.00	----
(B) β-cristobalite Si	6.50	0.06	0.77
(C β-cristobalite Si	22.88	0.11	0.87
(D) β-cristobalite Si	26.25	0.12	-0.57
Si(100)	43.96	0.15	0.96
Si(100)	46.31	0.16	0.96
Si(100)	53.36	0.17	0.96
Si(100)	55.72	0.17	0.96

Table B-39: Shadowcone Radii for z distances, which is the <111> direction, for a 3.05 MeV He^{++} atom interacting with the (A) β-cristobalite Si atom of Set 2.

Atom Type	Absolute Distance along <111> axis (Å)	Shadow cone Radius (Å)	Horizontal Distance (Å)
(D) β-cristobalite Si	0.00	0.00	
Si(100)	17.71	0.10	1.54
Si(100)	20.06	0.10	1.54
Si(100)	27.12	0.12	1.54
Si(100)	29.47	0.12	1.54

Table B-40: Shadowcone Radii for z distances, which is the <111> direction, for a 3.05 MeV He^{++} atom interacting with the (D) β-cristobalite Si atom of Set 2.

APPENDIX C

PRESENTATIONS, PAPERS, AND PATENTS

Q. X. Bradley, N. Herbots, M. Hart, J. D. Bradley, B. J. Wilkens, D. A. Sell, Clive H. Sell, H. M. Kwong Jr., R. J. Culbertson, S. D. Whaley, *Ion Beam Analysis of Silicon-Based Surfaces And Correlation With Surface Energy Mesurements*, Application of Accelerators in Research and Industry, AIP Conf. Proc. 1336, 201-207 (2011)

M. Hart, S. D. Whaley, J. D. Bradley, D. A. Sell, N. Herbots, R. Culbertson, V. Atluri, *Low Temperature Bonding of Si to Silicates using Langmuir-Blodgett molecular Films as precursors for a bonding SilOxSi Interphase*, 2008 Joint Fall Meeting of the Texas and Four Corners Sections of American Physical Society (APS), AAPT, and Zones 13 and 16 of SPS, and the Societies of Hispanic & Black Physicists, October 17–18, 2008, El Paso, Texas.

N. Herbots, J. D. Bradley, S. D. Whaley, M. Hart, R. J. Culbertson, D. A. Sell, M. Cassetti, *NanoOxides™ & Nanobonding™ - A New Class Of Silicate Molecular Sheets For High Efficiency Solar Cells With Ordered Interfacial Oxides And High Longevity Bonding Interphases For Solar Cell Encapsulation*, Nanotech 2009 Conference & Expo, May 3-7, Houston, TX

R. B. Bennett-Kennett, S. D. Whaley, N. Herbots, J. D. Bradley, R. J. Culbertson, M. A. Hart, D. A. Sell, Q. X. Bradley, R. L. Rhoades, S. N. Drews, Entrepix, Inc., *Nanobonding between 2-nm β-crystobalite SiO 2 on OH(1x1)Si(100) and SiO x for Monolithic Electronics by Surface Smoothing via Wet Chemical and Spin Processing: TMAFM Study and Modelling of Interphases,* Surface Science Division Session, AVS-58 Symposium, Nashville, TN

R. B. Bennett-Kennett, S. D. Whaley, S. J. Farmer, A. M. Murphy, D. B Hudzietz, M. T. Bade, *Role of Surface Energy, Hydroaffinity, & Topography in Nano-bonding™ of Si(100) with silica polymorphs using a β-cristobalite precursor phase: A Quantitative analysis and atomistic model*, Abstract submitted to the Student Poster competition for the NanoTechnology Session, AAAS 2012 annual meeting, Feb. 16 – 20, Vancouver, Canada

S. D. Whaley, N. Herbots, J. D. Bradley, R. J. Culbertson, M. A. Hart, D. A. Sell, Q. X. Bradley, R. L. Rhoades, S. N. Drews, *Wafer Bonding between b-cristobalite SiO_2 on OH(1x1)Si(100) and Silica for Monolithic Electronics: Characterization and Phemenological Model for Nano-bonding*, In submission to Journ. Appl. Phys.

A Method for Wafer Bonding and for Nucleating Bonding Nanophases
Inventor(s): N. Herbots, J. D. Bradley, M. Hart, D. A. Sell, S. D. Whaley, R.J Culbertson Provisional Patent Application SN 61/174,138 , Arizona State University/Arizona Technology Entreprise (filed March 30, 2009).

Molecular films for controlling hydrophobic, hydrophilic, optical, condensation and geometricproperties of silicone implants surfaces, including intra-occular lenses used in cataract surgeries. Inventor(s): N. Herbots, J. D. Bradley, M. Hart, D. A. Sell & S. D. Whaley
Arizona State University/Arizona Technology Entreprise Provisional patent application filed October 2, 2009

Methods for Wafer Bonding and for Nucleating Bonding Nanophases Using Wet and Steam Pressurization, N. Herbots, S.D. Whaley, Ross Bennett-Kennett, R.J. Culbertson, A.M. Murphy, S.J. Farmer, US Patent filed October 31, 2011

Molecular Film Containing Polymeric Mixture for Hydrophobic Implant Surfaces N. Herbots, A, M. Murphy, R. Kennett-Bennett, D.A. Sell S.D. Whaley, R.J. Culbertson, US Patent filed October 31, 2011

ASU/AZTE Technology Disclosure M11-163P "H2O Nano-Bonding " Synthesis via compressive strain from sursaturated water vapor at low temperatures (T< 175°C) of a siloxane--silica mixed nano-bonding phase catalyzed by H2O, nano-scale smoothing and ordering of Si(100) & silica, and room temperature chemical reactivity arising from surface polarization through surface charge generation in SiO2. N. Herbots, S.D. Whaley, Ross Bennett-Kennett, R.J. Culbertson, A.M. Murphy, S.J. Farmer, filed June 24th, 2011